

Research Topics in Wind Energy 8

Lorenzo Battisti *Editor*

Wind Energy Exploitation in Urban Environment

TUrbWind 2018 Colloquium



Research Topics in Wind Energy

Volume 8

Series Editors

Joachim Peinke, University of Oldenburg, Institute of Physics & ForWind,
Oldenburg, Germany

Gerard von Bussel, Delft University of Technology, TU Delft Wind Energy Group,
Delft, The Netherlands

The series Research Topics in Wind Energy publishes new developments and advances in the fields of Wind Energy Research and Technology, rapidly and informally but with a high quality. Wind Energy is a new emerging research field characterized by a high degree of interdisciplinarity. The intent is to cover all the technical contents, applications, and multidisciplinary aspects of Wind Energy, embedded in the fields of Mechanical and Electrical Engineering, Physics, Turbulence, Energy Technology, Control, Meteorology and Long-Term Wind Forecasts, Wind Turbine Technology, System Integration and Energy Economics, as well as the methodologies behind them. Within the scope of the series are monographs, lecture notes, selected contributions from specialized conferences and workshops, as well as selected PhD theses. Of particular value to both the contributors and the readership are the short publication time frame and the worldwide distribution, which enable both wide and rapid dissemination of research output. The series is promoted under the auspices of the European Academy of Wind Energy. Indexed by SCOPUS and SpringerLink.

More information about this series at <http://www.springer.com/series/11859>

Lorenzo Battisti
Editor

Wind Energy Exploitation in Urban Environment

TUrbWind 2018 Colloquium

 Springer

Editor
Lorenzo Battisti
University of Trento
Trento, Italy

ISSN 2196-7806 ISSN 2196-7814 (electronic)
Research Topics in Wind Energy
ISBN 978-3-030-13530-0 ISBN 978-3-030-13531-7 (eBook)
<https://doi.org/10.1007/978-3-030-13531-7>

Library of Congress Control Number: 2019931541

© Springer Nature Switzerland AG 2019

This work is subject to copyright. All rights are reserved by the Publisher, whether the whole or part of the material is concerned, specifically the rights of translation, reprinting, reuse of illustrations, recitation, broadcasting, reproduction on microfilms or in any other physical way, and transmission or information storage and retrieval, electronic adaptation, computer software, or by similar or dissimilar methodology now known or hereafter developed.

The use of general descriptive names, registered names, trademarks, service marks, etc. in this publication does not imply, even in the absence of a specific statement, that such names are exempt from the relevant protective laws and regulations and therefore free for general use.

The publisher, the authors and the editors are safe to assume that the advice and information in this book are believed to be true and accurate at the date of publication. Neither the publisher nor the authors or the editors give a warranty, express or implied, with respect to the material contained herein or for any errors or omissions that may have been made. The publisher remains neutral with regard to jurisdictional claims in published maps and institutional affiliations.

This Springer imprint is published by the registered company Springer Nature Switzerland AG
The registered company address is: Gewerbestrasse 11, 6330 Cham, Switzerland

Preface

The volume contains the written versions of most of the contributions presented during the TURbWind Colloquium—Research and innovation on wind energy exploitation in urban environment organized by the University of Trento that took place in Riva del Garda, Italy, from September 6 to 7, 2018.

The purpose of this colloquium was to discuss the state-of-the-art and the recent developments on wind energy exploitation in urban and suburban area. The urban environment offers a peculiar wind resource, highly variable, and extremely turbulent. In order to harvest wind energy in an efficient and durable manner, urban wind turbines have to be properly designed. At the same time, this environment is where the human energy demand is mostly concentrated. Integration of wind turbines on existing or dedicated buildings or, where possible, as free-standing installation in public areas requires a different design approach compared to open areas. Such issues drive opportunities for innovation and development.

The TURbWind Colloquium was intended to provide a forum for experts on wind energy exploitation in urban areas to present and discuss the state of the art of the technology, exchange ideas, and get informed about the latest research trends in the domain. In particular, this colloquium aimed to bring the research community together for the first time under a dedicated event on the urban wind turbines and their integration in the anthropic areas.

I would like to thank all participants for their contributions to the colloquium program and for their contributions to these proceedings. I also acknowledge the important contribution of Prof. Gerard von Bussel in opening the colloquium program. My special thanks go to colleagues Dr. Ignacio Cruz and Dr. David Wood, for their assistance during the colloquium, and to the members of the Scientific Board. It is my pleasant duty to acknowledge the support of the InVento promoters in the overall organization of the colloquium.

Trento, Italy

Lorenzo Battisti

Contents

A Preliminary Assessment of the Impact of Gurney Flaps on the Aerodynamic Performance Augmentation of Darrieus Wind Turbines	1
Daniele Di Rosa, Francesco Balduzzi and Alessandro Bianchini	
Experimental Characterization of VAWT Airfoils Under Turbulent Flows	21
Andreu Carbó Molina, Sander Van de Maele, Gianni Bartoli, Tim De Troyer and Mark Runacres	
Numerical Simulation and Measurement for Location Optimization of a Vertical Axis Wind Turbine (VAWT)	39
Giuseppe Ruffino, Susan Schaar, Daniel Lehser-Pfeffermann, Danjana Theis, Frank Ulrich Rückert, Tobias Müller and Franz Joos	
The Effect of Tail Fin Size on the Yaw Performance of Small Wind Turbines Operating in Unsteady Flow	55
David Bradney, Samuel Evans and Philip Clausen	
Installation of a Small Building-Mounted Wind Turbine: A Case Study from Idea to Implementation	71
Quentin Deltenre and Mark C. Runacres	
Evaluation of the Causes of Vibration and Oscillation in a Vertical Axis Small Wind Turbine (VASWT) and Its Reduction	89
Alexander Hirschl, Mauro Peppoloni and Kurt Leonhartsberger	
Assessment of the Impact of a Low-Rise Flat Roofed Building on Ambient Wind Conditions	109
Stefan Hübl, Mauro Peppoloni, Kurt Leonhartsberger and Alexander Hirschl	

A Detailed Analysis of the Centrifugal Pumping Phenomenon in HAWTs Through the Use of CFD Models	129
Stefano Mauro, Rosario Lanzafame, Michele Messina and Sebastian Brusca	
Measuring the Torque and Thrust Loading on the Blades of a Small Horizontal Axis Wind Turbine Operating in Highly Turbulent Flow Regimes	151
Shaun M. Nay and Philip D. Clausen	
Dynamic Identification of a Vertical Axis Wind Turbine	165
Luisa Pagnini, Giuseppe Piccardo, Maria Pia Repetto and Giuseppe Riotto	
Experimental Assessment of an Actuator-Line Simulation Tool for VAWTs	177
Pier Francesco Melani, Paolo Schito and Giacomo Persico	
Wind Regimes in Urban Environments: Experimental Comparison with the IEC 61400.2-2013 Open Terrain Wind Model	201
Muhammad Iftekharul Rakib, Shaun Nay, Samuel Evans and Philip Clausen	
Structural Optimisation of 3D Printed Small Diffuser Augmented Wind Turbine Blade Using Bi-directional Evolutionary Layout Optimisation Method	215
Mariana S. P. da Costa, Joss Kesby and Philip D. Clausen	
Experimental Investigation of the Aerodynamic Interaction Between Ducts and Actuator Discs	229
J. Tang and G. J. W. van Bussel	
Analyzing the Unsteady Dynamic Behaviour of a Small Wind Turbine for Urban Applications	245
Francesco Castellani, Francesco Berno, Matteo Becchetti, Davide Astolfi and Emanuele Piccioni	
Effectiveness of Wind Turbines in Urban Environment	255
L. Battisti, S. Dell'Anna, M. Raciti Castelli and A. Brighenti	

A Preliminary Assessment of the Impact of Gurney Flaps on the Aerodynamic Performance Augmentation of Darrieus Wind Turbines



Daniele Di Rosa, Francesco Balduzzi and Alessandro Bianchini

Abstract Gurney Flaps (GFs) can enhance the aerodynamic performance of airfoils, making them generate more lift and delaying the onset of stall. Since their potential was discovered in the early '70s, GFs have been applied in several fields, including wind turbines. Here, the research has been focused mostly on the use of GFs in Horizontal Axis Wind Turbines (HAWTs), whereas a lack of studies involving the application of these devices on Darrieus Vertical-Axis Wind Turbines (VAWTs) is apparent in the literature. The benefits induced by GFs could actually be particularly interesting for this type of wind turbines, which are presently receiving a renewed attention from the industry. In the present study, the possible benefits of mounting GFs on a VAWT have been evaluated. The aerodynamic behavior of a single rotating NACA0021 airfoil equipped with different GF configurations has been investigated by means of unsteady CFD simulations. The effect of varying the size of the GF, as well as the different effects of this device at two different functioning regimes of the rotor were also analyzed. The results clearly suggested that properly-mounted GFs could notably improve the performance of a Darrieus VAWT (up to more than +20% for the 1-blade test case), especially at low tip-speed ratios.

Keywords Gurney flap · Darrieus · Wind turbine · CFD · Power augmentation

List of Symbols and Abbreviations

A	Turbine Swept Area [m^2]
AoA	Angle of Attack [$^\circ$]
c	Blade Chord [m]
C_D	Drag Coefficient
C_L	Lift Coefficient
c_P	Power Coefficient

D. Di Rosa · F. Balduzzi · A. Bianchini (✉)
Department of Industrial Engineering, Università degli Studi di Firenze, Via di Santa Marta 3,
50139 Florence, Italy
e-mail: alessandro.bianchini@unifi.it

c_T	Torque Coefficient
CFD	Computational Fluid Dynamics
D	Diameter of the rotating region [m]
f_S	Shedding Frequency [Hz]
GF	Gurney Flap
h_{GF}	Gurney Flap Height [m]
HAWT	Horizontal Axis Wind Turbine
N	Blade Number
PS	Pressure Side
R	Turbine Outer Radius [m]
RANS	Reynolds-Averaged Navier-Stokes
Re	Reynolds Number
S	Blade Area [m ²]
SS	Suction Side
St	Strouhal Number
TSR	Tip-Speed Ratio
U	Undisturbed Wind Speed [m/s]
VAWT	Vertical Axis Wind Turbine
W	Relative Wind Speed [m/s]
y^+	Dimensionless Wall Distance

Subscripts

max	Maximum Value
ave	Average Value

Greek Letters

ϑ	Azimuthal Angle [°]
ρ	Air Density [kg/Nm ³]
π	Pressure Coefficient on the Blade
Ω	Turbine Revolution Speed [rpm]
ω^*	Dimensionless Vorticity

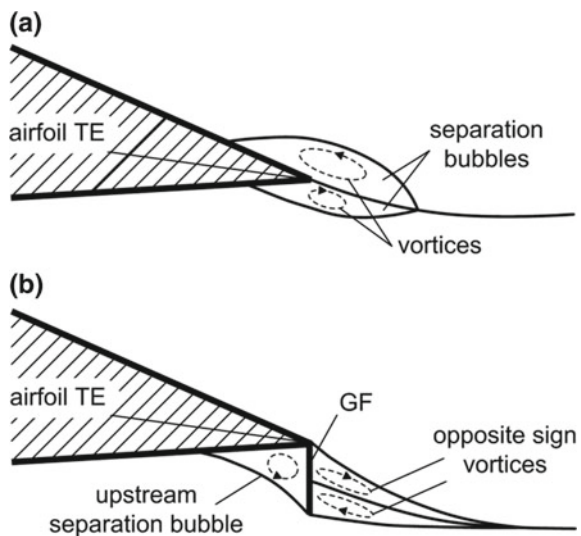
1 Introduction

1.1 Background

Gurney Flaps (GFs) are simple devices consisting in small tabs that can be applied perpendicularly to the trailing edge of airfoils, on their pressure side, to increase their aerodynamic performance. They were firstly implemented in the early '70s on the rear spoilers of F1 vehicles by the US driver Dan Gurney, who experienced an increase of the downforce thanks to these devices. Later, Liebeck [1] conducted a systematic experimental campaign on a Newman airfoil (a wedge-shaped airfoil with an elliptical leading edge), actually confirming that GFs could enhance the lift force of airfoils. He also suggested that GF height should be kept below $2\%c$ to maximize the aerodynamic benefits, which would be otherwise nullified by a noticeable increase in drag. In his study, Liebeck assumed that the flow field around the airfoil underwent a change that could be theoretically described by the picture reported in Fig. 1, where a comparison with the flow over the smooth airfoil is also shown.

This change basically consists in the formation of a stagnation zone upstream of the GF, i.e. a separation bubble characterized by an adverse pressure gradient, and a couple of counter-rotating vortices downstream the GF. Many studies [2–9] later confirmed the presence of this characteristic vorticity, pointing out that it was responsible for an increase of suction on the airfoil's upper surface and of pressure on its lower surface, and accordingly for a substantial increase in the lift coefficient. Furthermore, it was found that the aft-loading of the airfoil was augmented and the flow was pushed downwards after it leaves the trailing edge. The same works also highlighted that the stall was achieved at a lower angle of attack in comparison with

Fig. 1 **a** Flow field around a smooth airfoil;
b hypothesized flow field around an airfoil with a Gurney flap



the baseline smooth airfoil, and the zero-lift angle of attack became more and more negative as the GF height was increased, suggesting that the effective camber of the airfoil was augmented. Lastly, as remarked by several other works [10–13], the deployment of GFs involved also the presence of a von Karman vortex street of alternately shed vortices in the wake of the airfoil.

As one can easily imagine, the effects linked to the use of GFs strongly depend on their configuration, i.e. their geometrical features as well as their mounting details. Among them, the height of the GF is surely one of the pivotal parameters, since the lift enhancing effect of the flap is strengthened as soon as its height is increased. At the same time, the drag force is likewise emphasized, such that its magnitude could nullify the GF benefits if a certain threshold of the flap height is exceeded.

Accordingly, many authors [8, 14, 15] concur with the fact that the GF size should be kept below the boundary layer thickness measured at the trailing edge on the pressure side of the airfoil, in order to obtain a beneficial lift-to-drag ratio.

1.2 Motivation

The GF has proven to have interesting prospects in a wide range of applications. The works by Wang et al. [16], as well as that of Troolin [12], provide indeed an extensive overview of the GF applications, which include both low and high-speed airfoils, aircrafts, wings, helicopter rotors and, recently, wind turbines. Focusing on this latter application, many literature instances suggest the GF as a promising device not only for active flow control [17–21], but also for turbine performance increase [22–25]. Notwithstanding this, it's worth remarking that all the aforementioned works coped with the application of GF on HAWTs, whereas the lack of studies concerning the deployment of this device on VAWTs was apparent. Only a few papers were indeed found addressing specifically this issue [26, 27], even though the analyses are often based on lumped aerodynamic coefficients, discarding several unsteady aerodynamic phenomena, which are however of capital relevance for a correct description of the GF effects.

The present work thereby is aimed at preliminary investigating the effects of GFs on the performance of a Darrieus wind turbine, by means of 2D unsteady CFD simulations. In particular, both a low (left-hand side of the power coefficient curve) and a high (right-hand side of the power coefficient curve) TSRs were studied. Different GF sizes and mounting configurations were also tested.

Table 1 Main features of the case study rotor

Model feature	Value
Blades number (N)	3
Blades shape	Straight
Blades airfoil	NACA0021
Blade-spoke connection point	0.5c
Radius (R) (m)	0.5150

2 Methodology

2.1 Case Study

To analyze the effect of GFs on the blade performance, a case study was first selected. The 2D model used in CFD calculations was extrapolated from the turbine, which has been tested recently in the wind tunnel of the Politecnico di Milano (Italy) by Dossena et al. [28]. The same rotor, whose main geometrical features are listed in Table 1, was also exploited in several works by some of the authors, by means of both 2D [29–31] and 3D [32, 33] CFD simulations.

In particular, most of previous works were focused on the rotational regime corresponding to $TSR = 3.3$, since it was deemed to be particularly interesting within the whole functioning range of the turbine. On one hand, this condition is characterized by a fairly high power coefficient (near to the peak of the power curve) and thus it represents a possible working condition for the rotor; on the other hand, it involves several complex aerodynamic phenomena, including stall, because of the relatively large variation of the incidence angle occurring during a revolution, and thus it poses remarkable challenges in terms of CFD study. Based on this significant amount of past numerical experience concerning the regime of $TSR = 3.3$, this functioning condition was selected as the starting point for the present investigation, while then a higher TSR —belonging to the right-hand side of the power curve—was also tested. According to [34–36], the authors also decided not to simulate the complete three-blade rotor, but to reproduce a hypothetical one-blade turbine having the exact features of Table 1. On one side, this allowed to mitigate the computational burden associated with the simulations, while, on the other side, it allowed them to isolate the aerodynamic effect of GFs—which was the main focus of the present analysis—from the complicated aerodynamic phenomena involved by multiple blade/wake interactions occurring in a multi-blade rotor.

The research program presented in this study was developed through four main conceptual steps, detailed below:

- (1) the suitability of the numerical approach in replicating the aerodynamic effect of Gurney flaps was first assessed on the static NACA0021 airfoil; in particular, provided the lack of literature studies concerning the GF effects on this specific

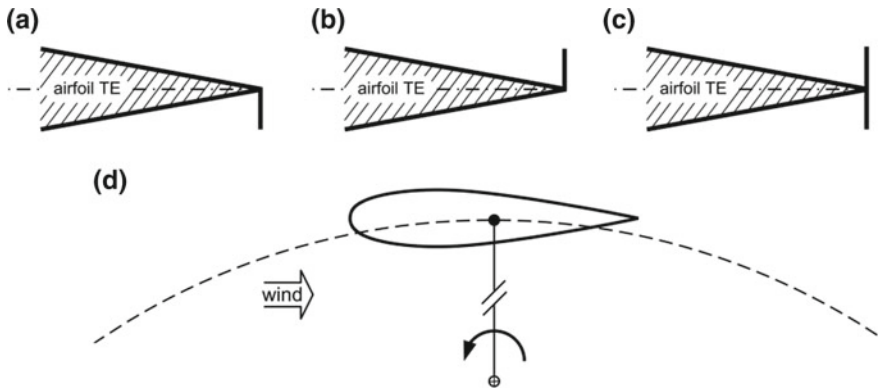


Fig. 2 **a** *GFin* configuration; **b** *GFout* configuration; **c** *GFboth* configuration; **d** convention on blade mounting in the Darrieus rotor

airfoil, the static polars using a GF were calculated and compared to those of the smooth airfoil;

- (2) moving to the 1-blade Darrieus turbine, the functioning point corresponding to $TSR = 3.3$ was studied and a sensitivity analysis was carried out on different configurations of the GF, keeping its height fixed at a value of $2\%c$. More in detail, the following configurations of the GF, which differed one from each other according to the side of the blade where the GF was mounted (see Fig. 2), were simulated and compared:

- *smooth* configuration: baseline airfoil with no GF;
- *GFin* configuration: flap mounted on the inner side of the airfoil, that is, the one facing the axis of rotation of the turbine;
- *GFout* configuration: flap mounted on the blade's outer side, that is, the one facing the boundaries of the computational domain;
- *GFboth* configuration: flap mounted on both sides of the airfoil.

The reasons why these three different options were chosen for the GF, as well as the corresponding expected outcomes in terms of performance for the wind turbine, will be better clarified in the Results section;

- (3) a sensitivity analysis on different heights of the GF (h_{GF}) was carried out, in order to assess the optimal value for the present rotor. Hence, in addition to the previously investigated $2\%c$ height, also $3\%c$ and $4\%c$ sizes were simulated.
- (4) the analysis was extended to a functioning point corresponding to the stable part of the power curve, namely the $TSR = 6.0$. In this case, the size of the GF was kept at $2\%c$, whereas its mounting configuration was varied within the ones reported above.

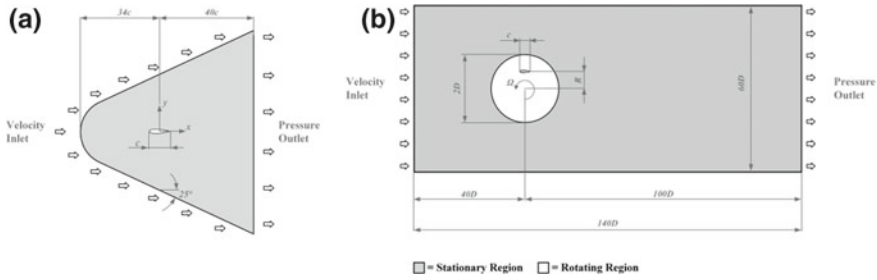


Fig. 3 **a** Computational domain for the static polars calculation; **b** computational domain for the rotating blade analysis

2.2 Numerical CFD Approach

The works by Balduzzi et al. [34, 37] were taken as the reference in order to select the most suitable numerical settings for the CFD simulations of the airfoil in Darrieus-like motion. For the sake of completeness, however, a brief overview on the main settings of the simulation model is given below.

The commercial code ANSYS® FLUENT® [38] was used in the two-dimensional form to solve the time-dependent unsteady Reynolds-Averaged Navier–Stokes (U–RANS) equations in a pressure-based formulation. The fluid was air, modeled as an ideal compressible gas with standard ambient conditions, i.e. a pressure of 1.01×10^5 Pa and a temperature of 300 K. The turbulence closure was achieved by means of Menter’s shear stress transport (SST) model [39], which is derived from the $k-\omega$ two-equation formulation and coupled with the Enhanced Wall Treatment for the computation of the boundary layer in the near-wall regions. The *Coupled* algorithm was employed to handle the pressure-velocity coupling. The second order upwind scheme was used for the spatial discretization of the whole set of RANS and turbulence equations, as well as the bounded second order for time differencing to obtain a good resolution. The global convergence of each simulation was monitored by considering the difference between the mean values of the torque over two subsequent revolutions. The periodicity error threshold was set to 0.1%.

To simulate the rotation of the turbine, the sliding mesh technique was employed [40, 41]. The physical domain was then split into two subdomains (Fig. 3b), i.e. a circular zone containing the airfoil, rotating with the same angular velocity of the rotor, and a rectangular fixed outer zone, determining the overall domain extent. Given the purpose of this analysis, only the airfoil was taken into account, neglecting the presence of the spoke and the shaft. According to [29–31], a velocity-inlet boundary condition of 9 m/s was imposed at the inlet section, which was placed 40 rotor diameters upwind from the rotating axis. The ambient pressure condition was imposed at the outlet boundary, 100 rotor diameters downwind, while a symmetry condition was defined on lateral boundaries, placed at a distance of 30 rotor diameters.

In case of the static polars used for the first assessment of the numerical approach (calculated at $Re = 1.5 \times 10^5$), the domain was instead made of the conventional bullet shape (Fig. 3a), featuring an overall widening angle of 50° and distances of 34 and 40 chords upstream and downstream of the airfoil, respectively.

The meshes generated for the two study cases were of unstructured type. Triangular elements were used for the discretization of the core flow region, whereas a structured O-grid was created to accurately resolve the blade boundary layer. The first element height was always chosen so as to guarantee that the y^+ values at the grid nodes of the first layer above the blade wall did not exceed the limit of the SST turbulence model, i.e. $y^+ \sim 1$. The expansion ratio for the growth of elements starting from the surface was kept below 1.05 to achieve good mesh quality. The airfoil surface was discretized with 760 nodes, resulting for the rotating blade in a mesh of 5.6×10^5 elements for the rotating region and of 1.7×10^5 elements for the stationary region. Overall, the mesh fulfilled the requirements in terms of limiting the dimensionless vorticity proposed by Balduzzi et al. [34]. The mesh for the static polars was instead made of 4×10^5 elements. Figure 4 shows some details of the computational grid used for the simulations of the rotating airfoil, with particular focus on the refinement zones used to properly discretize the leading and trailing edges of the airfoil and its wake. As an example, the *GFboth* configuration is reported there.

Regarding the temporal discretization, the static polars were calculated using a steady RANS approach up to the static stall angle, while after that the method was switched to a U-RANS one, with a timestep of 2×10^{-3} s. In the rotating blade, additional care in comparison to conventional Darrieus simulations was requested by the selection of the angular spacing between two consecutive timesteps (angular timestep). Firstly, this had to be proportionally adapted to the revolution speed of the airfoil, i.e. it had to be reduced for small TSRs, in order to match the requirements in terms of limiting the Courant number in proximity of the blades as proposed by Balduzzi et al. [34, 37]. Moreover, in the present application, the presence of the shedding vortices generated by the flow over the GF could not be disregarded, because a too coarse temporal discretization could prevent the phenomenon itself from being detected.

Accordingly, the pressure fluctuations associated with the shedding would not be captured by the CFD and this could potentially lead to a wrong prediction of the torque and power curves. Consequently, a maximum threshold for the value of the angular timestep was established in order to ensure that at least 10 points per shedding cycle were captured by the simulations. More in detail, the angular sector corresponding to a shedding cycle was calculated by Eq. 1:

$$\Delta\vartheta_s = \frac{\Omega}{f_s} \frac{180}{\pi} \quad (1)$$

where f_s was the expected shedding frequency and was evaluated in Eq. 2, accordingly to the definition of the Strouhal number (St):

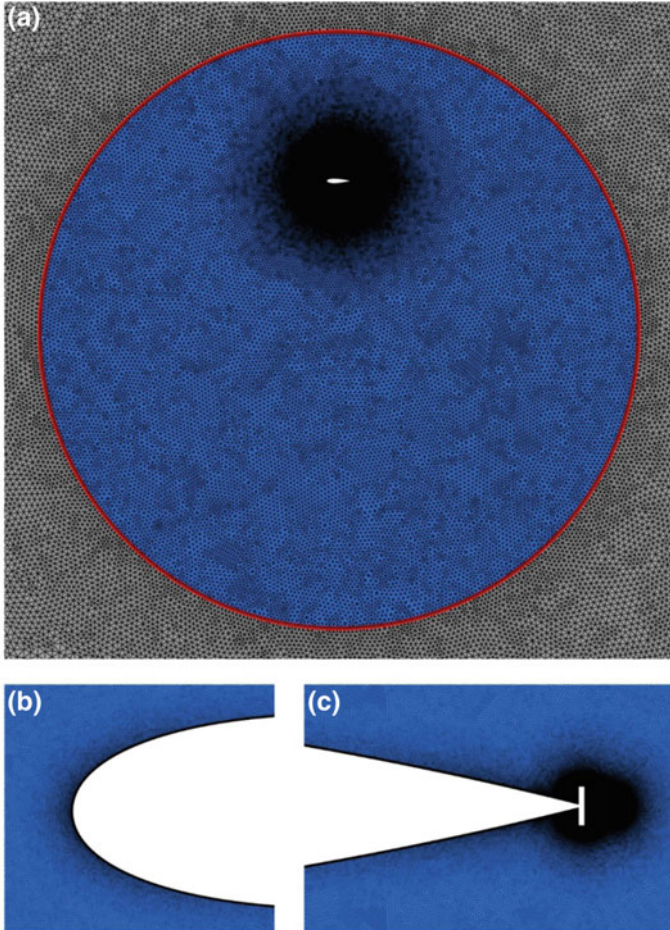


Fig. 4 Some details of the computational grid: **a** rotating region with sliding interface (in red) and grid refinement around the airfoil; **b** grid clustering in the leading edge region; **c** grid refinement in the region downstream of the GF

$$f_S = St \frac{W_{max}}{h_{GF}} \tag{2}$$

In the previous equation, $W_{max} = (U^2 + \Omega R^2)^{0.5}$ is the highest relative velocity experienced by the airfoil and h_{GF} is assumed to be the characteristic length governing the shedding development. After each simulation, the consistency of the selected timestep was verified using the actual shedding frequency detected by the simulations. As a result, timestep sizes of 0.08° for the *GF_{in}* and *GF_{out}* configurations, as well as 0.16° for the *GF_{both}* one, were used, respectively.

3 Results

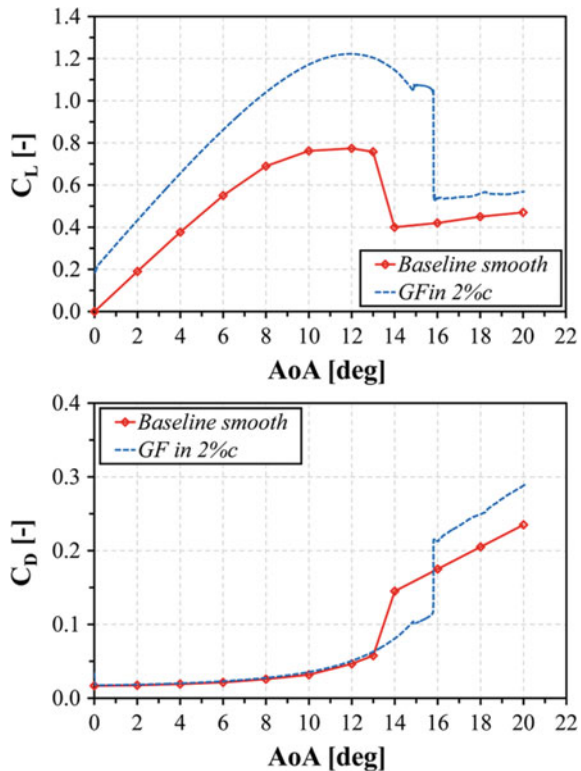
3.1 Assessment of GF Effect on Static Polars

Figure 5 reports the calculated lift and drag coefficients (Eq. 3 where ρ is the air density, S the blade area, W the relative speed) of the NACA0021, both for the baseline smooth and the *GF* configurations. For the latter, a h_{GF} of 2% c was selected.

$$c_L = \frac{\text{lift force}}{0.5 \cdot \rho \cdot S \cdot W^2} \quad c_D = \frac{\text{drag force}}{0.5 \cdot \rho \cdot S \cdot W^2} \quad (3)$$

Please note that, due to the complicated flow structures originated in correspondence to the GF, the simulations of this configuration required a much more refined angular discretization of the polar with respect to the smooth airfoil; markers for the GF curve were not reported for readability. The results were in good agreement with expectations. In particular, an enhancement is apparent in the lift curve of the NACA0021 with the GF, whose peak value was increased by 58% in comparison with the baseline configuration. The angle of attack corresponding to this peak turns

Fig. 5 Static polars of the NACA0021 for baseline smooth and GF in 2% c configurations



out to be mildly affected by the GF, having a value of roughly 12° in both cases. The effective camber augmentation is likewise apparent from Fig. 5, since a positive C_L is obtained for the zero incidence in case of the NACA0021 with the flap. It is also interesting to note that the lift-enhancing effect of the GF increases as the AoA is raised within the pre-stall region, leading to a steeper trend for the modified airfoil. The stall occurs right after the highest C_L for the smooth airfoil, i.e. at an AoA of 13° . A small decrease of the C_L is instead clearly outlined for the airfoil with the GF up to 15° , where a narrow zone of instability anticipates the abrupt onset of stall at an AoA of 16° . According to [8], this kind of stall may be induced by a sudden leading-edge bubble burst, rather than a progressive separation starting from the rear region of the airfoil. Besides, the stall of the airfoil with the GF is coupled with a sharp rise of the C_D , which—as expected—is higher than that of the smooth airfoil, particularly after the arising of stall.

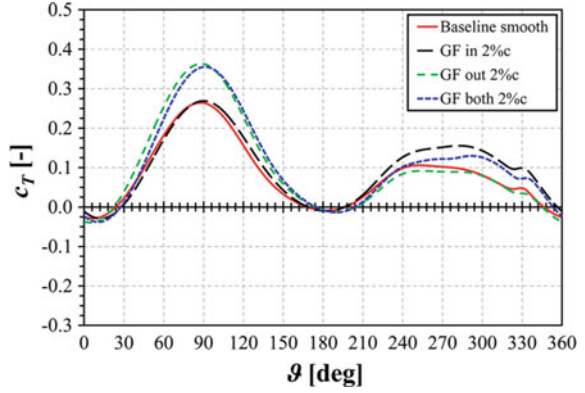
3.2 Sensitivity Analysis on the GF Configuration

Some preliminary considerations can be made on the effects achievable by adding the GF with different configurations on the airfoil, simply based on the study of the velocity triangles obtained during revolution of the turbine. According to the inherent functioning principle of the Darrieus turbine, each side of the blade acts alternatively as pressure side (PS) or suction side (SS), depending on whether the blade itself is passing through the upwind or the downwind zone. Namely, the outer side of the blade acts as PS in the upwind half of the revolution, whereas it acts as SS in the downwind one. Conversely, the opposite happens for the inner side of the blade. Provided that the GF exhibits its benefits within a restricted range of positive incidence angles, its effects might be expected to be favorable only within narrow portions of the revolution, whereas they might be mild, or even detrimental, within others. Broadly speaking, the *GF_{in}* and *GF_{out}* configurations were likely to enhance the lift on the airfoil, and hence the power extraction, only within the downwind and the upwind zone, respectively, i.e. where the relative velocity incidence and the GF position matched favorably. On the other hand, the *GF_{both}* configuration was expected to give an overall in-between result, since reasonably it would have taken the benefits of both the cases above, introducing however a higher drag force due to the larger size of the flap. These theoretical expectations were confirmed by the results at $TSR = 3.3$ of Fig. 6, where the torque coefficient profiles (Eq. 4) for each configuration are reported.

$$c_T = \frac{2 \cdot \text{torque}}{\rho \cdot A \cdot U^2 \cdot R} \quad (4)$$

As expected, when the GF is mounted on the inner side of the blade, it provides approximately the same energy extraction of the smooth airfoil in the upwind zone, whereas it significantly enhances the torque in the downwind one, leading to an

Fig. 6 Torque profiles for different GF configurations, $h_{GF} = 2\%c$, $TSR = 3.3$



increase of $c_{T,ave}$ of 23.3% in comparison with the baseline smooth configuration. On the other hand, when the GF is located on the outer side of the airfoil, it leads great benefit in the upwind zone, while the performance in the downwind zone are mildly worsened in comparison to the baseline configuration. The increase of the $c_{T,ave}$ is of 23.6% in this case, i.e. very close to the value associated with the previous situation: interestingly, the enhancement led by the *GF_{in}* configuration within the downwind zone and the one provided by the *GF_{out}* configuration in the upwind region are of the same order of magnitude, resulting in basically the same energy extraction even if this is obtained with completely different torque profiles over the revolution.

Focusing now on the *GF_{both}* configuration, it is apparent that the envisaged outcomes were correct in this case, too. In particular, the resulting torque profile is affected by both the advantages and disadvantages of both the *GF_{in}* and *GF_{out}* configurations. This is proven by the fact that its trend seems to be reasonably well predictable on the basis of the torque profile of the baseline smooth airfoil, adding up to it the positive or negative contributions deriving by both the *GF_{in}* and the *GF_{out}* configurations, for each of the azimuthal positions. Notwithstanding this, it is also apparent that the final profile may be affected by other non-linear effects which clearly make the actual result deflect from this mere algebra procedure. However, what matters is that apparently the advantages overcome the disadvantages, resulting in a 35.3% increase in the $c_{T,ave}$.

3.3 Sensitivity Analysis on the GF Height

In order to contain the calculation burden, only one GF configuration was selected for the sensitivity analysis on h_{GF} . Namely, provided that the *GF_{both}* configuration was shown to guarantee the best results through the previous subsection, it was deemed to be also the most reasonable choice for the investigation described below.

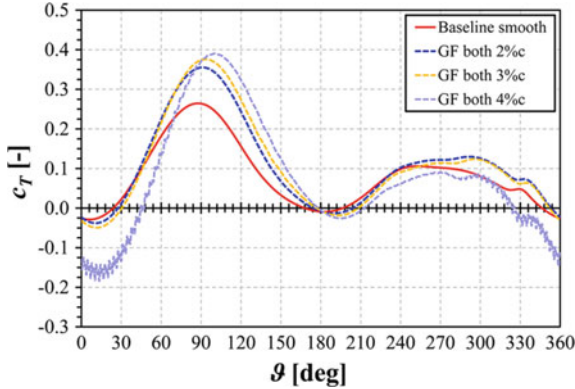


Fig. 7 Torque profiles for the *GFboth* configuration with different h_{GF} , at $TSR = 3.3$

From a perusal of Fig. 7, where the torque profiles obtained for different h_{GF} are reported, some observations can be done. First, increasing h_{GF} from 2%c to 3%c did not bring any additional performance improvement in terms of average torque over a revolution: the $c_{T,ave}$ increases by 35.7% in comparison with the baseline smooth airfoil, which is basically the same value provided by the 2%c flap. Apparently, although a slight growth of the torque is noticeable for ϑ ranging approximately from 75° to 180°, this is then nullified by the mildly poorer performance occurring in the whole downwind region, as well as within the first 70° sector of the upwind half of the revolution. Second, it's readily apparent that a further increment of h_{GF} from 3%c to 4%c is totally detrimental for the performance of the turbine. In fact, despite a mild augmentation of the $c_{T,ave}$ still exists in comparison with the smooth airfoil (+10.3%), a large portion of the revolution is clearly affected by pretty strong oscillations of the torque coefficient: this is distinctly an indication of the presence of shedding vortices within the flow field interacting with the blade. These fluctuations seem to onset for a ϑ between 270° and 300°, and they persist until the blade reaches the 90° position, achieving their highest amplitude between 0° and 20–30°. The energy extraction of the turbine is seriously penalized by this phenomenon, which gives rise to a steep drop of the torque coefficient since the very beginning of the shedding, leading the c_T to become even negative from approximately 325° to 45°. One may question why the shedding arises precisely when the 4%c flap is mounted on the blade, whereas no such issue was found for the 2%c and the 3%c flaps.

This can be explained taking into consideration the physics underlying the functioning of Darrieus turbines: the larger the upwind torque extraction, the lower the energy content within the downwind flow, which results in a smaller absolute wind speed acting on the blade in that region and hence in a smaller incidence of the relative velocity on the airfoil.

In this specific case, a smaller angle of attack of the flow over the airfoil with the GF is deemed to further promote the shedding, since the flow tends to interact more and more perpendicularly towards the flap itself as the incidence tends to

zero. Accordingly, the 4%*c* GF, providing the highest peak torque within the upwind region among the investigated h_{GF} , is therefore deemed to lead to the most conducive situation in terms of shedding promotion. Conversely, the 2%*c* and 3%*c* flaps involve a smaller upwind energy extraction, resulting in a downwind incidence which is high enough to prevent shedding developing: the flow is indeed assumed to generate a thicker boundary layer or even separate on the suction side of the airfoil, leading to an asymmetrical interaction with the GF and thus hampering the generation of organized vortex structures.

Finally, it is interesting to note that the increase of h_{GF} produces two effects: first, the torque peak becomes higher, and second, it is achieved later during the revolution. This is likely due to the combination of different factors. On one hand, the lift enhancement effect of the GF becomes stronger as its height is increased, thereby the blade is capable of extracting additional energy even for incidence conditions which would already become unfavorable for the baseline smooth airfoil. Namely, the torque coefficient begins to decrease just after $\vartheta \approx 87.8^\circ$ for the latter, whereas it is still increasing there for the GF-airfoils: in particular, the peak c_T of the 4%*c* airfoil is achieved for an azimuthal position of $\vartheta \approx 94.4^\circ$. On the other hand, as the h_{GF} is increased, so does the drag force, and this is particularly apparent in the first 30° range of the upwind region: here, the flow incidence is almost null, hence the GF has the only effect of exacerbating the drag force, leading to a poor performance. Accordingly, the beginning of positive torque production is delayed, shifting the whole trend to the right. This is especially noticeable for the 4%*c* case, for which the situation is further worsened by the presence of shedding, as discussed above. In fact, despite of the highest slope of this curve, due to the greatest boost action of the GF, the torque turns positive only after $\vartheta \approx 45^\circ$. Subsequently, it quickly achieves its top value and then it cannot be any longer risen, since the airfoil has already reached an adverse azimuthal position, where the enhancing effect of the GF cannot outweigh the fact that the airfoil begins to stall, no matter of how long the GF itself is.

3.4 Sensitivity Analysis on TSR and Power Curves Prediction

Figure 8 reports the power coefficient (Eq. 5) obtained with the various GF configurations as a function of the TSR; the reference power curve for the hypothetical 1-blade turbine provided by [33] and based on a state-of-the-art, free-wake, lifting-line method embedded in open source code QBlade is also displayed as a reference.

Focusing on the results obtained for $TSR = 3.3$, it's readily noticeable that the values of c_P reflect the observations reported in Sect. 3.2. The percentage c_P enhancements of each GF configuration in comparison with the baseline are logically the same values therein reported in terms of $c_{T,ave}$. For the reasons explained in Sect. 3.2, the highest performance improvement in comparison with the baseline case is provided by the *GFboth* configuration, whereas the *GFin* and *GFout* arrangements turn out to be equivalent to each other. As regards the regime of $TSR = 6.0$, the most evident fact is that the *GFboth* configuration makes the c_P dramatically dropping down to a

Fig. 8 Power coefficients corresponding to the different GF configurations, at $TSR = 3.3$ and $TSR = 6.0$

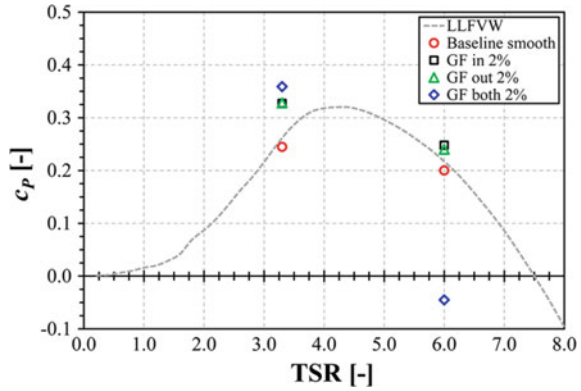
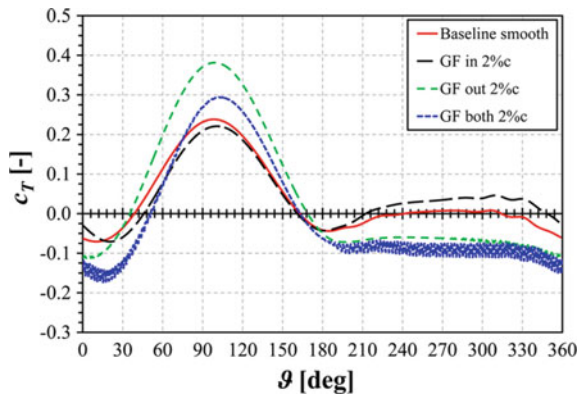


Fig. 9 Torque profiles for different GF configurations, $h_{GF} = 2\%c$, $TSR = 6.0$



negative value, which implies that the turbine is producing a resistant torque there, rather than extracting energy from the wind: this case is indeed characterized by a 122.5% lower c_p in comparison with the smooth airfoil. On the other hand, the GF_{in} and GF_{out} configurations still keep ensuring higher efficiency than the baseline case, leading to an enhancement of the c_p of 24 and 20%, respectively. Accordingly, this different behavior turned out to draw up an overall flatter power curve in comparison with the GF_{both} case, which instead would give rise to a very steep trend. Such a selective functioning curve would involve serious handling problems within the rotational speed control, eventually making the rotor less cost-attractive. To better understand the physical reasons underlying the obtained outcomes in terms of c_p , a detailed analysis of the torque coefficient as a function of the azimuthal position of the blade was carried out for the $TSR = 6.0$ case, similarly to what has already been done in Sect. 3.2 for $TSR = 3.3$. The reason why the GF_{both} configuration involves such a poor power extraction is readily understandable from Fig. 9, where the torque profiles deriving from this analysis are reported. A massive presence of vortex shedding is indeed clearly visible over most of the downwind half and the beginning of the upwind one for the torque profile corresponding to this configuration.

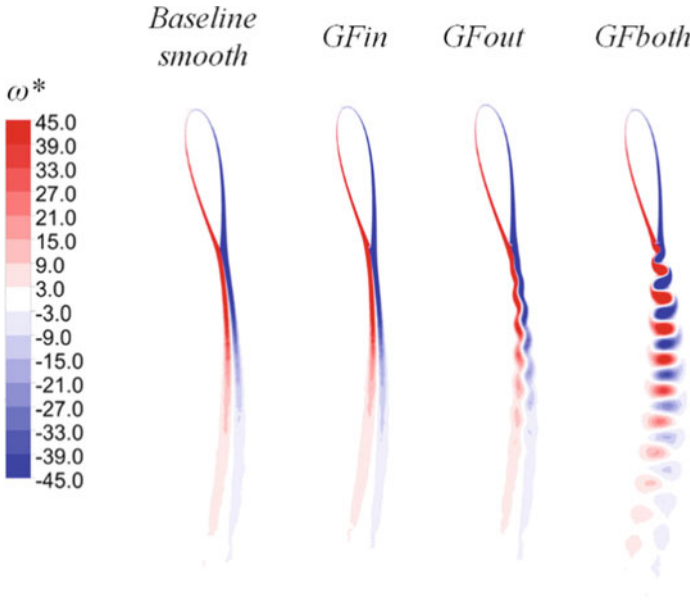


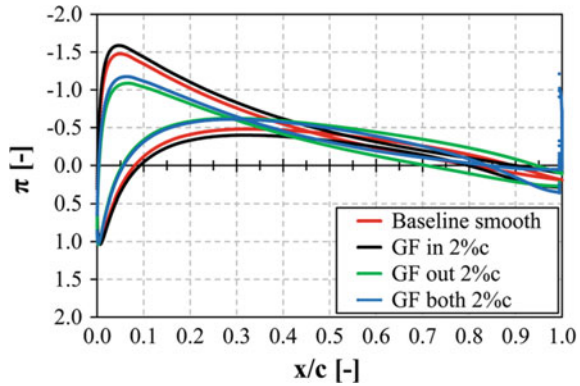
Fig. 10 Dimensionless vorticity contours (TSR = 6.0, $\vartheta = 280^\circ$, $h_{GF} = 2\%$)

$$c_P = \frac{\text{power}}{0.5 \cdot \rho \cdot A \cdot U^3} \quad (5)$$

As one can conclude from the discussion provided in Sect. 3.3 for the 4% flap, this is indeed the worst situation in terms of shedding promotion: in fact, despite the smaller GF, the TSR is now increased, hence the angle of attack over the airfoil is averagely decreased and eventually the 2% flap becomes big enough to make shedding vortices arise. By the way, looking closely to the last 70° of the downwind torque profile of the *GFout* configuration, it's possible to identify a barely outlined oscillation of the c_T : this means that not even this GF arrangement is able to totally prevent the onset of vortex shedding, because of the excessive energy extraction within the upwind region of the revolution.

These observations are confirmed by Fig. 10, where the contours of the dimensionless vorticity are reported for the four analyzed airfoil configurations at the azimuthal position of 280°. As a further evidence, Fig. 11 provides the pressure coefficient (π) distribution on the airfoil, for the same azimuthal position. As apparent, the *GFin* configuration turns out to be the only one that allows a torque enhancement without involving the onset of the aforementioned shedding instabilities.

Fig. 11 Pressure coefficient distributions (TSR = 6.0, $\vartheta = 280^\circ$, $h_{GF} = 2\%c$)



4 Conclusions

In the present study, the effects of mounting Gurney flaps on a rotating NACA0021 airfoil intended for Darrieus VAWT applications have been examined through CFD unsteady calculations. A specific sensitivity analysis on the mounting configuration has been carried out at TSR = 3.3: three different arrangements were studied, featuring a 2%*c* GF on the inner, on the outer and on both of the sides of the rotating airfoil.

Furthermore, the effect of different sizes of the GF on the power extraction capability of the blade was investigated, focusing the analysis only on the latter of the previous three GF configurations and varying its height among 2%*c*, 3%*c* and 4%*c*. Finally, the research was extended to a functioning point corresponding to TSR = 6.0, where the 2%*c* GF was tested within the configurations reported above. For each of the study cases, the performance of the airfoil was compared with its baseline smooth configuration, paying particular attention to the different torque profiles over the complete revolution.

The results show that, if the proper GF configuration is selected, it could provide a notable increase of aerodynamic performance especially at medium-low TSRs. More in detail, when the 2%*c* GF was applied on the inner side of the airfoil, it was proven to guarantee a 23.3% and 24% increase of the power coefficient at TSR = 3.3 and TSR = 6.0, respectively. Moreover, this GF arrangement avoided the onset of vortex shedding at the high-TSR rotating regime, and it provided also a flatter power curve trend with an earlier peak in comparison with the baseline configuration, suggesting promising prospects for future applications. Nevertheless, further research is necessary in order to better assess the benefits of GFs for VAWTs: their effects at other TSRs, their application on a complete multi-blade rotor and the GF influence on the structural stresses of the turbine represent only a few examples of the possible investigations that could be carried out about this topic.

Acknowledgements Thanks are due to Prof. Giovanni Ferrara of the University of Florence for supporting this research activity.

References

1. Liebeck RH (1978) Design of subsonic airfoils for high lift. *J. Aircr* 15(9):547–561
2. Neuhart DH, Pendergraft OC Jr (1988) A water tunnel study of Gurney flaps
3. Storms BL, Jang CS (1994) Lift enhancement of an airfoil using a Gurney flap and vortex generators. *J Aircr* 31(3):542–547
4. Myose R, Heron I, Papadakis M (1996) Effect of Gurney flaps on a NACA 0011 airfoil. In: 34th aerospace sciences meeting and exhibit, p 59 (1996)
5. Myose R, Heron I, Papadakis M (1996) The post-stall effect of gurney flaps on a NACA-0011 airfoil (No. 961316). SAE technical paper
6. Jang CS, Ross JC, Cummings RM (1998) Numerical investigation of an airfoil with a Gurney flap. *Aircr Des* 1(2):75–88
7. Katz J, Dykstra L (1989) Study of an open-wheel racing-car's rear-wing aerodynamics (No. 890600). SAE technical paper
8. Li Y, Wang J, Zhang P (2002) Effects of Gurney flaps on a NACA0012 airfoil. *Flow Turbul Combust* 68(1):27–39
9. Liu T, Montefort J (2007) Thin-airfoil theoretical interpretation for Gurney flap lift enhancement. *J Aircr* 44(2):667–671
10. Jeffrey D, Zhang X, Hurst DW (2001) Some aspects of the aerodynamics of Gurney flaps on a double-element wing. *J Fluids Eng* 123(1):99–104
11. Troolin DR, Longmire EK, Lai WT (2006) Time resolved PIV analysis of flow over a NACA 0015 airfoil with Gurney flap. *Exp Fluids* 41(2):241–254
12. Troolin DR (2009) A quantitative study of the lift-enhancing flow field generated by an airfoil with a Gurney flap. University of Minnesota
13. Gopalakrishnan Meena M, Taira K, Asai K (2018) Airfoil-wake modification with gurney flap at low Reynolds number. *AIAA J* 56(4):1348–1359
14. Brown L, Filippone A (2003) Aerofoil at low speeds with Gurney flaps. *Aeronaut J* 107(1075):539–546
15. Giguere P, Lemay J, Dumas G (1995) Gurney flap effects and scaling for low-speed airfoils. In: 13th applied aerodynamics conference, p 1881
16. Wang JJ, Li YC, Choi KS (2008) Gurney flap—lift enhancement, mechanisms and applications. *Prog Aerosp Sci* 44(1):22–47
17. Van Dam CP, Chow R, Zayas JR, Berg DE (2007) Computational investigations of small deploying tabs and flaps for aerodynamic load control. In: *Journal of physics: conference series*, vol 75. IOP Publishing, p 012027
18. Frederick M, Kerrigan EC, Graham JMR (2010) Gust alleviation using rapidly deployed trailing-edge flaps. *J Wind Eng Ind Aerodyn* 98(12):712–723
19. Pechlivanoglou G (2013) Passive and active flow control solutions for wind turbine blades. Ph.D. thesis, University of Berlin
20. Williams TJH (2014) Compliant flow designs for optimum lift control of wind turbine rotors. Ph.D. thesis, University of Notre Dame
21. Bach AB (2016) Gurney flaps and micro-tabs for load control on wind turbines. Ph.D. thesis, University of Berlin
22. Fuglsang P, Bak C, Gaunaa M, Antoniou I (2004) Design and Verification of the Risø-B1 airfoil family for wind turbines. *J SolEnergy Eng* 126(4):1002–1010
23. Tongchitpakdee C, Benjanirat S, Sankar LN (2006) Numerical studies of the effects of active and passive circulation enhancement concepts on wind turbine performance. *J SolEnergy Eng* 128(4):432–444

24. Chen H, Qin N (2017) Trailing-edge flow control for wind turbine performance and load control. *Renew Energy* 105:419–435
25. Alber J, Pechlivanoglou G, Paschereit CO, Twele J, Weinzierl G (2017) Parametric investigation of gurney flaps for the use on wind turbine blades. In: ASME turbo expo 2017: turbomachinery technical conference and exposition. American Society of Mechanical Engineers, pp V009T49A015-V009T49A015
26. Frunzulica F, Dumitrescu H, Dumitrache A (2014) Numerical investigations of dynamic stall control. *INCAS Bull* 6(Special 1):67–80
27. Ismail MF, Vijayaraghavan K (2015) The effects of aerofoil profile modification on a vertical axis wind turbine performance. *Energy* 80:20–31
28. Dossena V, Persico G, Paradiso B, Battisti L, Dell’Anna S, Brighenti A, Benini E (2015) An experimental study of the aerodynamics and performance of a vertical axis wind turbine in confined and non-confined environment. *J Energy Res Technol* 137(5):051207
29. Balduzzi F, Bianchini A, Gigante FA, Ferrara G, Campobasso MS, Ferrari, L (2015) Parametric and comparative assessment of Navier-Stokes CFD methodologies for Darrieus wind turbine performance analysis. In: ASME Turbo Expo 2015: turbine technical conference and exposition. American Society of Mechanical Engineers, pp V009T46A011
30. Bianchini A, Balduzzi F, Ferrara G, Ferrari L (2016) Aerodynamics of Darrieus wind turbines airfoils: the impact of pitching moment. In: ASME turbo expo 2016: turbomachinery technical conference and exposition. American Society of Mechanical Engineers, p V009T46A013
31. Bianchini A, Balduzzi F, Ferrara G, Ferrari L (2016) Influence of the Blade-Spoke connection point on the aerodynamic performance of Darrieus wind turbines. In: ASME turbo expo 2016: turbomachinery technical conference and exposition. American Society of Mechanical Engineers, p V009T46A012
32. Balduzzi F, Drofelnik J, Bianchini A, Ferrara G, Ferrari L, Campobasso MS (2017) Darrieus wind turbine blade unsteady aerodynamics: a three-dimensional Navier-Stokes CFD assessment. *Energy* 128:550–563
33. Balduzzi F, Marten D, Bianchini A, Drofelnik J, Ferrari L, Campobasso MS, Pechlivanoglou G, Nayeri CN, Ferrara G, Paschereit CO (2018) Three-dimensional aerodynamic analysis of a Darrieus wind turbine blade using computational fluid dynamics and lifting line theory. *J Eng Gas Turbines Power* 140(2):022602
34. Balduzzi F, Bianchini A, Ferrara G, Ferrari L (2016) Dimensionless numbers for the assessment of mesh and timestep requirements in CFD simulations of Darrieus wind turbines. *Energy* 97:246–261
35. Bianchini A, Balduzzi F, Ferrara G, Ferrari L (2016) Virtual incidence effect on rotating airfoils in Darrieus wind turbines. *Energy Convers Manag* 111:329–338
36. Rainbird JM, Bianchini A, Balduzzi F, Peiró J, Graham JMR, Ferrara G, Ferrari L (2015) On the influence of virtual camber effect on airfoil polars for use in simulations of Darrieus wind turbines. *Energy Convers Manag* 106:373–384
37. Balduzzi F, Bianchini A, Maleci R, Ferrara G, Ferrari L (2016) Critical issues in the CFD simulation of Darrieus wind turbines. *Renew Energy* 85:419–435
38. ANSYS® Fluent®, ©2015 ANSYS, Inc., release 16.1.0
39. Menter FR (1994) Two-equation eddy-viscosity turbulence models for engineering applications. *AIAA J* 32(8):1598–1605
40. Maître T, Amet E, Pellone C (2013) Modeling of the flow in a Darrieus water turbine: wall grid refinement analysis and comparison with experiments. *Renew Energy* 51:497–512
41. Raciti Castelli M, Englaro A, Benini E (2011) The Darrieus wind turbine: proposal for a new performance prediction model based on CFD. *Energy* 36(8):4919–4934

Experimental Characterization of VAWT Airfoils Under Turbulent Flows



Andreu Carbó Molina, Sander Van de Maele, Gianni Bartoli, Tim De Troyer and Mark Runacres

Abstract Vertical-Axis Wind Turbines are receiving the attention of the wind energy community for urban wind harvesting. However, their practical application is still far from maturity, due to the lack of understanding of urban flows. High turbulence is one of the main characteristics of wind in complex environments, so special attention has been paid to modelling it inside wind tunnels for prototype testing. Previous experiments showed a considerable boost in VAWT performance when turbulence intensity increases, but the explanation of this increase still has to be determined. This study analyses the effect of turbulent flows on the performance of a NACA0018 airfoil, using a blade model provided with pressure tabs and a traverse system to analyze the wake. The model is subjected to the same angles of attack and Reynolds numbers that would be found in normal VAWT operation, while turbulence intensity and integral length scale are kept at levels similar to those found in urban environments. The effect of turbulence is evident as it considerably delays the stall angle of the blade. Using a Single Streamtube model, the results from this parametric study are compared with the overall turbine ratings, in order to find a way to optimize turbine blades using a simplified set-up.

Keywords VAWT · Urban flows · Airfoils · Turbulence

Nomenclature

b	Grid bar width [m]
c	Blade chord [m]
C_D	Drag coefficient [–]

A. Carbó Molina (✉) · G. Bartoli
Department of Civil and Environmental Engineering, Università degli Studi di Firenze,
Via di Santa Marta 3, 50139 Florence, Italy
e-mail: andreu.carbo.molina@dicea.unifi.it

A. Carbó Molina · S. Van de Maele · T. De Troyer · M. Runacres
Thermo and Fluid Dynamics (FLOW), Vrije Universiteit Brussel, Pleinlaan 2,
1050 Brussels, Belgium

© Springer Nature Switzerland AG 2019

L. Battisti (ed.), *Wind Energy Exploitation in Urban Environment*,

Research Topics in Wind Energy 8, https://doi.org/10.1007/978-3-030-13531-7_2

C_L	Lift coefficient [-]
C_N	Normal force to the blade coefficient [-]
C_p	Pressure coefficient [-]
C_P	Turbine power coefficient [-]
$C_{P_{sf}}$	Turbine power coefficient in smooth flow (low turbulence) [-]
d	Distance to grid [-]
D	Drag [N]
I_u	Turbulence intensity in the flow direction [%]
L_{ux}	Integral length scale of turbulence in the flow direction [m]
P	Pressure [Pa]
Re_c	Chord Reynolds number [-]
u	Local wind speed in the flow direction [m/s]
U	Incident wind speed in the blade/turbine [m/s]
x	Distance along the blade chord [m]
α	Angle of attack [°]
δ	Uncertainty
λ	Tip-speed ratio [-]
ρ	Air density [kg/m^3]
θ	Azimuthal angle [°]
<i>HAWT</i>	Horizontal-Axis Wind Turbines
<i>SST</i>	Single Streamtube
<i>rms</i>	Root mean square
<i>VAWT</i>	Vertical-Axis Wind Turbines

1 Introduction

During the last years, harvesting the urban wind resource has become an objective for the wind energy community [1]. Placing small turbines on the roofs of high buildings would allow reaching large heights while saving the cost of tower constructions, and at the same time promote on-site consumption avoiding energy transport losses [2]. Contrary to the general trend, Vertical-Axis Wind Turbines (VAWT) have been considered as a viable alternative to conventional horizontal-axis ones for urban wind harvesting [3]. Although their efficiency is lower, their omnidirectionality and lower rotational speeds allow them to adapt better and be less noisy under the highly turbulent flows present in urban environments [4]. Among the variety of VAWT designs, H-Darrieus turbines have been selected for this research, as their higher efficiency and simple geometry make them the option with the highest potential [5].

Operation of wind turbines in urban environment is, however, not straightforward. Due to the increased terrain roughness (buildings, infrastructures...) the atmospheric boundary layer is shifted upwards in the cities, resulting in significantly lower wind speeds [1]. This flow is, furthermore, very complex, exhibiting high variability in wind speed and incidence angles that make the positioning of the turbine and its energy yield prediction a complicated issue [6].

All those features contribute to increase the level of turbulence of the flow, which makes that in urban environments the average turbulence vales are significantly higher ($I_u > 10\%$) than those in open terrain [7]. Turbulence is not often considered in the design process of VAWTs, and the study of its effect in the turbine's performance is limited to on-field data with the wind turbulence measured by a nearby meteorological station. The impossibility to control all external conditions make the results from those studies not definitive, offering contradictory results between them [8–10].

Wind tunnel experiments could be used to isolate the effect of turbulence from other parameters in order to provide precise and repeatable turbine ratings. However, few difficulties have to be tackled first: common experimental facilities have very low background turbulence ($I_u < 1\%$), and therefore this value should be augmented by the use of grids and other equipment. To date, few studies addressed the topic of turbulence [11, 12], with not enough data available to support solid conclusions.

An experimental set-up, presented in the last TUrbWind Conference [13], was developed within a collaboration between the University of Florence and the Vrije Universiteit Brussel to model urban flows in the wind tunnel. The optimization of turbulence grids allowed to study the effect of turbulence intensity on the mechanical power generated by a H-Darrieus VAWT. The results showed a considerable increase in turbine performance for moderate turbulence levels. Understanding the nature of this power increase could help to develop a new generation of more efficient Urban Wind Turbines.

A study on the near wake revealed that turbulence promoted faster wake recovery and reduced the losses caused by the shaft [14]. However, the main candidate to justify the performance increase is the impact of turbulent flows in the stall of the blades [3]. Hoffman in 1991 already detected positive influence of turbulence in the Cl-alpha curve of a symmetric NACA0015 airfoil [15]. And the subject has been studied in detail for non-symmetrical HAWT airfoils, always resulting in a very positive influence of turbulence on the stall of the airfoils [16–18]. But none up to the moment combined the characteristics of the airfoils with the overall VAWT performance measured under different turbulence flows. The objective of this work is to establish a relationship between the overall behavior of the turbine and the effect on the airfoils of different flows, in order to set a benchmark that would allow to optimize the performance of urban VAWTs with a more simplified set-up.

2 Methodology

2.1 Wind Tunnel Settings

The Facility

The research is performed at the Vrije Universiteit Brussel, in Belgium. The boundary layer wind tunnel has a length of 11 m that allows to develop stable turbulence intensity and length scale levels before the test section. The test section, with 1.04 m



Fig. 1 VUB low speed wind tunnel with turbulence grid

of height and 2 m width, permits testing scaled buildings and small wind turbines. Figure 1 shows the wind tunnel interior with the turbulence grid.

Measurement Techniques

Pressure measurements on the blade taps are performed using a Scanivalve ZOC33 electronic pressure scanner equipped with 16 channels. It has a full scale range of 2.5 kPa, providing an accuracy of 0.15% of this range (approximately 3.7 Pa). The sampling frequency for the pressure tabs data is 10 Hz, as high time resolution is not required, and 30 s are sampled to reduce the random error.

The wind flow characteristics are measured with a Constant Temperature Hot-Wire Anemometer, model Dantec mini-CTA 54T42. Its calibration is done using a Pitot tube. The time histories obtained from the hot-wire are acquired by a National Instruments Card and processed using Labview software to obtain the mean speed and turbulence levels. To register the wind speed of the wake, the hot wire is mounted 1 chord downstream in a traverse system controlled by Arduino. As hot wire allowed us to obtain higher resolution in frequency, the samples were taken at 1 kHz, with also 30 s of measurement.

The turbulence intensity was calculated as usual by using the root mean square (*rms*) and the incoming longitudinal flow speed (Eq. 1), while the longitudinal integral length scale L_{ux} was calculated according to Taylor's frozen-eddy hypothesis.

$$I_u = \frac{u_{rms}}{U} \quad (1)$$

Generation of Turbulent Conditions

A squared-mesh wooden grid (Fig. 1) is placed upstream of the model to generate different levels of turbulence intensity (I_u) and integral length scale (L_{ux}), following the recommendations by Lanneville (Eq. 2) and Roach (Eq. 3) [19, 20]:

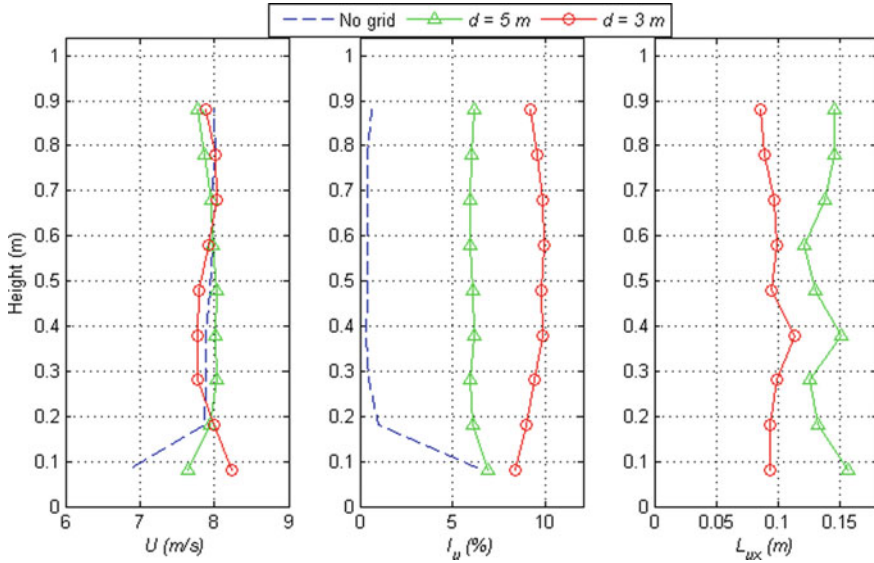


Fig. 2 Wind speed and turbulence profiles obtained with the different positions of the grid

Table 1 Mean flow values obtained in the test section with the different grid positions

Grid position d	No grid	5 m	3 m
Mean windspeed U (m/s)	7.94	7.97	7.90
Mean I_u (%)	0.45	6.00	9.58
Mean L_{ux}	–	0.136 m	0.096 m

$$I_u = 2.58 \left(\frac{d}{b} \right)^{-8/9} \tag{2}$$

$$L_{ux} = 0.2b \left(\frac{d}{b} \right)^{1/2} \tag{3}$$

where d is the distance to the grid and b the bar size. The profiles obtained by moving the grid upstream and downstream are enounced in Fig. 2. The power delivered to the wind tunnel fan is modified in order to obtain a similar wind speed in all cases. It can be observed how the uniformity of the values is maintained over the height of the wind tunnel (the most limiting dimension), to be able to obtain a clear indication of the influence of turbulence. In fact, Fig. 2 represents the profiles under which the VAWT performance was measured ($U = 8$ m/s), while to obtain the same Re_c values in the airfoil other wind speeds were used. However, the I_u and L_{ux} remained not affected by the different wind speeds. This and other details of the procedure of the building of the grid and the obtention of the profiles can be consulted at [13].

The average values obtained with the grid positions are enounced in Table 1.

Fig. 3 VAWT prototype in the wind tunnel



2.2 Turbine Prototype

The rotor is a two-blade H-type Darrieus turbine with two NACA0018 blades with a 5 cm chord (c) and two inclined struts per blade (see Fig. 3). Due to the small size of the rotor, angular speeds (and thus centrifugal loads) were high in order to achieve the suitable Reynolds numbers on the blades ($Re_c \sim 10^5$). To ensure proper mechanical properties, the rotors were manufactured using carbon-epoxy composite. Even when at low Reynolds numbers laminar separation is important no high-lift devices were added to the blade. Transition could be forced by e.g. transition strips, but preliminary tests with such strips on the VAWT did not give the expected result, so this avenue was not pursued further.

The VAWT rotor was connected via a torque sensor and a drive belt (with gear ratio 100/28) to a brushed-DC motor. This motor was used to drive the VAWT rotor during start-up, while acted as a generator in normal operation. The electrical output of the motor was fed to a circuit of variable resistance for angular speed control. A torque sensor was used to measure the mechanical torque and angular speed of the VAWT. The torque sensor, drive belt, DC motor, and measurement equipment were housed inside an aluminium frame. The torque sensor was a Lorenz Messtechnik

DR-3000 sensor with an accuracy of $\pm 2 \times 10^{-3}$ Nm. It was fitted between two torsionally-stiff couplings to allow for possible misalignments.

2.3 Airfoil Model

In order to obtain the Reynolds numbers of 1×10^5 within the windspeed range of the wind tunnel, a model was selected with a chord of 10 cm. The location of the pressure tabs was chosen from literature [21] (Table 2).

To ensure the desired structural properties, the blade was made by laminating fiberglass, using an aluminum mold to obtain the desired shape. The mold was manufactured with a CNC-milling machine using CAD-drawing and CAM-software by Autodesk Inventor. After the machining, the mold was polished by hand and finished with the use of a conventional mill.

In the first step of making the blade, fiberglass was laminated into the molds. The entire mold was cured inside a vacuum bag in order to prevent air bubbles. The pressure tabs were drilled into a brass tube positioned underneath the surface of the blade. The positioning of these tubes was critical, therefore jigs were made to hold the tubes in the correct place (Fig. 4).

After all tubes were positioned, the mold was closed and both halves were glued to each other. In order to prevent buckling of the thin fiberglass skin, the model was filled with polyurethane foam.

Table 2 Positions of pressure tabs along the chord of the airfoil model

Tap	1	2	3	4	5	6	7	8	9	10	11	12	13
x (cm)	0.125	0.250	0.5	1	1.5	2	3	4	5	6	7	8	9

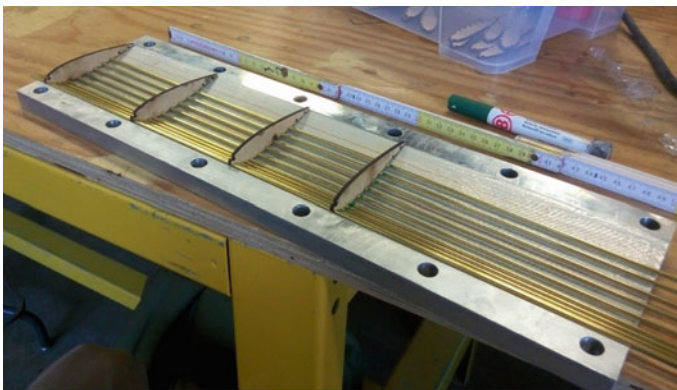


Fig. 4 Positioning of the tubes with the aid of jigs



Fig. 5 Airfoil model overview, with end plates and traversing system

The drilling of the pressure tabs was made with a fine 0.7 mm drill with the help of a drill guide to enhance hole precision. By using this method two rows of pressure tabs were drilled, with the idea that if one hole was oriented different than the other this would result in a different pressure reading. By using two holes this error would be averaged out.

The blade was clamped into an aluminum block for stiffness, and an end plate was glued on the block. The end plate on the other end of the model was already installed in the wind tunnel, and could not be adjusted in height. For this reason a platform was made with 4 bolts on which the model could be mounted. End plates were used to limit 3-D effects, so the flow could be considered 2D for simplicity in the calculations. Figure 5 gives a clear overview of all components.

2.4 Data Analysis

Calculation of aerodynamic coefficients:

The differential pressure obtained from the pressure tab readings is used to calculate the pressure coefficient C_p for each position along the blade chord (Eq. 4):

$$C_p = \frac{P - P_\infty}{\frac{1}{2}\rho U^2} \quad (4)$$

From here, the normal force (perpendicular to blade chord) coefficient is calculated by integrating the difference between the C_p in the upper and lower part of the blade (Eq. 5):

$$C_N = - \int_0^1 (C_{P,up} - C_{P,low}) d\left(\frac{x}{c}\right) \quad (5)$$

Supposing low angles of attack ($\alpha < 20^\circ$) and $C_L > C_D$, the lift coefficient C_L can be approximated by (Eq. 6):

$$C_L = C_N \cos \alpha \quad (6)$$

Drag is calculated by the wake survey method, or scanning transversally the wake of the profile. This method, based in the integral momentum conservation, permits calculating the forces acting on a body from their reactions on the flow. The model is limited due to its assumptions of constant static pressure and negligible turbulent and viscous stresses, but its simplicity makes it useful in this preliminary study. The formulation from Jones (Eq. 7) will be used [22]:

$$D = \int \rho u(U - u)dy \quad (7)$$

Resulting in Eq. 8:

$$C_D = \frac{D}{\frac{1}{2}\rho c U^2} \quad (8)$$

Streamtube modelling:

To extrapolate the obtained blade coefficients into the overall turbine performance, a single streamtube (SST) model as in [3] is used. This simple model was first developed by Templin [23] to calculate the aerodynamical performance of a curved-blade Darrieus, but has been adapted for the H-rotor as in Fig. 6 [24]. It is based in the actuator disk theory, assuming the induced velocity is the same in both faces of the turbine.

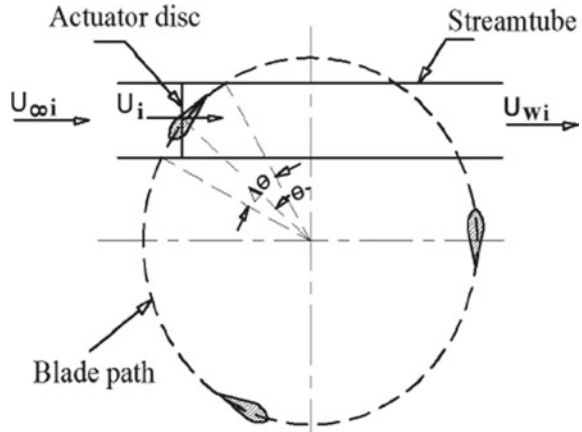
The code delivers reasonable results given its simplicity, although it fails to describe accurately the stall region [3]. This is not a major inconvenience as the study focuses in the optimal point of operation of the turbine, where blades are mostly not stalled. In our case, the overall performance is highly overpredicted, as the code does not account for shaft, struts and tip losses, or mechanical friction. But the matter of interest is to determine if it is able to describe the differences in turbine performance caused by increased turbulence, as the main inputs of the code are the C_L and C_D curves of the blades.

Uncertainties calculation:

Uncertainties are calculated by the error propagation method, enounced in Eq. 9 [25]:

$$\delta_R = \sqrt{\sum_i^N \left(\frac{\partial R}{\partial x_i} \delta_{x_i}\right)^2} \quad (9)$$

Fig. 6 2D schematic of the streamtube model [24]



The error in the power curves is explained in [13], and increases with turbulence as the wind speed profile uniformity descends.

For the measurements obtained with the pressure tabs in the airfoil, several contributions are analyzed. As the sampling time was set long enough to minimize sampling error, the uncertainties contributions were determined after the accuracy after the different measurement equipment. These errors range from under 5% in high pressure points, low turbulence wind, to 15% at low pressure points in the presence of high turbulence flow. The main error sources are:

- Accuracy of the pressure transducer (3.7 Pa)
- Uncertainty in the measured wind speed: in which contributes pitot sensitivity (4 Pa) and wind profile uniformity (depending of I_u).

For the wake survey measurements, the uncertainty in wind speed is the most limiting factor, as the positioning system precision is very accurate. In percentage, the uncertainty is the order of 20% in the laminar zone, due to the low values, while in stall this calculated error is the order of 5%.

These error values are relatively high, but difficult to reduce with the available equipment. However, the results are still considered meaningful. For simplicity in the presentation of data, only some error bars will be presented as illustrative examples.

3 Results

3.1 Turbine Power Curves

Figure 7 presents the power curves around the maximum efficiency obtained with the VAWT model in the turbulence conditions presented in Table 1. Due to confidentiality reasons, the values were normalized by the maximum C_p obtained under smooth

Fig. 7 Power curves obtained with the VAWT under different turbulence conditions, normalized with the optimum C_p in smooth flow

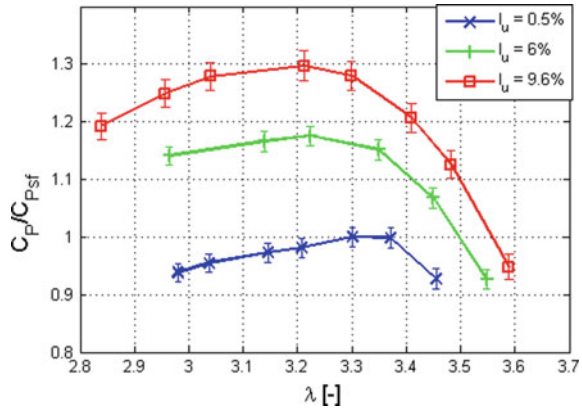


Table 3 Test conditions for the airfoil measurements

Reynolds numbers Re_c	8×10^4 and 1×10^5
Angle of attack α	0° to 20°
Turbulence intensity I_u	0.5, 6.0 and 9.6%

flow conditions. It is evident that the increased I_u provided a notable increase of the turbine performance, up to +30% for the higher turbulence case, while the increase for medium turbulence levels is around 17%. This increase is more evident for lower λ , when a larger part of the rotation occurs under stalled conditions. The curves also show a displacement of the optimal λ upon lower values when turbulence is increased. The following sections will try to analyze until which point this behavior depends in the performance of the blade under turbulence flows.

3.2 Airfoil Measurements

The conditions for the airfoil measurements are selected from the SST results. Figure 8 presents the expected values of α and Re_c that the blade encounters along one rotation at around the optimum point of operation ($\lambda = 3.3$). It can be seen how at $\theta = 0^\circ$ the blade, facing the flow, reaches the maximum Reynolds number but at a zero α . Minimum Re_c is obtained at the opposite side of the rotation, while during the rest of the rotation the wind reaches the blade with an angle of attack, varying from -11° to $+11^\circ$ approximately.

Considering this, and the various limitations (set-up, structural, time), a set of test conditions was selected (Table 3). Two values of Reynolds are selected: 8×10^4 to compare with literature and 10^5 because it is more similar to the values shown at Fig. 8. Those Reynolds values are low in comparison to large wind turbines, but in the same order of magnitude of the small VAWTs that can be found in urban environments. Being the NACA0018 a symmetrical airfoil, only positive α are considered.

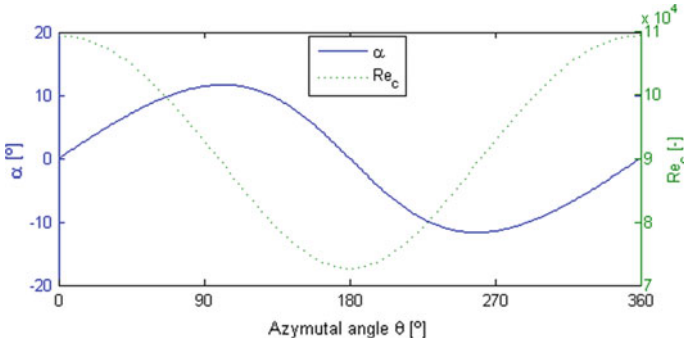


Fig. 8 Values of α and Re_c encountered by the blade along a rotation at $\lambda = 3.3$, calculated with the SST

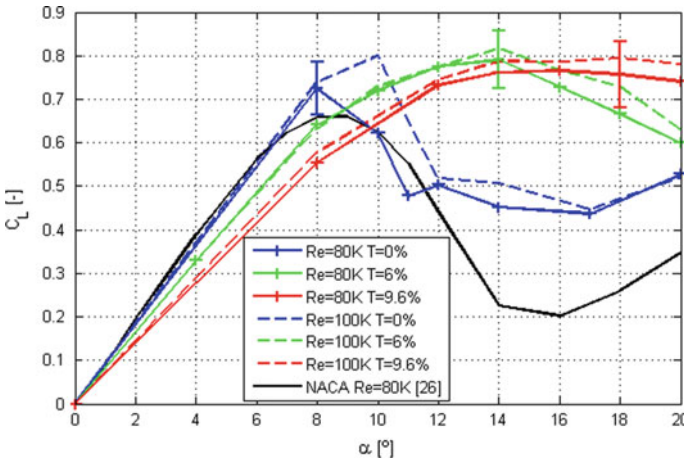


Fig. 9 C_L - α curves obtained with different Re_c and I_u conditions, compared with literature data [26]

Figures 9 and 10 present the C_L and C_D curves obtained with the different Reynolds and turbulence conditions presented in Table 3, compared with literature data collected in the Sandia project [26] in a low-turbulence wind tunnel facility. It can be seen how the lift curve obtained at $I_u = 0.5\%$ coincides with the literature one for angles of attack lower than 12° , while afterwards the registered lift value is significantly higher than in literature. Considering the drag coefficient, the values obtained with the wake survey method are considerably higher than the ones from literature. For low angles this can be attributed to the finishing of the model, while for high α the high values can be explained by the difference in the experimental methodology. The Jones method, presented in Sect. 2.4, is of limited use for stall conditions as neglects viscous and turbulence effects, while the measurements in [26] were performed with an aerodynamic balance. However, the focus of this study

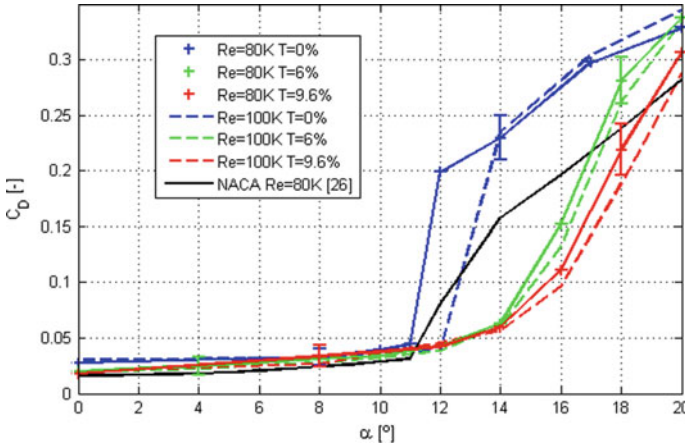


Fig. 10 C_D - α curves obtained with different Re_c and I_u conditions, compared with literature data [26]

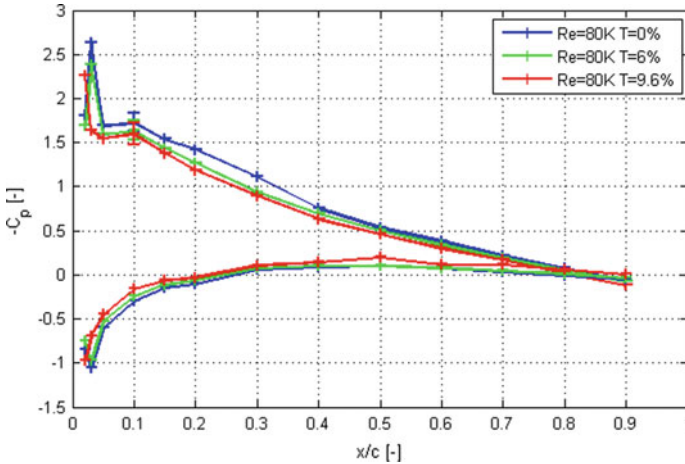


Fig. 11 C_p coefficients measured along the chord with different I_u conditions at $\alpha = 8^\circ$

was to compare between the different turbulence levels, and in those cases all measurements have been obtained with the same methodology. Examples of the error bars for each curve at $Re_c = 80 \times 10^3$ are also presented.

When comparing between the different flow conditions, it can be appreciated how Re_c exerts a positive effect both in C_L and C_D , however it is only considerable with the low turbulence case (minimum in the others). On the other hand, the effect of I_u in the polar curves is evident. Although there is a slightly higher C_L slope for small angles in the low turbulence case, it can be appreciated how the effect of turbulence is basically a large delay of the stall, as predicted in literature [3, 17]. When increasing

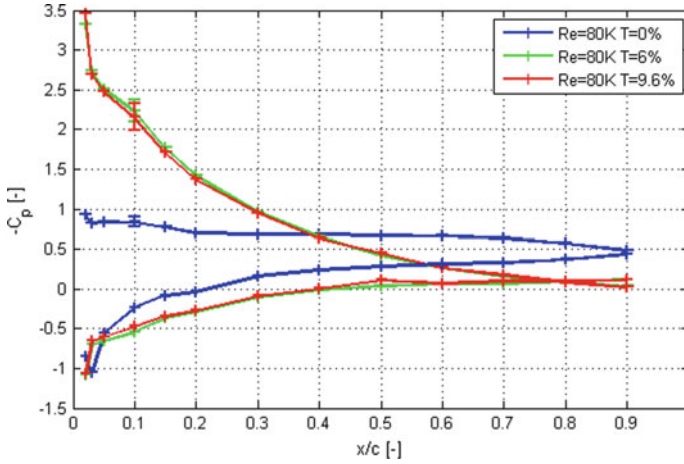


Fig. 12 C_p coefficients measured along the chord with different I_u conditions at $\alpha = 14^\circ$

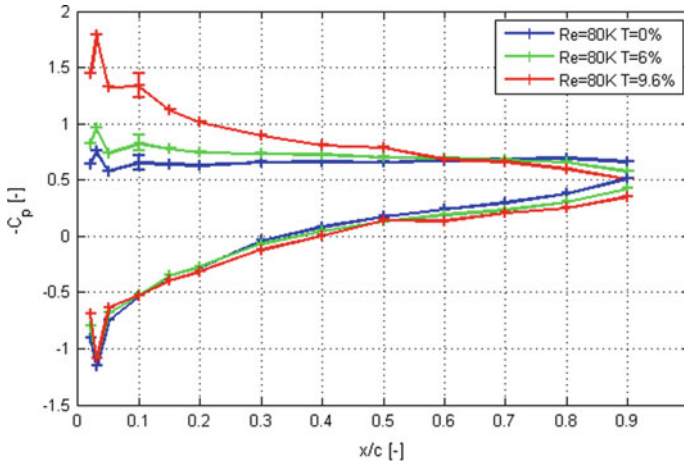


Fig. 13 C_p coefficients measured along the chord with different I_u conditions at $\alpha = 20^\circ$

the turbulence, the stall is later and smoother, while the maximum values of C_L remain generally constant (but occur also at higher α).

The pressure taps set-up also allowed to measure the local pressure along the blade chord. It is interesting to see how the pressure distribution is affected by the turbulence increase. Figures 11, 12 and 13 present the normalized pressure distribution along the blade at $\alpha = 8^\circ$, $\alpha = 14^\circ$ and $\alpha = 20^\circ$. The C_p values are inverted so the suction side distribution appears at the top. At 8° , still in the linear phase, it can be seen how the distribution is similar in the 3 cases, just with slightly higher pressure in the low turbulence case. Figure 12 at 14° shows how the blade at low turbulence is completely stalled, while, in this case, the two turbulent cases are still lifting (even

more than at $\alpha = 8^\circ$), and nearly with exact values between them. At 20° , in all three conditions the blade appear stalled, except for the high turbulence case, where near the leading edge there is still some suction in the upper part of the blade. Therefore, it can be concluded that the effect of I_u is that, instead of a sudden detachment of the flow in all the blade, in turbulent flow the detachment occurs progressively from the trailing to the leading edge as α increases. Those results show perfect agreement with the C_L and C_D values in Figs. 9 and 10.

3.3 VAWT Performance Prediction Using Single Streamtube Model

As stated in Sect. 2.4, the limitations of the SST prevent obtaining realistic values in the C_P curves. Moreover, because of time limitations the curves are only available for two Re, therefore limiting very much the accuracy. So the results observed in Fig. 14 are only a first approximation of the potential of the technique. Comparing it with Fig. 7 it is clear that the curve for smooth flow decays too fast when encountering blade stall, while in the turbulent cases stall does not occur in any moment and the curves are much less pronounced. This fact can be explained because of the lack of data, but mostly because the dynamic stall is not considered. However, even with the simplicity of the model, it is remarkable how the optimal λ is accurately predicted: around 3.2, and slightly lower as turbulence is increased.

The increase of peak performance is also accurately described for the medium turbulence case (20% against 19%), but in this case the highest turbulence case presents intermediate values. This is clearly appreciated in Fig. 15 where the max C_P obtained with the SST code is compared with the experimental case. The reason

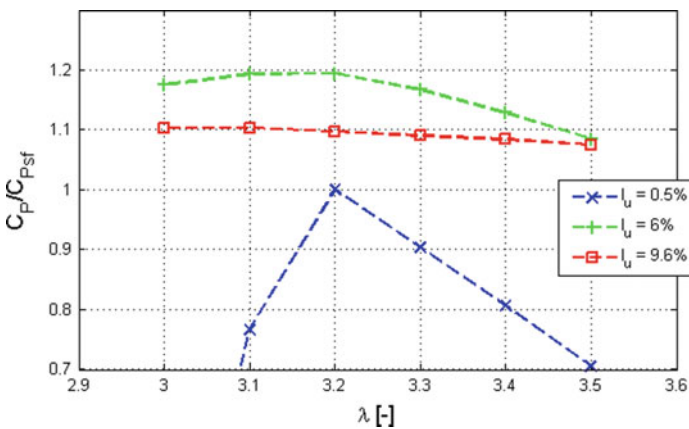


Fig. 14 Power curves (normalized with the max. C_P in smooth flow) obtained by introducing C_L and C_D curves in the SST model

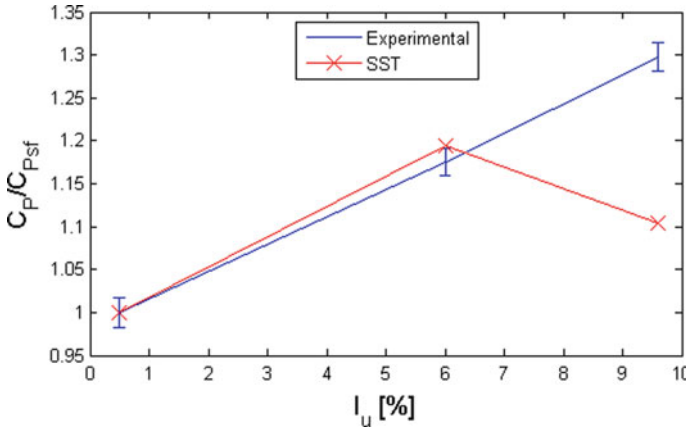


Fig. 15 C_{Pmax} evolution with incoming I_u , for VAWT tests and SST modelling. Normalized with the C_P obtained in the smooth flow case

of this differences for high turbulence can be found in the limitations of the model, which does not consider dynamic stall neither the effect of the shaft, two factors in which it was proven that the increase of turbulence had a positive influence in VAWT performance [3, 14, 17]. Therefore, the model should be further improved to be able to predict accurately the performance of a VAWT for high turbulent cases.

4 Conclusions

The study proposed a set-up that would allow to optimize VAWTs for turbulent flows. Following previous studies and literature, it was shown that the using passive grids turbulent conditions could be generated inside the wind tunnel. Under those conditions, a small H-Darrieus VAWT was tested, revealing a power increase due to turbulence at low Reynolds numbers. Aiming to relate those results to the blade aerodynamics, a NACA0018 blade provided with pressure tabs was built to observe the evolution of pressure distribution in the different turbulent conditions.

C_L curves obtained with this method present good agreement with existing literature, and show that the main effect of turbulence is an increase of the stall angle. At a Re_c number of 80×10^3 , the stall angle of a NACA0018 at low turbulence ($I_u = 0.5\%$) is around 11° , while for medium values ($I_u = 6\%$) the stall angle happens over 16° , and for higher values ($I_u = 9.6\%$) the blade stalls smoothly after 18° . The pressure distributions also showed that as turbulence increase this stall is much less pronounced, with the detachment of the flow occurring progressively towards the leading edge as α increases. On the other hand, for low angles of attack C_L was slightly higher at low turbulence, while its maximum value overall was similar in all turbulent cases (just happening at different α).

C_D curves obtained with the wake survey method tended to overestimate the values from literature, a fact that can be caused by the different methodology and due to the roughness of the model. In general the stall angles were correctly predicted, and it was found that the maximum values of C_D (after stall) were also similar between all turbulent cases. It is also worth noticing that the effect of Reynolds was lower as turbulence increases.

Even when the airfoil curves suggested a substantial increase of performance with turbulence (as measured with the turbine prototype in previous work), the first try to model this performance numerically was not successful. Introducing the experimental polar curves into a Single Streamtube code detected the rise of C_{Pmax} for medium turbulence increases (I_u from 0.5 to 6%), but was not able to describe accurately the case with higher turbulence. The influence of dynamic stall and the turbine shaft, that were not considered but in which turbulence exerts a significant effect, are the main suspects for this discrepancy.

4.1 Future Developments

This work represented only the first step into finding a way to predict more accurately the effect of turbulence in VAWT performance. Therefore, the continuation of the work will be devoted into improving the accuracy of the method.

Experimentally, the measurements can be recreated at more Reynolds numbers and different values of turbulence. A set-up with oscillating blade like in Amandolèse [17] would allow obtaining the curves with the dynamic stall effects. It will be interesting also to double-check the measurements with an aerodynamic balance, specially to explain the difference against literature data in values after stall.

The numerical code, also, was revealed too simple to describe accurately the behavior of the whole turbine. The use of more refined codes (like multiple streamtube [3]) or CFD modelling, and including the effect of the shaft is recommended to try to obtain better agreement with experimental results.

References

1. Mertens S (2006) Wind energy in the built environment. Multi-Science, Brentwood
2. Barlow JF, Drew DR (2015) Wind flow in the urban environment. From WINERCOST Workshop 'trends and challenges for wind energy harvesting'. Coimbra, Portugal, pp 15–24
3. Paraschivoiu I (2002) Wind turbine design: with emphasis on Darrieus concept. Presses inter Polytechnique, Monreal
4. Bianchini A, Ferrara G, Ferrari L (2015) Design guidelines for H-Darrieus wind turbines: optimization of the annual energy yield. Energy Convers Manag 89:690–707
5. Aslam Bhutta MM, Hayat N, Farooq AU, Ali Z, Jamil SR, Hussain Z (2012) Vertical axis wind turbine—a review of various configurations and design techniques. Renew Sustain Energy Rev 16(4):1926–1939

6. Bianchi S, Bianchini A, Ferrara G, Ferrari L (2014) Small wind turbines in the built environment: influence of flow inclination on the potential energy yield. *J Turbomach* 136
7. Janajreh I, Su L, Alan F (2013) Wind energy assessment: Masdar City case study. *Renew Energy* 52:8–15
8. Bertényi T, Wickins C, McIntosh S (2010) Enhanced energy capture through gust-tracking in the urban wind environment. 48th AIAA aerospace sciences meeting including the new horizons forum and aerospace exposition. Orlando, Florida
9. Pagnini LC, Burlando M, Repetto MP (2015) Experimental power curve of small-size wind turbines in turbulent urban environment. *Appl Energy* 154
10. Lee KY, Tsao SH, Tzeng CW, Lin HJ (2018) Influence of the vertical wind and wind direction on the power output of a small vertical-axis wind turbine installed on the rooftop of a building. *Appl Energy* 209
11. Miao JJ, Huang SW, Tsai YD, Liang SY, Hsieh CH, Chen SJ, Hu CC, Cheng JC, Leu TS (2012) Wind tunnel study on aerodynamic performance of small vertical-axis wind turbines. Cheng Kung University, Taiwan
12. Ahmadi-Baloutaki M, Carriveau R, Ting DSK (2015) Performance of a vertical axis wind turbine in grid generated turbulence. *Sustain Energy Technol Assess* 11
13. Carbó Molina A, Bartoli G, De Troyer T (2018) Generation of uniform turbulence profiles in the wind tunnel for urban VAWT testing. In: Battisti L, Ricci M (eds) *Wind energy exploitation in urban environment. TUrbWind 2017. Green energy and technology*. Springer, Cham
14. Carbó Molina A, Massai T, Balduzzi F, Bianchini A, Ferrara G, De Troyer T, Bartoli G (2018) Combined experimental and numerical study on the near wake of a Darrieus VAWT under turbulent flows. *IOP Conf Ser J Phys Conf Ser* 1037
15. Hoffmann JA (1991) Effects of freestream turbulence on the performance characteristics of an airfoil. *AIAA J* 29(9)
16. Devinant P, Laverne T, Hureau J (2002) Experimental study of wind-turbine airfoil aerodynamics in high turbulence. *J Wind Eng Ind Aerodyn* 90(6):689–707
17. Amandolèse X, Széchényi E (2004) Experimental study of the effect of turbulence on a section model blade oscillating in stall. *Wind Energy* 7:267–282
18. Maldonado V, Castillo L, Thormann A, Meneveau C (2015) The role of free stream turbulence with large integral scale on the aerodynamic performance of an experimental low Reynolds number S809 wind turbine blade. *J Wind Eng Ind Aerodyn* 142
19. Laneville A (1973) Effects of turbulence on wind induced vibrations of bluff cylinders. Ph.D. thesis, University of British Columbia, Vancouver, Canada
20. Roach PE (1982) The generation of nearly isotropic turbulence by means of grids. *Int J Heat Fluid Flow* 8(2)
21. Barlow JB, Rae Jr WH (1999) *Low-speed wind tunnel testing*, 3rd edn. Wiley, USA, p 701
22. Schlichting H (1979) *Boundary layer theory*. McGraw Hill
23. Templin RJ (1974) *Aerodynamic performance theory for the NRC vertical-axis wind turbine*. National Research Council Canada, National Aeronautical Establishment
24. Biadgo AM, Simonovic A, Komarov D, Stupar S (2013) Numerical and analytical investigation of vertical axis wind turbine. *FME Trans* 41:49–58
25. Dénos R (2005) Fundamentals of data acquisition and processing. Course Note 171, von Karman Institute for Fluid Dynamics
26. Sheldahl RE, Klimas PC (1981) Aerodynamic characteristics of seven symmetrical airfoil sections through 180-degree angle of attack for use in aerodynamic analysis of vertical axis wind turbines. Sandia National Laboratories energy report

Numerical Simulation and Measurement for Location Optimization of a Vertical Axis Wind Turbine (VAWT)



Giuseppe Ruffino, Susan Schaar, Daniel Lehser-Pfeffermann,
Danjana Theis, Frank Ulrich Rückert, Tobias Müller and Franz Joos

Abstract Wind power plays a decisive role in supplying cities with renewable energy. Combined with short transport routes, it is essential to establish site-specific small wind turbines on urban environments. With the help of *computational fluid dynamics* (CFD) simulations, location-optimized wind turbines can be built. In this paper a vertical small wind turbine (VAWT) is investigated for a representative location. First, rotor blade profiles and then the entire rotor are examined using CFD. After additive manufacturing of the airfoil, the results are validated experimentally in a low speed wind tunnel.

Keywords Small wind turbine · Computational fluid dynamics (CFD) · Experimental investigations · Low speed wind tunnel · Additive manufacturing (AM) · Design optimization · ANSYS CFX · Vertical small wind turbine (VAWT) · Fused deposition modeling (FDM)

1 Introduction

Wind energy as a source of renewable energies has become a daily encounter. Therefore, the market of small energy conversion facilities has grown and given the innovative role of Vertical Axis Wind Turbines (VAWT) in this market. Now and in future, engineers and designers seem to continue to be challenged. Although Albert Betz has already proven that the wind is capable of producing a maximum of 59.2% of

G. Ruffino · S. Schaar · D. Lehser-Pfeffermann (✉) · D. Theis · F. U. Rückert
University of Applied Sciences Saarbrücken, Goebenstraße 40,
66117 Saarbrücken, Germany
e-mail: Daniel.Pfeffermann@htwsaar.de

T. Müller
University of Applied Sciences Würzburg-Schweinfurt, Ignaz-Schön-Straße 11,
97421 Schweinfurt, Germany

F. Joos
Helmholtz-Schmidt-Universität/Universität der Bundeswehr Hamburg, Holstenhofweg 85,
22043 Hamburg, Germany

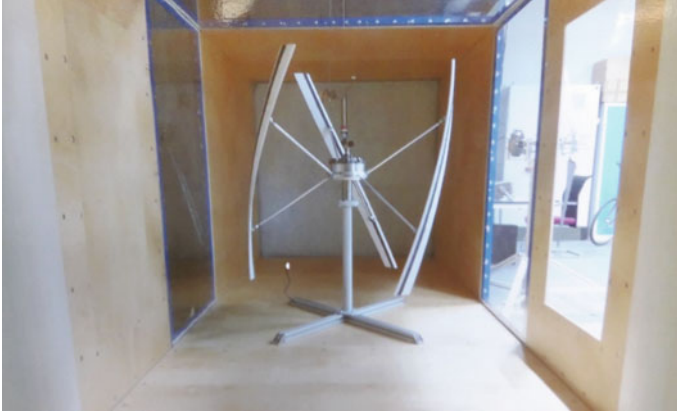


Fig. 1 Prototype of a vertical axis wind turbine (VAWT) in a low speed wind tunnel, which was designed on the basis of the measurement results described in this work

its power, this fact does not prevent from getting as close as possible to this maximum by increasing efficiency in the energy-converting system [1]. To improve the design of the VAWT, a special wind tunnel for small wind turbines was developed and constructed at University of Applied Sciences Saarbrücken (htw saar).

The best possible adaptation of the rotor blades to the available wind speeds is therefore of paramount importance. This requires knowledge of all forces acting on the rotor blade. The demonstration wind tunnel at the htw saar offers the possibility of aerodynamically investigating different rotor designs and blade profiles at varying inflow speeds on a handy scale to obtain meaningful information for larger applications. Main data for the setup of the VAWT shown in Fig. 1 is given at Lehser-Pfeffermann et al. [1]. Flow simulations (computational fluid dynamics CFD) also provide important conclusions on the behavior of a wind turbine and its maximum performance.

To achieve the described improvement of wind turbines, mainly focusing on the variation of blade characteristics associated with the maximization of the energy output, different approaches have already been made. First the flow field is calculated with a CFD approach, the latter applied it alongside an optimization algorithm. Therefore, alternative optimization algorithms have been used. While Mendez and Greiner [2] applied genetic algorithms (GA) and the Blade Element Momentum (BEM) theory to optimize aerodynamic aspects considering blade chord and twist angle, Kenway and Martins [3] solved the problem of optimizing a wind turbine blade by applying a multidisciplinary design approach as well as a gradient based optimization algorithm. Regarding the airfoil, Li et al. [4] offered a technique to optimize the lift-to-drag ratio for 2D airfoils using response surface methods and using numerical optimization. Graaso [5] especially focused on the tip region of the blade of the airfoil design. Chen and Agarwal [6] as well as Riberio et al. [7] used CFD for analysis. Benim et al. gave a good overview over this work [8].

Also, Ju and Zhang [9] took advantage of the CFD approach for obtaining the flow field information. They as well maximized the lift to drag ratio and the lift coefficients of the airfoil and with it developed an optimization procedure for wind turbine airfoils. In the given approaches for aerodynamic analysis by [4, 6], some important details as the used turbulence model, near-wall treatment and the applied models and methods are not sufficiently addressed.

The blade shape is represented by a finite number of degrees of freedom. If quality and possible yield of profiles are to be compared among each other, the lift and resistance or drag coefficients of the individual profiles are determined either mathematically or experimentally an optimization criterion. This leads to two different optimization goals. Determining the resistance at a certain angle of attack. The following equation convert lift force F_{lift} as well as F_{drag} bracket size bra to the two optimization output parameters:

$$c_{lift} = \frac{F_{lift}}{\frac{\rho}{2} \cdot w_R^2 \cdot l \cdot \Delta r} \quad (1)$$

$$c_{drag} = \frac{F_{drag}}{\frac{\rho}{2} \cdot w_R^2 \cdot l \cdot \Delta r} \quad (2)$$

The formulas contain the relative flow w_R , which is determined by the velocity triangle, the profile chord l , the differential profile height Δr and the aerodynamic characteristics of the VAWT airfoil. The lift coefficient c_{lift} is decisive for the lift force and c_{drag} for the resistance. Both parameters provide information about the quality of a profile and dependent on angle of attack [10].

The different rotor blades can be simulated and should be compared to measurement results. Thanks to additive manufacturing technology, a full workflow was developed, so these profiles can be printed out at the htw saar with a FDM printer (Fused Deposition Modeling, e.g. Ultimaker 2+) and mounted on a universal test rig.

2 Additive Manufacturing and Model Validation

Additive manufacturing (AM) becomes more and more important because of a growing amount of available FDM printers on the market. At htw saar we work with the *Ultimaker 2* and *Ultimaker 2+* printers. They are used for producing airfoils of the examined VAWT. To improve efficiency of a VAWT and validate designs a new workflow was developed which is depicted in Fig. 2. The geometry parameters are also transfers to a mesh generator to create a discretization of the domain.

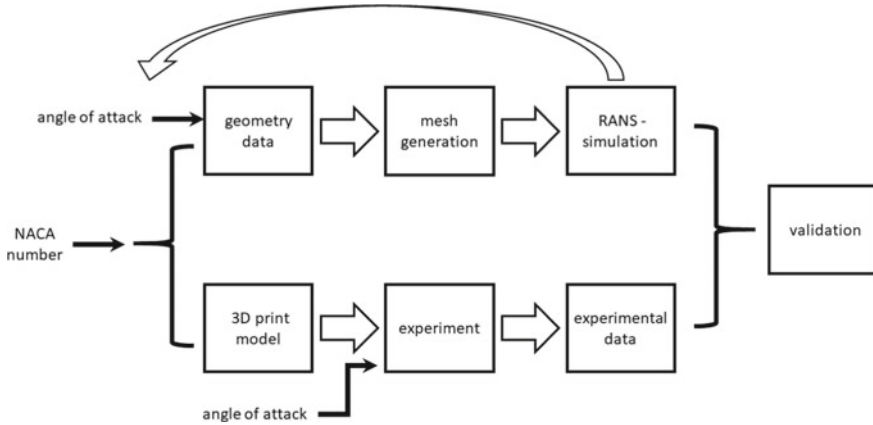


Fig. 2 Overview over the additive manufacturing workflow for the VAWT airfoil design and validation process

2.1 Design Workflow

At the first version of the workflow, the geometry parameters are, however, not generated by the optimization algorithm but stem from the original geometry definition of NACA 0018. NACA is an acronym for National Advisory Committee for Aeronautics and stands for the characteristic geometry of a wing. The geometry generation module defines the aerodynamic operation points according to certain rules that are fed to the flow solver as boundary conditions, together with the discretization of the profile.

Based on the CFD results, two values are calculated and passed over to the validation module. These are the average thrust, that is, the tangential force components in the direction of rotation that generates the power and its standard deviation within the considered space of flow variables. The maximization of the former and the minimization of the latter are the objective functions efficient and stable operation under varying wind conditions. Parallel to the simulation process the geometry will be generated (*Format: *.stl*) and is printed on the FDM printer (Fig. 3).

The design process proposes a new set of geometry parameters for the better fulfilment of these objectives, which closes the cycle. The lift and resistance coefficients are not only dependent on angel of attack, but also on the Reynolds number. Which is defined as follows:

$$Re = \frac{v \cdot l}{\nu} \quad (3)$$

The Reynolds number Re is the quotient of friction forces to inertial forces in the flow and characterizes the flow state [10], where v is the incident flow velocity, l the

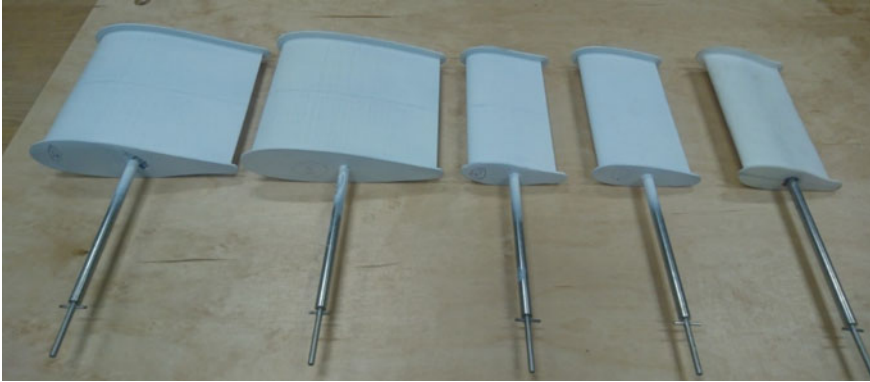


Fig. 3 Additive manufactured prototype airfoils of the VAWT for validation simulation result of the wing design against measurement

characteristic length (here of the profile) and ν the kinematic viscosity of air at given temperature (*here*: $T = 25\text{ }^{\circ}\text{C}$).

In frame of this work, only a constant temperature is used for calculation. The profile geometry is also constant. The Reynolds number is controlled by changing the inflow velocity around flow domain. Profile polars can be created for each Reynolds number and provide information on the aerodynamic behavior at different wind speeds. The inflow wind speed variation is between a minimal velocity of 4 m/s and a maximum velocity of 28 m/s.

2.2 *Mathematical Model and Numerical Simulation*

The flow is assumed to be three-dimensional (3D) and statistically in the steady state. For a rotating turbine with fixed blades, this setting resembles a blade-to-blade surface at a fixed radial section, where the turbine rotational speed and the wind speed are constant in time, in a moving (i.e., rotating) reference frame. In the sense of a quasi-three dimensional procedure, which is also quite common in steam and gas turbines [11], a three-dimensional model can be constructed by an assembly of such blade-to-blade sections. It shall be noted that the resemblance is, however, approximate in so far, that a curved blade-to-blade surface resulting from a radial section is represented by a flat plane in minimization of the latter are the objective functions (efficient and stable operation under varying wind conditions). The optimization algorithm (to be described later in more detail) proposes a new set of geometry parameters.

The Computational Fluid Dynamics (CFD) analysis is based on the general-purpose code CFD ANSYS CFX [11], applying the Finite Volume Method (FVM) for discretizing the governing differential equations. Given the scarcely used method of CFD-simulation with solving the Navier-Stokes equations, these settings and bound-

ary conditions are essentially needed for comparison. Looking at the former listed works, Riberio et al. [7] and Ju and Zhang [9] described those details of the mathematical and numerical formulation adequately.

Comparing these two, both times a one-equation turbulence model was applied, and the angle of attack was varied. Benim et al. [8] otherwise used for the mathematical CFD formulation a two-equation turbulence model, which is more precise, and not only used different angles of attack but the approach velocity magnitude was varied as well.

In a first step, the transport equations are established, discretized and solved in numerical flow simulation. A closer look at all equations reveals that their structure is very similar. Therefore, it was possible to generalize these transport equations as follows [12]:

$$\frac{\partial(\rho\Phi)}{\partial t} + \frac{\partial(\rho v_j \Phi)}{\partial x_j} = \frac{\partial}{\partial x_j} \left(\Gamma \frac{\partial \Phi}{\partial x_j} \right) + S_\Phi \quad (4)$$

The dependent variable Φ is replaced by the flow size that is currently of interest. Here Γ is the diffusion coefficient. If any transport equation is to be adapted to the general form, all terms that do not belong to convection or diffusion are gathered in the source term [12]. The convective terms are discretized by a formally third-order accurate QUICK discretization scheme [11, 12] for the Navier-Stokes equations and a second-order upwind discretization scheme (UDS) [11, 12]. After the transport equations have been established, they are discretized to solve the fluid mechanics problem numerically. The total volume of the fluid is divided into small, discrete volumes. These are also called control volumes or cells [12].

Turbulence is modelled by a two-equation turbulence model, that is, by the Shear Stress Transport (SST) model [11, 13], which were shown to perform quite reliably especially for wall-driven turbulent flows with potential to predict transitional effects [13]. In this work, the turbulent kinetic energy k and the inverse time ω are used to describe the turbulent linear dimension L . The conservation equation for kinetic energy is modified as follows [14]:

$$\frac{\partial(\rho k)}{\partial t} + \frac{\partial(\rho \bar{u}_j k)}{\partial x_j} = P_k - \rho \beta^* k \omega + \frac{\partial}{\partial x_j} \left[\left(\mu + \frac{\mu_t}{\sigma_\omega^*} \right) \frac{\partial \omega}{\partial x_j} \right] \quad (5)$$

For the inverse time measure ω the following conservation equation can be used.

$$\frac{\partial(\rho \omega)}{\partial t} + \frac{\partial(\rho \bar{u}_j \omega)}{\partial x_j} = \alpha \frac{\omega}{k} P_k - \rho \beta \omega^2 + \frac{\partial}{\partial x_j} \left[\left(\mu + \frac{\mu_t}{\sigma_\omega^*} \right) \frac{\partial \omega}{\partial x_j} \right] \quad (6)$$

This results in the following correlation between linear measure L , vortex frequency ω and the turbulent kinetic energy k [14].

$$\omega = \frac{\sqrt{k}}{C_\mu L} \quad (7)$$

The k - ω model achieves very good and reliable results especially near the wall, while in the far field it shows worse results [14]. The eddy viscosity is defined as:

$$\mu_t = \rho \frac{k}{\omega} \quad (8)$$

Flow turbulence is modelled within a RANS (Reynolds Averaged Numerical Simulation) approach [15], where the time-averaged equations are solved for the time-averaged variables in steady-state. The results presented in Figs. 9 and 10 show disadvantage in prediction stall effects at high angles of attack. These uncertainties are known from literature [16].

A more accurate approach would be Large Eddy Simulations (LES) [15, 16], which, being a three-dimensional and unsteady approach, would, however explode the frame in the present case. The present results will further explain, the advantage of LES.

The coupling of the discretized Navier-Stokes equations is treated by a coupled solver for the transport equations of the two-equation turbulence model [11, 17]. Here the Shear-Stress-Transport model (SST model) combines the properties of the two equation models presented above. The turbulent kinetic energy k as well as the dissipation rate is used near the wall to obtain reliable results. As soon as the wall distance is increased and the conditions are insufficient for the k - ω model, the k - ε model is used. This combines the advantages of both models. In the present work only the SST model was used [13]. Convergence criterion for the residual of each equation was set to $10E-5$.

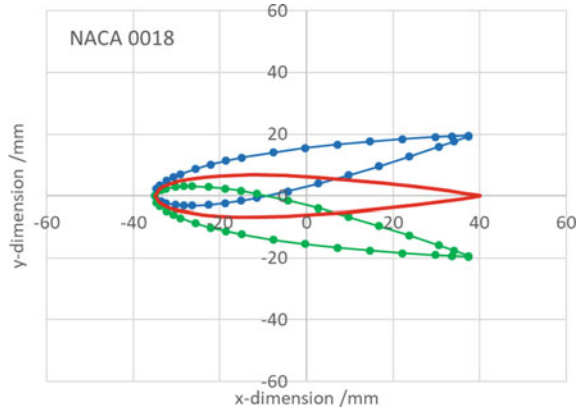
2.3 Design Generation and Boundary Conditions

The design of the VAWT depends strongly on the profile of its airfoils. Every wing is positioned in a cylindrical flow domain, with periodic boundaries on both sides in the circumferential direction, along with an opening boundary condition at the surrounding walls. A typical flow domain with boundary definitions are shown in Fig. 4, where the velocity vector relative to the airfoil, the flow angle and blade angle are also indicated. The inlet and outlet boundaries are placed as an opening around the profile and may be considered to be sufficiently far that the boundaries do not influence the results.

At the opening the distributions of the velocity components are calculated by vector quantities and turbulence quantities are prescribed. The inlet values of the turbulence quantities are estimated assuming a turbulence intensity of 4% and a macro-mixing length [15] of 25% of the chord length. In Fig. 4 the NACA 0018 airfoil is presented as an example for this work. The two leading 0's show that our profile is symmetrically to the axis.

At the opening, a constant static pressure is prescribed along with zero-gradient conditions for the remaining quantities.

Fig. 4 Parametrized splines for automatic geometry generation of the NACA 0018 airfoil



For a full model of the VAWT a pair of periodic boundaries, obviously, periodic boundary conditions are applied. The extension of the domain between the two periodic boundaries corresponds to the space between two neighboring blades in a turbine wheel. In an application, in general, this size varies with the number of blades on the wheel, as well as the radial position of the considered blade-to-blade section.

2.4 Discretization of Physical Domain

A high-quality hex-dominant numerical grid has to be generated around the physical domain of the profile, which interfaces with the essentially tetrahedral grid in the outer domain of the flow region. By an in-house developed algorithm implemented in Microsoft Excel the parametrized geometry was generated for the grid generator *Design Modeler* from ANSYS [11] and used in the ANSYS Workbench 18.2. Different grids for different blade designs and positions can be generated automatically.

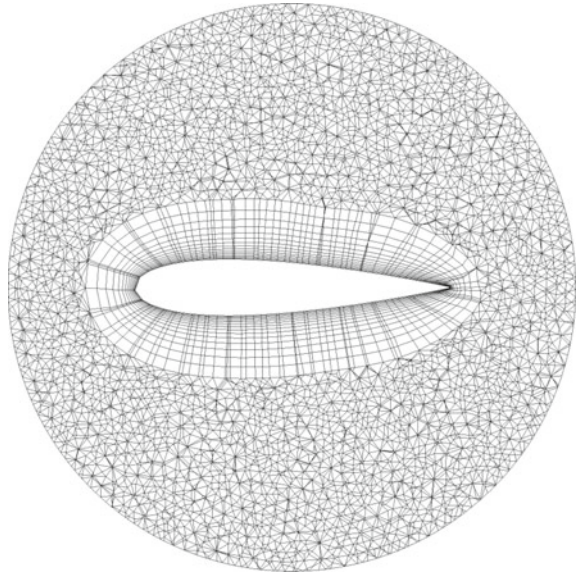
Prompted by the geometry controlling parameters, the mesh generation module calculates the spline curves, manipulates the previous grid accordingly and prompts the ANSYS Design Modeler to generate the new mesh with the new replay script and transfers the mesh to the solver module.

These processes are controlled by scripts written in ANSYS Workbench.

Profile polars can be created for each Reynolds number and provide information on the aerodynamic behavior at different wind speeds. The inflow wind speed variation is between a minimal velocity of 4 m/s and a maximum velocity of 28 m/s. Resulting from this variation the following Reynolds numbers are used for the different experiments: V01 $Re = 48,000$; V02 $Re = 72,000$.

A function for turbulence modelling near the wall regions have been used, the grid resolution near the wall needs to be sufficiently finer than in the far field region of the airfoil. In generating the grids, it is ensured that the non-dimensional wall-distance y^+ is everywhere smaller than 1 for the next-to-wall cells and at least 3 cells

Fig. 5 Discretization of the NACA 0018 airfoil for the numerical simulation with hexahedral inflation layer near the boundary and the tetrahedral grid in the far field



remain within the region $y+ < 5$ [15] which corresponds to a local Courant number [12]. The structure of the used grid is displayed in Fig. 5. This discretization had about 40,000 control volumes. Even very high aspect ratio (see Fig. 5) can be solved by the mathematical solver of CFX. This was checked by a parameter study. High aspect are necessary to fulfill resolution demands of the boundary layer as described at Menter et al. [13]. Changes in the grid are confined to the inflation layer grid surrounding the airfoil. A variation in the discretization because of different angle of attack was not necessary, due to changes of the vector quantities of velocity for boundary conditions. The automatic parametrization mode in ANSYS Workbench 18.2 was used to change the direction of the different wind velocities.

2.5 Numerical Results

During simulation procedure for every airfoil geometry about 75 different angles of attacks had to be calculated. From 0° up to 360° rotating angle around the airfoil axis. This can be displayed in so called profile polars. In Fig. 6 are the velocity distributions around the NACA 0018 airfoil for rotation angles of -15° , 0° and $+15^\circ$ are shown as an example. Two different velocities are used as boundary conditions ($v = 10$ m/s and $v = 15$ m/s) for all angle variations.

As expected, much higher gradients of the velocity distributions can be found at the case with the higher velocities set as boundary conditions. With angle of attack

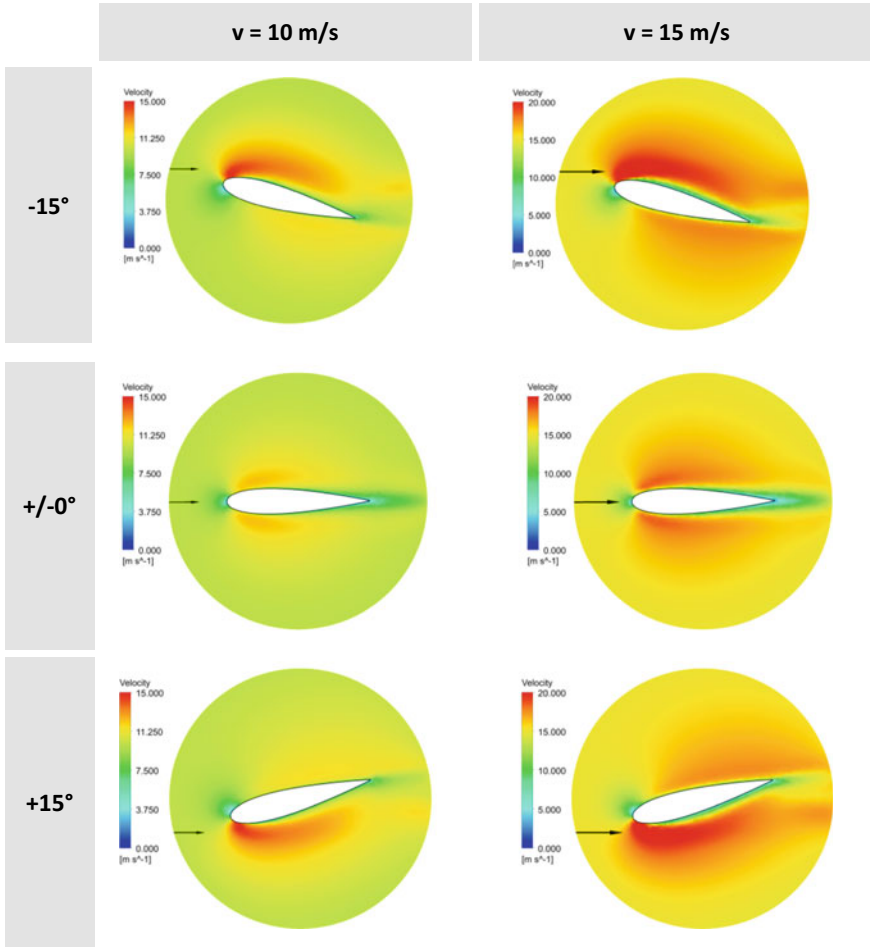


Fig. 6 Numerical results of velocity distribution around the NACA 0018 profiles for different angles of attack and different Reynolds numbers

of +15° distribution of higher velocities can be found beneath the foil. Wake regions can be identified.

The velocity distribution corresponds to the pressure field around the airfoil, which is presented in Fig. 7. In the figure over and under pressures are displayed. For the same boundary conditions as used in Fig. 6. By changing the angle of attack the pressure field around the airfoil changes, which leads to higher forces on the surface in the region of high pressures (*red areas*).

Regions of high velocity as shown in Fig. 6 lead to low pressure distribution at this position (see Fig. 7). Regions of low velocity lead to higher pressure field. As

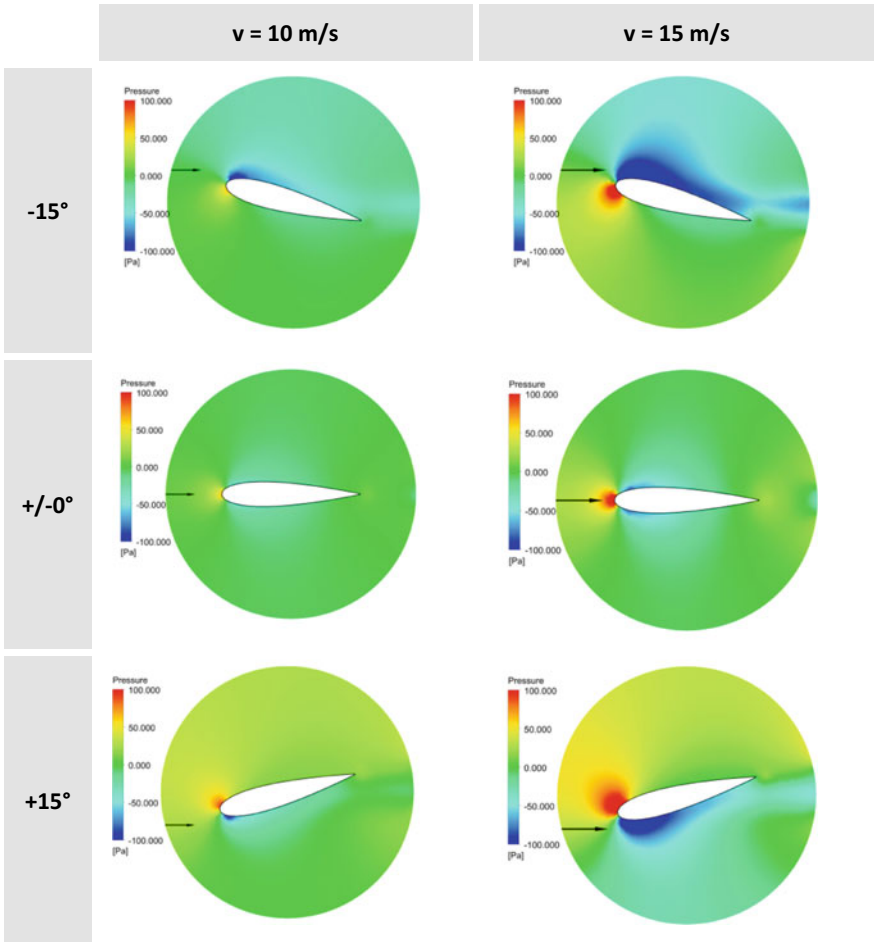


Fig. 7 Numerical results of pressure distribution around the NACA 0018 profiles for different angles of attack and different Reynolds numbers

expected pressure gradients get higher with higher velocity and higher Reynolds numbers.

3 Low Speed Wind Tunnel Experiments

For validation of the numerical results, experiments in the low speed wind tunnel of htw saar has to be performed as also described in [18]. It has to be clarified with the help of these experimental investigation, the best rotor design for the VAWT can be

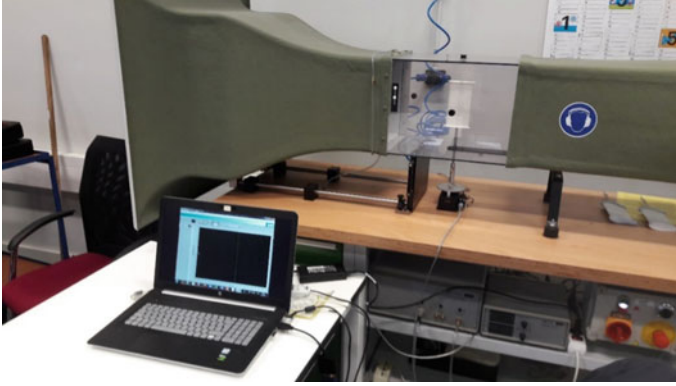


Fig. 8 Setup of low speed wind tunnel and force measurement acting on an airfoil for Vertical Axis Wind Turbine (VAWT) at htw saar (Saarbrücken)

identified and numerical results of the blade profile can be validated against these experiments measured test space during the start-up process. Different Reynolds numbers can be given by the different wind speeds.

The first approach to analyze the flow field around a vertical axis wind turbine was developed by Templin (1974), who considered the rotor to be an actuator disk enclosed in a simple stream tube. The induced velocity through the swept volume of the turbine was assumed to be constant [19]. An extension of the blade-element momentum theory resulted in the Multiple Stream Tube (MST) model, introduced by Strickland (1975), who considered the swept volume of the turbine as a series of adjacent stream tubes [20]. Paraschivoiu (1981) proposed the Double Multiple Stream Tubes (DMST) model that divides a multiple stream tube systems into two actuator disks where the upwind and downwind components of the induced velocities are evaluated as a function of the blade position for each stream tube [21]. More advanced aerodynamic methods for modeling wind turbines are based on vortex theory (Nguyen 1978) [22]. Within this project, a MST model (VAWT_POWER) which has already been described by Müller et al. [1] is used. Especially the consideration of local Reynolds number effect dependent lift and drag coefficients of asymmetrical airfoils distinguish this tool particularly.

In principle, it is always important to compare a simulation with experimental investigations. If they agree well, this increases the credibility of the simulation. For this purpose, a small wind tunnel is available at htw saar as shown in Fig. 8.

In this experimental setup the profile polarities, which were created within the scope of this work, are compared with the profile polarities of the same profile, which were determined in an experimental way in a wind tunnel.

The wind tunnel has a force measuring system for determining the lift and drag forces. This is mounted on the table top of the test bench. The sensors are positioned so that one sensor measures forces in the direction of flow and a second sensor measures forces at 90° to them. In addition, an angle measuring system is implicated

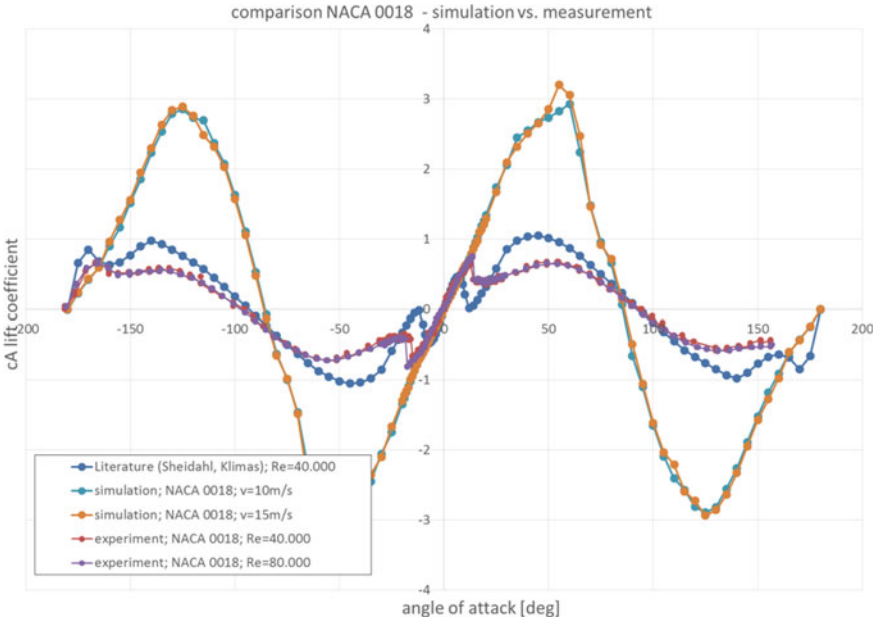


Fig. 9 Comparison of lift forces over angle of attack based on computational fluid dynamics (CFD) simulation of the NACA 0018 profile with experimental investigations theory

via an incremental encoder, which makes the angle of attack available as a measured value.

3.1 Validation of Airfoil Flow Field

For the simulative investigation, the rotor blade profiles are simulated first. These results can then be used to recalculate the complete rotor. In addition, the resulting drive torques can be estimated at different operating points. Figures 9 and 10 show profile polarities which have been determined experimentally, but independently of each other. The curve “experiment; NACA 0018; Re = 40,000” (red) and “experiment; NACA 0018; Re = 80,000” (violet) was created as part of a project at the Saarland University of Applied Sciences. While the curve “literature (Sheidahl, Klimas)” originate from other sources from literature [23]. The data from another institute should be used as a cross check of our work.

The incident flow angle and the incident flow velocity are varied by changing the boundary conditions. If good agreements between simulation and experimental investigations are now achieved, the result is very reliable and can be used as a basis for further investigations. An example of this is the scaling of a small wind turbine

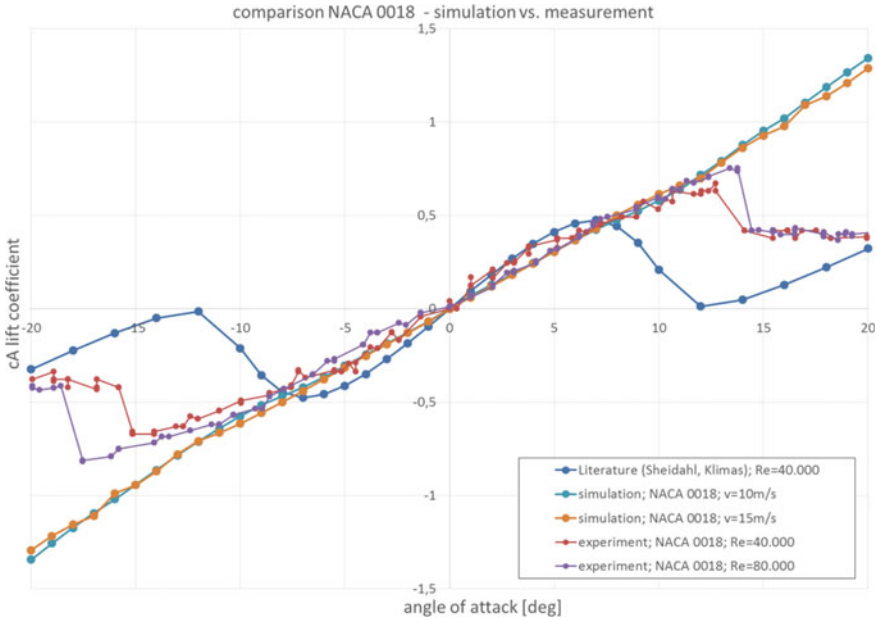


Fig. 10 Comparison of lift forces over 20 degrees of angle of attack based on computational fluid dynamics (CFD) simulation of the NACA 0018 profile with experimental investigations theory

into a large wind turbine. Drag coefficients are already discussed at Ruffino [24] and will not be presented here.

As can be seen from Fig. 9, at higher angles of attack (about 7°–16°) the difference between the measured profile polars and the numerical simulation start to get high. This unexpected result can be explained and is well known from literature [12, 16].

In the angle of attack range between -15° and 15°, the results agree well and are almost congruent as showed in Fig. 10. All three graphs show a linear increase of the lift coefficients and have their zero crossing in the origin. Details from the data presented in Fig. 9 can be identified better in the diagram presented in Fig. 10. It can be identified that prediction quality of the numerical simulation changes with different Reynolds numbers which can be also explained by the use of SST.

These differences lead to the large deviations between simulation and measurement. During the simulation, the stall is not resolved in detail by the SST model used, which leads to significantly increased coefficients.

Afterwards, the critical angle of attack is reached in both experimentally determined profile polarities at which an abrupt drop in the lift coefficient can be detected. This critical angle of attack is not visible in the simulation. Instead, the values continue to rise. The maximum of the simulated profile polar is nearly 3 and is therefore about 300% higher than the other two curves. The zero crossing at 90° is again close to each other for all three curves.

4 Conclusions and Outlook

Numerical simulation results are validated against measurement from our htw saar low speed wind tunnel. By these method design and efficiency improvements of airfoil blades from our VAWT can be made. The full workflow of automatic design generation, simulation, additive manufacturing by FDM printing and measurement in the low speed wind tunnel is present.

Using a two-equation turbulence model within the fluid flow simulation, which is based on Shear Stress Transport (SST) model [11, 13] as expected cannot predict stall effects at high angles of attack around the blade. Also, this is not a problem for further design steps of the VAWT. It should be aim of future work to model these effects with advanced methods. Here a Large Eddy Simulation (LES) is planned to improve the prediction of the forces.

References

1. Lehser-Pfeffermann D, Müller T (2016) Development process of a vertical axis wind turbine. In: 7th world summit for small wind, Husum Germany
2. Mendez J, Greiner D (2006) Wind blade chord and twist angle optimization by using genetic algorithms. In: Proceedings of the 5th conference on engineering computational technology, Las Palmas de Gran Canaria, Spain
3. Kenway G, Martins JRA (2008) Aerostructural shape optimization of wind turbine blades considering site-specific winds. In: Proceedings of the multidisciplinary analysis and optimization conference, Victoria, BC, Canada
4. Li JY, Li R, Gao Y, Huang J (2010) Aerodynamic optimization of wind turbine airfoils using response surface techniques. Proc Inst Mech Eng Power Energy 224:827–838
5. Grasso F (2012) Hybrid optimization for wind turbine thick airfoils. In: Proceedings of the 53rd structural dynamics and materials conference, Honolulu, HI, USA
6. Resch M, Currel-Linde N, Küster U, Risio B. A grid framework for computational mechanics applications. In: Proceedings of the 2nd WSEAS international conference on applied and theoretical mechanics, Venice, Italy, 20–22 Nov
7. Ribeiro AFP, Awruch AM, Gomes HM (2012) An airfoil optimization technique for wind turbines. Appl Math Model 36:4898–4907
8. Benim AC, Diederich M, Pfeiffelmann B (2018) Aerodynamic optimization of airfoil profiles for small horizontal axis wind turbines. Computation 6:34
9. Ju YP, Zhang CH (2012) Multi-point robust design optimization of wind turbine airfoil under geometric uncertainty. Proc Inst Mech Eng Part A J Power Energy 226:245–261
10. Hau E (2014) Windkraftanlagen: Grundlagen, Technik, Wirtschaftlichkeit. 5. Springer, Heidelberg
11. Engineering Simulations and 3-D Design Software. Available online www.ansys.com
12. Noll B (1993) Numerische Strömungsmechanik. Berlin
13. Menter F, Esch T, Kubacki S (2002) Transition modelling based on local variables. In: Rodi W, Fueye N (eds) Proceedings of the fifth international symposium on engineering turbulence modelling and measurements, Mallorca, Spain, 16–18 Sept 2002. Engineering turbulence modelling and experiments 5. Elsevier, Amsterdam, pp 555–564
14. Wursthorn S (2001) Numerische Untersuchung kavitierender Strömungen in einer Modelkreiselpumpe. Universität Karlsruhe, Dissertation, Karlsruhe

15. Durbin PA, Petterson Reif BA (2011) *Statistical theory and modeling for turbulent flows*, 2nd ed. Wiley, Chichester
16. Benim AC, Nahavandi A, Syed K (2005) URANS and LES analysis of turbulent swirling flows. *Prog Comput Fluid Dyn Int J* 5:444–454
17. Deng GB, Ferry M, Piquet et al (1992) New fully coupled solutions of the Navier-Stokes equations. In: *Notes on numerical fluid mechanics (NNFM)*, proceedings of the 9th GAMM, Lausanne, Switzerland, 1991. Springer, Wiesbaden
18. Barlow J, Rae W, Pope A (1999) *Low-Speed wind tunnel testing*, 3rd edn. Wiley, New York
19. Templin RJ (1974) *Aerodynamic performance theory for the NRC vertical-axis wind turbine*. Technical report N-76-16618, United States
20. Strickland J (1975) *The Darrieus Turbine: A performance prediction model using multiple streamtubes*. Sand75-0431-report
21. Paraschivoiu I (1981) *Double-multiple streamtube model for Darrieus wind turbines*. In *NASA Lewis Research Center Wind Turbine Dynamics*, pp 19–25, United States
22. Van Nguyen T (1978) *A vortex model of the Darrieus turbine*. Master Thesis, Texas Tech University
23. Chen XM, Agarwal R (2012) Optimization of flatback airfoils for wind-turbine blades using a genetic algorithm. *J Aircr* 49:622
24. Ruffino GA (2017) *CFD-Simulation von Rotorblattsegmenten und Rotor zur Entwicklung einer vertikalen Windturbine*. Bachelor Thesis; htw saar; Saarbrücken
25. Paraschivoiu I (2009) *Wind turbine design*. Presses internationales Polytechnique, Canada
26. Alaimo A, Esposito A, Messineo A, Orlando C, Tumino D (2015) 3D CFD analysis of a vertical axis wind turbine. *Energies* 8:3013–3033
27. Rückert FU, Ströhle J, Sabel T, Schnell U, Hein KRG (2001) Advantages of combining different grid types for 3D furnace modelling. In: *Sixth international conference on technologies and combustion for a clean environment*, Porto (Portugal), 09–12 July 2001
28. Benim AC, Chattopadhyay H, Nahavandi A (2011) Computational analysis of turbulent forced convection in a channel with a triangular prism. *Int J Therm Sci* 50:1973–1983
29. Benim AC, Cagan M, Gunes D (2004) Computational analysis of transient heat transfer in turbulent pipe flow. *Int J Therm Sci* 43:725–732
30. Leonard BP (1979) A stable and accurate convective modelling procedure based on quadratic upstream interpolation. *Comput Methods Appl Mech Eng* 19:59–98
31. Barth TJ, Jespersen D (1989) The design and application of upwind schemes on unstructured meshes. In: *Proceedings of the AIAA 27th aerospace sciences meeting*, Reno, NV, USA, 9–12 Jan 1989. Technical Report AIAA-89-0366
32. Sheidahl RE, Klimas PC (1981) *Aerodynamic characteristics of seven symmetrical airfoil sections through 180-degree angle of attack for use in aerodynamic analysis of vertical axis wind turbines*, Sandia National Laboratories, SAND80-2114

The Effect of Tail Fin Size on the Yaw Performance of Small Wind Turbines Operating in Unsteady Flow



David Bradney, Samuel Evans and Philip Clausen

Abstract This paper presents measurements and predictions of the yaw performance of a small 5 kW horizontal-axis wind turbine operating in unsteady flow fitted with a delta wing tail fin of two different sizes. Measurements show the smaller of the two tail fins causes the turbine to operate at a higher mean yaw error than the larger tail fin and to respond at a higher yaw rate than the larger tail fin, over most of the operating wind speed range for the turbine. Unsteady slender body theory was used to predict the dynamic performance of the tail fin. The dominant steady lift term in this theory assumes lift is linear with flow angle of attack, α , a valid assumption for $\alpha < 40^\circ$. Experimentally determined coefficient of lift and drag data and an analytical non-linear relationship for the coefficient of lift and drag as a function of α for the delta wing were also used in steady lift term. The relative motion of the yawing tail fin and the effects of the reduced wake velocity on the tail fin performance were also considered. Unsteady slender body theory incorporating experimentally determined data, with the inclusion of relative motion and reduced wake velocity gave the highest correlation with experimental results.

Keywords Small wind turbines · Unsteady flow · Yaw performance · Tail fin

1 Introduction

Small wind turbines, defined by the International Electrotechnical Commission standard IEC 61400.2-2013 as machines with a power output of less than 50 kW and rotor swept area of less than 200 m², often operate in unsteady wind conditions and predominately track the wind using a tail fin. The combination of unsteady wind conditions, which includes both wind speed and wind direction changes, and a tail fin have been shown to lead to high yaw errors and high yaw rates, the latter resulting in high gyroscopic loading on the blades, Wilson and Clausen [14], Wilson et al. [15], Evans et al. [8]. Furthermore, turbine yaw error, that is the difference between

D. Bradney · S. Evans (✉) · P. Clausen
School of Engineering, The University of Newcastle, Callaghan, NSW 2308, Australia
e-mail: samuel.evans@newcastle.edu.au

© Springer Nature Switzerland AG 2019
L. Battisti (ed.), *Wind Energy Exploitation in Urban Environment*,
Research Topics in Wind Energy 8, https://doi.org/10.1007/978-3-030-13531-7_4

the direction of the wind and the direction of the turbine, leads to a reduction in turbine power output between \cos^2 of the yaw error, Pedersen [13], and \cos^3 of the yaw error, Bechly et al. [2]. Consequently to maximise turbine power output whilst minimising loading on turbine components during operating in unsteady flows, will require the turbine to follow the flow at relatively low yaw rates with minimized yaw error. Before undertaking this optimization task, a clear understanding is required on how tail fin size effects yaw and yaw rate response of the turbine operating in unsteady flows.

There have been several studies investigating the yaw behaviour of the tail fins for small wind turbines including Nishizawa et al. [12], Ebert and Wood [7] and Corbus and Prascher [6], however most of these studies are based on wind tunnel testing without the blade rotor, furling wind turbines, or tests undertaken in low turbulence wind environments. Furthermore there is little published research work undertaken on the size of tail fins with most tail fin size selections relying on manufacturer's experience or a trial-and-error approach. The general "rule-of-thumb" for a tail fin area is about 5% of the swept rotor error, Windynation [16]. As such, the lack of experimental data from field measurements in the literature presents a substantial knowledge gap for improving the dynamics and energy capture of small-scale wind turbine systems. The work described in this paper is aimed at reducing this knowledge gap through the analysis of detailed experimental performance data acquired from an operating small wind turbine.

The wind energy group at the University of Newcastle, Australia has a 2-bladed 5 kW Aerogenesis experimental wind turbine located in a low speed, unsteady wind site on the University's main Callaghan campus; Fig. 1 shows the turbine at the Callaghan site. Figure 2 shows the measured turbulence intensity level at this site as a function of the 10 min average wind speed and the turbulence intensity assumed in IEC 61400.2. As can be clearly seen in Fig. 2, the site is highly turbulent. The Aerogenesis turbine has been extensively instrumented to measure key turbine performance parameters including turbine yaw and yaw rate, turbine power output and rotor speed plus instrumentation to measure strain in one of its composite-constructed blades during operation. The tail fin has also been instrumented to measure the moment the tail fin applies to the turbine during operation. Furthermore both wind speed and direction were measured by a cup anemometer a wind vane located 3 m below the hub height; both instruments can be seen in Fig. 1.

This paper consists of 5 sections. Section 2 presents unsteady slender body (USB) theory which is used to solve the 2nd order differential equation that describes the rotational motion of the wind turbine about the yaw axis, Wood [17]. The standard form of USB theory has short comings with respect to its predictive accuracy at high yaw angles and operation in the wake of the turbine rotor. Here standard USB theory is present as well as modifications to improve accuracy at high yaw angles, account for the relative motion of the yawing tailfin and operation in the turbine's wake. The experimental results are presented in Sect. 3 and a statistical comparison between predictions and measurements in Sect. 4 of this paper. Section 5 discusses the results of both predictions and measurements and draws conclusions from this work.



Fig. 1 The Aerogenesis 5 kW turbine at the Callaghan site

Fig. 2 Callaghan turbulence intensity and IEC61400.2-2013

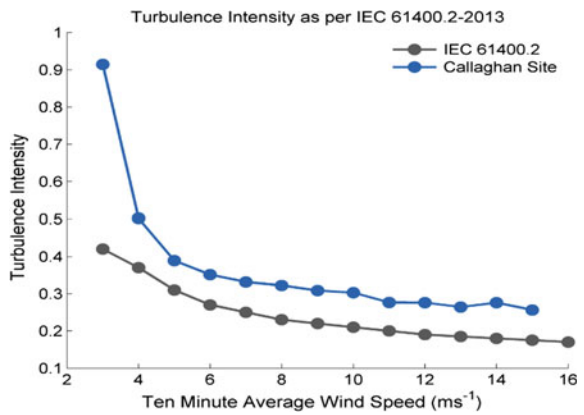
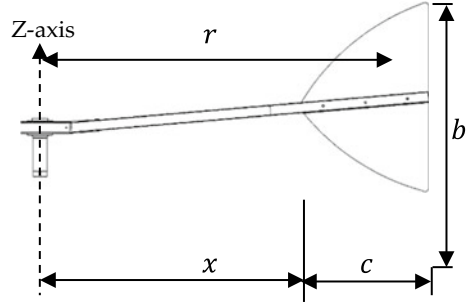


Fig. 3 Critical tail fin dimensions corresponding to Table 1



2 Tail Fin Theory

2.1 Unsteady Slender Body Theory

The dynamic behavior of the tail is often described by unsteady slender body (USB) theory, with the total moment of the tailfin about the yaw axis is given by:

$$\sum M_{tailfin} = M_1(\theta - \varphi) + M_2\dot{\theta} - M_3\dot{\varphi} + M_4\ddot{\theta}, \quad (1)$$

where the yaw misalignment angle of attack, $\alpha = (\theta - \varphi)$ in radians is the difference between the wind turbine direction, θ , and wind direction, φ . Factors M_1 , M_2 , M_3 and M_4 are defined in Eqs. (2)–(6) respectively.

M_1 is the steady lift term and is the lift generated by the delta tailfin and is given by:

$$M_1 = \frac{1}{4}\pi\rho b^2 U_0^2 \left(\frac{2}{3}c + x \right), \quad (2)$$

where c and x are defined in Fig. 3 and ρ is the density of air and U_0 is the upstream velocity. This term assumes that the coefficient of lift, C_l is linear, and is defined by Eq. (3), for all yaw misalignment angles.

$$C_l = \frac{\pi b}{c} \alpha \quad (3)$$

The restoring moment is assumed to act from the centre of pressure of the delta wing, defined as $2/3$ of the chord length from the front of the delta wing. For a delta wing, the assumption of steady lift remains valid up to α of approximately 40° due to the leading-edge vortices delaying the stall point, Katz and Plotkin [9]. During field testing of the Aerogenesis turbine, α regularly exceed 40° so it is likely that theory could over-predict the contribution from the lift term.

M_2 and M_3 in Eq. (1) are the downwash term and arises from the change in trajectory of the leading and trailing edge vortices of the tail fin, as part of the lift generation. The shape of the delta wing causes the leading-edge vortices to dominate the flow, consequently the implementation of the unsteady slender body theory neglects the effects of the trailing edge vortices. There are two independent downwash components which act in opposite directions, with the difference in their relative strength, which governs the direction of the yaw moment.

The downwash terms are:

$$M_2 = \frac{1}{4}\pi\rho b^2 U_0(c+x)^2, \text{ and} \quad (4)$$

$$M_3 = \frac{1}{4}\pi\rho b^2 U_0\left(\frac{c^2}{4} + \frac{cx}{3}\right) \quad (5)$$

M_4 , the final term in Eq. (1), is the added mass term, a consequence of moving air in front of the delta wing area, and as such is a function of the yaw angular acceleration of the turbine.

$$M_4 = \frac{1}{4}\pi\rho U_0 c\left(\frac{c^2}{5} + \frac{x^2}{3} + \frac{cx}{2}\right) \quad (6)$$

2.2 Approximation Method

Equation (3) shows that the unsteady slender body theory assumes C_l has a linear relationship with the angle of attack, α , an assumption which is not correct for $\alpha > 40^\circ$. During field testing, the yaw misalignment often exceeded 40° , so the lifting moment term, M_1 is modified to reflect this. M_1 is given by:

$$M_1 = \frac{1}{2}\rho\left(\frac{1}{2}cb\right)U_0^2 C_l r. \quad (7)$$

C_l is approximated by:

$$C_l = K_p \sin \alpha \cos^2 \alpha + K_v \cos \alpha \sin^2 \alpha, \quad (8)$$

where K_p and K_v are functions of the aspect ratio, AR, Bertin and Cummings [3] and Wright [18], with AR defined by Eq. (9).

$$AR = \frac{s^2}{A}, \quad (9)$$

where s is the span of the wing in m and A is the area of the wing in m^2 .

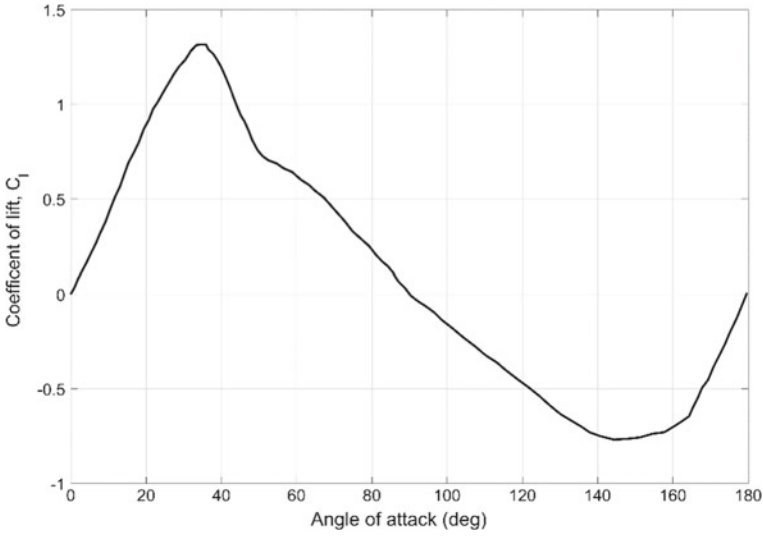


Fig. 4 Coefficient of lift for a delta wing as a function of the angle of attack. Data from Bechly et al. [2]

2.3 Experimental Estimation

The C_l and C_d terms for a delta wing have been determined from the experimental data presented in Bechly et al. [1] which has been validated previously using a scaled delta wing in a wind tunnel. Figures 4 and 5 show respectively C_l and C_d as a function of α ; this experimental data will be used in Eq. (8) to give another estimate of M_1 .

2.4 Relative Motion of the Tail Fin

The tail fin modelling approaches documented in Sects. 2.1–2.3 inclusive have not accounted for the relative velocity between the yawing tail fin and the wind. Narayana et al. [11] and Nishizawa et al. [12] have implemented a simple relative velocity correction for a rectangular tail fin. Figure 6 shows the relative velocities and force components acting on a tail fin at an angle of θ to the wind direction. The velocity term in Eqs. (2), (4), (5), (6) and (7) inclusive is replaced by:

$$U_{rel} = U_0 - \psi_y r \cos\left(\theta - \frac{\pi}{2}\right), \quad (10)$$

where ψ_y is the angular velocity of the tail fin about the turbine's yaw axis in rad s^{-1} and $\pi/2$ is included to account for the tail fin moving towards or away from the

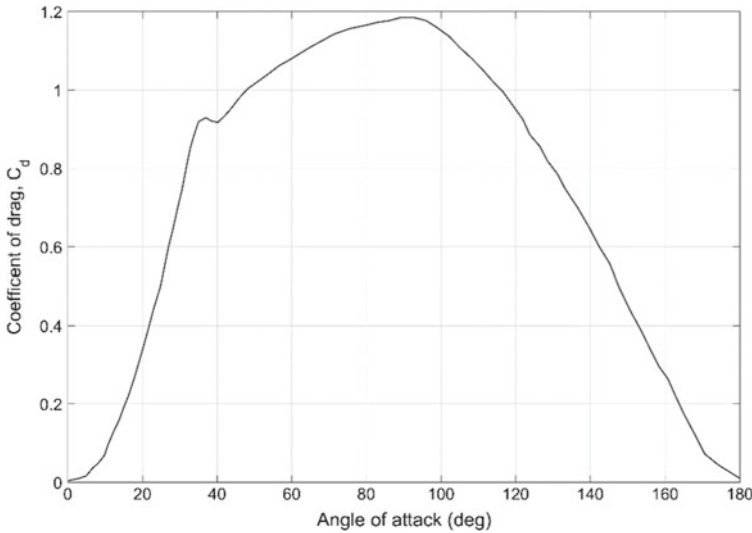
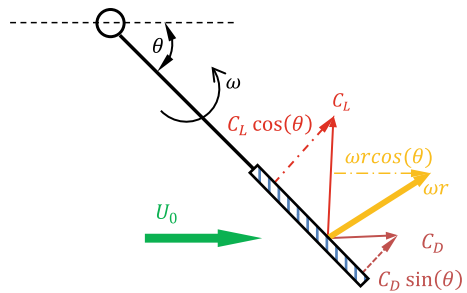


Fig. 5 Estimated drag curve for a delta wing tail fin. Data from Bechly et al. [2]

Fig. 6 Tail fin moment contributions from lift and drag forces



incoming wind velocity vector, thereby increasing or decreasing the relative velocity respectively.

The components of C_l and C_d acting normal to the tail fin should also be included. For α less than 40° , the effect of the drag component is small and usually neglected, but, when considering larger yaw misalignment, the addition of drag becomes more significant, and consequently should be included.

2.5 Wake Velocity

The tail fin resides in the wake of the rotor and will experience a reduction in velocity. Blade element momentum theory uses a dimensionless axial induction factor, a , to

account for the reduction in wind speed as the air passes through the rotor plane. That is at the rotor plane:

$$U_{wake} = U_0(1 - a) \quad (11)$$

The axial induction factor is assumed to change from 0 upstream of the turbine to twice this value far downstream. Detailed measurements in the wake of a 10 kW Bergey Excel wind turbine by Corbus and Prascher [6] indicated the wake velocity was highly dependent on the rotor configuration with $U_{wake}/U_0 = 0.53-0.6$, and for the optimal axial induction factor of $1/3$ [17], Eq. (11) gives $U_{wake}/U_0 = 0.67$. For the work reported in this paper, the velocity experience by the tail fin will be equal to $0.67U_0$.

2.6 Unsteady Wind Term

A previous study by Bechly et al. [1] had found that unsteady wind direction change had minimal effect on the tail fin performance of a 400 W turbine. For their study, the ratio of the tail fin size to the wind turbine inertia and rotor size was larger than that of the 5 kW Aerogenesis used in this study. As a consequence of this, it was deemed worthwhile to add an unsteady term to the tail fin moment balance of Eq. (1):

$$M_5 = \frac{du}{dt} \frac{1}{4} \pi \rho b^2 \left(\frac{1}{3} xc + \frac{1}{4} c^2 \right) \quad (12)$$

3 Experimental Work

As previously stated, the Aerogenesis wind turbine was fitted with two delta wing shaped tail fins with an area of 0.26 and 0.65 m^2 ; Table 1 and Fig. 3 show details of both the small and large tailfin. With the small tail fin, the turbine exhibited extremely poor yaw performance at low (turbulent) wind speeds, and in extreme wind conditions, resulted in a yaw error of up to 180° . As a consequence of the poor yaw performance, it was decided to test a larger sized tail fin to assess whether it improves the turbine's yaw performance.

Table 1 Critical tail fin information and dimensions

Tail fin size	Material	b (m)	c (m)	x (m)	Thickness (mm)
Small	Steel	0.85	0.6	1.32	3
Large	Aluminium	1.54	0.85	1.32	3

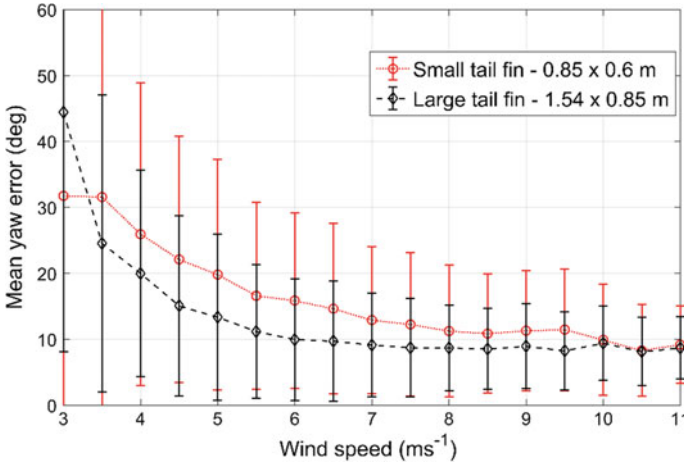


Fig. 7 Mean absolute tail fin yaw error and the bounds of the measurements as a function of wind speed for both the small and large tail fin

A custom-designed load measurement device was built to measure the bending moment applied from the tail fin to the boom arm of the wind turbine. Details of this device can be found in Bradney [4], however here it is sufficient to note that signals from the load cells in this device were acquired simultaneously with other performance measuring sensors on the turbine.

A series of experiments were run with both tail fins during the same measurement campaign, by interchanging the tail fins during a series of short experiments. Figure 7 shows the mean absolute yaw error for both tail fins and the absolute bounds of all measured yaw errors as a function of wind speed; as can be clearly seen, there is significant difference between the absolute mean and the absolute bounds for the tail fins, for most wind speeds. The results show that the large tail fin has a mean yaw error of 15° more than the small tail fin for wind speed less than 3.5 ms⁻¹. A possible reason for this could be the larger damping due to the increased tail fin area. For wind speeds between 4 and 11 ms⁻¹, the large tail fin has a smaller mean yaw error, converging to a mean yaw error close to 8.5°. The wind turbine will lag changes in wind direction due to the inertia about the yaw axis ($I = 108 \text{ kg m}^2$ —for the turbine fitted with the small tail fin), and so it is expected that it will always operate with some amount of mean yaw error. For the small tail fin, the average yaw error does not converge to the range of the large tail fin until a wind speed of 10 ms⁻¹, indicating the wind turbine is performing at a sub-optimal level below this wind speed.

When considering the effect of tail fin size on the yaw behaviour, it is also important to consider the wind turbine’s yaw rate. High yaw rates have a detrimental effect on the blade root bending fatigue life Wood [17], as they induce gyroscopic loading via the relationship shown in Eq. (12):

$$\sum M_x = I_z \omega_y \psi_z \tag{12}$$

where M_x is the pitching moment on the blades in Nm, I_z is the total moment of inertia about the yaw axis in kg m^2 , and ω_y is the rotational speed of the rotor in rad s^{-1} . As such, it is essential that the increased responsiveness for the large tail fin to wind direction changes does not result in significantly higher yaw rates.

The yaw rates of the two tail fins show that the small tail fin operates at a higher yaw rate than the large tail fin for wind speeds up to 8.5 ms^{-1} . This increased yaw rate is presumably due to the lower damping of the small tail fin, and the larger wind direction misalignment. The small tail fin shows a decreasing yaw rate trend with wind speed. This trend indicates that the small tail fin does not become effective in following wind direction changes until higher wind speeds, at which point the yaw error is small, and so the required direction change of the wind turbine would also be less.

In contrast, the maximum yaw rate of the large tail fin starts to plateau at 30° s^{-1} for a wind speed of 6 ms^{-1} coinciding with the wind speed at which the large tail fin reaches its mean yaw error convergence. These results suggest that the large tail fin is responding to changes in wind direction at all wind speeds between cut-in and cut-out. As such the wind turbine does not reach the greater yaw errors of the small tail fin, which would require a significant and rapid direction change for re-alignment to occur.

As has been previously observed in Wright [18], the scatter plot of yaw rate and yaw error shown in Fig. 8 produces a diamond shape. The region of points formed by the large tail fin is approximately half the size for that of the small tail fin. This is an interesting result, given the fact that the small tail fin has just under half the aerodynamic area of the large tail fin.

4 Comparison Between Measurements and Yaw Modelling Theory

Given the unsteady nature of the wind flow and therefore response of the turbine, a statistical approach will be adopted to compare predictions with the measured yaw response of the turbine. The correlation coefficient, r , was chosen to provide a definitive measure of the instantaneous simulated yaw behaviour of the turbine.

The correlation coefficient, r is defined as:

$$r = \frac{\sum_{i=1}^n (x_i - \bar{x})(y_i - \bar{y})}{\sqrt{\sum_{i=1}^n (x_i - \bar{x})^2 \sum_{i=1}^n (y_i - \bar{y})^2}}, \quad (13)$$

where x is the measured data set and y is the simulated data set.

As detailed in Sect. 2, there are three theoretical methods:

1. *USB*—implementation of unsteady slender body theory using a linear C_1 slope [Sect. (2.2)];

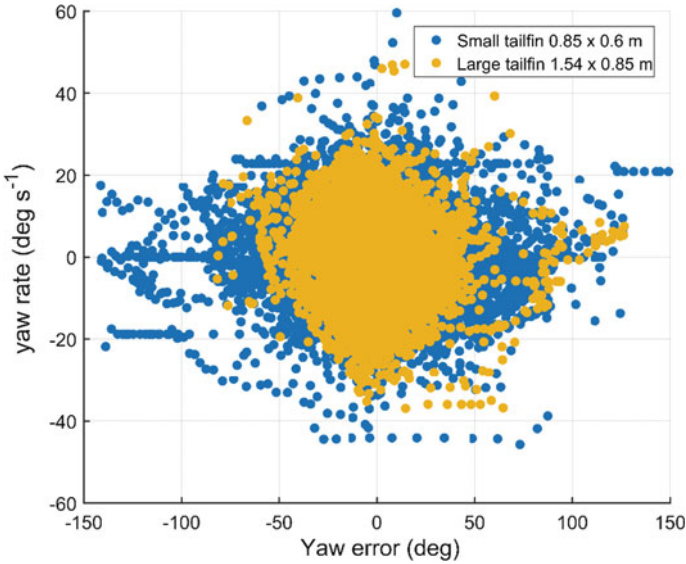


Fig. 8 Yaw rate as a function of yaw error for both tail fins

2. *Exp*—using experimentally estimated C_l and C_d (Sect. 2.3), and
3. *Approx.*—using the lift approximation method (Sect. 2.2).

Each method has three variations:

1. The standard implementation of the method
2. The addition of the unsteady wind term (Sect. 2.6), and
3. The addition of the relative velocity term (Sect. 2.5).

4.1 Large Tail Fin Simulations

Figure 9 show the performance of the three models with three variations against the measure tail fin yaw rate for the large tail fin; details of the complete aeroelastic models are given in Bradney [4].

The measured signal (red box) had a yaw rate range of approx. $\pm 30^\circ \text{ s}^{-1}$, a mean yaw rate of 0° s^{-1} , and a standard deviation of 5° s^{-1} . It can be seen that the three *USB* methods over predicted the yaw rates when compared to the measured signal, whereas the *experimentally estimated* and *approximation* methods under-predicted the maximum yaw rate. A possible reason for this is that the latter two methods are more heavily damped and hence do not allow for the extreme yaw rate case, whereas the *USB* methods showed more extreme movement variations and hence the higher yaw rate predictions.

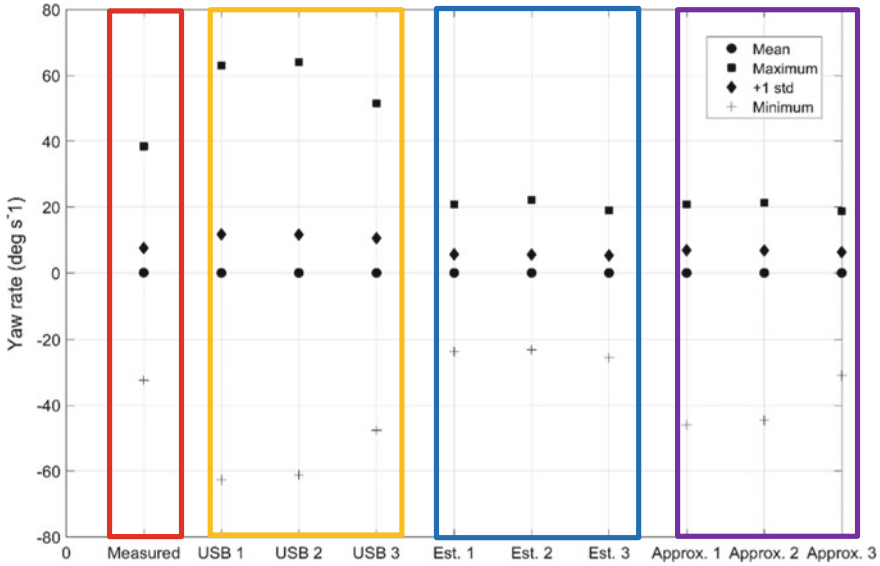


Fig. 9 Mean, maximum, standard deviation and minimum values of the measured data set and the nine different tail fin modelling methods for the large tail fin

Overall statistics, however, do not provide a complete representation of the wind turbines predicted performance. A more meaningful approach is to consider the instantaneous performance of each method, as the instantaneous yaw alignment affects the power quality, and predicted blade and drivetrain loading. Figure 10 shows the correlation coefficients for each of the simulations, where each point represents a five-minute simulation, at a sample rate of 5 Hz.

As can be clearly seen, there is a significant distribution of the values shown; the *USB* methods have a correlation coefficient ranging from $r = 0.35$ to 0.85 , the *experimentally estimated* methods range from $r = 0.55$ to 0.95 , and the *approximation* methods range from $r = 0.48$ to 0.92 . Despite the spread of values, the *experimentally estimated* methods consistently provided the highest correlation within each measurement set—with $r = 0.95$ – 0.97 for the highest correlating data set (green). The corresponding *approximation* methods had $r = 0.85$ – 0.9 , while the *USB* methods were between $r = 0.7$ and 0.73 . For the data set with the lowest correlation coefficient (pink), this trend still continues. Despite the *experimentally estimated* method having $r = 0.52$ – 0.55 , the *approximation* methods were still lower with $r = 0.48$ – 0.51 . The *USB* methods again performed the poorest with all correlation coefficients below $r = 0.4$. Within the three methods, the results of the three variations were similar, however, the inclusion of the relative velocity component, consistently gave a higher correlation.

It is also worth noting that the relative difference between each method did not appear to scale in a linear manner, as demonstrated by the green and navy data

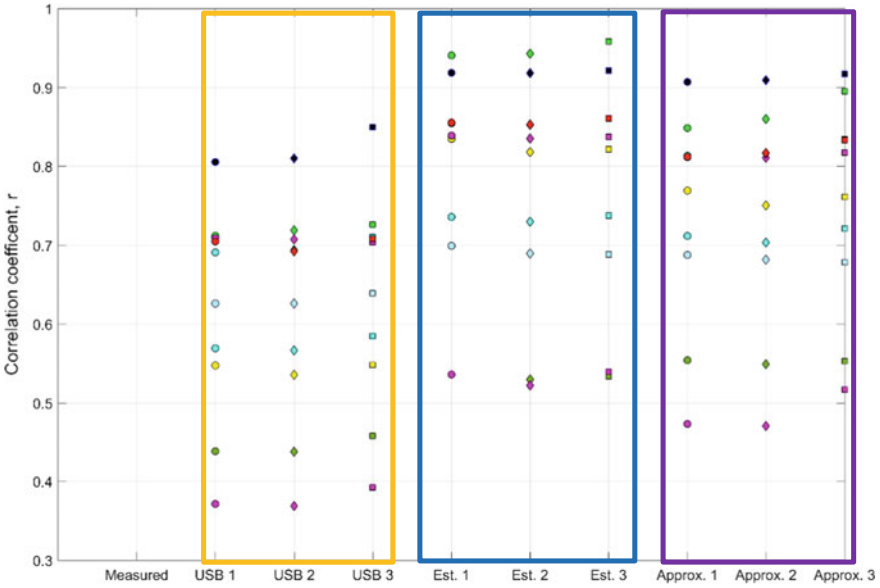


Fig. 10 Correlation coefficients for the nine different tail fin models for the large tail fin. Each data point represents the correlation coefficient for a 5-min measured sample

sets. The difference between the correlation coefficients of the *experimentally estimated* methods was 0.03, whereas the *USB* methods had a much larger difference of 0.1. An explanation for the relative performance of the three methods is found by considering their fundamental differences. The *USB* methods result in a significant moment produced from large wind direction changes. As such, this method leads to predictions which over-track the wind signal, resulting in higher yaw rates. The reason for the over-estimation is that this approach assumes that the moment varies linearly with the angle of attack (i.e. misalignment angle), meaning that as the angle of attack increases so too will the applied moment. In contrast, the *approximation* and *experimentally estimated* methods included the presence of a stall angle. The stall angle is important, as the moment of inertia of the 5 kW wind turbine is significant ($I = 108 \text{ kg m}^{-2}$), and the rapid wind direction changes result in the wind turbine frequently exceeding 40° yaw misalignment. The presence of a stall angle leads to a reduced restoring moment, and consequently a much slower response frequency, which is significant, as the accuracy of these estimates impacts both the overall wind turbine model and the predicted gyroscopic moments experienced by the blades and shaft.

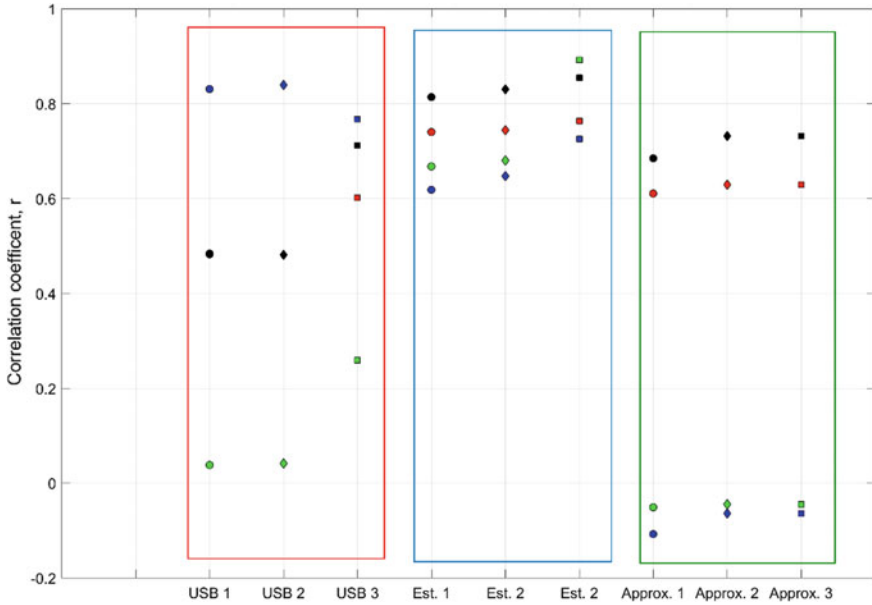


Fig. 11 Correlation coefficients for the nine simulation methods using the small tail fin. Each data point represents the correlation coefficient for a 5-min measured sample

4.2 Small Tail Fin Simulations

On the whole, for the large tail fin, the *experimentally estimated* methods showed good to excellent correlations with the measured signal. It is now worth considering the effectiveness of the modelling approach with the small tail fin. Figure 11 shows the correlation coefficients for the data sets that used the small tail fin.

In both the *approximation* and *USB* methods, there is a significant distribution of correlation coefficients—far larger than of the large tail fin. The results range from $r = 0.82$ to almost 0 for the *USB* methods and $r = 0.75$ to -0.15 for the *approximation* methods. Again, like the large tail fin simulations, the *USB* methods consistently showed an over-sensitivity to the wind direction, whereas the measured wind turbine yaw motion was far more chaotic. The over-sensitivity to wind direction changes resulted in the significant spread of correlation coefficients seen here. The *experimentally estimated* methods showed good correlation to the measured signal with the simulations all falling between the range of $r = 0.6$ – 0.8 . The presence of the stall angle became even more significant for the small tail fin simulations, as the wind turbine regularly exceeded 40° yaw misalignment. As such, the reduced restoring moment allowed for a slower response, far more indicative of the measured yaw behaviour.

5 Discussion and Conclusions

The experimental measurements clearly show that the larger of the two tail fins significantly improved the yaw performance of the Aerogenesis 5 kW turbine by reducing the mean yaw error for wind speeds $>3.5 \text{ ms}^{-1}$ and by reducing the maximum yaw rate of the turbine to approximately 30° s^{-1} for wind speeds $>4 \text{ ms}^{-1}$. Specifically the small tail fin was found to cause the mean yaw errors to be 50% higher than the large tail fin up to the reference wind speed of 10.5 ms^{-1} . Furthermore, the small tail fin was found to constantly change from a shaft speed above the synchronous generator speed of 1440 rpm to below. This resulted in the turbine switching from being controlled to uncontrolled, which led to four separate component failures in the inverter unit.

The performance of nine different yaw modelling methods were evaluated for both the large and small tail fins. For both tail fins, the experimentally estimated method which utilizes a pseudo delta wing C_l and C_d curves gave the most consistent and accurate results. Within this approach, the inclusion of the relative tail fin velocity and unsteady wind speed effects led to the highest correlation with the measurements.

As previously stated, the general “rule-of-thumb” for a tail fin area is about 5% of the swept rotor area, Windynation [16]. By this “rule-of-thumb”, the large tail fin was 4.5% of the swept rotor area. Variations of this rule were found to work successfully on different boom lengths and rotor configurations; a small tail fin and a long boom arm has been proposed by Calvert [5], and minimizing the offset between the yaw axis and rotor plane by Kentfield [10].

References

1. Bechly M, Gutierrez H, Streiner S, Wood D (2002) Modelling the yaw behaviour of small wind turbines. *Wind Eng* 26(4):223–239
2. Bechly M, Clausen P, Ebert P, Pemberton A, Wood D (1996) Field testing of a prototype 5 kW wind turbine. In: Anderson M (ed) British wind energy association annual conference 1996. Mechanical Engineering Publication Ltd
3. Bertin J, Cummings R (2009) *Aerodynamics for engineers*, 5th edn. Pearson Prentice Hall, Upper Saddle River
4. Bradney D (2017) Measured and predicted performance of a small wind turbine operating in unsteady flow. Ph.D. thesis, University of Newcastle. <http://hdl.handle.net/1959.13/1350180>
5. Calvert N (1979) *Windpower principles: their application on the small scale*, 3rd edn. Butterworth-Heinemann, London
6. Corbus D, Prascher D (2005) Analysis and comparison of test results from the small wind research turbine test project. In: Proceedings of the 43rd AIAA aerospace sciences meeting and exhibit, Reno, Nevada, 10–13 Jan 2005
7. Ebert P, Wood D (1995) On the dynamics of tail fins and wind vanes. *J Wind Eng Ind Aerodyn* 56(2–3):137–158
8. Evans S, Bradney D, Clausen P (2018) Assessing the IEC simplified fatigue load equations for small wind turbine blades: how simple is too simple? *Renew Energy* 127:24–31
9. Katz J, Plotkin A (2002) *Low-speed aerodynamics*, 2nd edn. Cambridge University Press, New York

10. Kentfield J (1996) *Fundamentals/wind-driven water*. Gordon and Breach Science Publishers, Canada
11. Narayana M, Putrus G, Leung P, Jovanovic M, McDonald S (2012) Development of a model to investigate the yaw behaviour of small horizontal-axis wind turbines. *Proc Inst Mech Eng Part A J Power Energy* 226(1):86–97
12. Nishizawa Y, Tokuyama H, Nakajo Y, Ushiyama I (2009) Yaw behaviour of horizontal-axis small wind turbines in an urban area. *Wind Eng* 33(1):19–30
13. Pedersen T (2004) On wind turbine power performance measurements at inclined airflow. *Wind Energy* 7(3):163–176
14. Wilson S, Clausen P (2007) Aspects of the dynamic response of a small wind turbine blade in highly turbulent flow: part 2 predicted blade response. *Wind Eng* 31(4):217–231
15. Wilson S, Clausen P, Wood D (2008) Gyroscopic moments on small wind turbines blades at high yaw rates. *Trans Inst Eng Aust J Mech Eng* 5(1)
16. Windynation (2016) Sizing your wind turbine tail. <http://www.windynation.com/jzv/inf/wind-turbine-tail-fin-sizing-your-wind-turbine-tail>. Last accessed 22 May 2018
17. Wood D (2011) *Small wind turbines: analysis, design and application, green energy and technology*. Springer, London
18. Wright A (2005) *Aspects of the aerodynamics and operation of a small horizontal-axis wind turbine*. Ph.D. thesis, University of Newcastle, Australia

Installation of a Small Building-Mounted Wind Turbine: A Case Study from Idea to Implementation



Quentin Deltenre and Mark C. Runacres

Abstract In Belgium, the installation of a small wind turbine on rooftops is still very uncommon. Currently, there is no dedicated legal framework governing the installation on a building. Nevertheless, over the past years, our research group has received several demands from building owners wanting to install one or several turbines on their rooftop. The lack of a dedicated framework requires increased attention throughout the whole procedure. To prevent potentially harmful installations, we developed an approach to assess the feasibility of such initiatives. This paper reports a complete feasibility study to install a 3 kW wind turbine on the South Tower (the highest building in Belgium). The paper reviews the main steps from the concept towards the installation of a turbine on a high-rise rooftop. In overall terms, the installation of a 3 kW turbine on top of the South Tower has little impact on the building and its nearby environment. From an environmental perspective, the installation of a small building-mounted wind turbine on a rooftop can be meaningful. However, even in good wind conditions, the economic viability of the 3 kW turbine is low. This is mainly caused by the high study cost. Therefore, their global cost might still hold back potential investors.

1 Introduction

In Europe, decentralised energy production has become an increasing trend [1]. This is partly explained because Europe has set a goal to produce 20% of renewable energy by 2020 [1]. This growth is also observed for small wind turbines where the market has experienced a rise of 5 and 8% in 2014 and 2015 respectively [2, 3]. Although less pronounced, the average cost of a small turbine has declined with an annual average decrease of 2.7% [3]. While one observes an increasing demand and

Q. Deltenre (✉) · M. C. Runacres
Vrije Universiteit Brussel, Pleinlaan 2, 1050 Brussels, Belgium
e-mail: Quentin.Deltenre@vub.be

M. C. Runacres
e-mail: Mark.Runacres@vub.be

a decreasing cost, it must be emphasised that the market is still very immature and the quality standard of several turbines is very poor [4].

In cities, wind energy production is rather marginal because of insufficient space. However, rooftops in cities offer a good potential for energy production. Generally, photovoltaic panels are installed to produce electricity. Yet, there is a growing interest to install small wind turbines on rooftops [5]. In fact, tall buildings often have a good wind resource thanks to their height and reduced shadowing by their immediate surroundings [6].

While research is often optimistic about the installation of small building-mounted wind turbines (SBMWT), no experimental projects have been found to be viable. Two fairly recent reports have gathered results of approximately 30 SBMWT projects after a few years of installation [7, 8]. The primary objectives of these projects were threefold: raise awareness about renewable energy production, increase the building visibility and have a viable project. While the two first goals were often met, none of these projects have demonstrated good profitability. The reason why these projects failed comes mainly from a poor feasibility study, e.g., no proper micro-siting, wrong annual energy production (AEP) predictions and poor-quality turbines. Other famous turbine projects, that were originally promoted by the media, provide no public reports after several years of installation (e.g. Eiffel Tower (Paris) [9] and Strata Tower (London)).

However, the tallest rooftops of a city often have a good potential for wind energy production. We performed measurements in Brussels supporting this conclusion [10]. Having good contact with the building owner of the tallest high-rise in Belgium, we were able to do a full feasibility study and submit a building permit for the first pilot project on their roof.

With this project, we want to verify whether a building-mounted project is feasible and viable in Belgium. This paper describes every step of the feasibility study performed on the South Tower, including the steps towards the installation of the turbine. Based on the feasibility study, a methodology for further projects is proposed.

The article is divided as follows: Section 2 proposes a methodology based on the feasibility study and the encountered difficulties. Section 3 concludes the paper and discusses the perspectives for new projects.

2 Feasibility Study for the South Tower

Our research group conducted several studies in the Brussels Region showing that only tall buildings can achieve good wind conditions [10, 11]. To a certain extent, small wind turbines installed on these roofs show good return on investment. An economic analysis revealed that the dynamic payback period for turbines between 3 and 6kW was between 7 and 10 years [10]. Aside from the profitability of the turbine, there are a number of other concerns that must be verified before the actual installation. In this section we discuss the different aspects of the feasibility study realised for the South Tower, a high-rise of 150m high (Fig. 1).

Fig. 1 Picture taken at 400 m from the South Tower



The very first part of a feasibility study is to determine the wind conditions above a rooftop. Unfortunately, because of time constraints, we could not measure the wind conditions with a wind measurement mast on the South Tower. However, we did measure the wind conditions on other high-rises in Brussels, e.g. the Hotel (103 m). We intentionally write some of the measurement results of the Hotel in the introduction of this section because they are not part of the feasibility study realised for the South Tower. Further sections focus entirely on the South Tower.

After 13 months of measurement, the average annual wind speed on the Hotel was 5.8 m/s with a maximum at 21.9 m/s. The annual average turbulence intensity was 25.7%. A wind rose of the average turbulence intensity per orientation can be observed in Fig. 2.

The annual average turbulence intensity is higher than 18%, the value assumed for small wind turbines in IEC 61400-2. One should be aware that wind measurements on the Hotel have been realised at 9 m in height while the recirculation region in the centre of the roof is 12.3 m. This partly explains the high turbulence level. A recent article [12] studied the suitability of IEC 61400-2 and the normal turbulence model (NTM) for small wind turbines built in complex environment. They found out that the standard method is not applicable for these turbines (the model they developed result in loadings being generally higher than the ones calculated with the standard). Therefore, it is very important for the wind turbine developers to use caution while determining the design loads. For the South Tower pilot project, extra control/maintenance should be organised.

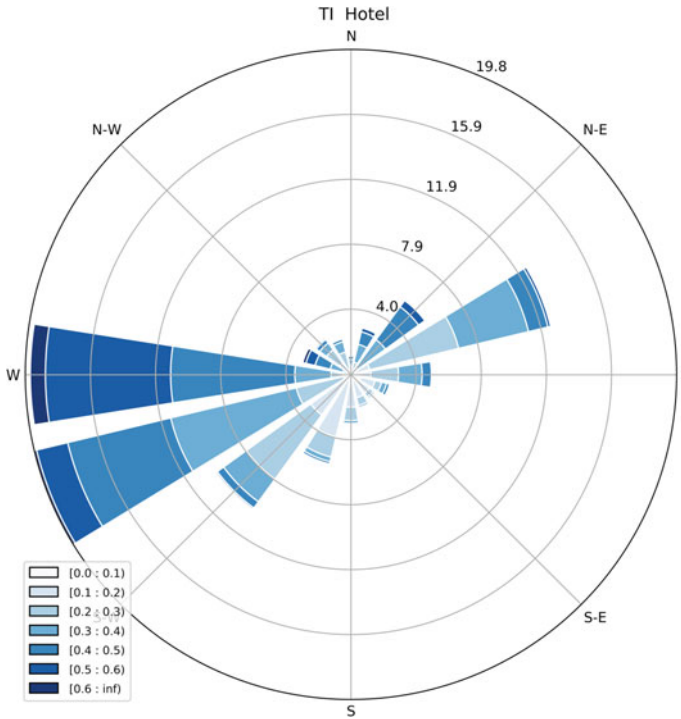


Fig. 2 Wind rose of the average turbulence intensity at 9 m high on the Hotel. The radial scale represents the number of data for each direction and the colour gradient represents the turbulence intensity of these data

2.1 Micro-siting

The wind conditions above a rooftop are strongly affected by its surroundings and by its massing, i.e. height and dimension. Without guidance, these conditions make it difficult to install a wind turbine in the most effective position. Therefore, proper micro-siting is essential to ensure an optimal energy production of the turbine [6].

Calculations were performed for the southwestern wind direction, which is the dominant wind direction in Brussels. CAD models were constructed of the building where the wind turbine would be installed, and of a number of surrounding buildings (Fig. 3).

The CAD model is then introduced in the CFD code OpenFOAM, to produce a three-dimensional wind map of the wind over the building. By producing the appropriate slices (horizontal above the building at a height above the roof that is appropriate for a wind turbine, and vertical along the length-axis of the building) the optimal locations for the installation of a rooftop-mounted wind turbine can be determined.

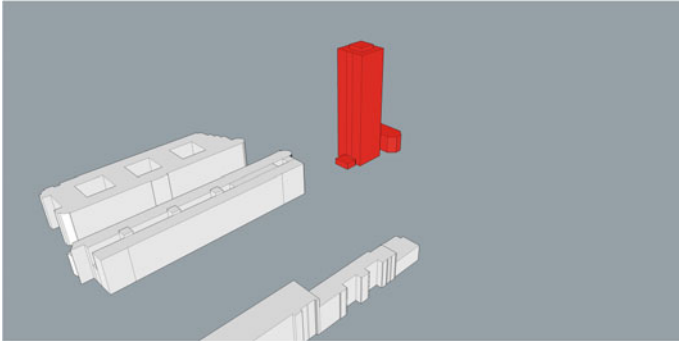


Fig. 3 3D model of the South Tower built with Google SketchUp. The South Tower is painted in red

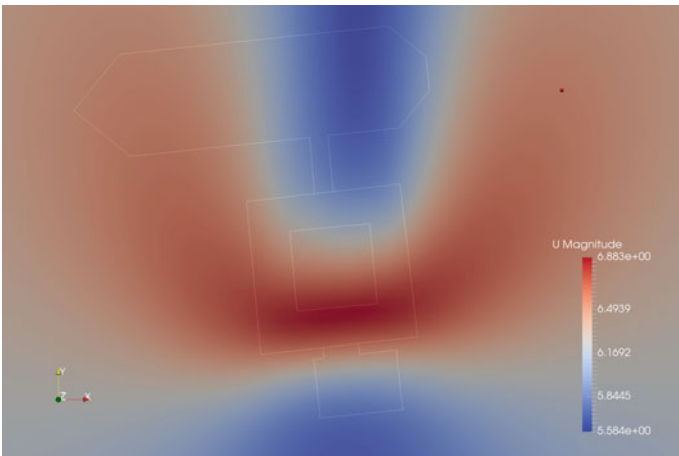


Fig. 4 Horizontal slice of the wind speed at 10m above the roof of the South Tower. The outline of the underlying roof is shown in white

The wind pattern over the South Tower is very simple, and has a profile typical of a forward step. A detailed quantification of uncertainties, although useful, falls outside the scope of the present paper. A wind turbine is best placed on the upstream side of the upper part of the roof, on the left bottom corner of the square (Fig. 4). This location would ensure higher wind speeds. It is not necessary to use a mast higher than 10m.

2.2 Stability Assessment

A stability office assessed the possibility to install a 5 kW turbine on the roof of the South Tower [13]. For safety reasons, but also because this is a pilot project, we

preferred to limit the power of the turbine. The main goal is to design an anchoring system between the mast of the turbine and the roof of the building. The existing structure of the building will then be verified to check whether reinforcement is required. The stability assessment is performed with the Eurocodes [14–16]. The structural integrity of the mast and the rotor will not be assessed in this document because this was already done in the certification process of the turbine (IEC 61400).

In Europe, Eurocodes are a set of norms that are used for the design and sizing of buildings and structures. Specific structures (e.g. masts, chimneys, steel bridges) have their own standard that specifies the steps to be properly dimensioned. Small building-mounted wind turbines, being rather marginal, have no dedicated Eurocode that gives all these steps. Therefore a combination of different norms was used to make the assessment.

There are three main steps in this assessment: wind forces acting on the turbine, static verification and dynamic verification. These steps are explained in the next paragraphs.

1-Wind Forces Acting on the Turbine

The goal of this first part is to determine all forces acting on the wind turbine. These forces will be used in the two other paragraphs. With the Eurocodes, it is possible to calculate the wind loading on the mast, the rotor and also measure the maximal internal forces inside the new structure (the anchoring system).

2-Static Verification

The static verification aims to size the structure under extreme wind conditions. Based on the loadings assessed in the first part, an anchoring system between the mast of the turbine and the rooftop was developed. The system is an ‘X’ bracing composed of two HEA300 steel beams (Fig. 5, left). The mast of the turbine is positioned in the center of the ‘X’. Then, it is verified that the steel beams will not buckle and that they can support fatigue (welded connections).

When the anchoring setup is chosen, the next step is to decide how to connect the setup to the roof. To avoid water infiltration by drilling the roofing membrane, counter-weights (1.11 m^3 on each foot) were designed to fix the structure to the roof. Finally, existing concrete beams and columns of the building are verified for these new loadings. Only the beams request a reinforcement, realised with steel elements.

3-Dynamic Verification

This last part focuses on the calculation of maximal accelerations caused by the turbine. By means of finite element modelings (Fig. 5, right) the eigenmodes of the structure can be calculated. With these modes, it is possible to calculate the maximal accelerations and displacements (horizontal and vertical) in the building. Comparing these results with the comfort criteria of the standard [17], it is safe to predict that these accelerations and displacements are too small to be perceived by the user. It means that nobody working in the building will suffer from vibrations caused by the turbine installation.

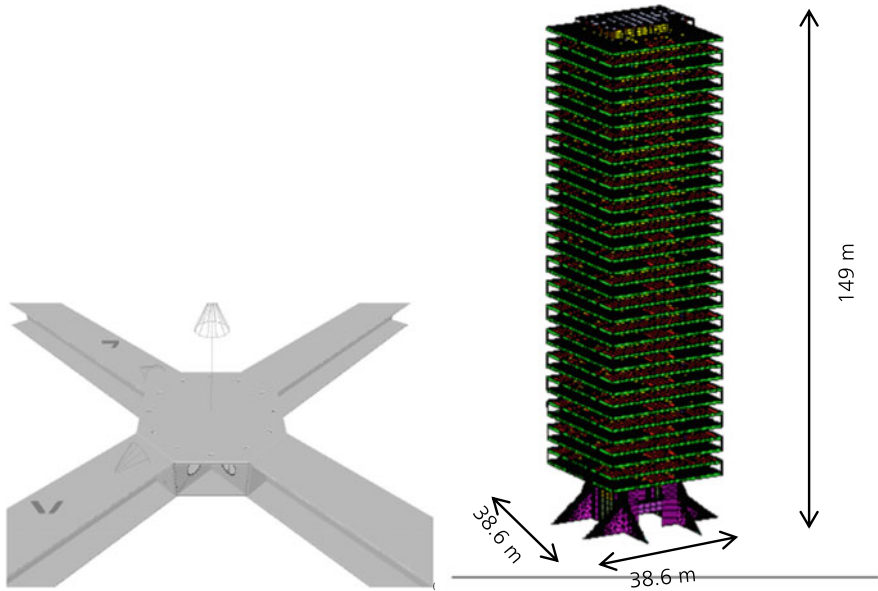
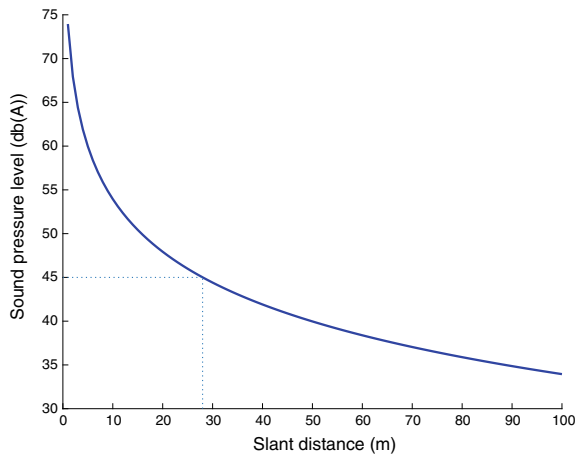


Fig. 5 Anchoring system that is proposed to fix the mast of the turbine to the rooftop (left). Finite element model that is used to determine the accelerations and displacements caused by the wind turbine (right)

Fig. 6 Sound pressure level as a function of the slant distance from the hub height of the turbine. This graph is derived from the relation between the sound power and the sound pressure level, using the sound level from the certification. One can observe that the noise level is below 45 dB(A) at 30 m from the hub height (noise reflection and absorption is not considered). This 45 dB(A) noise level is acceptable for offices



2.3 Environmental Concerns

Wind turbines often raise several relevant concerns on their nearby environment, i.e., noise, shadow, visual impact, biodiversity and air transport. These concerns are addressed in the following paragraphs, for the South Tower (Fig. 6).

2.3.1 Noise

We performed several on-site noise measurements for a 5 kW turbine installed on a field test in Puyenbroeck. The results of that study are shown in Fig. 7. The figure indicates the minimum slant distance between the rotor axis and the ground at which someone must stand to have a sound level below a certain limit. For example, if one considers the red curve, it points out that for an average wind speed of 6 m/s, the noise at 57 m from the rotor is below 40 dB(A). This is a reassuring result because direct noise emissions from a SBMWT are low, especially compared to the average urban sound pressure level (50–70 dB(A)) [18].

For the South Tower, we studied theoretically the ambient noise before and after the installation of a turbine. This study was realised for a wind turbine of 10 kW (three times more powerful than the one that is foreseen on the roof) and for a wind speed of 8 m/s. Using the average wind speed at the location and a Raleigh distribution, the amount of time the wind speed exceeds 8 m/s is around 28.5%. A 5 kW turbine operating at that particular wind speed produces a noise equivalent to 45.1 dB(A) at 60 m slant distance from the hub (Fig. 7).

Finally, the certification of the turbine that will be installed on the roof also provides a noise level. This study indicates that the turbine produces 49 dB(A) at 25 m distance at a wind speed of 8 m/s [19]. Using the relation between sound pressure level and sound power, it is possible to plot the sound pressure level reduction as a function of the slant distance for that turbine (Fig. 6). One can observe that the noise

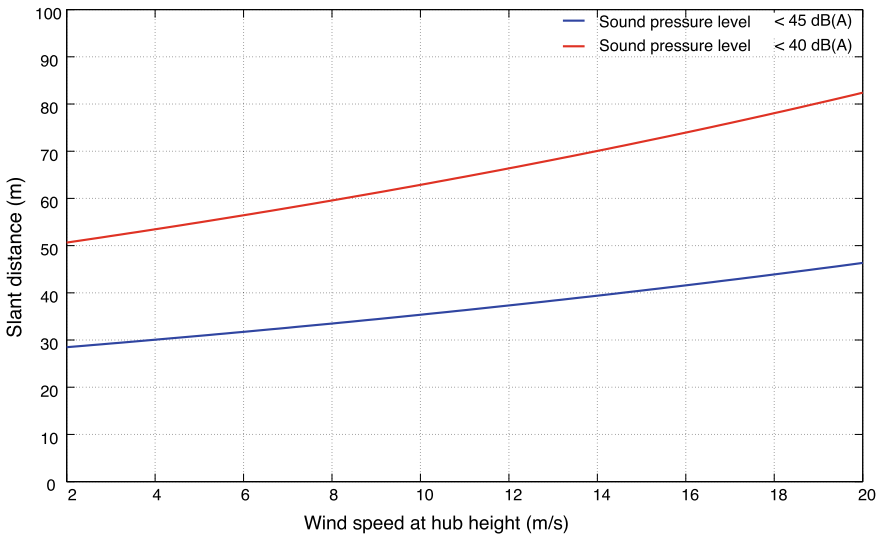


Fig. 7 Experimental results of the acoustic study performed on a 5 kW turbine. The red line (above) represents the 40 dB(A) limit, the blue line (below) indicates the 45 dB(A) limit. The graph gives the necessary minimal slant distance between a turbine and a point as a function of the wind speed. For a wind speed of 6 m/s, the minimal slant distance to reach a noise level below 40 dB(A) is 55 m

level is below 45 dB(A) at 28 m from the hub height (noise reflection and absorption are not considered). This noise level is acceptable for offices. The first office floor below the wind turbine is approximately at 30 m from the hub. Taking into account the noise absorption and reflection, one can expect lower noise level in reality.

These estimated noise values are small and will not be perceived by people walking in the streets around the building. Employees working at the last inhabited floor might perceive the noise during wind gust periods. Nevertheless a technical floor increase the distance between the last office floor and the roof, which reduces the noise hindrance. Moreover, the technical floor contains the machinery that operates the lifts in the building. These lifts produce vibrations and noise during their use, i.e., during daytime. It is safe to say that the turbine direct noise will be hardly noticeable above the noise produced by the lifts and the HVAC systems on the roof. The structure-borne sound caused by such a small turbine is also believed to be smaller than that of HVAC systems and lifts.

2.3.2 Shadow Flicker

The shadow cast by an operating wind turbine can sometimes be perceived by an observer as *flickering*. Because of the low solidity of the rotor (typically three blades), light from the sun is only periodically blocked, resulting in a flickering shadow. When such a shadow falls on windows of nearby residences or offices, a certain nuisance can be experienced. Therefore a proper shadow flicker study cannot be omitted when assessing the possible impact of the installation of a wind turbine.

To be able to encounter such an event, following conditions must be met simultaneously:

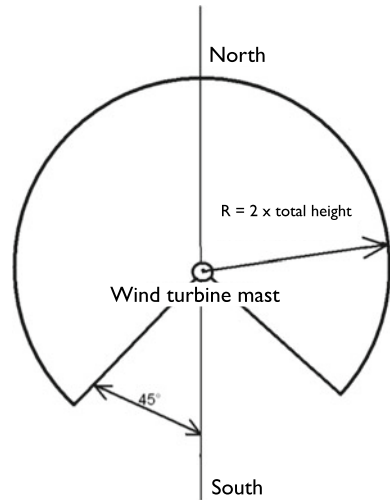
- The wind turbine must be in operating condition, i.e. the rotor must be spinning.
- It must be daytime with clear skies. Diffuse light that penetrates clouds is insufficient to generate distinct shadows.
- The observer should not be in the rotor plane.
- Only properties within 135 degrees on either side of north of the turbine can be affected at Belgian latitudes [20].

Within the framework of the regional planning of Flanders, a technical note was published describing guidelines that are to be considered when evaluating a potential site for the installation of a small wind turbine [21]. The guideline prescribes a minimum distance of two times the total height of the turbine, i.e., tip height including building height when mounted on a structure (top view is provided in Fig. 8).

Situation for the South Tower

The South Tower, with a height of 150 m, is a clear example of the guidelines being too conservative. In Fig. 9, a disk is drawn conform to the prescribed radius. The indicated area is clearly oversized. This claim is supported by the following 3 observations:

Fig. 8 Minimum required distance to avoid nuisance from shadow flicker



- We observed the tower shadowing from Google Maps. In Fig. 10, one can see the South Tower and its projected shadow on the close environment. The shadow of the mast (more than 10m high and 1 m wide) is not identifiable. It is therefore reasonable to believe that the shadow of a small wind turbine would also not be distinguishable.
- Legislations limit the shadow flicker effect at 30 hours per year and 30 minutes per day [22]. To analyse the shadow throughout the year, a 3D model of the South Tower was built in Google SketchUp. The programme is able to assess the shadow of any object at any time of the year. The shadow will move very fast over the surrounding buildings, only affecting a single observer for a few minutes. Since in a few days the path of the sun will also already have changed, a single building will never be in the path of the shadow of the turbine for more than a few minutes a year.
- Several rules of thumb are used for quick shadow assessment [23]. The shadow flicker effect does not exceed a distance equals to 10 times the rotor diameter of the turbine. The 3kW turbine having a diameter of 4.4 m, the shadow flicker would be limited to a sphere of 44 m. In the surroundings of the South Tower, the tallest buildings are 45 m high, which is still far from the shadow flicker boundary.

The South Tower was evaluated and no considerable risk for shadow flicker was found. It is worth noting that, in the case a residence is located within the prescribed safety radii, nuisance cannot be accurately determined until an assessment has been made of e.g. the windows widths, the uses of the rooms and the effect of intervening topography and other vegetation [22].

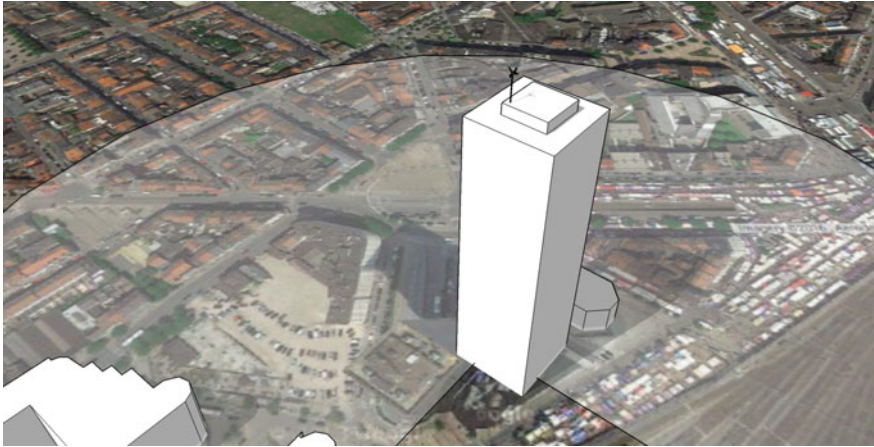


Fig. 9 Shadow flicker study performed in Google SketchUp. A 3D model of the building was designed. A small wind turbine was installed on a potential location. The shadow of the turbine in this Figure is taken the 2nd of July, at 1 PM. In summer, the shadow is completely projected on the rooftop surface



Fig. 10 Real shadow of the South Tower on its surroundings

2.3.3 Visual Impact

The visual impact of a wind turbine on the South Tower is expected to be small. Since the rooftop is already rather crowded with equipment (Fig. 1), the visual impact of the turbine should be minimal (Fig. 11).

Fig. 11 Mock-up of a wind turbine installed on the South Tower



2.3.4 Biodiversity

To quantify the impact of a SBMWT on the biodiversity (i.e. birds and bats), it is necessary to verify that the turbine is not installed close to sensitive zones (e.g. green spaces, migratory routes, natural reserves). Brussels offers a ‘biodiversity map’ where all these zones are highlighted [18]. The South Tower being far from these zones, we can expect a low impact on biodiversity [11].

A research has published a synthesis of Human-related Avian Mortality in Canada. This study indicates that birds killed by wind energy (in general) is less than 1 on 100,000 deaths [24]. These results support our expectations that the impact on biodiversity in the city will be small.

2.3.5 Air Traffic

The Belgian legislation proposes a memorandum that legislate beacons for obstacles [25]. This document requires that a notice must be sent for all installations that present a danger for aviation. Every object having a height larger than 150m is considered as an obstacle and should be equipped with beacons. Nevertheless, if another obstacle on the same rooftop is higher than the new one (i.e. the turbine), it is not necessary to install such a device.

During the building permit procedure, the Brussels Region asked the advice of the Federal Public Service of Mobility. Because no beacons were already present on the South Tower, they required the installation of a beacon on one of the tallest obstacles of the roof. This beacon has nothing to do with the wind turbine per se, but was done to comply with the actual regulations from the Region.

2.4 Economic Viability

Research on economic viability of SBMWT has been limited. As stated above, a report listed the energy production results of 24 wind turbines in the UK [7]. Walters, R. et al. converted the energy production from these 24 turbines into revenues, in a net present value (NPV) framework [26]. This paper reveals that the investment for small wind turbines in an urban environment is unfavourable. More than 95% of the locations would score low NPVs. Another report, equivalent to the Warwick case studies, examined 6 building-mounted turbines installed in the USA [8]. This report provides the discounted payback period (DPP) (if available) for the 6 turbines. Results show that none of these turbines are profitable, all having a payback period larger than their lifetime.

Having a closer look at the profitability of small wind turbines, results are better but not ideal. A publication from the Internal Energy Agency on wind energy reveals a levelised cost of energy (LCOE) varying between 0.15 and 0.35 USD/kWh (i.e. 0.13–0.31 EUR/kWh) [27]. In 2016, another publication analysed 50 installed small wind turbines installed in the USA [28]. The LCOE varies a bit more: 0.05–0.45 USD/kWh (0.04–0.39 EUR/kWh). In Belgium, the cost of electricity neighbours 0.20 EUR/kWh [29], which is much lower than the higher limits from these two reports.

Based on these reports, one observes that building-mounted turbines are still rarely economically viable. Conclusions of these reports mention several reasons for this low return: wrong prediction of the energy production, wrong power curves from the manufacturers or numerous downtime periods.

In the framework of this feasibility study we assessed the LCOE and DPP of small wind turbines installed on the South Tower. The LCOE can be defined as the total life-cycle cost (TLCC) divided by the discounted energy production (TDEP). The total life-cycle cost can be expressed as

$$TLCC = \sum_{n=0}^N \frac{C_n}{(1+r)^n}, \quad (1)$$

where C_n is the cost in year n , N the lifetime of the turbine in years and r the discount factor. In this study, we assume that the only costs were the investment cost (I_0) and the operation-and-maintenance costs (C_{OM}). Then, the total discounted energy production can be expressed as

$$\text{TDEP} = \sum_{n=1}^N \frac{E_n}{(1+r)^n}, \quad (2)$$

where E_n is energy production in year n . If we assume that the OM costs and the energy production are constant every year, a represents the annuity factor and is defined by

$$a = \sum_{n=1}^N \frac{1}{(1+r)^n} = \frac{1 - (1+r)^{-N}}{r}. \quad (3)$$

Using Eqs. (1), (2) and (3), the LCOE is calculated with

$$\text{LCOE} = \frac{I_0 + aC_{\text{OM}}}{aE}, \quad (4)$$

where E is the annual energy production of the turbine.

The DPP is the required time to recover the money invested in a project, taking the time value of money into account. This metric is of interest when risk is an issue (i.e. significant uncertainties in the project). It gives the investor a reliable duration for which his capital is at risk [30].

The discounted payback period is calculated based on the NPV

$$\text{NPV} = \sum_{n=1}^N \frac{CF_n}{(1+r)^n} - I_0, \quad (5)$$

where I_0 is the investment cost, CF_i is the cash flow in year n , r is the discount rate and N is the power plant's lifetime. The NPV sums all discounted cash flows over the lifetime of the project at a determined rate (i.e. the discount rate) and subtracts the investment cost. When the NPV of a project is positive, it indicates that the expected earnings are higher than the foreseen costs. Although the NPV is positive, it does not mean that the investment is cost effective. The analyst must be careful and compare the result with other potential investments.

These two factors have been studied for different wind speeds and wind turbines. Having no wind measurement data for the South Tower, we consider 3 average wind speeds that we can expect on such a building. According to wind measurements realised on other buildings (i.e. the Hotel, see Sect. 2), 4 m/s is very unlikely, 5 m/s is slightly underestimated and 6 m/s is a bit overestimated. The annual energy production of the turbines is taken from the turbines' certifications. The values of the parameters in Eqs. (4) and (5) can be found in Table 1. The South Tower being an office building, we took into account the related incentives. We also considered that all the energy produced would be consumed by the building, as stated by the owner. In the framework of this pilot project, we wanted to limit the impact of the installation by choosing a smaller wind turbine (3 kW). We also calculated these two economic factors for more powerful turbines (5 and 10 kW). Nevertheless, the impact of a

Table 1 Values of the parameters of the economic study

Parameters	Values
Investment cost	5,500EUR/kWh
O&M cost	2%
Discount rate	4%
Lifetime	20 years
AEP	IEC certifications
Energy loss	5%
Tax depreciation	10 years
Environmental investment	30%
Cost of electricity	0.19EUR/kWh
Green certificates	83EUR/MWh
Green certif. duration	10 years
Supereductibility	13.5% × investment cost
Superdeduc. year	2nd year
Tax rate	33.99%
Feasibility study	15,000EUR
Environm. Invest. max	80,000 EUR

Table 2 Economic parameters calculated for a 3 kW turbine, based on the Belgian incentives. Left results do not consider the cost of the feasibility study (about 15,000 EUR)

3 kW turbine	4 m/s	5 m/s	6 m/s	4 m/s	5 m/s	6 m/s
AEP (kWh)	3210	5870	8375	3210	5870	8375
LCOE (EUR/kWh)	0.51	0.28	0.20	0.95	0.52	0.36
DPP (years)	above 20	10.2	6.7	above 20	above 20	above 20

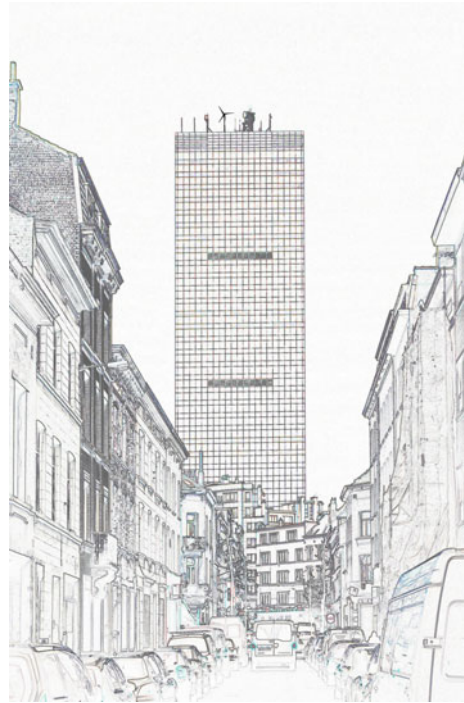
Table 3 Economic parameters calculated for a 5.2 and a 10kW turbine, based on the Belgian incentives. These results consider the cost of the feasibility study (about 15,000 EUR)

5 and 10kW turbines	4 m/s	5 m/s	6 m/s	4 m/s	5 m/s	6 m/s
AEP (kWh)	4629	8949	13882	24590	37360	47240
LCOE (EUR/kWh)	0.93	0.48	0.31	0.28	0.18	0.15
DPP (years)	above 20	above 20	12.0	9.5	6.2	4.9

10kW turbine has not been studied yet, and it might be that such a project is not feasible. Results of the 3 turbines can be seen in Tables 2 and 3.

Regarding the 3kW turbine, one must reach at least 6 m/s to get an equivalent LCOE than the network. The discounted payback period is reasonable for the two largest wind speeds, but remains low compared to another renewable energy production system, say photovoltaic. The 5kW turbine does not show better results than the 3 kW turbine. However, the 10kW turbine presents some convincing results. For

Fig. 12 Mock-up of a wind turbine installed on the South Tower



expected wind speeds on top of the tower (between 5 and 6 m/s), the LCOE is much lower and the payback period is below 7 years. Although these are good results, one must verify the structural integrity of the building for such a machine.

2.5 Building Permit and Future Installation

In addition to the usual documents asked by the Brussels Region, we provided the complete feasibility study of the tower, some mock-ups (Figs. 11 and 12) as well as the agreement of the Brussels airport. The building permit for the first small-building mounted wind turbine in the Brussels Region was submitted in February 2017. Both the Region and the commune granted the permit in November 2017. The future challenges are the development of technical specifications for the public offer. The technical service of the South Tower wishes to install the turbine by the end of 2018.

2.6 Summary of the Approach

In the previous subsections, we review the feasibility of a small building-mounted WT on the South Tower in Belgium. For any future projects, we recommend to follow this approach to ensure a good operation of the turbine and the safety of its environment. These criteria are essentials to promote small building-mounted WT in the future. Here is a summary of the complete study and its different objectives.

Micro-siting gives the optimal locations to install the turbine, as well as the minimal height of the hub to avoid the turbulence zone. If time permits, measuring the wind conditions on the site ensures an accurate prediction of the energy production of the turbine. The stability study must confirm that the building can support the extra loads induced by the turbine installation. Reinforcements of the building might be required. This study also verifies that the vibrations of the turbine will not be perceived by the building's users. The impacts on the turbine's environment are then assessed (noise, shadow flicker, visual, biodiversity and air traffic). All these assessments are crucial to avoid potentially harmful installations. Finally, it can be of interest to perform an economic study of the project. An economically viable project can be better perceived by future investors and the public.

3 Conclusions

This paper reviews the full feasibility study for the installation of a small wind turbine of 3 kW on the South Tower, the tallest building in Belgium. Throughout this study, we demonstrated that the global impacts of the turbine on its environment are weak, if not nonexistent. However, even with good wind conditions, the economic viability of the 3 kW turbine is low. When the cost of the feasibility study is included on the total cost, the turbine is not profitable at all. For a 10 kW turbine, the return on investment is much better. The feasibility for such a turbine have not been studied yet and should be carefully done before the installation.

For the smallest turbine, this poor return on investment illustrates that incentives provided by the Region remain too low. Comparing the incentives for the wind turbines and the photovoltaic panels, one realises that the two technologies do not benefit from the same chances. As mentioned in the introduction, the market is still evolving and the costs are decreasing. Therefore one can soon expect a better future for the wind turbines installed in urban areas.

Nevertheless, a small building-mounted wind turbine in urban areas can provide other benefits than profitability, i.e., raise awareness about renewable energy and underscore the building's sustainability commitment. These benefits are tangible but are complex to quantify in monetary terms.

For future installations, the remaining challenges are the reduction of the total project cost, mainly by lowering the research costs, and help the government to develop a clear legal framework to prevent hazardous installations.

References

1. Altmann M et al (2010) Decentralized energy systems. Report. European Parliament, Policy department A: economic and scientific policy
2. Pitteloud J-D et al (2016) Small wind world report 2016. World wind energy association
3. Pitteloud J-D et al (2017) Small wind world report 2017. World wind energy association
4. Maegaard P et al (2016) Catalogue of small wind turbines. World wind energy association
5. Blackmore P et al (2007) Micro-wind turbines in urban environments. BRE Press, England
6. Blackmore P (2010) Building-mounted micro-wind turbines on high-rise and commercial buildings. BRE Press, England
7. Hailes D (2009) Warwick wind trials project: final report. Encraft
8. Fields J et al (2016) Deployment of wind turbines in the built environment: risks, lessons, and recommended practices. National renewable energy laboratory
9. Le Parisien (2015) Paris: la Tour Eiffel passe au vert avec deux éoliennes. (26th of February)
10. Vermeir J (2015) Feasibility and performance assessment of small and medium-sized wind turbines. PhD thesis. VUB press, Brussels
11. Runacres M (2014) Identificatie sites, opzetten windmetingscampagnes en uitvoering van haalbaarheidsstudies in het Brussels Hoofdstedelijk Gewest. Leefmilieu Brussel. Available via http://document.leefmilieu.brussels/opac_css/index.php?lvl=author_see&id=26
12. Evans SP et al (2017) The suitability of the IEC 61400–2 wind model for small wind turbines operating in the built environment. *Renew Energy Environ Sustain*
13. Duchêne Y (2015) Structural effects of vibrations induced by wind turbine placed on the roof of the Midi Tower building. Technical report, Bureau Greisch
14. Bureau de normalisation. NBN EN 1990, Eurocode - basis of structural design. Belgium
15. Bureau de normalisation. NBN EN 1991, Eurocode - actions on structures. Belgium
16. Bureau de normalisation. NBN EN 1993, Eurocode - design of steel structures. Belgium
17. Bureau de normalisation. NBN EN 1991, Eurocode 1, actions on structures - Part 1-4: general actions - wind actions. Belgium
18. Environnement Bruxelles (2016) Cartes et exposition des populations au bruit multi-exposition 2016. Bruxelles Environnement
19. ClassNK certification (2015) No. TC-0011. Certificate delivered to Ennera energy and Mobility SL
20. Van Mechelen D et al (2009) Beoordelingskader voor de inplanting van kleine en middelgrote windturbines. Omzendbrief LNE/2009/01—RO/2009/01, Vlaamse regering
21. Vlaamse Regering (2009) Omzendbrief LNE/2009/01 – RO/2009/01 Beoordelingskader voor de inplanting van kleine en middelgrote windturbines
22. Brinckerhoff Parsons (2015) Update of UK shadow Flicker evidence base. Technical report, Department of energy and climate change, London
23. Brinckerhoff P (2004) Update of UK shadow flicker evidence base. Technical report, Department of energy and climate change, 3 whitehall place, London
24. Calvert AM et al (2013) A synthesis of human-related avian mortality in Canada. *Avian conservation and ecology*
25. Service public fédéral mobilité et transports. (2006) Directives concernant le balisage d'obstacles pour l'aviation
26. Walters R et al (2015) Examining the financial performance of micro-generation wind projects and the subsidy effect of feed-in tariffs for urban locations in the United Kingdom. *Energy policy*
27. International renewable energy agency (2012) *Renewable energy technologies: cost analysis series*
28. Orrell A et al (2015) 2015 Distributed wind market report. Pacific Northwest National laboratory
29. VREG (2015) De prijs per kWh elektriciteit voor particulieren en kmo's. Vlaamse Regulerings instantie voor de Elektriciteits- en Gasmarkt
30. Short W et al (1995) A manual for the economic evaluation of energy efficiency and renewable energy technologies. National renewable energy laboratory

Evaluation of the Causes of Vibration and Oscillation in a Vertical Axis Small Wind Turbine (VASWT) and Its Reduction



Alexander Hirschl, Mauro Peppoloni and Kurt Leonhartsberger

Abstract It is well known that there is a good wind resource in a few meters over the average roof height. Due to the high building density in urban and populated areas, roof installed SWTs are usually the only feasible way for harvesting wind energy. However, under operation many factors such as mass imbalances, aerodynamic imbalances and gusts can result in the vibration and oscillation of small wind turbines (SWT). Therefore, major interest attaches to the reduction of small wind turbine vibration, in order to minimize the risk of damages on buildings and the plant. Currently the influence of SWT vibration and oscillation on the plant itself and the immediate area is not entirely analyzed. In order to obtain an insight into the range of oscillation of SWTs, this work investigates the oscillation characteristics of a VASWT (Darrieus rotor) by means of accelerometers in direct proximity to the generator and on the mast. The results reveal which driving forces are causing alternated vibration and that limit values for humans and components are exceeded at a specific number of revolutions per minute. In contrast, the use of a decoupling element significantly reduces the vibration and oscillation intensity.

Keywords Small wind turbine · Vibration · Decoupling

1 Introduction

One central issue of our time is the supply of regenerative energy. The threat of dwindling fossil fuel resources and climate change are only some of the reasons for the current change in the energy system. Due to advantageous wind conditions in eastern Austria, the expansion of large wind turbines has boomed in recent years. At the end of 2015, 1119 large wind turbines with a total output of 2.4 GW covered 8.7% of the Austrian electricity demand. For the year 2020, an increase of the installed capacity to 3 GW is predicted [1]. In Austria, the regional planning law requires a minimum distance between large wind turbines and inhabited areas. As a result, the

A. Hirschl (✉) · M. Peppoloni · K. Leonhartsberger
University of Applied Sciences FH Technikum Wien, Giefinggasse 6, 1210 Vienna, Austria
e-mail: hirschl@technikum-wien.at

© Springer Nature Switzerland AG 2019
L. Battisti (ed.), *Wind Energy Exploitation in Urban Environment*,
Research Topics in Wind Energy 8, https://doi.org/10.1007/978-3-030-13531-7_6

installation of large wind turbines is not permitted on every site with good meteorological conditions. Hence, not every profitable location is exploited with large wind turbines [2].

Beside photovoltaic panels, small wind turbines (SWT), defined as turbines with a swept rotor area of up to 200 m² according to IEC/EN 61400-2, are one solution for the generation of renewable energy in urban and inhabited areas [3]. Due to the high building density, roof installed SWTs are usually the only solution [4].

Meteorological studies have shown that the city of Vienna offers a significant wind resource at about 10 m above the average building height. Hence, building roofs offer a reasonable potential for the harvesting of electric energy using small wind turbines [5].

1.1 Scientific Issue

There are several challenges that producers of small wind turbines have to tackle (in order to be successful on the market). Quality deficiencies, arbitrary power ratings and inconsistent approval procedures hinder the market penetration [6]. During the operation of SWTs many factors such as mass imbalances, aerodynamic imbalances (pitch tolerance), magnetic effects in the generator, vertical cross wind, turbulences and gusts may result in the vibration and oscillation of the entire system [4]. Previous scientific studies showed that especially fluctuating gusts and turbulences might impose high dynamic loads on the turbine and cause resonant vibration. These conditions typically occur in a complex terrain, such as urban areas. Cases of turbine failures and material fatigue indicate that the current standard IEC 61400-2 does not meet the structural requirements of small wind turbines and especially VASWT to endure high turbulent wind conditions in the build environment [2].

Although both large and small wind turbines are subject to oscillation, the oscillation of building-mounted SWTs in inhabited areas must be seen critically as vibrations can be transduced to nearby buildings via the mast. The current solution for this issue is to install an emergency shut-down system or damping elements, also known as decoupling elements, between the generator and the mast [4]. The IEC 61400-2 gives the advice to analyze all frequency spectra in a Campbell-diagram to detect possible resonant vibration within the operation range. The standard gives no measures to analyze, reduce and avoid vibration and oscillation especially on vertical-axis small wind turbines (VASWT) [7].

An unbalanced mass distribution of the rotor blades caused by manufacturing tolerances is for the most part responsible for the oscillation of SWTs. However, irregular airflow, turbulence or pitch deviations of the rotor blades, tower shadow effect and variation in the blade geometry can result in aerodynamic imbalances. With vertical-axis small wind turbines in particular, aerodynamic imbalances are a systemic problem and need to be considered. The reason for this is the inhomogeneous blade geometry of the rotor. In addition to rotor-induced oscillation, the generator causes high-frequency oscillation. As numerous excitation frequencies can occur

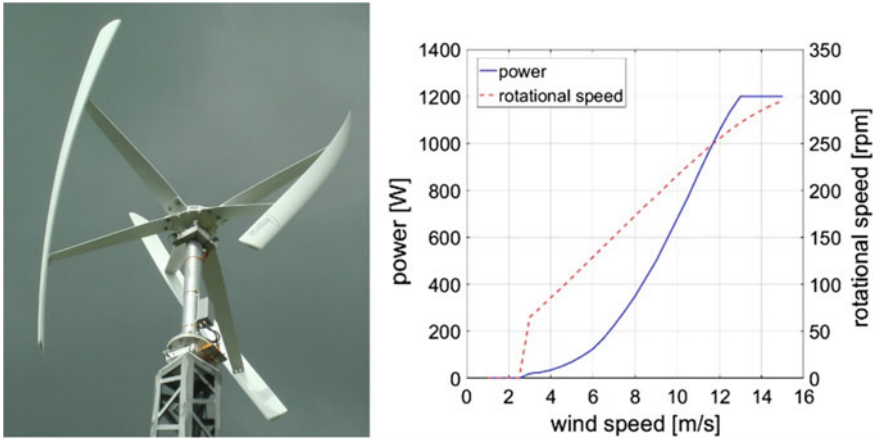


Fig. 1 Darrieus rotor Amperius VK-58; power and speed curve

over the entire speed range, the stimulation of natural frequencies of the structure is a common phenomenon for SWTs [4].

Frequent resonant oscillation may result in material fatigue of the plant. To avoid resonant oscillation and ensure a reliable and efficient operation, knowledge of the frequency range, the displacement, the oscillation velocity and the oscillation acceleration of SWTs is crucial. Subsequent adjustments such as rotor-blade balancing and the installation of decoupling elements lead to high costs. Oscillation may also cause structural damage to the building in the case of rooftop installations. Additionally, there have been no studies to determine whether there are significant energy-yield losses caused by vibrating components. Decoupling elements are the current solution for strongly oscillating components of SWTs [4].

1.2 Aim of Work

To ensure the safe operation of small wind turbines in inhabited areas, major interest attaches to the range of vibration and oscillation and the effectiveness of decoupling elements. This article focuses on the underlying formation mechanisms of oscillation of a Darrieus rotor type (vertical-axis small wind turbine—see Fig. 1) as well as on the range of oscillation during its operation. The evaluation of the monitored data is expected to reveal the formation mechanism of different types of oscillation. In detail, there are four fundamental values which had to be determined:

- \ddot{x} Oscillation acceleration [m/s^2 —measurement in x, y and z direction
- \dot{x} Oscillation velocity [mm/s —measurement in x, y and z direction
- x Oscillation displacement [m]—measurement in x, y and z direction
- f Oscillation frequency [Hz]—measurement in x, y and z direction

With the aid of these values, conclusion will be drawn on the influence on the power plant itself as well as on its immediate surroundings. Another point of interest is the energy yield. The monitoring of the wind turbine is expected to show if high-oscillation events have an influence on turbine energy yield.

1.3 Method

The evaluation of the oscillation behavior of one VASWT type requires a concept to determine all essential quantities on the power plant. A sensitive measurement equipment consisting of a measurement unit and oscillation sensors enabled the detection of all oscillation parameters. In addition to these internal parameters, external parameters such as the wind speed, turbulences, vertical cross winds and gusts were also detected.

Owing to a lack of urban sites with small wind turbines and good wind conditions, the investigation was transferred to the Lichtenegg energy research park, which is located on a hillside in Lower Austria. An annual average wind speed of approximately 5.1 m/s and a turbulence intensity ranging around 12% at this location guarantees measurement data over the whole operation range of the VASWT.

2 Vibration and Oscillation of Small Wind Turbines

Oscillation is defined as a harmonic alternation of a physical quantity over time. Thus, oscillation is measured e.g. as the alternation of angle, pressure, displacement, acceleration, etc. [8]. Vibration on the other hand is a type of oscillation that is perceptible to living beings. Perceptible oscillation ranges between 10 Hz and 20 kHz. Permanent exposure to vibration via the hands and feet may lead to medical issues [9].

Due to the exposed location, the lightweight construction and a dynamic operation, wind turbines can be considered as highly resonant systems. Each component has a typical natural frequency defined by its size, shape, stiffness, weight and material characteristics. All external forces such as turbulences and gusts, and all rotating parts including the rotor, the generator and the hub, may stimulate a component at its natural frequency, causing resonance. In this situation, oscillation builds up to a point where stimulating and damping forces are balanced. Hence, this resonant oscillation results in elevated forces and strain. Over time, the stress caused by resonant oscillation may lead to material fatigue and system failures [10].

2.1 *Natural Frequencies*

The natural oscillation of a system is defined as the free oscillation of an undamped system with no external influence but one initial excitation. The natural frequency of a structure is influenced by its mass, size, shape stiffness and other material characteristics. Systems can have several eigenmodes resulting in multiple natural frequencies.

As mentioned before, if a system is stimulated periodically with exactly the same frequency as the natural frequency of the system, it will lead to resonant oscillation [10]. For instance, the natural frequency of the tower of a small wind turbine is 1 Hz due to its weight and geometry. If the rotor rotates at 60 rpm, the frequency of the rotor corresponds exactly to the natural frequency. As a result, the tower starts to oscillate and increases its amplitude with every half period. If the rotor maintains its rotational speed for an extended duration, the oscillation amplitude will rise until the energy dissipated in the tower matches the energy imposed by the excitation. The long and slim construction of wind turbine towers allows a variety of different oscillation patterns/eigenmodes. This example cannot be generalized, because each configuration consisting of a small wind turbine and a mast represents a system with unique and multiple natural frequencies.

Modern rotor blades are made of light materials and have sash profiles with minimal aerodynamic drag. Furthermore, fiberglass rotor blades are slim and long to create more aerodynamic lift. These performance-related advantages are disadvantageous in terms of oscillation because they lead to a highly resonant system. Studies of large wind turbines have shown that the value for the natural frequency of rotor blades is between 10 and 200 Hz, with higher frequencies being located in the middle and at the end of the rotor blades [10].

2.2 *Excitation Frequencies*

External influences such as turbulences and gusts as well as rotating parts of the wind turbine permanently excite the oscillation of components. As mentioned in Sect. 2.1, rotor blades are highly resonant systems and aerodynamic imbalances caused by pitch angle tolerances may excite oscillation. These excitation frequencies may excite different natural frequencies of a system leading to different eigenmodes. The order describes the excitation of these different eigenmodes [10].

Statistic evaluations of large-scale wind turbines have demonstrated the effect of pitch angle deviation relative to the other blades. Photometric measurements showed that 93% of all plants have pitch angle differences exceeding the pitch tolerance range. For HASWT this means an increased mechanical load along the generator axis. On vertical-axis small wind turbines, (VASWT) a blade angle malposition results in lateral mechanical loads on the generator axis. According to the GL Directive, wind

turbine rotor blades must not exceed a pitch angle malposition of $\pm 0.3^\circ$ relative to the other blades, to ensure that no power losses or high oscillations occur [10].

External influences such as the wind may also excite the oscillation of components when it alternates periodically. During operation, wind passes the rotor blades, and aerodynamic lift causes the rotor to start to spin. As it spins, the rotor blades pass the tower periodically, and the tower, an aerodynamic obstacle, reduces the aerodynamic lift. This so-called tower shadow effect affects each wind turbine type differently.

- Upwind turbines: the rotor blades pass the tower—the wind load decreases periodically.
- Downwind turbines: the rotor blades pass the tower—the aerodynamic lift reduces periodically.
- Darrieus turbines: the tower shadow causes both effects, wind load reduction on the rotor, and aerodynamic lift reduction resulting from the tower shadow effect [10].

Rotor mass imbalances are another source of vibration and oscillation caused by an unequal mass distribution on the blades. Small components such as the generator are easy to balance dynamically but for bigger parts like the rotor, dynamic balancing is often technical impossible. Studies have revealed that only static balancing is often insufficient. Mass imbalances may also occur during the operation or installation of the plant. There are different causes of mass imbalances on the rotor [11]:

- Ice accretion on the blades
- Erosion, water entrapment, rotor blade failures caused by lightning
- Mass imbalances caused during manufacturing [11].

3 Measurement Concept

The first step was the selection of a suitable wind turbine including a mast. The chosen VASWT has a rotor measuring 2.4 m in diameter and a rated output of 1.2 kW, which represents a typical VASWT for urban use. The plant was installed on a steel lattice mast at a height of 13.5 m. The measurement set-up included the alignment of the sensors for oscillation, wind speed, power output and rotational speed.

Different ranges of oscillation were recorded by using four sensors. Three different types of sensors were selected, each one having specific properties:

1. Piezoelectric accelerometer—range 2 Hz–5 kHz
2. Piezoelectric accelerometer—range 2 Hz–5 kHz
3. Capacitive accelerometer with MEM-technology—range 0.1 Hz–1 kHz
4. Electrodynamic inductive velocity sensor (Geophone)—range 4–500 Hz [4].

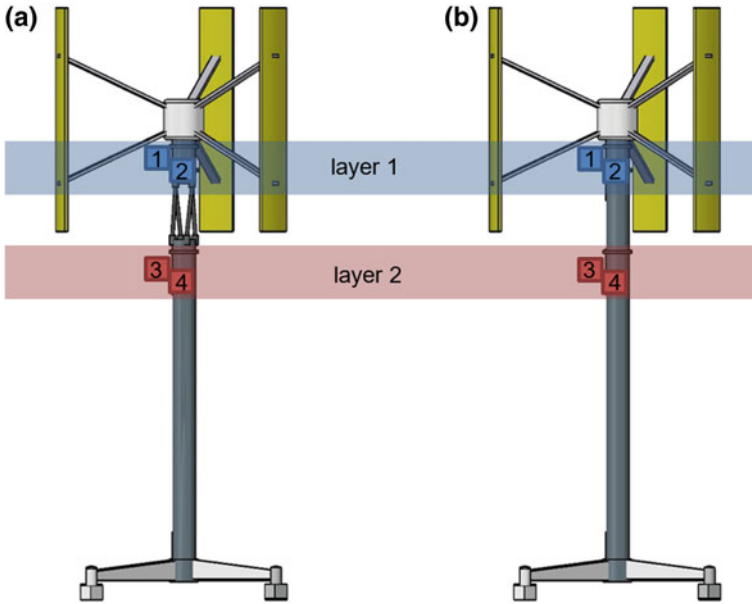


Fig. 2 Sensor alignment layer 1 and 2 on VASWT with (a) and without decoupling (b)

3.1 Measurement Set-Up

Oscillation was measured in two different measurement layers in order to distinguish between two cases. The definition of two layers was necessary to determine the decoupling element’s potential to reduce oscillation. Figure 2 demonstrates the alignment of four sensors, two on each layer.

Figure 2b is the assembly without a decoupling element. The plant in Fig. 2a is shown with the decoupling element consisting of four struts with rubber sockets to damp oscillation.

Oscillations are measured on two positions. The first layer is made of an aluminum angle which is strapped to the mast by a tension belt with a tension greater than 500 N. Two piezoelectric sensors, which are aligned at an angle of 90°, make it possible to distinguish between torsion and bending oscillation (see Fig. 3a). In layer 1 the piezoelectric accelerometers 1 and 2 are aligned (see Fig. 3a nr. 1 and 2). The second layer is constructed in the same way as layer 1 but the capacitive accelerometer 3 and an electrodynamic inductive velocity sensor 4 are likewise aligned at an angle of 90° (see Fig. 3b nr. 3 and 4).

First measurements in layer 1 (under the generator) revealed that vibrations with a frequency greater than 2 Hz were dominant. Therefore, the accelerometers 1 and 2 were placed in layer 1. Vibration measured on the mast proved to reach relevant frequencies down to 0.1 Hz. Consequently, in layer 2 sensors 3 and 4 were aligned here due to the adequate range close to 0.1 Hz.

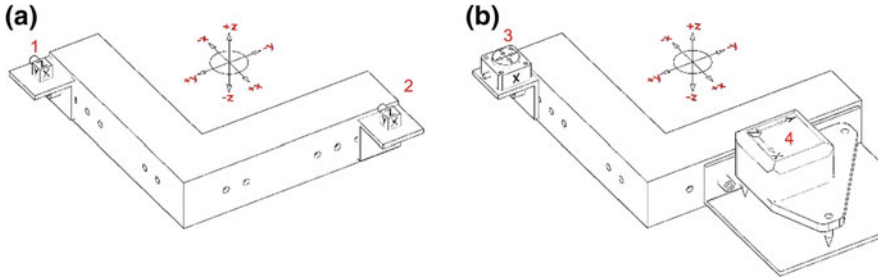


Fig. 3 Alignment of sensors on layer 1 (a) and layer 2 (b)

For the rotational speed and power output, existing equipment was utilized and integrated into the data acquisition unit.

The wind speed, turbulence intensity, vertical cross wind and wind direction were measured by means of a 3D ultrasonic anemometer on a preinstalled measuring mast at hub height. The main advantage of this anemometer is the measurement of the wind speed separately in three orthogonal vectors, which delivers a more accurate result. Contrary to the IEC 61400-2 standard, the wind speed was averaged to a 20-s mean value to be able to assign the wind speed more accurately to vibration events.

Turbulences cause a permanent and instantaneous fluctuation of the wind speed with respect to the mean wind speed. These changes of the wind speed can occur in longitudinal, transversal and vertical direction [12]. In order to characterize turbulent wind flows the turbulence intensity (TI) is obtained from the quotient of the standard deviation of the wind speed and its mean value [7]. According to the IEC 61400-2 standard, the turbulence intensity is based on the 10-min mean value of the wind speed. Owing the relatively short duration of vibration and oscillation events, the averaging period of the wind speed was set to 20 s in order to assign these events more accurately [4].

Vertical cross wind is defined as a rapid change of the vertical angle of the wind in relation to the horizontal plane, causing a non-perpendicular incoming wind on the rotor. In comparison to wind incoming perpendicular to the rotor, vertical cross wind can cause asymmetrical loads and strain on the rotor [12]. The design of a Darrieus rotor means that these plants can utilize wind vertically up to a certain extend and horizontally from each direction at the same time. Owing to the 3D ultrasonic anemometer sensor alignment in each direction in space, the vertical cross wind angle was recorded.

Initial investigations showed that the frequency of oscillation and vibration ranged between 0.1 and approximately 200 Hz. In order to display the oscillation curve accurately it is crucial to set an appropriate sample rate in the data acquisition unit. Practical experiences demonstrated that the sample rate should be 10 times higher than the maximum oscillation frequency. In this case, a sample rate of 2000 Hz was reasonable. Each accelerometer has three output signals as RMS-values, one in

each direction in space (x, y, z). To simplify the evaluation, the single vectors were aggregated to a oscillation vector in space according to ISO 7919-1:1996 [4].

As high sample rates produce a high number of data points, this high resolution rate was activated only at specific trigger events. A trigger event for high-resolution recording was activated when for instance the oscillation velocity exceeded 100 mm/s.

4 Results

4.1 *Measurement Without Decoupling Element*

To ensure consistent data analysis of the oscillation data captured on the Darrieus rotor, the analysis was performed in two ways. The first step was a statistical analysis of the oscillation data recorded for ten days. Statistical results allowed a conclusion to be made whether certain events caused potential for elevated oscillations or not. Hence, the frequency of occurrence of each oscillation velocity at a specific rotational speed was plotted in a three-dimensional diagram. Additionally, the following values were analyzed in terms of their potential to stimulate components of the VASWT:

- Wind speed [m/s]
- Turbulence intensity [%]
- Vertical cross wind [°]

Single events such as gusts, energy-yield losses and the oscillation-order analysis were evaluated in a spectral analysis.

Statistical analysis. The evaluation of the rotational speed covered measurement values from 50 to 300 rpm, whereby certain speeds led to high oscillation of the whole system. To reduce the amount of data, all values at a rotational speed of less than 50 rpm and a wind speed below 4 m/s were excluded because these occur out of the operation range of the plant. This data set was analyzed previously to ensure that there were no significant oscillation events.

As mentioned in Sect. 2.1, all components have a characteristic natural frequency, which can be excited. The dynamic forces caused by the revolution of the rotor represent such an exciting frequency (mass imbalances, aerodynamic imbalances) that covers a frequency range between 0.1 and 5 Hz. In addition, there are two orders of the rotational speed, firstly the frequency of the rotor blades passing the tower (tower shadow), and secondly the frequency caused by the torque of 20 generator poles passing permanent magnets. The oscillation frequency caused by three rotor blades covers a range of 0.1–15 Hz and the frequency of the torque of the generator poles ranges between 0.1 and 100 Hz. Figure 4 illustrates the frequency of occurrence of the oscillation velocity to each rotational speed class. On average the oscillation velocity does not exceed 80 mm/s and 20 mm/s is the most frequently occurring velocity, at about 50%.

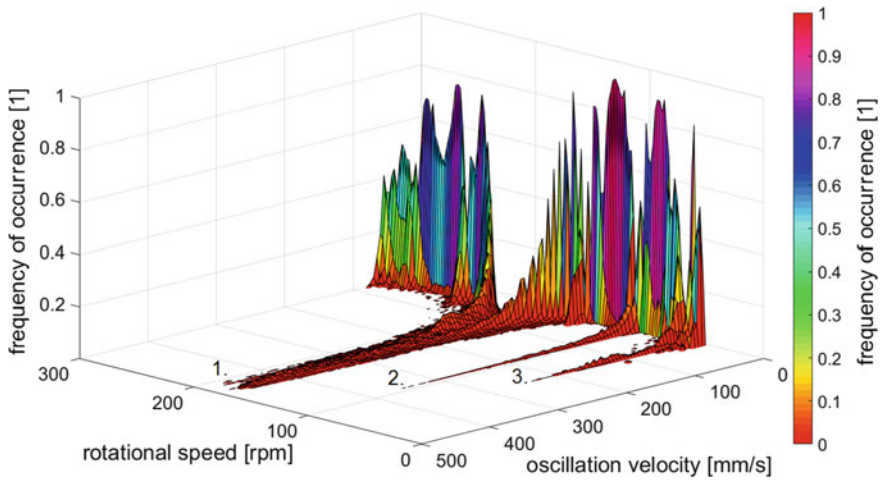


Fig. 4 Darrieus rotor without decoupling; rotational speed versus oscillation velocity

It is of special interest that there is a high oscillation velocity at certain speeds of the rotor. Although the frequency of occurrence of these events is relatively low (maximum 5%), their peak values may represent an extreme mechanical load. In detail, there are three speed values with peak values:

1. 175 rpm—maximum oscillation velocity 495 mm/s
2. 100 rpm—maximum oscillation velocity 300 mm/s
3. 60 rpm—maximum oscillation velocity 250 mm/s

As the wind forces the rotor to spin, it appears that the wind itself may also lead to increased oscillation. In Fig. 5, in a range of 200 and 500 mm/s, the wind speed ranges between 5 and 15 m/s. A separate analysis of the wind speed and the rotational speed has shown that this extremely scattered wind speed range is responsible for the critical rotational speed at 175 rpm in Fig. 4. Hence, the wind speed indirectly provokes the oscillation peaks in Fig. 4.

Figure 6 shows the frequency of occurrence (z-axis) and the oscillation velocity (x-axis) in relation to the turbulence intensity (y-axis). High turbulence intensities mainly occur at low wind speeds, in contrast low turbulence intensities occur at high wind speeds. Consequently, the force of a turbulent flow rises with the wind speed [12]. Therefore, the average wind speed that was recorded simultaneously with the turbulence intensity is overlaid as a color scale in Fig. 6 as a fourth dimension.

The curve of turbulence intensity (y-axis) in reference to the vibration velocity (x-axis) shows a homogenous distribution. No peak value is observable between 0 and 25% turbulence intensity. The wind speed indicated by the color pattern shows an even distribution. All wind speed classes appear at each turbulence intensity class, which appears to be a property of the location. For each turbulence class, all

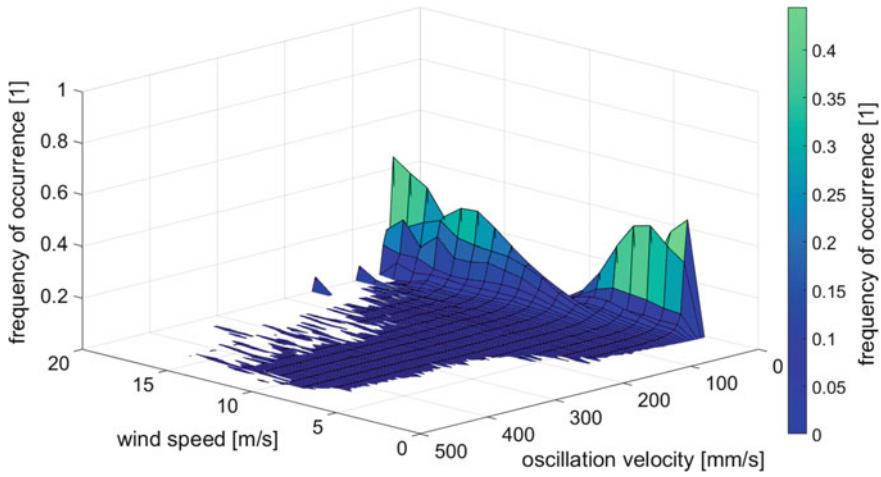


Fig. 5 Darrieus rotor without decoupling; wind speed versus oscillation velocity

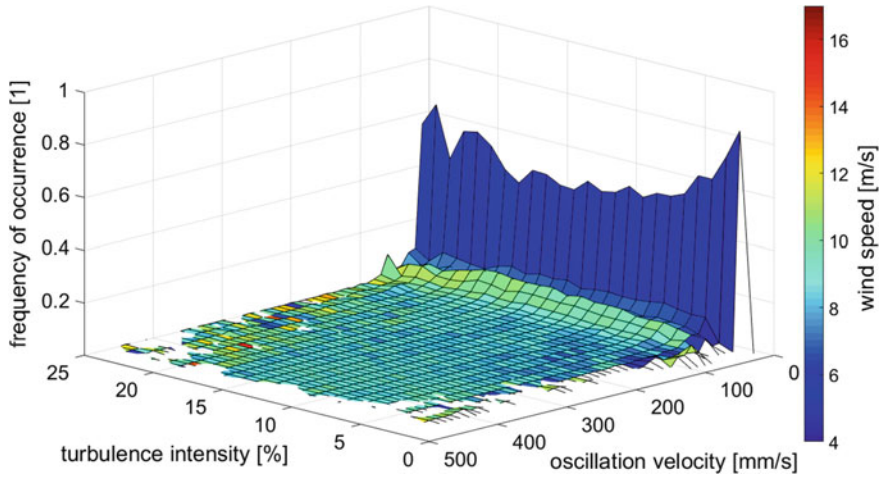


Fig. 6 Darrieus rotor without decoupling; turbulence intensity versus oscillation velocity

oscillation intensity classes occur with the same frequency, which indicates that there is no significant influence of the turbulence intensity on oscillation behavior.

One can see again the oscillation behavior according to the wind speed. The oscillation velocity rises continuously with a higher wind speed. Low oscillation velocities (0–100 mm/s) occur at a low wind speed range between 4 and 8 m/s. Higher oscillation intensities between 100 and 500 mm/s occur on average at a wind speed range between 9 and 11 m/s (see color pattern in Fig. 6). This range corresponds to the wind speed that drives the rotor at 175 rpm (cf. Fig. 1 power curve).

The frequency of occurrence of oscillation events in relation to the angle of vertical cross wind was analogously analyzed with respect to wind speed. The curve progression of vertical cross wind angle versus oscillation velocity was similar to the one in Fig. 6. This shows that there is no significant influence of vertical cross wind on the oscillation behavior because each oscillation velocity class has shown the same frequency of occurrence for each vertical cross wind class.

Spectral analysis. The analysis of the rotational speed has shown the highest impact on the oscillation intensity and indicated three significant speeds that have led to high oscillation. To verify the assumption if the two orders (3rd and 20th order) of the rotational speed led to high oscillation, the measurement values of the oscillation velocity were analyzed in a Fast-Fourier-Transformation (FFT). In Fig. 7, the frequency range of the oscillation velocity at 174 rpm is plotted and the amplitude (mm/s) is shown in a logarithmic scale. Three colored points indicate the orders of the rotational speed. The first order represents the speed of the rotor stimulating the components to vibrate with a frequency of 2.9 Hz (480 mm/s). Thus, the natural frequency of the system must range around 2.9 Hz as oscillation amplitude builds up at this frequency. The blue cross marks the third order in Fig. 7, which has its origin in the frequency of three rotor blades passing the tower. This order stimulates no natural frequency, as 1.7 mm/s is a very low value for the oscillation velocity. Similar to the third order, the 20th order is very low (see violet star mark). The 20th order is caused by the generator-poles passing the coils causing dynamic torque ripple.

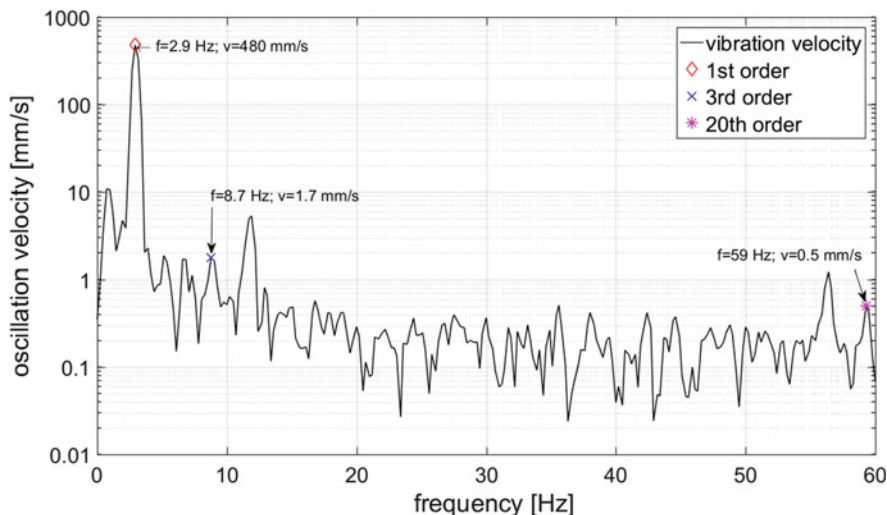


Fig. 7 Darrieus rotor without decoupling; FFT-analysis at 174 rpm

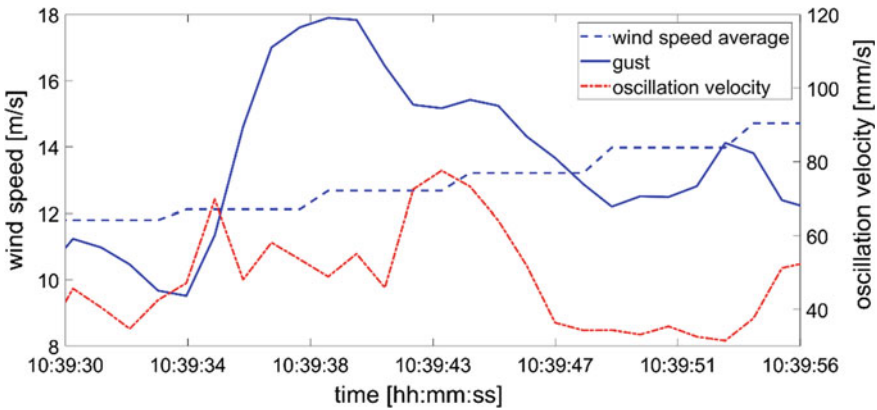


Fig. 8 Darrieus rotor without decoupling: gust

Gusts are sudden wind blasts that constitute an extreme mechanical load for the wind turbine. Given that definitions of gusts are uncertain, we adopted our own definition based on the standard EN 61400-2. A gust was defined as a minimum increase of the wind speed of 5 m/s using the 20-s mean value of the wind speed as Ref. [7]. Figure 8 shows an example of an extreme gust (10:39:38) with a wind speed increase of 6 m/s relative to the mean value and the corresponding oscillation velocity on the secondary axis.

The comparison of the oscillation of the VASWT and the extreme gust shows that this windblast did not increase the oscillation velocity significantly. During the gust event, the oscillation velocity increased from 40 to 80 mm/s. An FFT analysis demonstrated that the main oscillation (4.4 Hz) corresponded to the rotational speed of the rotor, indicating that the rotational speed is the main cause.

To verify this assumption, several gust events were analyzed, including events with high and low oscillation velocities. For each analysis, a spectral evaluation was conducted to identify the source of the oscillation. The FFT analysis revealed that high oscillation is not mainly caused by gusts themselves but by the rotational frequency of the rotor which stimulates natural frequencies of the system. These frequencies correspond to the three resonant rotational speeds 60, 100 and 175 rpm. Gust events with rotational speeds beyond the critical speed range did not show any sign of altered oscillation velocities. Nevertheless, gust may still represent an extreme mechanical load on the wind turbine resulting in strain.

Throughout the entire measurement sequence, the generated power was determined to evaluate whether oscillation has a significant influence on the energy yield or not. Figure 9 shows two power losses with and without increased oscillation velocity. The black line shows the estimated power output calculated according to the power curve given from the manufacturer of the plant. In contrast, the red line shows the real measured power output of the plant.

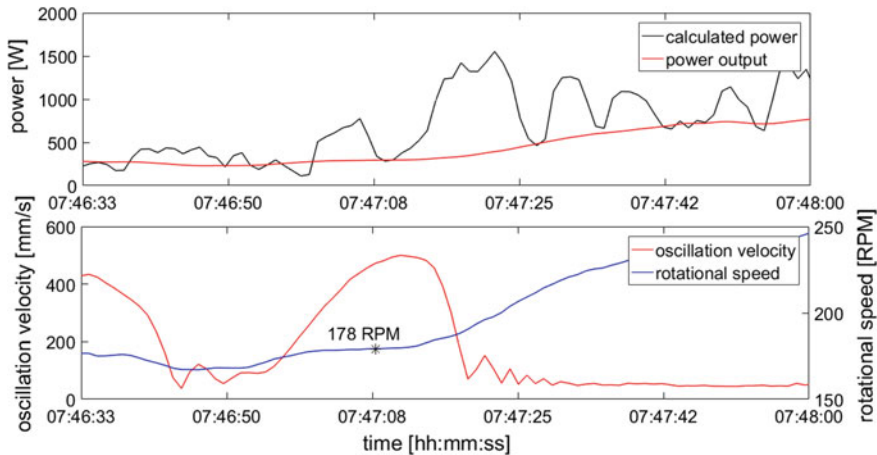


Fig. 9 Darrieus rotor without decoupling; correlation of power losses and oscillation

The first calculated power loss (07:47:15) of about 15% coincides with high oscillation of the mast (280 mm/s). During the second power loss (07:42:38), no increased oscillation velocity was noticeable. Over the entire measurement sequence there were several power loss events detected with high and with low oscillation. A closer inspection of the event with high oscillation in Fig. 9 shows that this high oscillation was stimulated by the critical rotational speed of 175 rpm.

These two exemplary cases have shown that oscillation does not have a significant influence on the power output of the plant. Additionally, the real power output (red line) increased monotonically with no abrupt power loss at 450 mm/s indicating no influence of high oscillation. During the measurement, there were no other definite coincidences between extreme power losses and high oscillation.

4.2 Measurement Results with Decoupling

Decoupling elements are useful devices to reduce the intensity of oscillation emitted by VASWTs. These elements reduce oscillation amplitude and frequency by two mechanisms. Installing a decoupling element between the generator and the mast reduces the natural frequency of the system. As the oscillation frequencies are linear dependent on the rotational speed of the turbine, resonances are excited at lower rotational speeds when wind speeds and thus loads are low. The second principle that reduces oscillation is the damping effect of a flexible material (polyurethane foam) that dissipates oscillation energy during displacement.

In the second measurement sequence, these characteristics of the decoupling element reduced the oscillation velocities by a factor of three over the whole operation range. Figure 10 illustrates the reduced oscillation in reference to the rotational speed

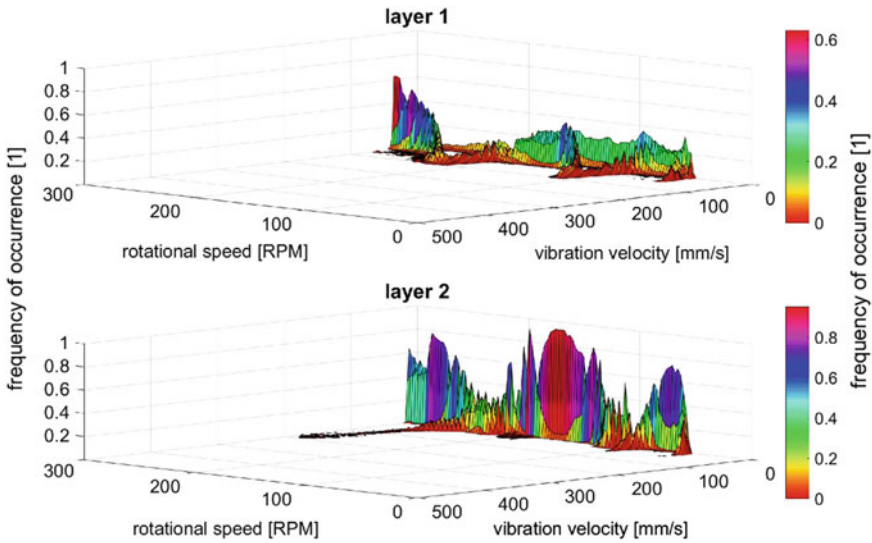


Fig. 10 Darrieus rotor with decoupling; rotational speed versus oscillation velocity

in each measurement layer. In layer 1, the oscillation was measured between the generator and the decoupling element. We found that in layer 1 the oscillation velocity at the peaks at 100 and 175 rpm were reduced from 500 to 100 mm/s on average.

The decoupling element elevated the natural frequency of the system consisting of mast and the plant; as a result, the spinning rotor no longer stimulates this frequency. Layer 2, which is located on the mast and under the decoupling element shows an even greater reduction as most of the oscillation energy has been dissipated above. There is a new significant peak of the oscillation velocity at about 280 rpm, probably caused by a physical overload at high wind speeds. A new dimension of the decoupling element would be necessary to eliminate this peak.

5 Discussion

Machines with periodically oscillating components transduce the inherent energy to the immediate environment and may cause damage. To reduce the impact it is important to know the source of oscillation and its formation mechanism. The statistical evaluation of the data concerning oscillation and external influences has shown that the tower shadow effect does not excite oscillation above 10 mm/s. Turbulences and vertical cross wind do not show enough periodicity and force to excite a resonant oscillation of a component. High external peak loads such as gusts apply high forces on the rotor, but these forces occur for a short period of time, which makes it unlikely to excite any natural frequencies.

A specific speed of the rotor that corresponds to the natural frequency of a component has a great potential to excite oscillation. In combination with mass imbalances, this influence has the greatest potential to cause oscillation on VASWT. The data captured on the Darrieus rotor have shown that the rotational speed is the major cause for oscillation (cf. Fig. 4).

5.1 *Range of Oscillation and Vibration in VASWTs*

The oscillation data obtained from the measurement sequence without the decoupling element provides information about the range of oscillation occurring on a VASWT. To enable a secure and cost-efficient operation of VASWTs, knowing the intensity of oscillation emitted by the wind turbine is crucial. In this case, the rotor caused high oscillation velocities ranging between 0.8 and 5 Hz and peak values up to 495 mm/s. During the operation, there was a mean oscillation acceleration of 11 m/s^2 and peak values of up to 80 m/s^2 . This indicates that wind turbines have a wide range of oscillation in terms of frequency, velocity and acceleration. Specifically in this case, the natural frequencies 1, 1.6 and 2.9 Hz were stimulated by the first order oscillation indicating a rotor mass imbalance.

According to VDI 3834/1, oscillation on large wind turbines can be divided in four different groups:

- Zone A: oscillation in stationary operation
- Zone B: oscillation during normal operation—these oscillations do not cause any damage
- Zone C: oscillation in this class leads to a high strain on components
- Zone D: oscillation leads to component failures

This classification was adapted for VASWTs to evaluate a warning value for high oscillation between classes B and C. A warning oscillation event is calculated with the energy-equivalent mean value of oscillation velocity and acceleration for at least 10 min during normal operation conditions. The warning value is finally obtained by multiplying the mean value by the factor 1.25 [11].

For this VASWT-type the following warning-values were calculated:

- Oscillation acceleration 11 m/s^2
- Oscillation velocity 60 mm/s

During the two weeks of measurement without the decoupling element, these warning-values were exceeded up to seven times for a longer period of time, which results in high strain for all plant components. A common method to avoid material fatigue due to high oscillation is an automatic shut-down system, which is activated when a pre-defined limit value is exceeded. As a result, machine downtimes reduce the energy yield of the plant. In contrast, the decoupling element kept the oscillation acceleration and velocity within the limits during normal operation conditions (see

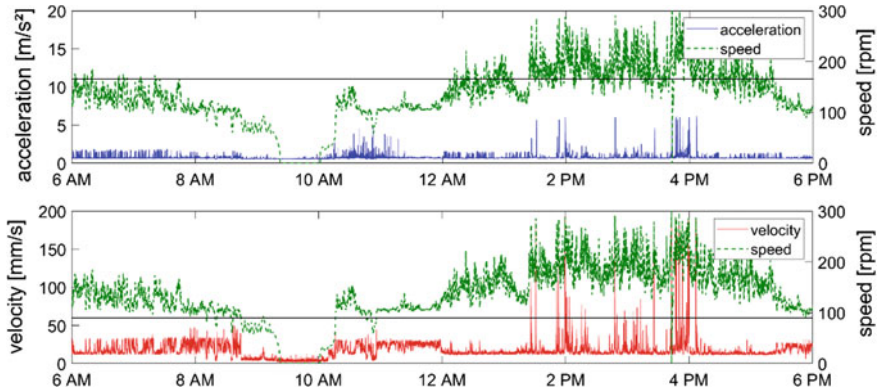


Fig. 11 Operation parameters—Darrieus rotor with decoupling element

Fig. 11). Thus, this decoupling element represents a feasible way to avoid or reduce these downtimes.

5.2 Influence on the Immediate Environment

In contrast to photovoltaic panels, small wind turbines are generating units with dynamically moving components. These parts can be considered as a possible threat to the immediate environment as well as a high mechanical strain for the plant itself. Hence, it is important to know about the possible impact on the surrounding area.

As VASWTs can be installed close to buildings or even on roofs, this means a potential health risk for humans. According to Directive 2002/44/EG human beings must not be exposed to vibration with an intensity more than 1.15 m/s^2 on average during an eight-hour working day [13]. The evaluation of the oscillation data without the decoupling element has shown that this limit value was exceeded up to 11.1 m/s^2 on average. It must be kept in mind that this value was measured directly under the generator. Depending on the components between a human being and a VASWT, the plant can also operate within these limit values due to damping effects from other installations.

5.3 Effectiveness of Decoupling Elements

When comparing the maximum oscillation intensity of the plant with and without the decoupling element, it has been shown that the intensity of oscillation during normal operation is reduced significantly. Figure 11 illustrates the operating parameters of the Darrieus rotor with the decoupling element during one day. The warning values for

oscillation acceleration (11 m/s^2 —black line) and for the velocity (60 mm/s —black line) were exceeded only at extreme rotor speeds ($250 \leq 300 \text{ rpm}$). In the present case, oscillation velocity was limited to 180 mm/s by the decoupling element (see Fig. 11 red line). This overview of one day shows how drastically the decoupling element reduces the oscillation intensity.

6 Conclusion

The investigation of a small “Darrieus rotor” type wind turbine served as an example for the range of vibration and oscillation. Due to the construction method and dynamically moving components, it is well-known that wind turbines vibrate. Piezoelectric and capacitive MEM sensors were used to determine the oscillation behavior of a darrieus rotor. As external parameters may influence the oscillation behavior of the plant, the wind speed, gusts and turbulences were measured simultaneously with the oscillation. Additionally, power output and rotational speed were determined.

It should be stressed that the results from the oscillation investigation are not representative for all types of VASWTs because different geometrical dimensions of the mast in combination with a VASWT lead to a different oscillation behavior. This measurement sequence has shown that during VASWT operation, high oscillation velocity peaks of 495 mm/s and oscillation acceleration peaks of 80 m/s^2 can occur. These parameters occurred in a frequency range between 0.8 and 5 Hz . It should be noted that these peak values occurred only at specific events, while the average value for the oscillation velocity ranged between 20 and 80 mm/s .

Statistical results revealed that external influences such as gusts, turbulences and the wind speed in general have no significant impact on the oscillation behavior of the plant. In contrast, internal influences such as rotational speed in combination with mass imbalances stimulate the VASWT’s natural frequencies.

As power loss events occurred frequently at high and low oscillation velocities, no definite correlation between oscillation and energy yield losses was detected.

While the VASWT with no oscillation-damping installations was subject to high-intensity vibration, the plant with decoupling elements showed a significantly reduced oscillation behavior. With these installations, the oscillation velocity and acceleration are kept within the limit values for the plant. However, the limit values for human beings are exceeded. It can be concluded from these findings that a greater reduction of VASWT vibration and oscillation is needed to enable a safe operation of VASWTs in inhabited areas.

References

1. IG-Windkraft (2015) [https://www.igwindkraft.at/fakten/?xmlval_ID_KEY\[0\]=1234](https://www.igwindkraft.at/fakten/?xmlval_ID_KEY[0]=1234). Last accessed 03 Mar 2016

2. Evans SP, Anup KC, Bradney DR, Urmee TP, Whale J, Clausen PD (2017) The suitability of the IEC 61400-2 wind model for small wind turbines operating in the built environment. *Renew Energy Environ Sustain* 2:31
3. KEF, AEE (2014) *Kleinwindkraft – Ein Leitfaden zur Planung und Umsetzung*, Wien, 2. Auflage, Herausgeber Daniel Reiterer M.A. Ing
4. Peppoloni M, Hirschl A, Leonhartsberger K (2017) Environmental Influences on SWT vibrations and oscillations. *Wind energy exploitation in urban environment TURbWind 2017 Colloquium*, pp 57–78
5. ZAMG (2015) Bericht – Windzonierungskarte für Kleinwindkraftanlagen für Wien, Wien, 1. Ausgabe, Mag. Hildegard Kaufmann, DI Dr. Hung Viet Tran, Alexander Orlik, Sebastian Pokorny
6. Warmuth H, Zimmer F, Prokschy H, Leeb K, Reiterer D, Sterrer R, Nennung T (2014) *ÖGUT, Kleinwindkraftanlagen – Qualitätssicherung, Netzeinbindung, Geschäftsmodelle und Information*, 2014, Wien
7. IEC/EN 61400-2:2013-06-01, Wind turbines—part 2: small wind turbines, edition 3.0
8. Magnus K, Popp K, Sextro W (2008) *Schwingungen – Eine Einführung in die physikalischen Grundlagen und die theoretische Behandlung von Schwingungsproblemen*, 8. Auflage. Vieweg + Teubner Verlag, Wiesbaden
9. BAUA (2016) http://www.baua.de/de/Themen-von-A-Z/Vibration/Vibration_content.html. Last accessed 21 Apr 2016
10. VDI Wissensforum GmbH, 6. VDI-Fachtagung Schwingungen von Windenergieanlagen 2015, 2015, Bremen, VDI-Verlag Düsseldorf, ISBN 978-3-18-092242-3
11. VDI 3834/1, Messung und Beurteilung der mechanischen Schwingungen von Windenergieanlagen und deren Komponenten – Windenergieanlagen mit Getriebe, Düsseldorf 2015
12. Hau E (2013) *Wind turbines—fundamentals, technologies, application, economics*, 3rd edn. Springer, Berlin, ISBN 978-3-642-27150-2
13. Hahn N, Pflaumbaum W (2015) IFA Report 4/2015 – Grenzwertliste 2015 – Sicherheit und Gesundheit am Arbeitsplatz. Medienhaus Plump, Berlin
14. Energiewerkstatt (2014) Publikationsbericht - Das realisierbare Windpotential Österreichs für 2020 und 2030. <https://www.igwindkraft.at/mmedia/download/2014.09.17/1410964769070667.pdf>. Last accessed 03 Mar 2016
15. Twele J (2013) Empfehlungen zum Einsatz kleiner Windenergieanlagen im urbanen Raum – Ein Leitfaden. HTW Berlin, Berlin

Assessment of the Impact of a Low-Rise Flat Roofed Building on Ambient Wind Conditions



Stefan Hübl, Mauro Peppoloni, Kurt Leonhartsberger
and Alexander Hirschl

Abstract Small wind turbines (SWT), representing a relatively new technology in the field of renewable energies, exhibit potential for a notable contribution to a sustainable urban energy supply accelerated by international climate agreements [1]. However, many uncertainties remain regarding site assessment, especially in the built environment. Wind conditions in areas below 30 m above ground, where small wind turbines are preferably installed, are affected by complex aerodynamic effects. Urban areas feature conditions often not considered by common CFD models and calculations. This paper focuses on the impact of low-rise flat roof buildings on the ambient wind flow. Contrary to other investigations on wind flow around complex obstacles relying on numerical fluid flow simulations or scaled wind tunnel experiments, the performed investigation relies on measurements over a flat-roofed building. The data acquired over a span of 7 months by several 3D-ultrasonic anemometers at the Lichtegg test site (Lower Austria) was examined. In order to determine the impact of the building on ambient wind conditions, the horizontal and vertical wind velocity, turbulence intensity and direction scatter at several locations were compared to the uninfluenced inflow conditions. Moreover, in addition to the commonly calculated horizontal turbulence intensity, the vertical turbulence intensity was considered to gain a deeper understanding for the occurring aerodynamic effects. The measurement results indicate that some locations on or around the building are not suited for installing wind turbines, while others show increased wind potential compared to undisturbed wind stream. Based on findings obtained by the wind assessment, recommendations for ideal placing of small wind turbines on low-rise buildings are given.

Keywords Small wind turbine · Urban · Building mounted · Site assessment · Micro-siting vertical turbulence intensity

S. Hübl (✉) · M. Peppoloni · K. Leonhartsberger · A. Hirschl
University of Applied Sciences, 1210 Vienna, Austria
e-mail: stefan.huebl@gmail.com

© Springer Nature Switzerland AG 2019
L. Battisti (ed.), *Wind Energy Exploitation in Urban Environment*,
Research Topics in Wind Energy 8, https://doi.org/10.1007/978-3-030-13531-7_7

1 Introduction

Small wind has the potential to act as a comprehensive supply of sustainable, renewable energy in urban areas, where it is generally not possible to install large wind turbines.

Unfortunately, most research related to wind energy has its roots in large wind research. However, some of those theories seem not to be applicable at low altitudes or in complex terrain where small wind turbines are mostly operated.

A special field of research in this context is the ideal location of installation on or around urban buildings. Some research has already been performed by other authors, who worked with 3D Computational Fluid Dynamics (CFD) simulations or based on 3D measurements of wind properties over two dimensional obstacles. Unlike these surveys, this investigation relies on an elaborated measurement set-up that was installed at Lichtenegg Energy Research Park, Austria to perform 3D measurements of wind properties.

What makes this series of measurements interesting is that measurements were performed both with undisturbed properties over open surface and with an installed flat roof obstacle in the wind stream. Thus, this setup allows a detailed analysis of both cases.

2 Measurement Set-Up

2.1 *Lichtenegg Energy Research Park*

Lichtenegg is located approximately 60 km south of Vienna, close by Wiener Neustadt. The area is located at a hilltop on the eastern foothill of the alps. The altitude of approximately 800 masl as well as its exposed location in the hilly range of the “Leithagebirge” makes it a location with comparably high wind speeds.

The surrounding area mainly consist of acres, while the surface of the measuring field is covered with grass and in further distance from the set-up (over 500 m) forest. The surface area is running slightly downhill in southern direction with $\Delta h = -1.8$ m.

As a result of the above described geographic conditions, the main wind directions are North-West and South. Below in Fig. 1 wind roses of measuring phase 1 (no obstacle in wind stream) and phase 2 (cubic obstacle in wind stream) are displayed.

The mean wind velocities for phase 1 and 2 are 4.41 and 4.54 m/s, while maximum wind velocities were measured at 18.39 and 19.35 m/s.

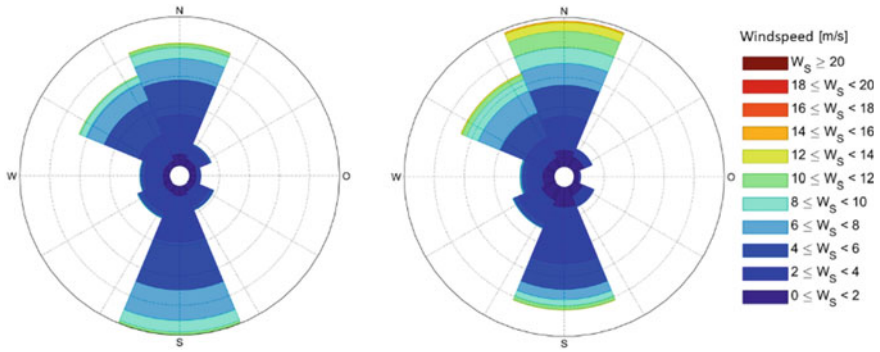
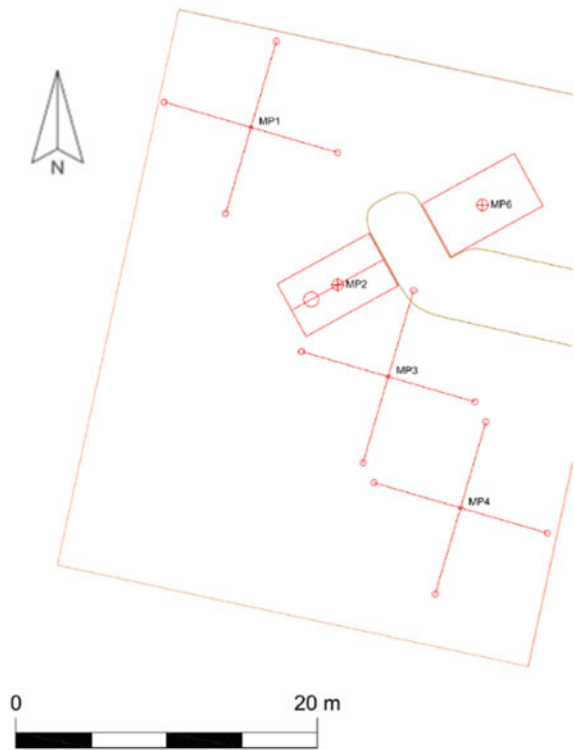


Fig. 1 Wind roses during measuring period. Left: phase 1, right: phase 2 [2]

Fig. 2 Orientation of set-up [3]



2.2 Set-Up

Four masts with measuring equipment in three different heights have been installed (MP1-MP4). Figure 2 shows the orientation of the masts and obstacle.

Table 1 Overview of measuring points

Measuring mast	Installation heights		Vertical wind speed measuring
	Phase 1 (m)	Phase 2 (m)	
MP1	10.5	10.5	No
	7	7	Yes
	3.5	3.5	No
MP2	10.5	9	Yes
	7	7	Yes
	3.5	5	Yes
MP3	7	7	Yes
	3.5	3.5	Yes
MP4	10.5	10.5	No
	7	7	Yes
	3.5	3.5	No

The masts are aligned with the main wind direction, North-South with a slight rotation of 28° in western direction. One Mast (MP1) is installed in the inlet flow (related to main wind direction) north of the obstacle. MP2 is installed on the building and MP3 and MP4 are supposed to capture the backlash of the wind flow after the obstacle. MP6, that is also displayed in Fig. 2, was not active during the measurements performed for this paper. This mast is installed for follow-up experiments over a pitched roof building.

MP1 is installed 15 m in front of the garage, MP2 is installed centered on the garage, MP3 is installed 5 m and MP4 15 m behind the garage.

Due to the reinstalling of MP2 for phase 2, the measuring heights of one of the sensors was slightly changed compared to phase 1. This change of heights is listed in Table 1.

Two different types of anemometers are used. On the one hand 3D-Ultrasound-anemometers, that also allow measurements of vertical wind speeds and on the other hand conventional cup-anemometers, that solely measure vertical wind speeds. An overview of availability of vertical wind velocities is given in Table 1.

Cup-anemometers used for the experiment exhibit an accuracy of measurement of ± 0.243 m/s according to calibration protocols, while for the ultrasound anemometers a precision of ± 0.01 m/s is expected.

The set-ups for phase 1 and 2 is displayed in Fig. 3. The obstacle analyzed within the experiment is a simple cubic garage building with dimensions of $6 \times 2.99 \times 3.35$ m (L \times W \times H).



Fig. 3 Measuring set-up phase 1 (left) and phase 2 (right) [4]

3 Measuring Execution

3.1 Data Basis

The data is collected continuously at a sample rate of 1 Hz for every measured property. The mean value over 60 s is calculated and stored internally by the data-loggers (two Ammonit Meteo 40 M), including standard deviation for every one-minute value generated in that manner. These one-minute averages serve as the base for all further calculations performed in Matlab. Processed properties are:

- Horizontal wind speeds
- Vertical wind speeds
- Wind direction

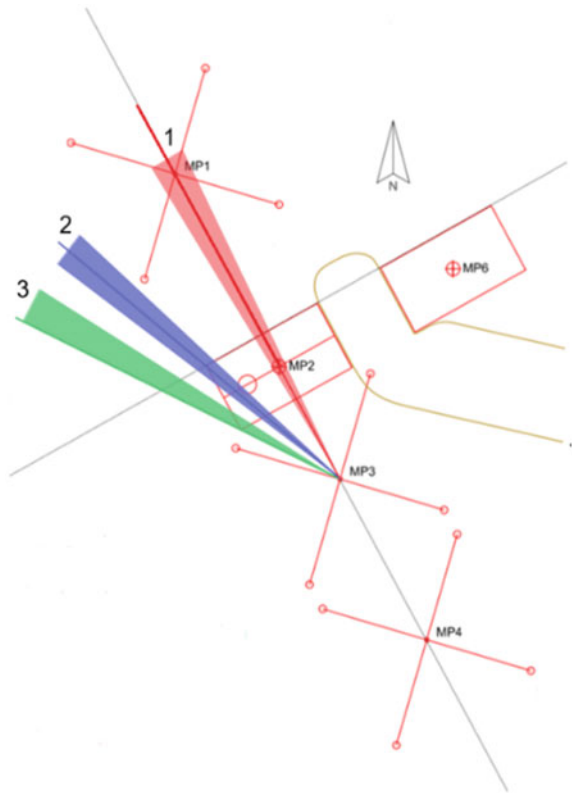
Several other properties such as temperatures, air pressure, humidity etc. are available but not considered within the performed research. Wind properties relevant for following calculations were measured with “first class adv” anemometers and “3D Ultrasonic” both produced by Adolf Thies GmbH & Co. KG.

Phase 1 measurements were taken from 07/06/2017-09/27/2017, followed by a short outage due to re-construction of the measuring set-up. Phase 2 started operating on 10/04/2017. For phase 2 only values stored before 12/10/2017 are considered for calculations in the present paper. Before starting the calculations, data sets had to be cleaned from in-complete or inaccurate measurements.

3.2 Binning

For all calculations the data is binned, both for inflow wind speed and inflow wind direction. This was done for two reasons. First, to reduce the amount of data for processing and second to evaluate representative values.

Fig. 4 Wind direction bins
(own depiction)



Three wind direction bins are defined. One represents direct inflow towards the building, one crosses the building from the North-West faced edge of the building and one just crosses the building. No change of direction is assumed for these definitions. The defined direction bins are marked in Fig. 4.

Inflow bins for both wind direction and wind speed are defined for MP1 at 7 m height. This point was chosen, because it is located in the inflow direction for the assessed wind direction and is therefore not influenced by aerodynamic effects of the building.

For all further calculations 0° is defined as North. The direction bins are defined as follows:

1. 90° related to container's front edge (direct inflow): $332 \pm 5^\circ$
2. 30° related to container's front edge: $311^\circ \pm 5^\circ$
3. 21° related to container's front edge: $301 \pm 5^\circ$

It is assumed that results are symmetric toward the connection line of MP1–MP4, thus only three wind direction bins are considered. Those were chosen from North-West direction, because most data are available from this main wind direction. No bins

from Southern direction are considered, due to the fact that only one 3D anemometer is installed at MP1 and thus no relevant results can be expected.

Wind speeds are binned as follows:

1. 2 ± 0.3 m/s
2. 4 ± 0.3 m/s
3. 6 ± 0.45 m/s
4. 8 ± 0.6 m/s
5. 10 ± 0.8 m/s
6. 14 ± 1.5 m/s

Wind speed bins are defined that way to cover the typical range of operation of small wind turbines. With increasing wind speed less values are available. Therefore, with higher wind speeds the range of fluctuation increases to allow a similar number of measurements per bin.

4 Results

Five different wind parameters have been assessed.

- Horizontal wind speed
- Vertical wind speed
- Horizontal turbulence intensity
- Vertical turbulence intensity
- Wind direction scatter

In accordance to the research on average determination for wind data in [5], all one-minute averages of wind speeds and direction scatter properties are used directly, while for turbulence intensities ten-minute averages are used.

One-minute mean values turned out not to be of sufficient fineness to deliver feasible results and are thus not discussed within this paper.

4.1 Horizontal Wind Speeds

This property is considered the most important in terms of wind turbine technology, because most installed turbines can only convert horizontal inflow. Additionally, the wind-power is dependent on the third power of the windspeed, as shown in the following Eq. (1).

$$P_w = \frac{1}{2} \rho v^3 A \quad (1)$$

Table 2 Number of available values for horizontal and vertical wind speed measurements

Number of measurements	2 m/s	4 m/s	6 m/s	8 m/s	10 m/s	14 m/s
Direction 1—phase 1	395	1118	1923	1151	550	18
Direction 1—phase 2	193	404	683	811	584	69
Direction 2—phase 1	310	960	759	307	73	0
Direction 2—phase 2	184	313	439	315	155	23
Direction 3—phase 1	310	541	348	193	85	2
Direction 3—phase 2	169	272	336	242	104	8

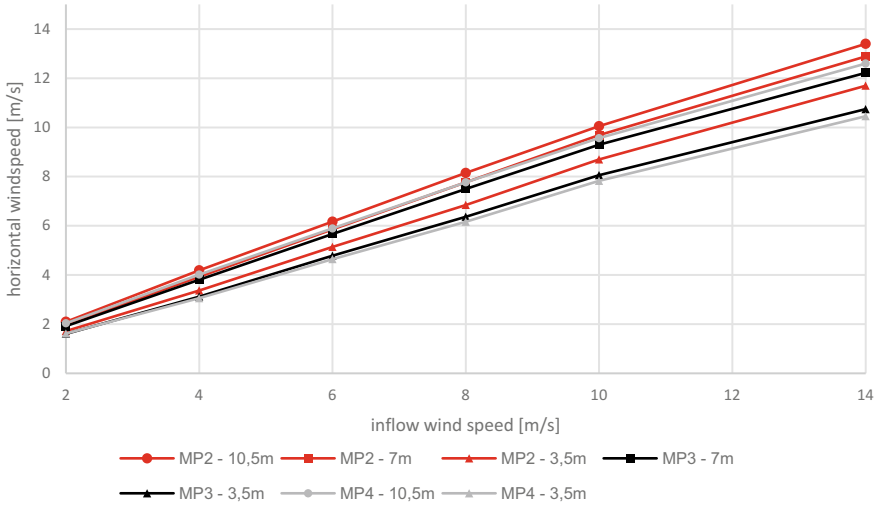


Fig. 5 Horizontal windspeed, phase 1, direction 1 (own depiction)

Table 2 shows the number of measurements for every bin area that is available for horizontal wind speed measurements. The same amount of values also applies to vertical wind speed measurements in Sect. 4.2.

Horizontal wind speeds direction 1. In Figs. 5 and 6 horizontal wind speeds for phase 1 and 2 for direction 1 are displayed.

In phase 2 an almost linear relation between inflow windspeed and measured wind speeds can be identified. Lower wind speeds for measurements in lower heights are noticeable, which can be explained by friction above ground.

In phase 2 all measurements at MP2 exhibit an increase in speed, which is justified by the continuity Eq. (2).

$$\frac{\partial \rho}{\partial t} + \text{div}(\rho \mathbf{v}) = 0 \tag{2}$$

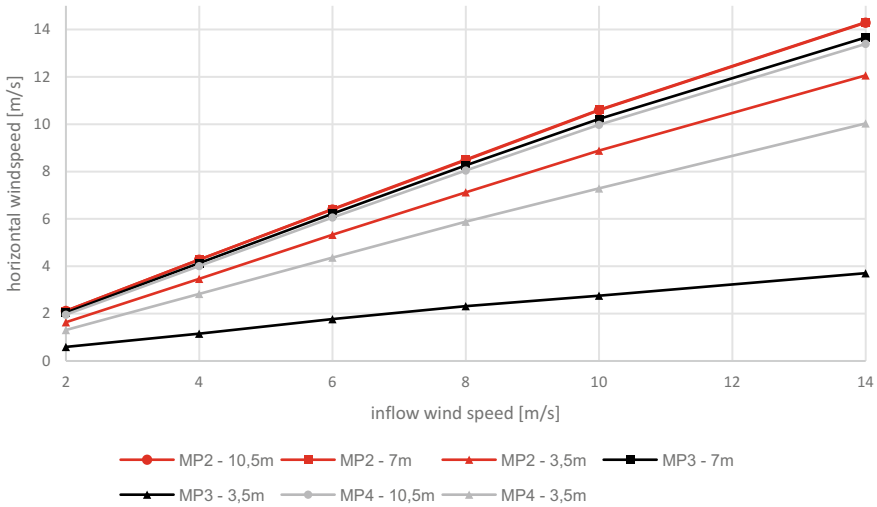


Fig. 6 Horizontal windspeed, phase 2, direction 1 (own depiction)

This effect can only be compared directly at 7 m height, as for both phases the measurements are taken at 7 m. At this height an increase of approx. 10% is investigated.

MP3 has a slight increase in windspeed at 7 m, while at 3.5 m a clear decrease is given. This anemometer is in the wake zone behind the building.

MP4 exhibits a slight decrease of wind speed at 3.5 m and a slight increase at 10.5 m. At a distance of 15 m, which equals approx. five times the height of the building, the impact of the obstacle is almost not distinguishable. This meets the findings of *The fence experiment – full-scale lidar-based shelter observations* [6] performed by DTU in 2016.

Horizontal wind speeds direction 2. In Fig. 7 horizontal wind speeds for phase 2 for direction 2 are displayed.

For measurements in phase 1 no different behavior compared to direction 1 can be observed.

In phase 2 at MP2 only at 7 m height a difference is investigated compared to direction 1. The impact of the obstacle at that height is stronger than for direction 1.

At MP3 at 7 m height no difference is given, but the decrease of wind speed at 3.5 m is approx. 30% less.

MP4 does not exhibit changes compared to direction 1.

Horizontal wind speeds direction 3. In Fig. 8 horizontal wind speeds for phase 2 in direction 3 are displayed. Again, no significantly different behavior for phase 1 can be observed compared to direction 1, hence it is not depicted herein.

The effects in direction 3 are no different from the other two directions. Only, the effects are not as strong as for directions 1 and 2.

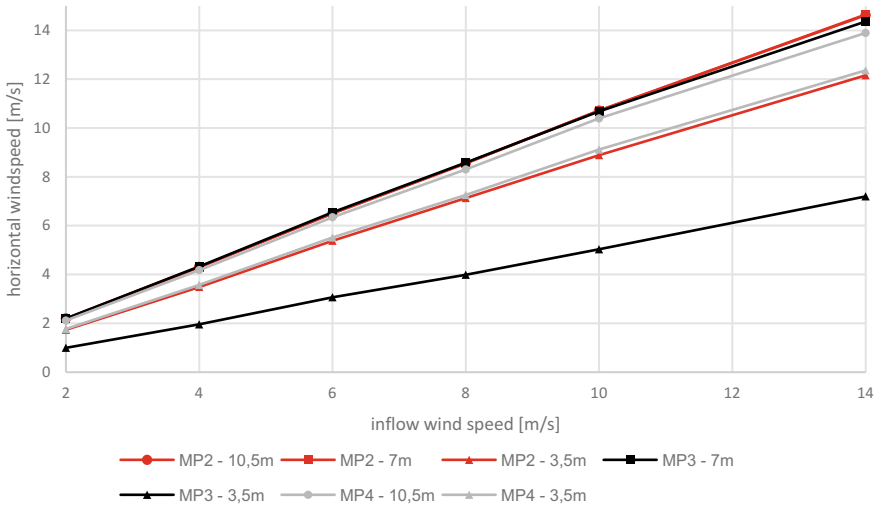


Fig. 7 Horizontal windspeed, phase 2, direction 2 (own depiction)

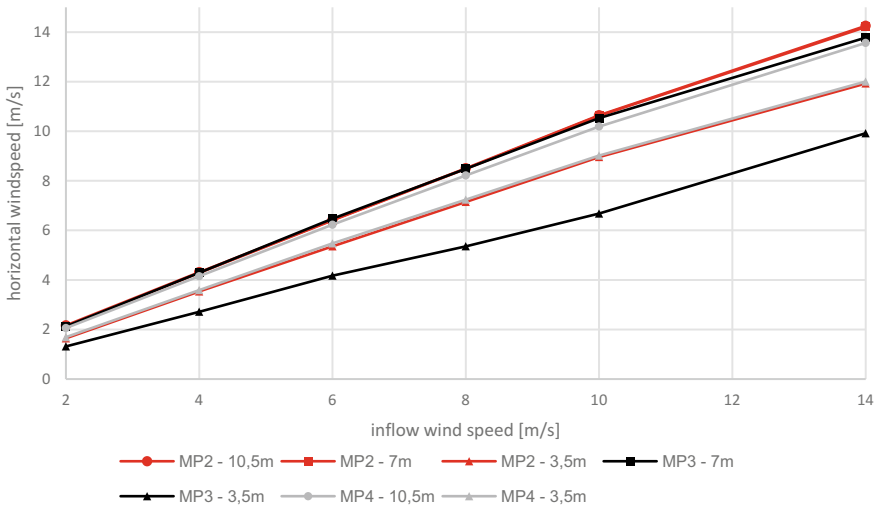


Fig. 8 Horizontal windspeed, phase 2, direction 3 (own depiction)

4.2 Vertical Wind Speeds

Vertical windspeeds are processed in order to gain an impression of how wind gets deviated from its' original flow. In regards of wind energy production, this vertical component generally means loss of potentially usable power as turbines can mostly not harvest vertical wind speeds.

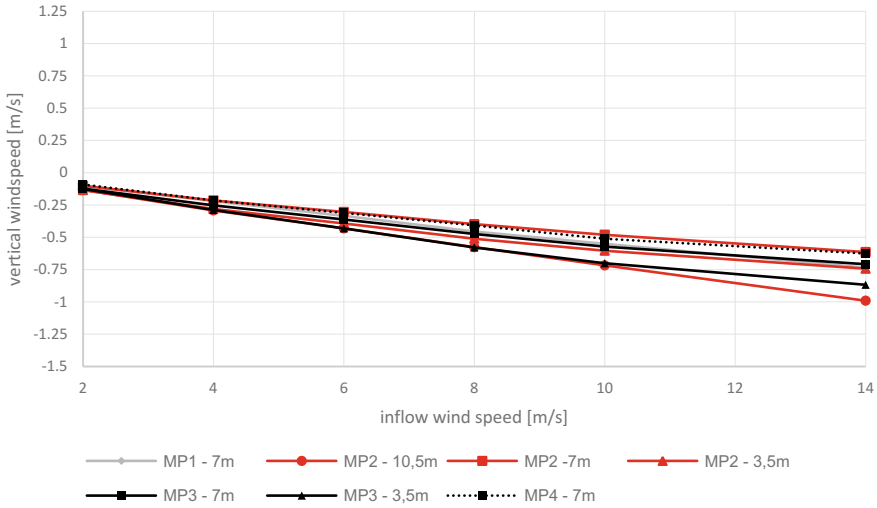


Fig. 9 Vertical windspeed, phase 1, direction 1 (own depiction)

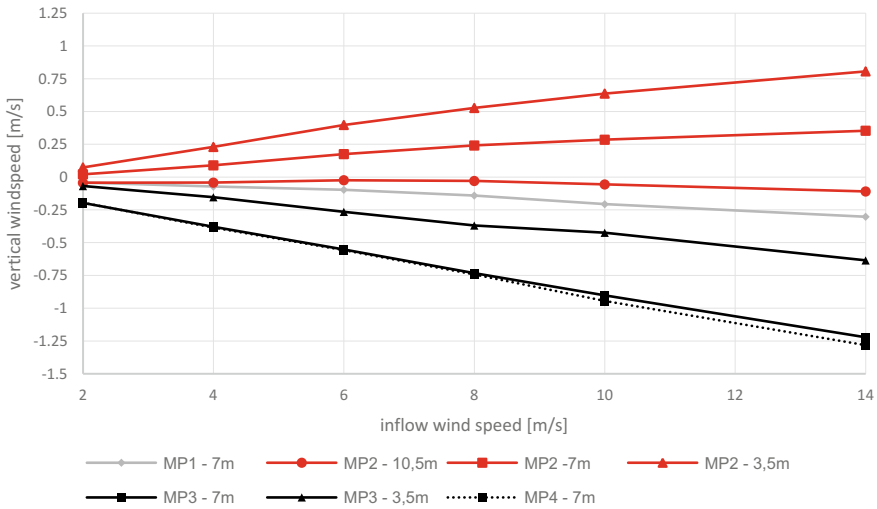


Fig. 10 Vertical windspeed, phase 2, direction 1 (own depiction)

It stands out that for all wind speeds the vertical wind speed component in phase 1 is negative. It is assumed that this effect occurs due to the downward slope of the site. To support this thesis vertical windspeeds in opposite direction ($152^\circ \pm 5^\circ$) were evaluated at MP2, which leads to the expected result of solely positive vertical wind speeds.

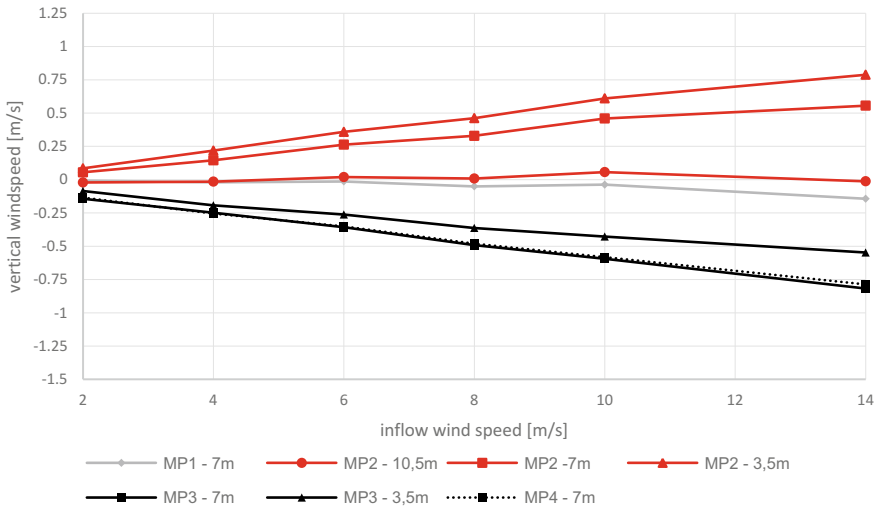


Fig. 11 Vertical windspeed, phase 2, direction 2 (own depiction)

Vertical wind speeds direction 1. In Figs. 9 and 10 vertical wind speeds for direction 1 in phase 1 are displayed. Again, on the x-axis horizontal wind speeds at MP1 in 7 m height are plotted as reference values.

Vertical wind speeds in phase 1 behave in a manner so that the wind flows parallel to the ground. This behavior is the same for all three observed directions.

Vertical wind speed measurements at MP1 at 7 m height are also included. It can be assumed that already at this distance to the obstacle an impact on the wind stream can be identified. The wind is accelerated upwards. Again, this effect can be explained with the principle of continuity. The air has to elude the building in order to avoid congestion.

At MP2 for inflow wind speeds below 3 m/s, the wind speed is accelerated in negative z-direction. Above 3 m/s this effect switches to the opposite and increases with decreasing measuring height above the building.

At MP3 an acceleration in negative z-direction is given at 7 m height while in positive z-direction at 3.5 m height. The same effect as for 7 m also occurs at MP 4 at 7 m height. The effect of acceleration in negative z-direction can be explained by the air sinking back down after the obstacle in order to reach air-pressure equalization.

The acceleration of the wind above the roof can be explained by the stream being compressed and therefore accelerated while passing over the building.

Vertical wind speeds direction 2 and 3. As for horizontal wind speeds, no different behavior for phase 2 in direction 2 or 3 for vertical wind speeds can be interpreted from the measuring results. Hence, only phase 2 results are plotted for direction 2 in Figs. 11 and 12.

For direction 2 the effects are the same as for direction 1, only slightly less distinct.

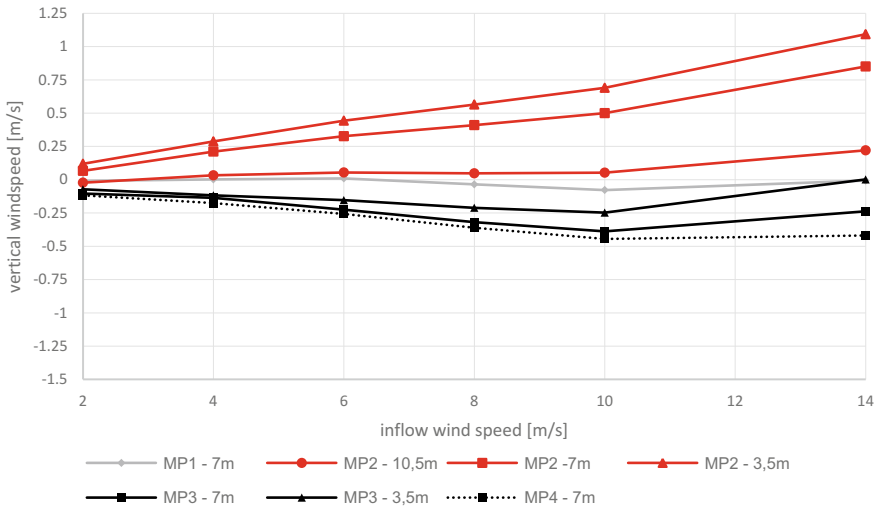


Fig. 12 Vertical windspeed, phase 2, direction 3 (own depiction)

Table 3 Number of available values for horizontal turbulence intensities

Number of measurements	2 m/s	4 m/s	6 m/s	8 m/s	10 m/s	14 m/s
Direction 1—phase 1	395	1118	1923	1151	550	18
Direction 1—phase 2	186	399	680	811	584	69
Direction 2—phase 1	310	960	759	307	73	0
Direction 2—phase 2	182	309	439	315	155	23
Direction 3—phase 1	310	541	348	193	85	2
Direction 3—phase 2	164	269	335	242	104	8

For direction 3 the accelerations in positive-z direction are stronger than in direction 1. For all other measuring points no significant difference in this situation can be identified.

4.3 Horizontal Turbulence Intensity

The horizontal turbulence is defined as usual in common literature (3).

$$Ti = \frac{\sigma}{u} \tag{3}$$

σ stands for the standard deviation, and u for the arithmetic mean over 10 min as defined in Sect. 3.1. Here the values are calculated from one-minute mean values

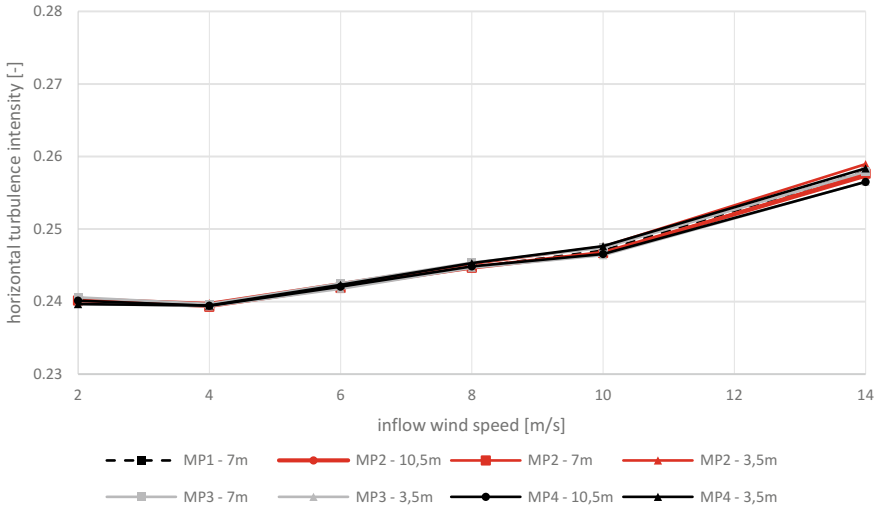


Fig. 13 Horizontal turbulence intensity, phase 1, direction 1 (own depiction)

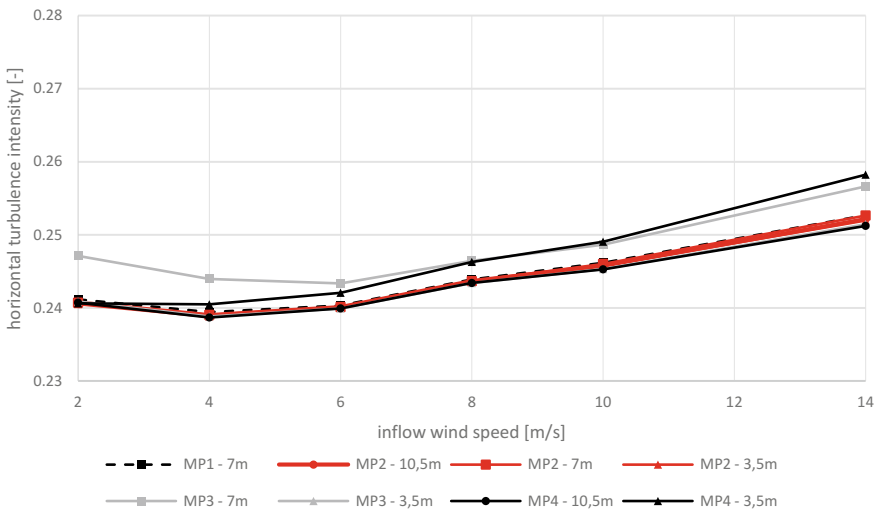


Fig. 14 Horizontal turbulence intensity, phase 2, direction 1 (own depiction)

from the data loggers and it is ignored that those already have standard deviations. The number of available datasets for processing of horizontal turbulence intensities is given in Table 3.

Horizontal turbulence intensities direction 1. In Figs. 13 and 14 the horizontal turbulence intensity for direction 1 phase 1 and 2 is displayed.

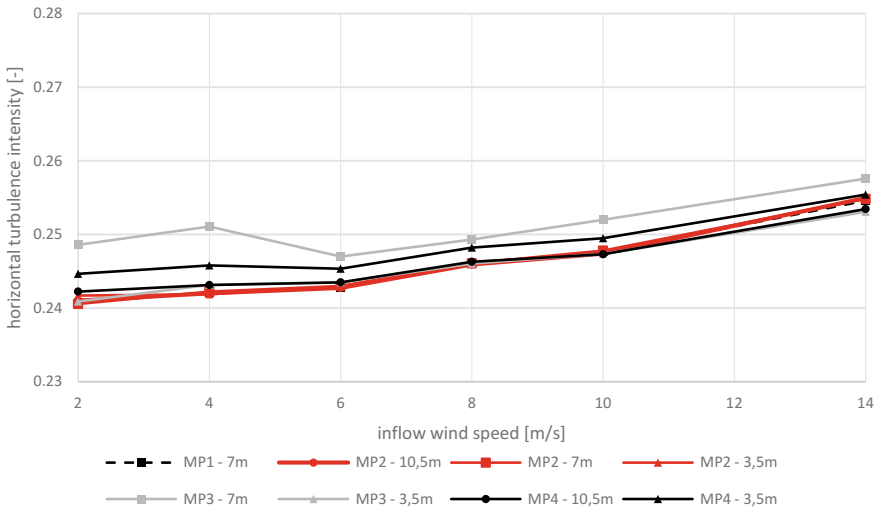


Fig. 15 Horizontal turbulence intensity, phase 2, direction 2 (own depiction)

In phase 1 with increasing inflow wind speed, the turbulence intensity increases. Additionally, no dependency on height can be interpreted for neither direction. In phase 2 for inflow wind speeds between 2 and 4 m/s horizontal turbulence intensity decreases. Above 4 m/s an increase similar to phase 1 is given. In general, horizontal turbulence intensities seem to be lower in case of obstacles in the wind stream, except for MP3 at 7 m height where at every inflow wind speed, an increase of horizontal turbulence intensity can be measured. This can be explained by the occurrence of eddies created at the edge of the building.

The impact of the building on the horizontal turbulence intensity can still be clearly measured at the highest measurements. So, the impact in vertical component of the wind is stronger than the impact on horizontal wind speeds. Also, an impact can clearly be measured at MP4 in 10.5 m height. Which means the effect of buildings on horizontal turbulence intensities is more significant than the impact on wind speeds.

Horizontal turbulence intensity direction 2 and 3. Figure 15 shows the results of turbulence intensity for direction 2 in phase 2. Phase 1 in direction 2 is no different from direction 1, phase 2.

The difference to direction 1 in phase 2 appears to be minimal, except for MP3 in 7 m height where an increase of horizontal turbulence intensity is verified especially for lower wind speeds.

Figure 16 shows results for phase 1 in direction 3.

The very different behavior in comparison to direction 1 cannot be explained within this research paper. It might be due to eddies, but this cannot be verified at this point. Only, the expected increase of horizontal turbulence intensity with increasing inflow speed can be identified.

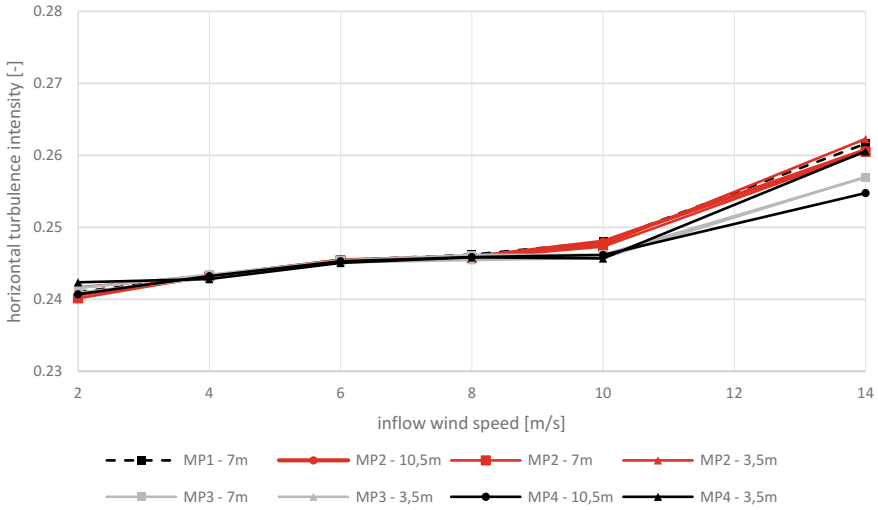


Fig. 16 Horizontal turbulence intensity, phase 1, direction 3 (own depiction)

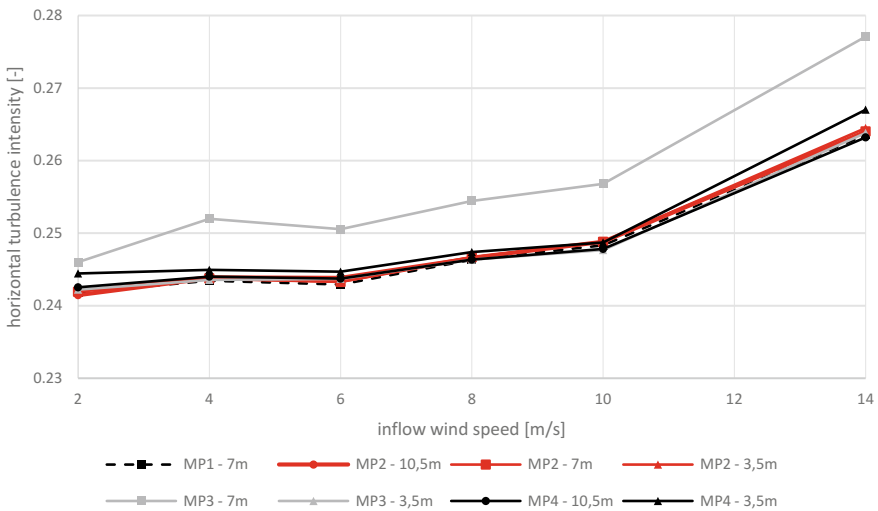


Fig. 17 Horizontal turbulence intensity, phase 2, direction 3 (own depiction)

Horizontal turbulence intensity results of direction 3 phase 2 are displayed in Fig. 17.

In comparison to direction 1, the effects are the same but less distinct, with only one exception at MP3 in 7 m height. At this point a clear increase for all wind speeds is given. Again, this effect comes from air being compressed and accelerated. The number of available datasets for processing of vertical turbulence intensities is given in Table 4.

Table 4 Number of available values for vertical turbulence intensities

Number of measurements	2 m/s	4 m/s	6 m/s	8 m/s	10 m/s	14 m/s
Direction 1—phase 1	392	1116	1922	1151	550	18
Direction 1—phase 2	188	398	674	802	580	69
Direction 2—phase 1	304	955	754	307	73	0
Direction 2—phase 2	174	307	439	312	152	23
Direction 3—phase 1	302	531	345	191	84	2
Direction 3—phase 2	159	264	332	240	104	8

4.4 Vertical Turbulence Intensity

The vertical turbulence intensity is a rather experimental property. The goal of introducing it is to gain insights on the stability of eddies caused by the influence of the building.

This property is inspired by turbulent kinetic energy [7], but rather than generating one property for all directions in space it is tried to focus on solely horizontal effects. This is done with the intention to capture effects on vertical wind speeds that are ignored with the calculation of the typical turbulence intensity. The common definition of turbulence intensity comes from large wind research which operates in heights and horizontal wind speed ranges where vertical effects can for the better part be ignored.

Vertical turbulence intensity herein is defined in the same way as horizontal turbulence intensity defined in Sect. 4.3, with the only difference that vertical wind speeds and standard deviations are used.

In Fig. 18 phase 1 and direction 1 for turbulence intensity are plotted.

In contrast to the horizontal turbulence intensity in phase 1, vertical turbulence intensity decreases with increasing inflow wind speed. This effect is given for all measurements and directions. In absolute values vertical turbulence intensity is clearly higher than the horizontal, even exceeding 1 at times. This effect comes from the fact that values are spread positive and negative around 0 while standard deviations are per definition solely positive.

In Fig. 19 vertical turbulence intensity for direction 1 during phase 2 is displayed.

It can be said that for all directions in phase 2 for the lowest measurement at MP2, the vertical turbulence intensity is clearly lower.

Apart from that, no pattern or tendencies can be interpreted from vertical turbulence intensity plots. All plots seem to be rather chaotic and randomly spread against inflow wind speed. Vertical turbulence intensity with this kind of definition or data, turn out not to be meaningful for wind conditions above flat roof buildings.

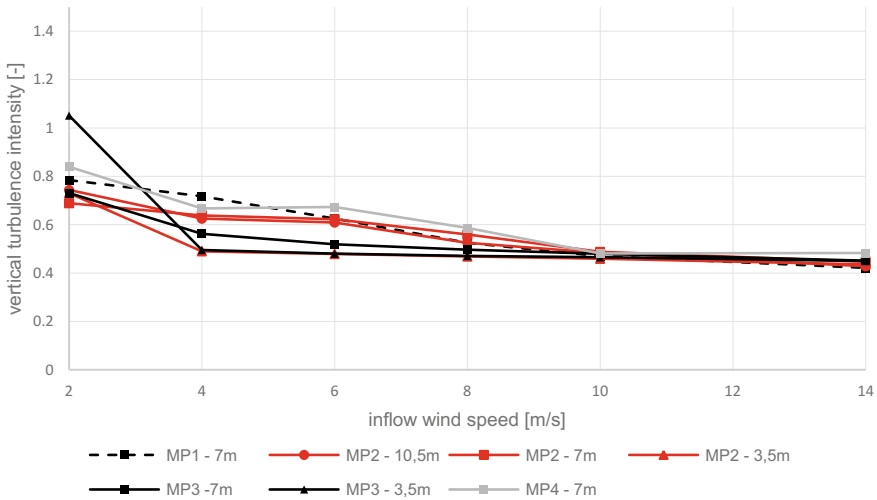


Fig. 18 Vertical turbulence intensity, phase 1, direction 1 (own depiction)

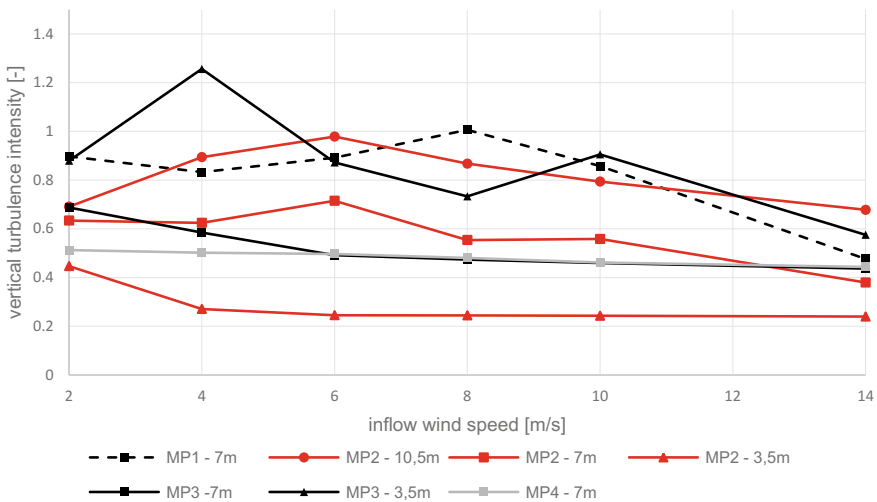
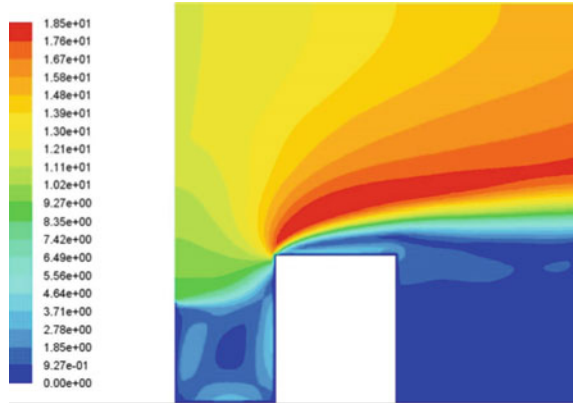


Fig. 19 Vertical turbulence intensity, phase 2, direction 1 (own depiction)

5 Conclusion

All results have been compared to the simulation results of the paper *Two-Dimensional Model of Wind Flow on Buildings to Optimize the Implementation of Mini Wind Turbines in Urban Spaces* [8] and mostly meet with their findings. This applies especially in direction 1 which is the direction in which the simulations were performed.

Fig. 20 Wind speed simulation over flat roof [8]



For all measurements it is found that wind speed increases above the building, as depicted in Fig. 20. This increase also causes a change of direction, which on the other hand leads to an increase of vertical wind speed.

In contrast to horizontal wind speed which increases almost linear with increasing inflow wind speed, vertical wind speeds show a saturating behavior. This leads to the assumption that air layers with same velocities get vertically packed tighter. This causes a higher wind speed gradient orthogonal to wind speed direction with higher wind speeds.

The results also cover with the findings in *The fence experiment—full-scale lidar-based shelter observations* [6], especially the decreasing effect of inflow other than straight.

Concluding from all reliably results (horizontal wind speed, vertical wind speed and horizontal wind speed), an installation of small wind turbines is on flat roof tops of single building is advisable in terms of wind resource. The reasons for that are an increase of power output due to higher horizontal wind speeds and less stress on the machines due to lower turbulence intensities. For free standing, a sufficient hub height and distances to the obstacle have to be respected to avoid shadow zones or highly turbulent areas.

It needs to be respected that all research was performed for one specific building far from any urban surroundings with undisturbed inflow. More research needs to be done to verify obtained results and especially improve the work on vertical turbulence intensity.

References

1. United Nations (2015) Paris Agreement. Paris, United Nations
2. Matlab R2017b (n.d.) Matlab R2017b. The MathWorks, Inc

3. Energiewerkstatt – Technisches Büro zur Förderung erneuerbarer Energie: Lageplan Energieforschungspark Lichtenegg. Friedburg (2017)
4. Tiefgraber, I.C.: Aufbauprotokoll Windmessung SmallWindPower@Home. Friedburg (2017)
5. Elliot D, Infield D (2012) An assessment of the impact of reduced averaging time on small wind turbine power curves, energy capture predictions and turbulence intensity measurements. Wiley Online Library, Glasgow
6. Peña A, Bechman A, Conti D, Angelou N (2016) The fence experiment—full-scale lidar-based shelter observations. Wind Energy Science Discussion, Roskilde
7. Šavli M (2012) Turbulence kinetic energy—TKE. University of Ljubljana, Ljubljana
8. Sáenz-Díez Muro JC, Jiménez EM, Blanco JMB, de la Parte MP, Blanco JF (2010) Two-dimensional model of wind flow on buildings to optimize the implementation of mini wind turbines in urban spaces. University of La Rioja, Logroño

A Detailed Analysis of the Centrifugal Pumping Phenomenon in HAWTs Through the Use of CFD Models



Stefano Mauro , Rosario Lanzafame , Michele Messina 
and Sebastian Brusca 

Abstract The centrifugal pumping, also known as rotational augmentation, is a 3D phenomenon which is of utmost importance in the aerodynamics of HAWTs. A clear physical explanation about the rise and development of this phenomenon is still missing in the scientific literature. Indeed, several empirical approaches have been proposed for taking into account the rotational effects inside 1D design codes. However, at the state, these approaches lead to results, which are quite different amongst each other. In the present paper the authors propose a thorough analysis of the rotational augmentation in an experimental micro HAWT. For this purpose, previously validated CFD 3D models were used. These models were developed using ANSYS Fluent solver with a calibrated RANS transition turbulence model. The post-processing analysis, presented in this paper, demonstrates that the strong increase of the aerodynamic forces is mainly due to the presence of a strong helical vortex which develops in the inner part of the blade. This vortex depressurizes the entire separated layer and it is found to be due to the combined effect of Coriolis and centrifugal forces along with the span-wise pressure gradient. Moreover, the essential contribution of the radial component of the Coriolis force was evidenced in contrast with the fact that this component is usually neglected.

Keywords HAWT · Rotational augmentation · CFD

1 Introduction

The problem of the comprehension and modeling of the rotational augmentation phenomenon in HAWTs is one of the most arduous problem of wind turbine aero-

S. Mauro (✉) · R. Lanzafame · M. Messina
Department of Civil Engineering and Architecture, University of Catania,
Viale A. Doria 6, 95125 Catania, Italy
e-mail: mstefano@diim.unict.it

S. Brusca
Department of Engineering, University of Messina, Contrada Di Dio,
98166 Messina, Italy

dynamics. Moreover, the low Reynolds number flows, which characterizes the mini and micro rotors, represents a further complication. This is due to the fact that the 3D phenomena become ever more important as stall delay and rotational augmentation are strictly related to the onset of the stall and, in turn, the low Reynolds number flows are notoriously more sensitive to flow separation. For this reason an accurate physical comprehension of the complex 3D flow over rotating blades is of utmost importance, specifically in all those conditions in which the separation is going to occur. Therefore, although the centrifugal pumping is a phenomenon which can arise in any HAWT, the mini and micro rotors are certainly more influenced, also because they use passive stall regulation for power control.

The reviewed literature [1–14] hypothesizes that the rotational augmentation is due to three essential contributions: the centrifugal force, the Coriolis force and the span-wise pressure distribution along the blade. These contributions act in the suction side of the blade therefore generating a complex radial flow, in incipient and deep stall conditions. This results in a further depressurization of the suction side which is much higher than in the case of 2D flows. Thus the aerodynamic forces are strongly augmented as well.

Most of the efforts in the literature [1, 3, 9, 13] were made in order to quantify the influence of the centrifugal pumping on the airfoil characteristics of rotating blades. This was of utmost importance for the 1D design codes in which simplified models of the 3D phenomena are necessary. However, from one hand the results agreed with the fact that the maximum augmentation is related to the inner part of the blade, from the other hand they are in contrast with one another in the methodology and quantification of the phenomenon. Indeed, most of the authors [2, 4, 9] emphasize the effect of the stream-wise component of the Coriolis force which would reduce the adverse pressure gradient in the chord-wise direction. Substantially, the dynamic of the rotational augmentation is explained as follows: the centrifugal force along with the span-wise pressure gradient acts within the boundary layer and triggers the onset of a radial flow. The Coriolis force, which appears as a consequence of the radial flow and is directed in the stream-wise direction, would reduce the adverse pressure gradient and thus the onset of the stall. However, the numerous attempts to model the rotational augmentation have demonstrated conflicting results [5, 10]. Even the most advanced models, based on the solution of the boundary layer equations [2, 11], have shown conflicting results and they are unable to provide reliable generalized solutions. Therefore, the breakdown of the boundary layer analysis under separated flow conditions is probably an inherent problem with these methods. This suggests that the philosophy, which underlies these models, may not be correctly representing the real flow physics. In fact, the considerations arising from the results of the present work suggest that the entire separated layer is somehow subjected to the rotational forces and thus the simple integration of the boundary layer equations is not sufficient for explaining and, even more so, for modeling the centrifugal pumping phenomenon.

The advent of modern CFD techniques has allowed the researchers to better analyze and quantify the rotational augmentation [1, 3, 8, 11, 13–16]. Based on the results obtained in previous work by the authors [3, 15, 16], the present paper attempts to provide a global physical explanation of the centrifugal pumping phenomenon. For

this purpose, a previously validated CFD 3D model [16] was used in order to extensively analyze an experimental micro rotor which was designed, built and tested in the subsonic wind tunnel owned by the University of Catania. In doing so, the aerodynamic coefficients were extrapolated for eleven radial stations and for a wide range of wind and rotational speed. Moreover, streamlines, pressure, velocity contours and pressure coefficients were obtained at different radial stations and operating conditions. The analysis of the results, which will be presented hereinafter, demonstrated the development of a coherent helical structure in the inner part of the blade at local AoAs (Angle of Attacks) between $10\text{--}15^\circ$ and $55\text{--}60^\circ$. This helical vortex generated a strong flow acceleration and, as a consequence, a strong depressurization of the suction side of the rotating blade compared to simple 2D flows. Therefore, the helical vortex strongly modified the flow-field over the blade causing a partial or total reattachment of the entire separated layer. Finally, the strong flow acceleration and the related depressurization was the most responsible factor for the augmentation of the aerodynamic forces.

In order to verify the source which triggered the onset of the helical vortex two further analyses were carried out. First of all, the forces which act within the separated layer were extrapolated and compared to the radial flow velocity component. The accordance between the radial velocity trend and the radial forces trend evidenced the essential contribution of the radial component of the Coriolis force compared to the centrifugal force and to the stream-wise component of the Coriolis force. Specifically, it was found that the radial component of the Coriolis force is the one that contributed in a decisive way to the onset of the helical vortex in the inner blade.

To further confirm this assumption, CFD 3D simulations of a fixed blade of the rotor was carried out. In this simulation, the blade had exactly the same geometrical features of the experimental rotor blade. The flow-field boundary conditions were set in such a way to reproduce the rotation. Specifically a complex UDF (User Defined Function) was implemented in order to obtain a velocity profile along the blade equal to the one generated by rotation. In the same UDF, two momentum sources were added for reproducing the centrifugal force and both the components of the Coriolis forces (radial and stream-wise components). The results demonstrated a fluid dynamic behavior surprisingly similar to that of a rotating blade. Moreover, this simulation allowed for the possibility to evaluate the contributions of the rotational effects separately. The results showed that the helical vortex in the inner blade and its strong effects on the flow-field and pressure distribution appeared only when the momentum due to the radial component of the Coriolis force was activated in the UDF.

Table 1 Experimental rotor geometrical features

Number of blades	3
Blade airfoil	NACA 4415
Rotor diameter	0.225 [m]
Hub diameter	0.054 [m]
Rotational speed	500–4500 [r/min]
Flow speed	5–30 [m/s]
Tip speed ratio	1–7
Chord	Variable
Twist	Variable

2 Numerical Models

2.1 CFD 3D Rotor Model

The CFD modeling used in this paper was widely presented and validated in previous works by the authors [17, 18]. For this reason, only a brief summarization is reported. The modeling procedure was firstly implemented and validated for the widely known NREL PHASE VI HAWT [18]. The 3D model was generated using ANSYS Fluent solver with a steady state, pressure based, coupled solver. Due to the low operating Reynolds number, the SST transition turbulence model by Menter [19, 20] was used. The transition turbulence model by Menter was specifically calibrated for wind turbines applications with excellent results [21].

Based on this experience, a micro HAWT rotor was designed for testing in the subsonic wind tunnel owned by the University of Catania. At the same time, a CFD 3D model of the micro rotor was developed using the same procedure used for the PHASE VI rotor and thus validated with very satisfactory results [17]. The experimental rotor was triple bladed, twisted and tapered, built with a 3D printer. The characteristics of the rotor are evidenced in Table 1 while in Table 2 the CFD 3D model setup is summarized. In Fig. 1 a detail of the polyhedral mesh, used for the experimental micro rotor modeling, is shown.

In order to obtain a full set of data for the in-depth analysis of the centrifugal pumping phenomenon, the experimental rotor was simulated and fully post-processed for rotational speeds between 500 and 4500 r/min, with a step of 500 r/min and for flow speeds between 5 and 30 m/s with a step of 5 m/s. Moreover, 2D CFD simulations of the NACA 4415 airfoil were carried out in such a way to have a meaningful 2D reference for 2D–3D flow-field comparison. The NACA 4415 airfoil was simulated for Reynolds numbers between 10,000 and 80,000 which were the minimum and the maximum rotor operating Reynolds number.

Table 2 CFD 3D model settings

Grid elements	~900,000
Grid features	Polyhedral cells $y^+ < 1$ Skewness < 0.85
Turbulence boundary conditions	Tu = 0.1 TVR = 10
Solution methods	Steady state Pressure based Coupled solver
Discretization methods	Least squares cell based method for gradients Second order upwind discretization for equations
Rotational model	Moving reference frame (MRF)
Turbulence model	Transition SST (Menter [19, 20])

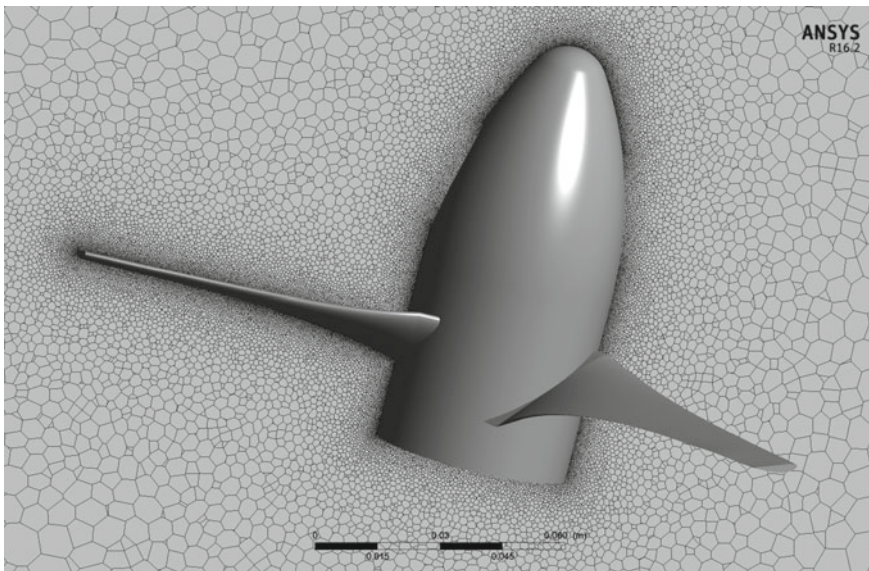


Fig. 1 Polyhedral mesh for the experimental micro rotor

2.2 CFD 3D Fixed Blade Model

As previously described in the introduction, in order to single out the contribution of the span-wise pressure gradient, Coriolis and centrifugal forces to the onset of the rotational augmentation, a CFD 3D model of a single blade, with identical geometrical features of the micro rotor blade, was implemented. Furthermore, the boundary conditions were set in such a way to reproduce the effect of rotation. Substantially, the idea of simulating a fixed blade allowed for a virtual separation of the single

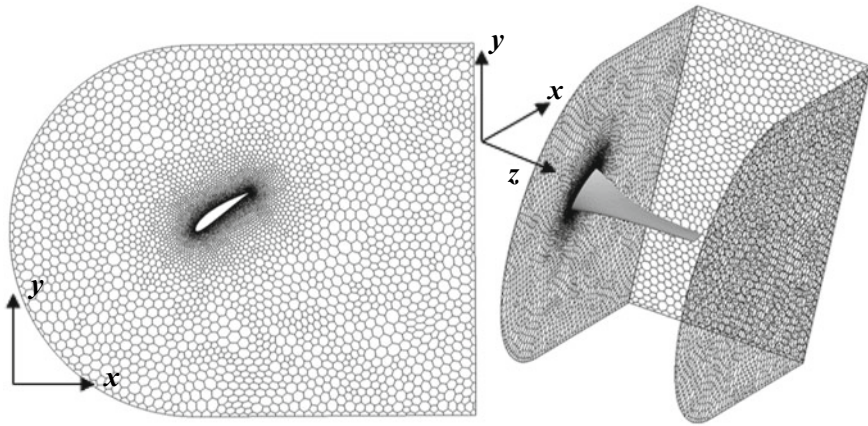


Fig. 2 Computational domain and grid details for the fixed blade CFD 3D model

contribution of the span-wise pressure gradient, the momentum due to centrifugal force and the momentum due to Coriolis force, which was further decomposed into a radial component and a stream-wise component. In this way, although the simulation of the fixed blade led to the modeling of a fluid dynamic behavior which was clearly different from that of a rotating blade, the global effect of the single contribution of the rotational forces on the onset on the centrifugal pumping phenomenon could be easily evaluated as will be shown hereinafter.

The CFD 3D model, in this case, was developed generating an extruded C-type domain. The mesh and the solver settings were equal to those used for the 3D model of the rotor (Table 2). Therefore the blade had the same grid refinement with a polyhedral mesh consisting of approximately 300,000 elements. In Fig. 2 details of the computational domain, reference frame and mesh are presented.

In order to simulate the rotation effects in the fixed blade domain, a complex UDF was structured, compiled in C language and finally interpreted by the Fluent solver. The span-wise pressure gradient is generated by the span-wise velocity gradient. Therefore, according to the reference frame in Fig. 2 the velocity profile components at inlet were implemented in the UDF as so:

$$V_x = \omega \cdot (z + 0.027) \quad (1)$$

$$V_y = V_w \quad (2)$$

$$V_z = 0 \quad (3)$$

In (1) ω is the angular speed of interest of the rotor, V_w is the undisturbed flow speed at inlet and the term $(z + 0.027)$ is the radial coordinate with an offset to take into account the distance of the blade from the hub. Therefore, the inlet velocity

profile, which reproduces the profile due to rotation, is the vector composition of V_x and V_y . The UDF, structured as so, allowed for an easy change of the velocity profile at inlet according to the rotor operating condition to be simulated.

In order to add the centrifugal force contribution, a momentum source in the z direction was implemented within the same UDF. The momentum, equal to the one generated by the centrifugal force, was imposed inside the entire separated layer. The momentum acted and linearly increased in the z direction (Fig. 2) as so:

$$M_{z,centr} = \omega^2(z + 0.027)\rho \quad (4)$$

where $M_{z,centr}$ is the momentum source in the z direction, ρ is the air density, thus the $M_{z,centr}$ unit is $[N/m^3]$ as required by Fluent solver.

The Coriolis contribution was finally implemented in the same UDF, starting from the widely known expression of the Coriolis acceleration:

$$\mathbf{a}_c = 2\boldsymbol{\omega} \wedge \mathbf{V}_r \quad (5)$$

According to the reference frame in Fig. 2, the local relative velocity \mathbf{V}_r with respect to the blade can be decomposed in the Cartesian directions x , y , z . So, while V_{ry} does not generate Coriolis acceleration components, V_{rx} and V_{rz} do generate acceleration components in z and x direction respectively. Thus a momentum source in z direction and a momentum source in x direction must be implemented in order to take into account the Coriolis contribution. The momentum sources were:

$$M_{x,cor} = 2\omega w\rho \quad (6)$$

$$M_{z,cor} = -2\omega u\rho \quad (7)$$

where $M_{x,Cor}$ is the momentum source due to the Coriolis acceleration in the x direction, $M_{z,Cor}$ is the momentum source due to the Coriolis acceleration in the z direction, u and w are the local velocity components in x ($u = V_{rx}$) and z ($w = V_{rz}$) direction respectively. The negative in (7) is necessary to consider that ω is in the clockwise direction. ρ is again the air density so as the unit of the momentum source is $[N/m^3]$ as well.

With such a UDF, modifying the angular speed ω , the effects of the centrifugal and Coriolis forces on the flow-field, for different rotational conditions can be simulated. Furthermore, it is possible to switch the use of the UDF in Fluent, individually simulating the effect of the velocity gradient, that of the centrifugal force and that of the Coriolis force or, moreover, all the effects simultaneously.

3 Results and Discussions

3.1 2D–3D Aerodynamic Coefficient Comparison

In this section the calculated 3D CFD lift and drag coefficients are compared to the 2D CFD data of the NACA 4415 airfoil in order to show the great influence of rotation on the forces which act on the blades. This analysis was made on eleven radial stations (from $r/R = 25\%$ to $r/R = 95\%$) and for the entire range of simulated rotor operating conditions (n between 500 and 4500 r/min and V_w between 5 and 30 m/s). In this way a very large set of AoAs was studied. The CFD 2D data were instead calculated for $10,000 < Re < 80,000$.

For the extrapolation of the 3D aerodynamic coefficients the methodology proposed by Johansen et al. [13] was used. The axial and tangential velocities were post-processed in cylindrical sections at each radial stations in order to calculate the local flow angle. Once the local flow angle was obtained, knowing the twist angle, the AoAs were calculated. The local normal and tangential loads were post-processed as well and subsequently integrated along the sectional airfoil profile. Then the lift and drag forces were obtained and non-dimensionalized in order to evaluate the aerodynamic coefficients at the correspondent AoA [16].

In Fig. 3 the calculated 3D lift and drag data are compared to the 2D simulation results. As can be seen, the 3D lift coefficients clearly follow those 2D at low and high AoAs, that is in attached ($0^\circ < \text{AoA} < 10^\circ$) and in fully separated ($\text{AoA} > 60^\circ$) flow conditions. This indicates that in these conditions the rotational effects are not influencing the flow-field so much. For $\text{AoA} > 10^\circ$, the rotational effects gradually become predominant with maximum C_l values between 30° and 40° in the inner blade region ($25\% < r/R < 57\%$). The maximum C_l is located in the inner blade, at $r/R 38\%$ with a value of 1.98 at $\text{AoA} = 36.5^\circ$. However, all the inner blade experiences strong lift augmentation and the peaks reduces and moves towards lower AoAs as the radial position increases. The rotational augmentation effect gradually decreases as the radial position increases. Finally, at high radial positions ($r/R > 88\%$) the tip effects prevail and the 3D lift coefficient becomes lower than the 2D. Globally, the data show a well-defined trend that highlights three area of influence: the inner blade, up to $r/R 57\%$, where the rotational augmentation reaches the maximum effects; the medium blade, $57\% < r/R < 88\%$, where the rotational augmentation gradually decreases and finally disappears; the outer blade, $r/R > 88\%$, where the widely known tip effects become predominant and the lift coefficient falls below the 2D values.

Similar considerations can be made on the C_d trend in Fig. 3. The inner blade confirms to be the area where the effects of the rotational augmentation are higher. However, the differences with the 2D data are much smaller and located at higher AoAs compared to the lift coefficient. A possible explanation for this is related to the fact that the rotational augmentation acts by increasing the global aerodynamic resultant. The strong change in the pressure distribution over the suction side, due to rotation, modifies the orientation of the aerodynamic resultant. It is found that in 3D conditions the resultant is oriented in such a way to provide higher contribution to lift

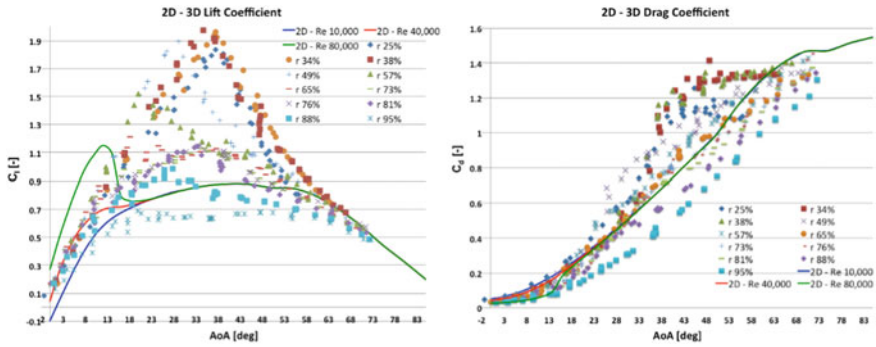


Fig. 3 2D–3D aerodynamic coefficient comparison

force than to the drag force, compared to the simple 2D condition. Therefore, the lift coefficient is much more augmented than the drag coefficient up to 40–42° of AoA. As long as the AoA increases, however, the contribution to the drag unavoidably increases due to geometrical reasons but, at the same time, the rotational augmentation effect is going to reduce. Therefore, the 3D drag coefficient is finally less influenced by the rotational effects.

In Fig. 4 the calculated 3D lift and drag coefficient distribution at a radial station $r/R = 34\%$, parameterized with respect to the rotational speed, is shown. It is remarkable that the data are compact and follow a precise trend that does not depend on rotational speed. For example, the same C_l peak is reached at $AoA \sim 37^\circ$ for a combination of $n = 1500 \text{ r/min}$ and $V_w = 10 \text{ m/s}$, $n = 3000 \text{ r/min}$ and $V_w = 20 \text{ m/s}$, $n = 4500 \text{ r/min}$, $V_w = 30 \text{ m/s}$. These combinations lead to the same tip speed ratio. The above indicates that the 3D aerodynamic coefficient trends do not depend on Reynolds number either, as instead happens in 2D case. Furthermore, this is an unexpected result because one expects that the higher the rotational velocities are, the higher the rotational augmentation will be. Indeed, as the centrifugal force increases with ω^2 , according to the literature hypotheses, higher rotational speed should lead to higher rotational augmentation. The charts in Fig. 4 demonstrated that this supposition is incorrect. Therefore, in the authors’ opinion, there must be a precise imbalance of centrifugal force, Coriolis force and span-wise pressure distribution which leads to the same rotational effects in the inner blade, depending only on the AoA. The simple supposition of a radial flow, which develops along the suction side of the rotating blade, is not sufficient to explain the particular behavior evidenced in Fig. 4. In the next section, the post-processing analysis demonstrates that the development of a helical vortex in the inner blade, which is triggered by the combined action of the radial component of the Coriolis force with the other rotational contributions, is the most responsible factor for the onset of the rotational augmentation.

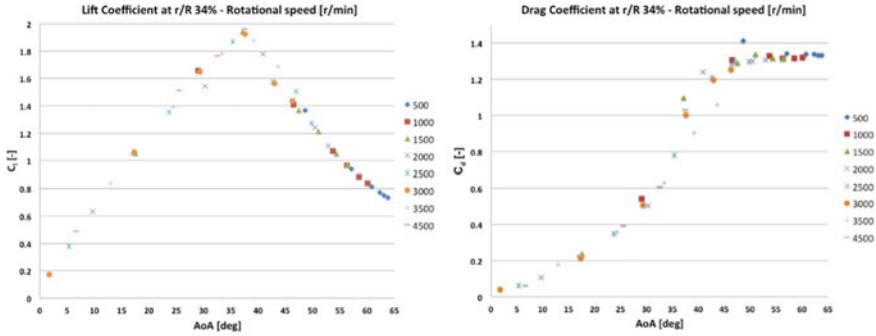


Fig. 4 3D lift and drag coefficients as a function of rotational speed at $r/R = 34\%$

3.2 2D–3D Post-processing Analysis

In order to try to clarify the dynamic of the rotational augmentation phenomenon and to find an explanation for the interesting trend of the aerodynamic coefficients showed in Figs. 3 and 4, in this section a thorough post-processing analysis of the CFD simulations of the experimental micro rotor is presented. Specifically, a condition related to the maximum lift augmentation, at medium AoAs ($\sim 37^\circ$) and r/R 34%, was analyzed. The results were compared to the 2D simulations of the NACA 4415 airfoil, at equal Reynolds number and AoA, in order to demonstrate how the flow-field was influenced by rotation. It must be specified that the CFD 2D simulations were carried out using a unitary chord length of 1 m while the sectional chord of the 3D blade was only few centimeters. For this reason the inlet flow speed in 2D was set in such a way to have equal Reynolds numbers.

As aforesaid, different rotor operating conditions which led to similar sectional 3D AoAs, and thus to similar tip speed ratios, presented a very comparable fluid dynamic behavior in terms of flow-field and forces augmentation [22]. For this reason only one of the conditions cited in the previous section is shown in this paper. This was the condition $V_w = 10$ m/s and $n = 1500$ r/min. In this condition the 3D sectional AoA at r/R 34% was approximately 37° and the local chord Reynolds number was 22,000. Therefore the data were compared to the 2D simulation at $Re = 22,000$ and $AoA = 37^\circ$. In Table 3 details of the extrapolated data are presented.

In Table 3 the strong augmentation of lift and drag coefficients is evident. The 3D lift coefficient is more than twice the 2D one but the force augmentation regards the entire resultant of the aerodynamic force as the drag is increased as well. Very similar results were obtained at $V_w = 10$ m/s, $n = 3000$ r/min and $V_w = 20$ m/s, $n = 4500$ r/min, $V_w = 30$ m/s. Therefore, only the local AoA and the consequent particular flow-field condition, leads to the generation of a phenomenon which, acting in the inner blade, determines a force augmentation of such strength.

In Fig. 5 the 3D–2D comparison of the surface streamlines and pressure coefficient (C_p) trend for the condition presented in Table 3 is shown. It is clear how the rotation

Table 3 3D extrapolated data at r/R 34% and comparison with 2D

	CFD 3D	CFD 2D
Flow speed [m/s]	10	–
Rotational speed [r/min]	1500	–
Radial station [%]	34	–
AoA [deg]	37.2	37
C_l [–]	1.92	0.87
C_d [–]	1.1	0.66
Reynolds number [–]	22,000	

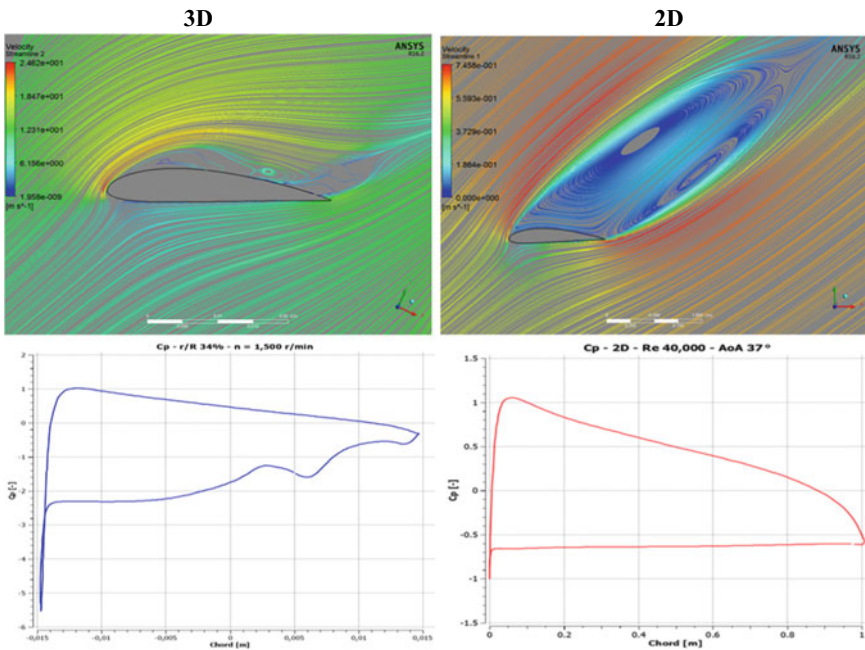


Fig. 5 3D–2D surface streamlines and pressure coefficient (C_p) comparison at r/R 34%

modifies the flow-field. All the separated area, which in 2D generates two counter-rotating vortices, is subjected to the rotation effects which push down and flatten the stall vortices. Such a drastic effect is clearly expressed by a strong depressurization of the suction side of this part of the inner blade as can be evaluated in C_p charts in Fig. 5. While the pressure distribution on the pressure side is almost the same in both 2D and 3D conditions, only the suction side is affected by such a strong depressurization. The pressure coefficient reaches a value of -6 near the leading edge. However, the depressurization is evident in the entire chord-wise direction as the 3D C_p value is below -1 for the largest part of the chord. Furthermore, the rotation induces a strong flow acceleration near the leading edge.

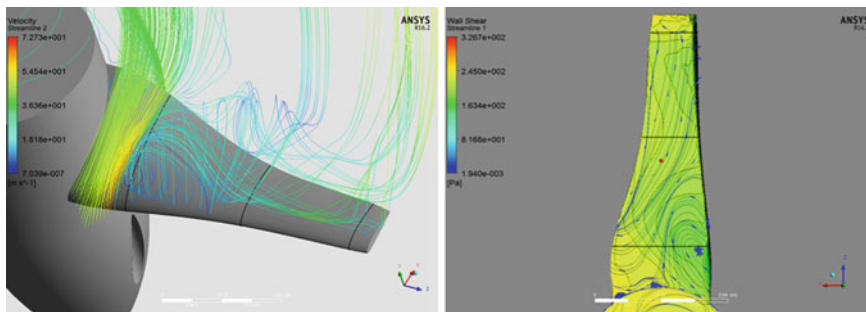


Fig. 6 3D streamlines at r/R 34% (left) and pressure contours and wall shear streamlines on suction side (right)

As evidenced in Fig. 6 (left), a 3D helical structure develops from the inner blade. The swirling structure is evidently responsible for the flow acceleration and, consequently, for the strong depressurization of the suction side. Therefore, the rotational forces must act with a precise balance, tangling the flow in a helical structure and, as a consequence, the flow strongly accelerates and depressurizes the entire separated layer. It is also interesting to notice that the helical structure is superimposed to an intense radial flow, directed toward the tip, which is in close proximity to the blade surface. The flow at a certain distance, higher from the blade, is instead clearly deflected toward the hub. This is an unexpected result as in the literature only the radial flow directed toward the outer blade is taken into account. The helical vortex, once detached from the inner blade, develops all the way up to mid-blade, where leaves it.

The above is confirmed in Fig. 6 (right) where wall shear streamlines show the onset of the helical vortex in the lower boundary layer near r/R 34% section. Furthermore, the depressurization generated by the helical structure is demonstrated by the pressure contours, which clearly follow the wall shear streamlines. Therefore, a big portion of the inner blade is subjected to a very strong depressurization. Thus the aerodynamic forces are considerably augmented. The generation of the helical vortex in the inner blade is therefore to be considered the most responsible factor for the rotational augmentation.

It is meaningful to demonstrate the differences between the flow-field at r/R 34% and at r/R 65%. In Table 4, the comparison between 3D data, extrapolated at r/R 65%, and the correspondent 2D is shown. Despite the fact that, at medium blade (r/R 65%), the centrifugal and Coriolis forces are certainly higher, the increase of the aerodynamic coefficient is considerably reduced. The absence of a helical structure leads to a 3D flow-field similar to the 2D one, as reported in Fig. 7. A strong radial flow is however present close to the blade surface, while the upper separated area is almost comparable to 2D. The rotational augmentation here is considerably lower. Moreover, from the 2D–3D C_p comparison in Fig. 7, the pressure distribution appears to be truly similar and it is typical of a fully stalled condition. Only a higher depressurization is

Table 4 3D extrapolated data at r/R 65% and comparison with 2D

	CFD 3D	CFD 2D
Flow speed [m/s]	10	–
Rotational speed [r/min]	1500	–
Radial station [%]	65	–
AoA [deg]	30	30
C_l [–]	1.05	0.83
C_d [–]	0.53	0.49
Reynolds number [–]	25,000	

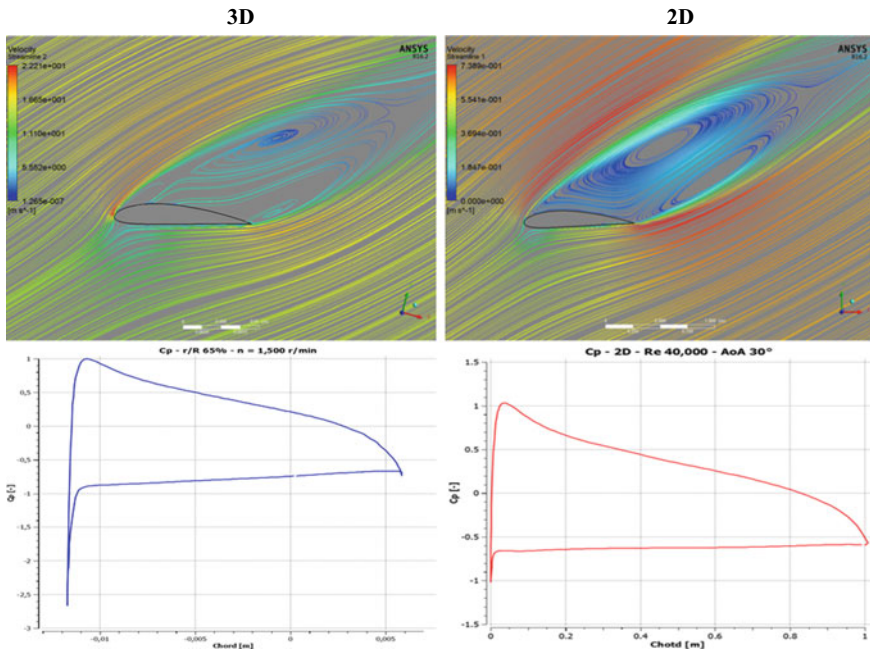


Fig. 7 3D–2D surface streamlines and pressure coefficient (C_p) comparison at r/R 65%

detectable in 3D, near the leading edge, where the C_p is below -2 . Then, the pressure distribution shows a slightly lower trend than in 2D which justifies the small increase of the lift and drag coefficients. In the condition presented above, is evident that the only presence of an intense radial flow is not sufficient to trigger a strong increment of the aerodynamic resultant.

In Fig. 8 (left) the streamlines and pressure distribution emphasizes the fact that, in the area in which the helical vortex is present, a strong depressurization occurs over the blade. This is further confirmed in Fig. 8 (right) where the pressure contours, in a section perpendicular to the blade, highlight the fact that the areas in which pressure is lower are exactly the area where helical vortices develop, that is approximately

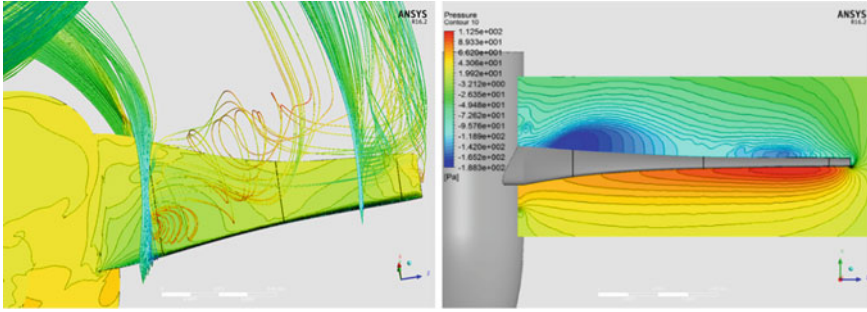


Fig. 8 Pressure contours on rotor surface with 3D streamlines (left) and pressure contour in a section perpendicular to the blade (right)

at r/R 34%. The pressure distribution on the pressure side is instead evidently quite regular.

3.3 Force Analysis in the Separated Layer

In Fig. 6 it is evidenced that at a certain axial distance from the blade, the flow is deflected toward the hub while, in close proximity to the blade, the flow is essentially radially directed toward the tip. This is somehow in contrast with the idea that the centrifugal pumping is simply related to a radial flow directed from inner to outer blade. Moreover, this means that in the blade proximity the forces directed toward the tip prevail while at a certain axial distance there must be strong forces directed toward the hub. Thus, it seems that it is just the reversal of the forces, and the shear related to it, that trigger the onset of the helical vortex with all the aforementioned consequences like flow deflection, strong depressurization and finally rotational augmentation. In order to demonstrate these assumptions, the radial forces acting at different chord positions are analyzed hereinafter and thus compared to the radial velocity component trend for the operating condition reported in the previous section (Table 2).

In order to analyze the forces in a rotating frame of reference, the equation of motion must be written in cylindrical coordinates [22] where θ is the azimuthal direction, r the radial direction, y the axial direction and ω the rotational speed. In such a frame of reference, the rotational forces per unit mass can be decomposed in the azimuthal, radial and axial direction as follows:

$$F_{\vartheta} = F_{Cor-\vartheta} = 2\omega v_r \quad (8)$$

$$F_r = F_{centr} + F_{Cor-r} = \omega^2 r + 2\omega v_{\vartheta} \quad (9)$$

$$F_y = 0 \quad (10)$$

where $\mathbf{F} = (F_\theta, F_r, F_y)$ and $\mathbf{v} = (v_\theta, v_r, v_y)$ are the external force vector and the local relative velocity vector, respectively. Furthermore, the pressure gradient force and the shear force play an essential role in the rotational augmentation dynamics. While F_{centr} is always directed toward the tip, $F_{\text{Cor}-\theta}$ in (8) and $F_{\text{Cor}-r}$ in (9) depend on the versus of v_r and v_θ respect to ω .

In order to extrapolate the radial component of the Coriolis force ($F_{\text{Cor}-r}$), the circumferential velocity profile v_θ is obtained using ANSYS Turbo-post. All the data are calculated along a line, which is orthogonal to the blade at r/R 34% and at three chord positions: near the leading edge (**L**), at a medium chord (**M**) and near the trailing edge (**T**). The radial velocity component v_r and the centrifugal force are obtained as well. In the charts of Fig. 9, the radial Coriolis force, the sum of the radial Coriolis and Centrifugal force (F_r) and the velocity v_r trends are reported. Only the data related to the suction side are shown because the suction side is where the rotational augmentation takes place. The forces are per unit mass thus having acceleration dimension. Clearly, the centrifugal force is a constant at each radial station thus causing a shift in the sum, as is evident in the charts. In Fig. 9, it is clear that the effects of the radial component of the Coriolis force $F_{\text{Cor}-r}$ are of the utmost importance, above all near the leading edge. Indeed, calculating the ratio between the maximum $F_{\text{Cor}-r}$ and F_{centr} a value of 4.3 is obtained. A similar value can be obtained if the ratio between the maximum $F_{\text{Cor}-r}$ and $F_{\text{Cor}-\theta}$ is calculated. The fact that the radial component of the Coriolis force, in this condition, is more than four times the centrifugal and azimuthal component of the Coriolis forces indicates that it is of crucial importance to take into account $F_{\text{Cor}-r}$ when analysing the rotational augmentation.

In detail, near the leading edge (Fig. 9 L) the radial component of the Coriolis force prevails and strongly accelerates the flow toward the hub. Correspondently, the radial velocity is entirely negative. Although in the lower boundary layer, low or slight negative values of v_θ cause low values of $F_{\text{Cor}-r}$, the presence of an upper intense acceleration increases the shear and the flow completely deflects toward the hub. At medium chord and at trailing edge (Fig. 9 M and T) the radial flow in the lower layers is instead forced toward the tip due to the effects of both radial forces and strong pressure gradient. The flow here is guided by the pressure gradient that causes a recirculation with negative v_θ in the blade proximity. This pushes the flow to positive radial direction with the help of both radial forces ($F_{\text{Cor}-r}$ changes its sign due to the reversal of v_θ). However, at a certain distance from the blade, the net radial force becomes negative as v_θ becomes positive. This has a marked effect on the radial velocity that quickly decreases both in M and T. Therefore, it can be assumed that, while at the leading edge the strong radial component of the Coriolis force accelerates the flow toward the hub, as long as a fluid element travels in the stream-wise direction, the combined effect of the pressure gradient and azimuthal flow deceleration, (or reversion) implies a change of the force direction in the lower layers that finally leads to a strong positive radial velocity toward the tip. The shear, due to the sudden change of radial velocity direction, seems to guide the onset of the helical vortex and ultimately the rotational augmentation.

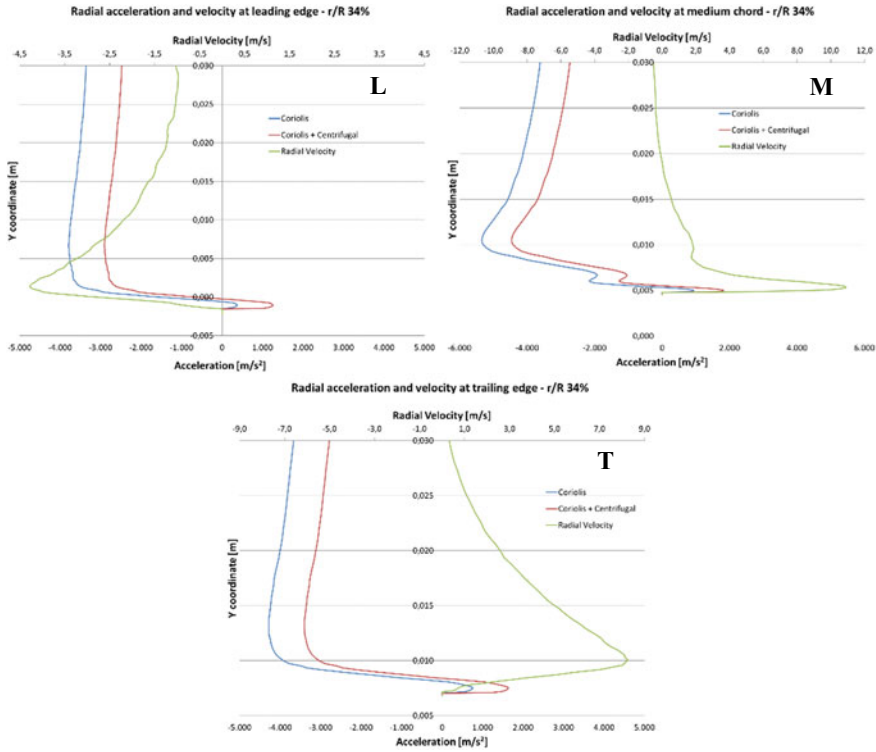


Fig. 9 Radial forces and Velocity at r/R 34% for $V_w = 10$ m/s and $n = 1500$ r/min

Thus, from a general point of view, the rotational augmentation phenomenon can now be summarized. In Fig. 10 a clear representation of the helical vortex dynamics is shown. Essentially, a fluid element, approaching the leading edge at the inner blade, begins to be subjected to the rotational forces. In the upper separated layer, the high values of the azimuthal velocity component v_θ , lead to high negative radial component of the Coriolis force. The net radial force F_r is thus negative, as evidenced in Fig. 10 by the red vector. For this reason, the flow is definitely deflected toward the hub. As long as the fluid element travels in the stream-wise direction, it is decelerated due to the pressure gradient and the strong low pressure at the leading edge. This reduces v_θ and finally F_{Cor-r} . Indeed, in the lower layer, where v_θ is minor or negative due to the suction and recirculation toward the leading edge, the centrifugal force prevails or is enforced when F_{Cor-r} is positive. Thus F_r becomes positive as it is denoted by the blue vector in Fig. 10. Here the flow is deflected toward the tip. The tilting of the radial force generates a strong vertical shear, which triggers the vorticity and helicity production in the separated layer and ultimately the onset of the helical vortex. Once the helical vortex develops, the incoming flow is further accelerated and a strong suction is produced.

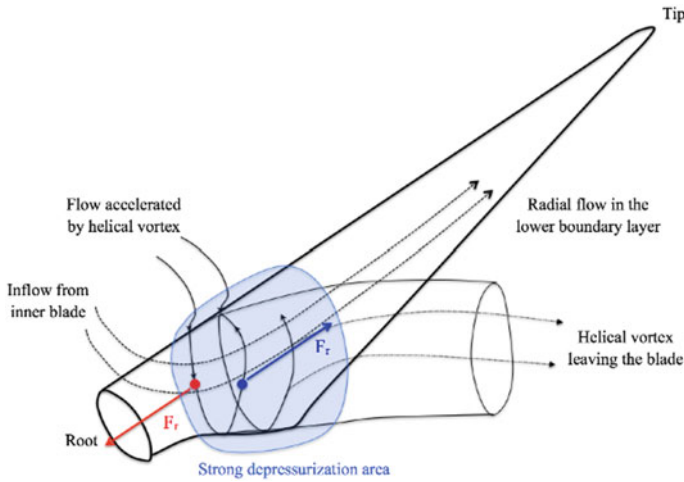


Fig. 10 Representation of the helical vortex dynamics

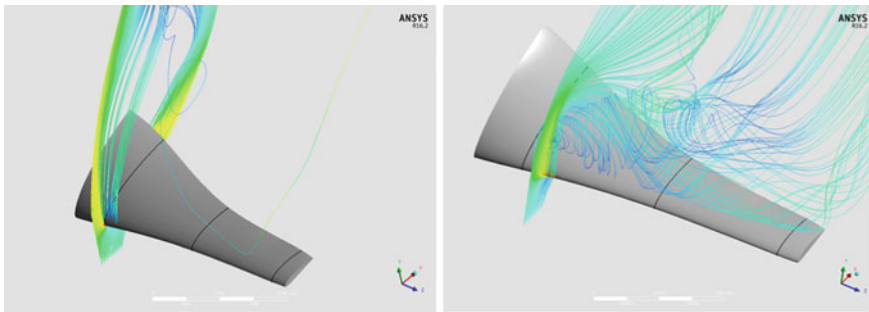


Fig. 11 3D Streamlines at r/R 34% for C^- (left) and C^+ simulations

3.4 Fixed Blade Simulation Results

A further confirmation of the importance of the radial component of the Coriolis force is obtained by modelling a fixed blade according to what is mentioned in Sect. 2.2. The advantage of simulating a fixed wing, replicating the effects of rotation, is that the hub influence is eliminated as well, as it can be a source of uncertainty. Moreover, the single rotational effects can be modelled separately, thus highlighting their weight on the augmentation. Indeed, the blade was firstly simulated by imposing the span-wise velocity gradient and the momentum due to centrifugal force and chord-wise component of the Coriolis force (named as simulation C^-). Then the momentum of the radial component of the Coriolis force was added (named as simulation C^+). The comparison of the results are really interesting and are shown in Figs. 11, 12, 13 and 14.

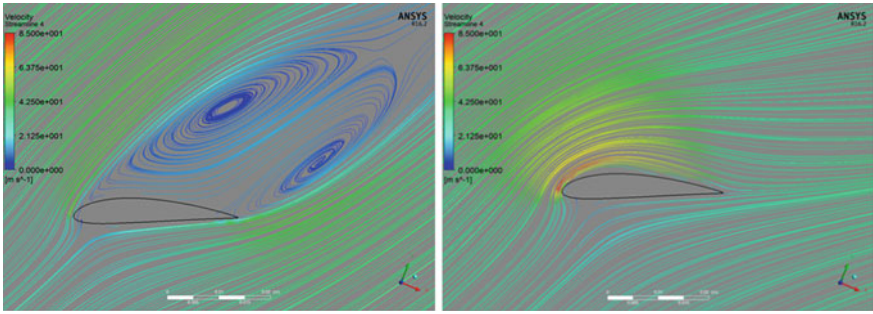


Fig. 12 2D Streamlines at r/R 34% for C⁻ (left) and C⁺ simulations

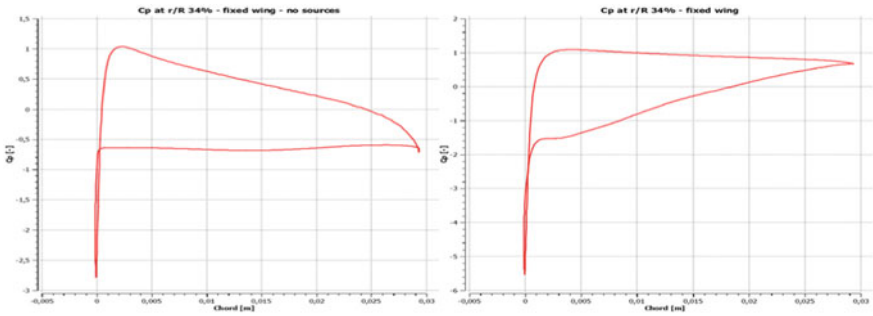


Fig. 13 Calculated C_p at r/R 34% for C⁻ (left) and C⁺ (right) simulations

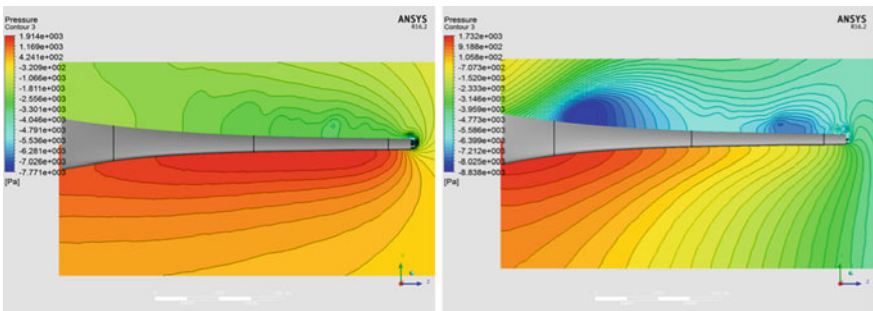


Fig. 14 Pressure contours in a section perpendicular to the blade for C⁻ (left) and C⁺ (right) simulations

From the streamline analysis in Figs. 11 and 12 the strong influence of the momentum due to the radial component of the Coriolis force is evident. While the simulation C^- leads to a flow-field similar to that of a 2D condition (Figs. 11 and 12 left), with a fully developed separation, the momentum addition, due to radial Coriolis force (C^+), triggers a helical structure in the inner blade, which is noticeably similar to that generated in rotating blades (Figs. 11 and 12 right). The strong analogy with Figs. 5 and 6 demonstrates the assumption that a particular radial force balance is mainly responsible for the generation of the helical structure over the inner blade. In this force balance, the radial component of the Coriolis force clearly plays an essential role.

The hypothesis that the rotational augmentation is strictly related to the helical vortex onset is confirmed in Fig. 13, where the pressure coefficient trends for the fixed wing at r/R 34% are presented. The strong depressurization of the suction side for simulation C^+ (Fig. 13 right) is almost equal to that in Fig. 5, while in simulation C^- only a slight depressurization near the leading edge is detected (Fig. 11 left).

Similar considerations can be made on Fig. 14. Here, the pressure contours are obtained in a section perpendicular to the blade at a mid-chord. What is remarkable is the strong similarity between the pressure distributions in Fig. 14 (right) and in Fig. 8 (right). Indeed, although in the pressure side, the contours are different, probably due to the lack of the curved flow, on the suction side both the low pressure areas, at the inner blade and near r/R 80%, are evident. These depressurization areas are clearly related to the development of helical structures, that are absent in C^- simulation (Fig. 14 left). This definitely confirms that the radial forces, and specifically the equilibrium between the radial component of the Coriolis force and the centrifugal force over the entire separated layer, generates the shear in such a way that helical vortices are triggered. The rotational augmentation is thus dependent on the intensity and extension of the helical structures, which in turns depend only on the AoA and on the consequent fluid force imbalance.

4 Conclusions

Based on the scientific literature considerations and by the use of accurate CFD models, the present work provides a thorough analysis of the rotational augmentation, leading the way for a better physical comprehension of this phenomenon. Carefully analysing the post processing results of an experimental micro rotor, the authors evaluate a wide range of operative conditions. Specifically, analysing a condition in which the rotational augmentation is maximum in the inner blade, an extremely complex flow-field is highlighted. The entire separated layer is subjected to the radial forces. The radial component of the Coriolis force, which is seen to be over four times higher than the other contributions, causes a flow-deflection toward the hub in the upper separated layer while, in the lower layer, the centrifugal force prevails and generates a strong radial flow in the opposite direction. Therefore, the change of the radial force direction causes an axial shear that triggers the onset of a helical vortex

in the inner blade. Through the use of pressure contours, streamlines and C_p charts, the helical structure is found to be mainly responsible for the strong depressurization of the suction side of the blade and finally for the noticeable increase of lift and drag coefficients at medium AoAs ($10^\circ < \text{AoA} < 60^\circ$ in this case).

The further analysis of the radial force and velocity in the separated layer, demonstrates the strong correlation between both of these and supports the supposition that the radial component of the Coriolis force is the one that contributes in a decisive way to the development of the rotational augmentation phenomena. Moreover, the idea of simulating a fixed wing, separating the single effects due to rotation, provides an important support in the comprehension of the physical mechanism that triggers the rotational augmentation. The development of the helical structure, and the consequent centrifugal pumping, arise only in presence of the radial component of the Coriolis force.

According to the authors' opinion, the above represents an important key step in the physical comprehension of the fluid-dynamics of rotating blades. The application of what has been inferred can be an improvement of the 1D centrifugal pumping models or a rather interesting performance improvements. Indeed, the helical vortex and its effects may be used in order to obtain a desired performance increment in off-design operating conditions. Moreover, the blade structural loads evaluation can certainly be improved, based on a more accurate knowledge of the rotational augmentation.

References

1. Elgammi M, Sant T (2017) A new stall delay algorithm for predicting the aerodynamics loads on wind turbine blades for axial and yawed conditions. *Wind Energy* 20(9):1645–1663. <https://doi.org/10.1002/we.2115>
2. Du Z, Selig MS (2000) The effect of rotation on the boundary layer of a wind turbine blade. *Renew Energy* 20(2000):167–181. [https://doi.org/10.1016/S0960-1481\(99\)00109-3](https://doi.org/10.1016/S0960-1481(99)00109-3)
3. Lanzafame R, Mauro S, Messina M (2015) Evaluation of the radial flow effects on micro HAWTs through the use of a transition CFD 3D model—part I: state of the art and numerical model review. *Energy Procedia* 82(C):156–163. <https://doi.org/10.1016/j.egypro.2015.12.011>
4. Snel H, Van Holten T (1994) Review of recent aerodynamic research on wind turbines with relevance to rotorcraft, data and riddles on dynamic inflow, flowfield of yawed rotors and rotating 3-D stall. In: *Proceedings of the 20th European rotorcraft forum*. Amsterdam, 4–7 Oct 1994
5. Lindenburg C (2004) Modelling of rotational augmentation based on engineering considerations and measurements. ECN-RX-04-131 EWEC, London
6. Hu D, Hua O, Hu Z (2006) A study on stall-delay for horizontal axis wind turbine. *Renew Energy* 31:821–836. <https://doi.org/10.1016/j.renene.2005.05.002>
7. Lindenburg C. Investigation into rotor blade aerodynamics: analysis of the stationary measurements on the UAE phase-VI rotor in the NASA-Ames wind tunnel. ECN-C-03-025
8. Herraez I, Stoevesandt B, Peinke J (2014) Insight into rotational effects on a wind turbine blade using Navier-Stokes computations. *Energies* 7:6798–6822. <https://doi.org/10.3390/en7106798>
9. Früh WG, Creech ACW (2015) A criterion for rotational augmentation based on a boundary-layer analysis. *Renew Energy Power Qual J (RE&PQJ)*. ISSN 2172-038X, No. 13

10. Breton SP, Coton FN, Moe G (2008) A study on rotational effects and different stall delay models using a prescribed wake vortex scheme and NREL phase VI experiment data. *Wind Energy* 11(5):459–482. <https://doi.org/10.1002/we.269>
11. Karimipannah MT, Olsson E (1993) Calculation of three-dimensional boundary layers on rotor blades using integral methods. *J Turbomach* 115(2):342–353. <https://doi.org/10.1115/1.2929240>
12. Schreck S, Robinson M (2002) Rotational augmentation of horizontal axis wind turbine blade aerodynamic response. *Wind Energy* 5:133–150. <https://doi.org/10.1002/we.68>
13. Johansen J, Sørensen NN (2004) Aerofoil characteristics from 3D CFD rotor computations. *Wind Energy* 7:283–294. <https://doi.org/10.1002/we.127>
14. Carangiu CE, Sørensen JN, Cambuli F, Mandas N (2007) CFD–RANS analysis of the rotational effects on the boundary layer of wind turbine blades. *J. Phys. Conf. Ser.* 75(2007). <https://doi.org/10.1088/1742-6596/75/1/012031>
15. Song Y, Perot JB (2015) CFD simulation of the NREL phase VI rotor. *Wind Eng* 39(3):299–309. <https://doi.org/10.1260/0309-524x.39.3.299>
16. Lanzafame R, Mauro S, Messina M (2015) Evaluation of the radial flow effects on micro HAWTs through the use of a transition CFD 3D model—part II: postprocessing and comparison of the results. *Energy Procedia* 82(C):164–171. <https://doi.org/10.1016/j.egypro.2015.12.013>
17. Lanzafame R, Mauro S, Messina M (2016) Numerical and experimental analysis of micro HAWTs designed for wind tunnel applications. *Int J Energy Environ Eng* 7(2):199–210. <https://doi.org/10.1007/s40095-016-0202-8> Springer
18. Lanzafame R, Mauro S, Messina M (2013) Wind turbine CFD modeling using a correlation-based transitional model. *Renew Energy* 52:31–39 <http://dx.doi.org/10.1016/j.renene.2012.10.007> (Elsevier)
19. Langtry RB, Menter FR, Likki SR, Suzen YB, Huang PG, Völker S (2004) A correlation based transition model using local variables part I: model formulation. *ASME J Turbomach* 128(3):413–422. <https://doi.org/10.1115/1.2184352>
20. Langtry RB, Menter FR, Likki SR, Suzen YB, Huang PG, Völker S (2004) A correlation based transition model using local variables part II: test cases and industrial applications. *ASME J Turbomach* 128(3):423–434. <https://doi.org/10.1115/1.2184353>
21. Mauro S, Lanzafame R, Messina M, Pirrello D (2017) Transition turbulence model calibration for wind turbine airfoil characterization through the use of a micro-genetic algorithm. *Int J Energy Environ Eng* 8:359–374. <https://doi.org/10.1007/s40095-017-0248-2>
22. Mauro S, Lanzafame R, Messina M (2017) An insight into the rotational augmentation on HAWTs by means of CFD simulations—part II: post-processing and force analysis. *Int J Appl Eng Res* 12(21):10505–10529. ISSN 0973-4562

Measuring the Torque and Thrust Loading on the Blades of a Small Horizontal Axis Wind Turbine Operating in Highly Turbulent Flow Regimes



Shaun M. Nay and Philip D. Clausen

Abstract This paper outlines the development of a novel instrumented system that allows the mechanical separation and measurement of the torque and thrust loads on the individual blades of a small two-bladed horizontal axis wind turbine. The siting of small wind turbine systems in the built environment is often accompanied by highly turbulent and unsteady wind conditions, with the consequence of diminished turbine performance, and reduced turbine fatigue life. The measured individual blade torque and thrust loads presented in this paper suggest significant dynamic loading effects experienced by blades of the turbine operating in turbulent, unsteady wind conditions. Further development of a comprehensive turbine instrument suite will provide a significant insight to the behavior and characteristics of small wind turbines in the built environment.

Keywords Built environment wind turbine · Turbulence · Small wind turbine · Wind turbine blade load measurement

1 Introduction

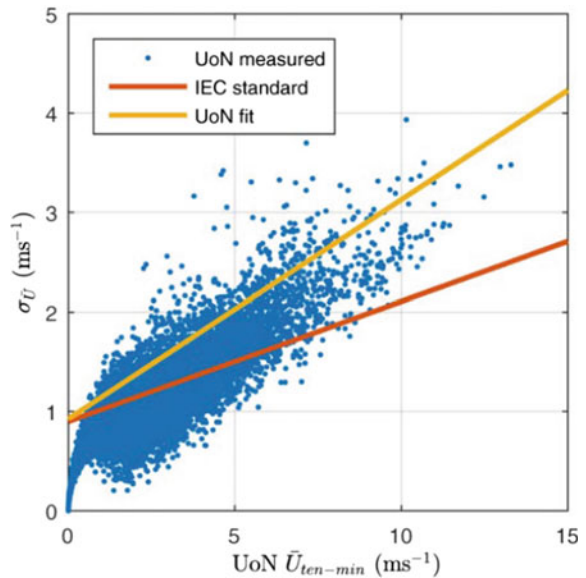
Small wind turbines situated in the built environment experience a significantly different regime of wind conditions to turbines situated in open terrain environments. In particular, turbines located in the built environment exhibit lower than ideal performance characteristics. The level of turbulence present in built environment sites can be shown to exceed the levels accounted for in International Electrotechnical Commission standard—IEC 61400.2–2013—design requirements for small wind turbines [1]. Furthermore, high turbulence is known to result in fatigue issues for many components of the turbine system. IEC6400.2 currently uses large factors of safety to account for the effects of turbulence, which can lead to “over designed” components resulting in a more expensive turbine that responds slower to changes in wind conditions.

S. M. Nay (✉) · P. D. Clausen
School of Engineering, The University of Newcastle, Callaghan, NSW 2308, Australia
e-mail: shaun.nay@uon.edu.au



Fig. 1 Callaghan turbine site, view from North-East

Fig. 2 90th percentile fit of measured data from University of Newcastle and IEC standard [5]



The wind energy group at the University of Newcastle, Australia has a 5 kW 2-bladed horizontal-axis Aerogenesis wind turbine located in a highly turbulent and unsteady wind site on its Callaghan (Newcastle) campus. Figure 1 shows a view of this turbine and the relative height of surrounding trees. Figure 2 shows wind measurement data acquired over a period of 4½ months, indicating this site experiences highly unsteady wind conditions and mostly exceeds the level of turbulence assumed in IEC64100.2. This turbine has been extensively instrumented to measure many aspects of its performance, Bradney [2] and Evans [3]. Their work has clearly shown the turbine operates on average at a low coefficient of performance, C_p , of around 0.18 with this design of turbine able to achieve C_p of 0.45 at a steady wind

site, Ebert et al. [4]. To investigate the effects unsteady flow has on the aerodynamic performance of the blades, requires instantaneous information about the torque and thrust contribution from each blade along with detailed information about the wind conditions, turbine yaw and yaw rate, turbine rotational speed and turbine power. To date, the group has anemometers and instrumentation on the turbine to measure all important aspects of the wind conditions and turbine's performance respectively except for a device to measure instantaneous blade torque and thrust. To measure the latter, a blade rotor has been designed and built that decouples and measures the torque and thrust loading contribution from each blade. This paper describes the important aspects of this rotor and presents and discusses some of the measurements.

2 Blade Loads

The loads experienced by the blades of a horizontal axis wind turbine (HAWT) can be divided into three primary categories: gravitational, inertial and aerodynamic. The gravitational loads are an unavoidable consequence of cantilevered rotating blades. Similarly inertial loads are inevitable due to the inherently dynamic nature of a turbine system. Centripetal forces can impose a significant radial load on the blades at operational speeds, gyroscopic forces are a consequence of the rotating blades yawing around the tower axis, and inertial moments are due to blade rotational acceleration. The simplified mathematic relationship for these forces is given in Eqs. (1)–(3) inclusive.

$$\text{Centripetal load: } = mr\omega^2 \quad (1)$$

$$\text{Gyroscopic moment: } M_G = I\Omega\omega \quad (2)$$

$$\text{Inertial moment } \tau_I = I\alpha \quad (3)$$

where m is the mass of the blade module, r is the distance from turbine shaft to blade module center of mass, ω is the angular velocity of the blade module about the turbine shaft, I is the moment of inertia of the blade module, Ω is the nacelle yaw rate, and α is the angular acceleration of the blade module. In the case of the system presented in this paper, a blade module comprises the 2.5 m glass-fiber reinforced polymer (GFRP) blade and the force measurement assembly.

The unsteady nature of the inflow wind conditions results in changes in the rotational speed of the turbine and turbine yaw rate, leading to fluctuating and potentially extreme inertial loads, Wilson and Clausen [6]. The aerodynamic component of load is critically important to the operation of a wind turbine with this load potentially leading to structural issues for the blades. Blade element theory is used to predict the aerodynamic performance of wind turbine blades, with software such as Fatigue, Aerodynamics, Structures, and Turbulence (FAST), developed by the

national Renewable Energy Laboratory (NREL), used to predict the overall performance of the turbine. Bradney [2] has shown that FAST is unable to accurately predict the performance of a small free yaw wind turbine operating in unsteady flow, in part due to FAST's inability to accurately predict unsteady aerodynamics. To help improve the accuracy of predicting the performance of small wind turbines operating in unsteady flow, comprehensive and detailed experimental data of blade response to operating loads is required.

3 Instrumentation and Data Acquisition

Earlier research work on the Aerogenesis wind turbine used a cup anemometer and wind vane to measure the wind speed and direction respectively. Recently, the cup anemometer and wind vane have been replaced by a trio of Gill Instruments WindMaster 3D sonic anemometers which offer a significant improvement in measurement accuracy and also allow the vertical wind velocity to be measured. These anemometers have been installed in equi-spaced array around the tower, see Fig. 3, to improve measurement resolution and to give measurement redundancy the when flow to one of the anemometers is subject to tower shadow effects. The wind velocity in three orthogonal directions for each anemometer is acquired at 20 Hz by the computer used to instigate data acquisition for the Arduino based data acquisition system.

Fig. 3 Ultrasonic anemometer array



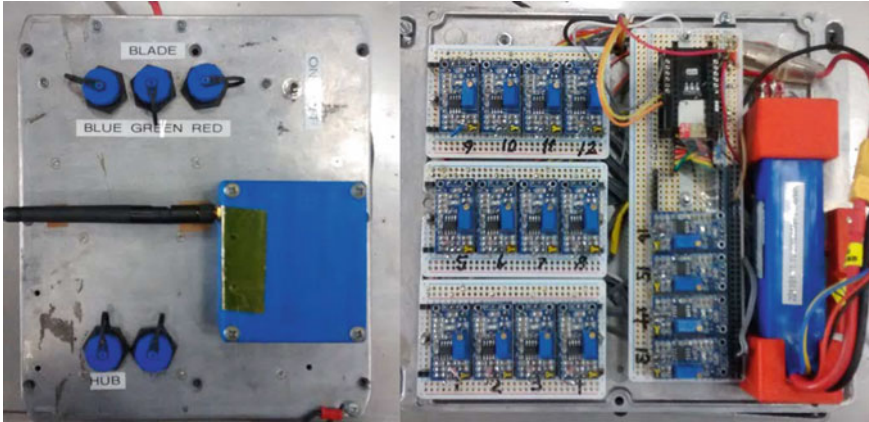


Fig. 4 High speed data logging system for turbine hub mounting

Turbine yaw tracking was recorded with the use of a visual image processing system. The system employed a GoPro© digital video camera mounted to the turbine nacelle, focused on a strip of printed numbers corresponding to turbine heading in degrees. An optical character recognition algorithm written in MATLAB resolves appropriate heading values at a frequency of 25 Hz, Bradney [2].

To avoid the necessity of a large number of complex and unreliable slip rings for signal transfer from a rotating assembly to a stationary data acquisition system, a self-contained data acquisition system (DAS) was used to obtain data from the spinning turbine hub. This system, shown in Fig. 4, consists of a Teensy 3.2 microcontroller module, a Li-Po battery, a micro-SD card module, an XBee radio module, and quarterbridge strain gauge amplifier modules allowing this DAS to record eighteen (18) 10-bit analogue channels at a rate of 500 Hz. The features and operation of this system are described in greater detail in Bradney [2].

Figure 5 shows a typical 60 s period of both horizontal and vertical wind speed measured at the wind turbine site. Figure 6 shows the horizontal wind direction and vertical wind direction for the same 60 s period as in Fig. 5. An instance of a full 360° horizontal flow direction change can be clearly seen in Fig. 6. Furthermore, the vertical angle of the flow is upwards of 70°, greatly exceeding the 8° angle assumed in the standard. These significant speed and direction fluctuations constitute the largescale turbulence, or unsteadiness experienced by the turbine system, and have been shown to reduce the power output of the turbine, Bradney [2] and Evans [3].

4 Blade Load Hub System

The goal of measuring and recording the loads generated and experienced by the turbine blades is critical to understanding the dynamic effects of turbines operating

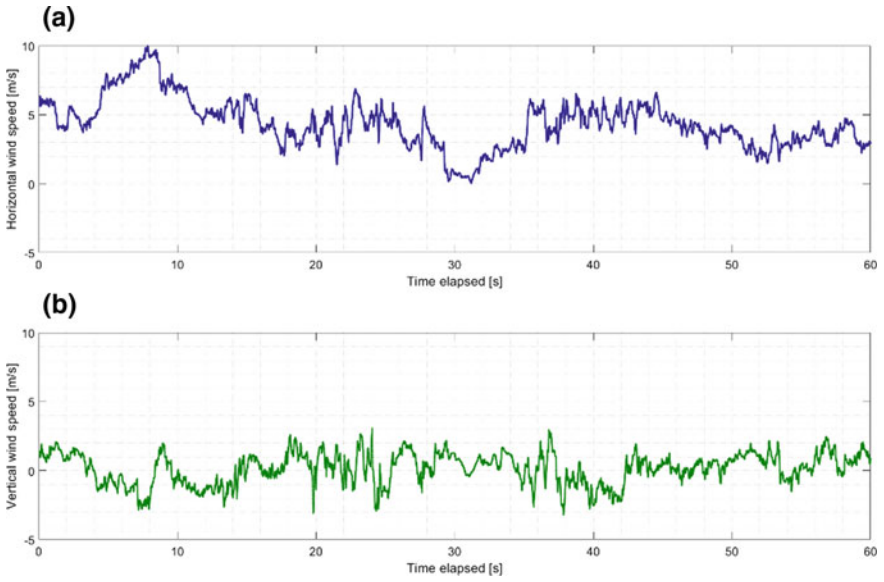


Fig. 5 Callaghan site wind speed: a horizontal, b vertical

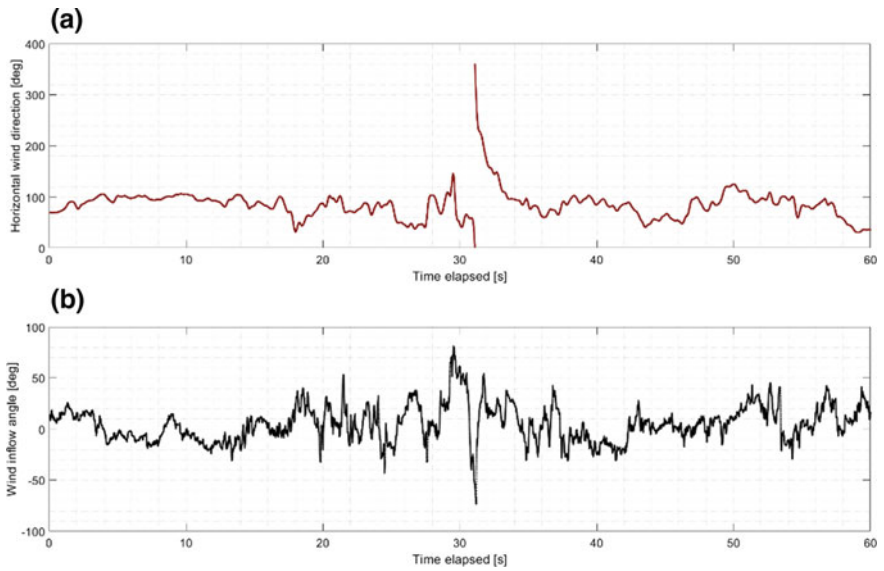


Fig. 6 Callaghan site wind direction: a horizontal heading, b vertical inflow angle

in turbulent flow. To achieve this, a new blade hub has been designed and built which decouples and measures the torque and thrust contribution from each blade to the blade rotor; Fig. 7 show this hub with DAS mounted on its front.

The new hub unit, shown as a picture of a CAD model in Fig. 8, has each blade attached via an adjustable pitch blade holder module to the central radial and axial restraint measurement unit. Each of these two measurement units is attached to the main turbine shaft via bearings, with these bearings prevented from rotating around the main shaft by an instrumented restraint strap. This allows the torque contribution from each blade to be measured individually. Blade thrust is measured using a four-bar pivot link-age system integrated into the measurement unit. The four-bar pivot system has been designed so that the blade forces parallel to turbine shaft are restrained only by an instrumented strain element, as can be seen in Fig. 9. This strap allows both positive and negative thrust effects to be measured.

Static calibration of the measurement device follows the methodology and the recommendations of [7], with the use of masses to simulate operational loading. Testing



Fig. 7 Aerogenesis turbine with measurement hub & DAS installed

Fig. 8 Blade load measurement hub (CAD)

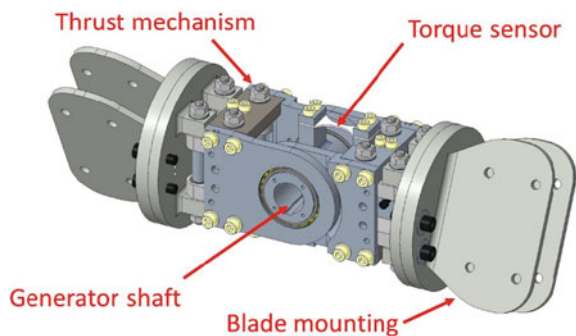
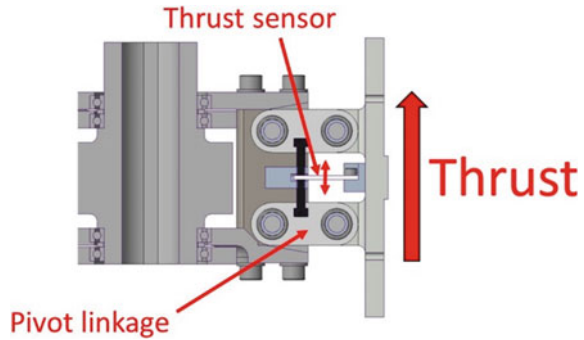


Fig. 9 Blade load measurement hub, Thrust mechanism cross-section



of the decoupling mechanisms indicated highly linear behavior and no discernable cross-talk between torque and thrust sensors during individual loading. The mechanical design and tolerance of manufacture resulted in extremely high resistance to any torsional interference.

A significant component of the torque experienced by the turbine shaft is due to gravitational loading acting on the rotating blades. This component can be easily accounted for if the blade angle is known. Prior instrumentation employed a single magnetically activated sensor to record the time when a blade had passed a single known position, which allowed the blade angular velocity and acceleration to be approximated. This method was found to be insufficiently accurate for start-up and periods of low rotor speed. An improved solution was developed, comprised of a stationary generator mounted ring gear and a hub mounted encoder capable of absolute positioning. The required ring gear assembly and reduction gearbox were designed to integrate into the existing hub and generator system. Additive manufacturing was employed to obtain the required complex geometry of the ring gear and gearbox housing.

Figure 10 shows the nature of the operational data recorded from the hub angle encoder system. Figure 10a shows consecutive “stripes”, plotting the angular position of the central shaft module as a function of time. The instantaneous gradients of this signal allows the rotor’s angular velocity and angular acceleration to be evaluated, Fig. 10b, c respectively. The instantaneous velocity and acceleration of each of the individual blade modules relative to the main rotor can be determined by analyzing the strain signals of the instrumented restraint straps. The inherent stiffness of the assembled measurement device and the straps results in very minor angular velocity/acceleration differences between the central shaft and individual blade modules.

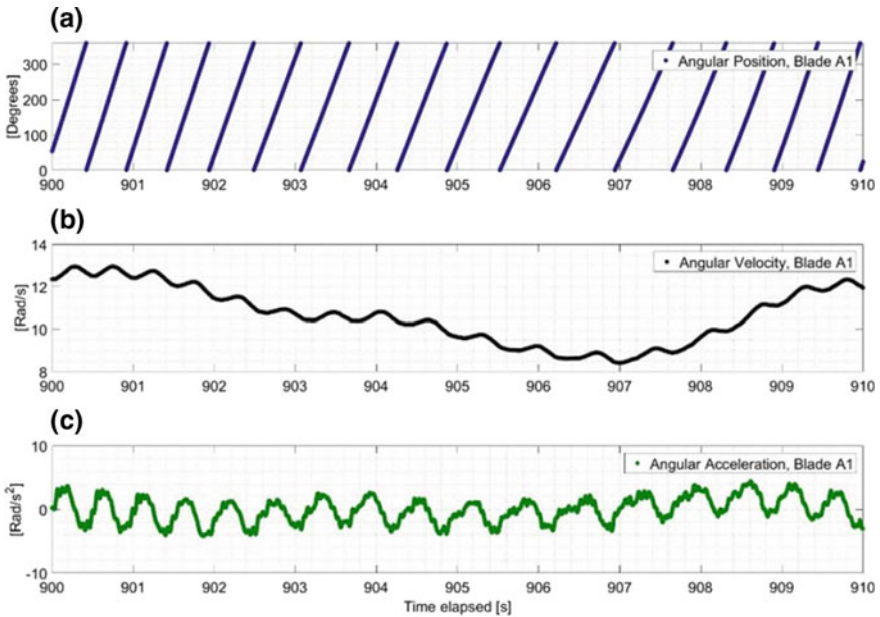


Fig. 10 Hub angle encoder system: **a** angular position, **b** velocity, **c** acceleration

5 Blade Load Hub System

A series of experimental campaigns were undertaken to determine the loading acting on each blade along with hub angular position, turbine yaw performance, wind speed, and turbine power output. Results of the analyzed data from one of these experimental campaigns for a range of sampling periods are shown in Figs. 11, 12, 13, 14, 15, 16 and 17 inclusive.

Figure 11a, b shows blade torque and thrust respective for one blade with turbine rotor speed shown in Fig. 11c and the horizontal wind velocity in Fig. 11d. The results show periodicity in blade torque and thrust measurement with the thrust measurements showing instances of negative thrust.

Figure 12 shows details of the measured torque for both blades over a 2 s sampling period. The measured torque from the blades exhibit a strong out-of-phase periodicity, as expected, with slightly different peaks and trough values due to a slight mass difference between the blades. Figure 13a shows the measured torque from one blade over a 2 s time period with Fig. 13b showing the calculated torque contribution from gravitation loading on the blade, and Fig. 13c showing the difference between the two. As expected the difference is positive and mostly due to aerodynamic loading from the blade.

Figure 14 shows the measured blade thrust and associated horizontal wind velocity over a 50 s period. The mean blade thrust appears to be following the wind velocity.

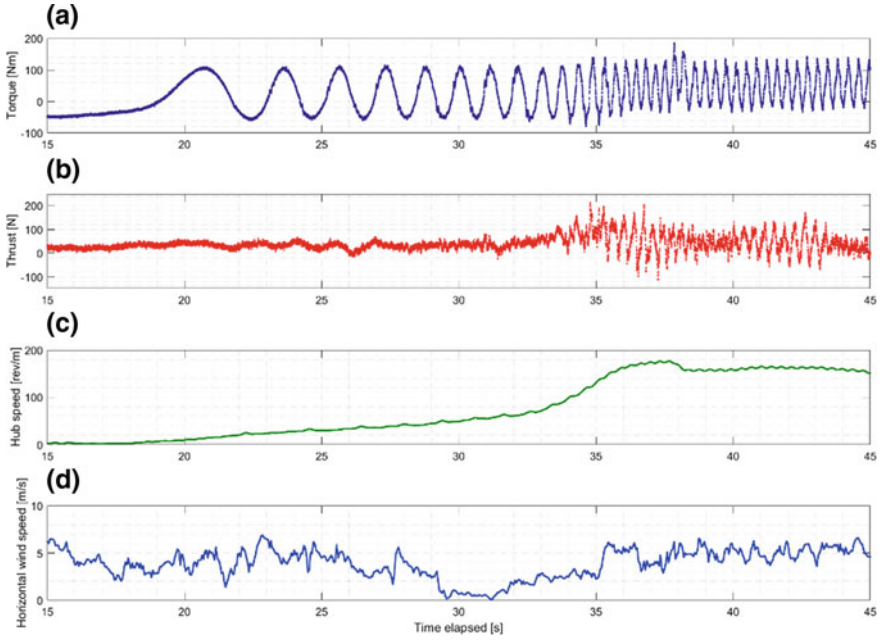


Fig. 11 Blade load data, start-up, 30 s: **a** torque, **b** thrust, **c** hub speed, **d** horizontal wind speed

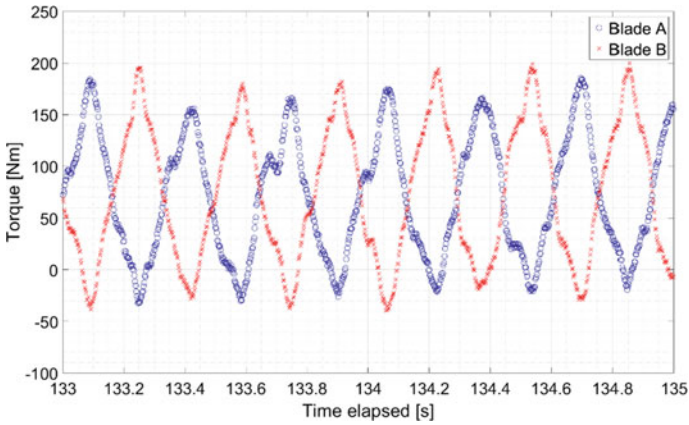


Fig. 12 Torque signal, two blades (A&B)

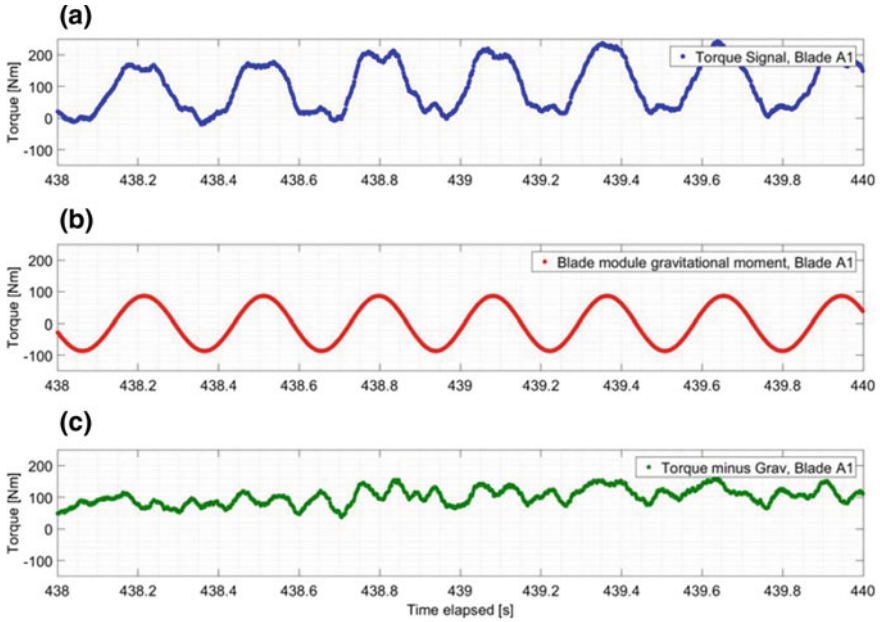


Fig. 13 Torque signal processing: a torque signal, b gravitational moment, c remaining difference

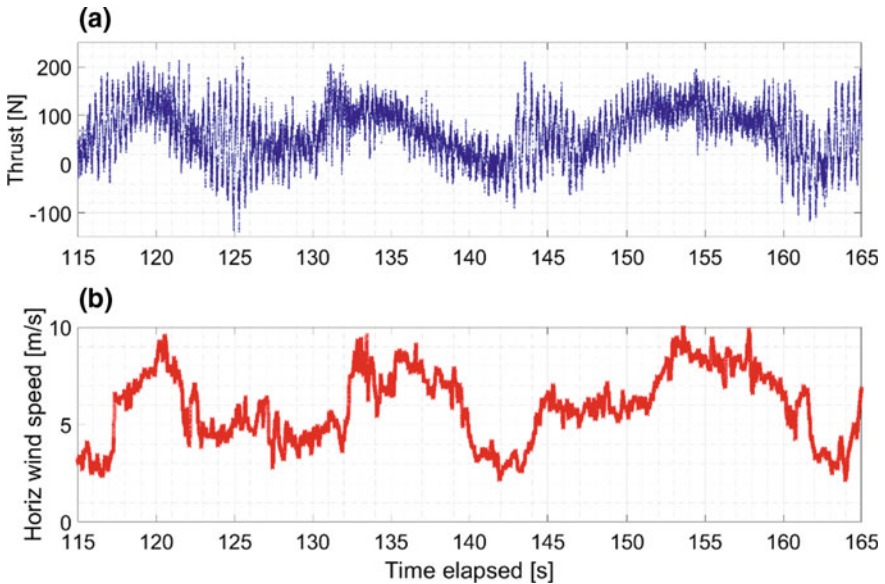


Fig. 14 a Thrust, b horizontal wind speed

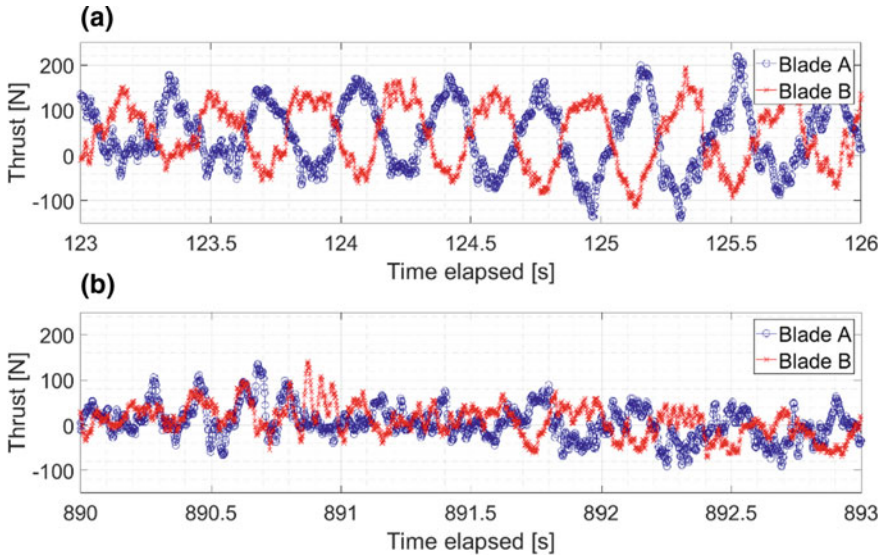


Fig. 15 Thrust signal characteristics: **a** periodic, **b** quasi-chaotic

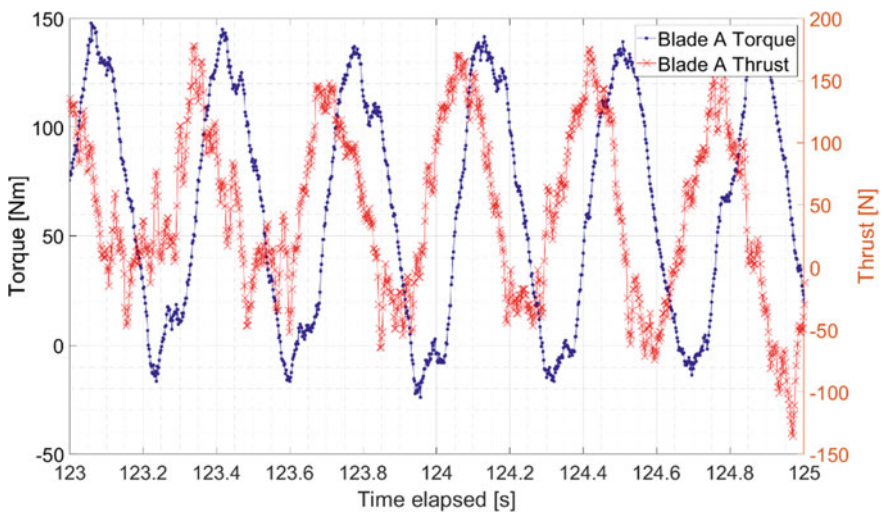


Fig. 16 Torque/thrust offset

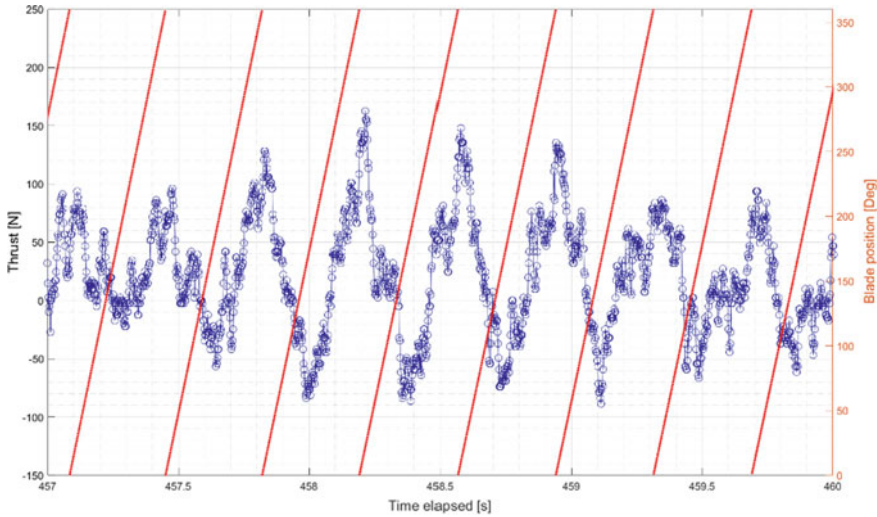


Fig. 17 Thrust blade angle

An examination of the detailed measured blade thrust shown in Fig. 15a indicates the thrust is periodic in nature with somewhat different features in its peaks and troughs. For this measurement time-period, both blades experienced both positive and negative thrust. Periodic fluctuations in thrust signals can be observed, with a similar 180° offset between the blades. These fluctuations are not always present, with instances of comparatively “chaotic” seeming, or offset shifted data. This can be seen in Fig. 15b.

It is tempting to assume that these regular periodic features in blade thrust are a result of coupling with the gravitational torque component. If this were so, then these features would be aligned, however, as shown in Fig. 16, these features are separated by approximately 90° of blade rotation. That is the peak and trough in blade thrust occurs when the blade is pointing vertically upwards or downwards where the gravitation load contribution to blade torque is zero. This can be clearly seen in Fig. 17 where the solid red lines correspond to the angular position of a blade through a cycle.

6 Discussion and Conclusions

A number of additional instrument subsystems are under development and are planned to be integrated into a comprehensive turbine experimental monitoring suite. Shortcomings in the video image processing yaw tracking system have spurred the development of an alternative, absolute position encoder solution. Improved monitoring of the turbines maximum power point tracking (MPPT) controller will also be

investigated. An improved tail moment measuring system has been designed and will be implemented in the near future. Additionally, an array of three-axis accelerometers previously used to assess tower harmonic characteristics, will be used to determine the tower angle, and thus the nacelle's attitude. This should allow for improved modelling of the gravitational loads acting on the blades and in so doing allow fine-tuning of the torque and thrust load profile for the blades.

The novel instrumentation developed permits the measurement of the true blade loads experienced by a turbine sited in an area of highly unsteady flow. Data from the anemometer array suggests that the typical operating conditions for the site in question will significantly exceed the turbulence levels and flow angle described in the standard. The data from the newly developed blade load hub displays many characteristics and features that suggest a very complex blade loading profile. The impact of gyroscopic and other inertial blade loads will be fully investigated when the instrumentation is available.

This paper is not intended to completely explain the phenomena that have been observed in the measurements to date, but to simply illustrate the range of load signal characteristics that can be measured with the newly developed measurement equipment.

The preliminary results suggest that, due in part to the high sampling rate, and mechanical performance of the hub device, that complex and previously unmeasured phenomena are now available for closer study. The individual blade torque and thrust data, coupled with data from the ultrasonic anemometer array, yaw data, and turbine power output, can provide a highly detailed picture of the practical implications of wind energy systems in the built environment.

References

1. IEC 61400.2-2013 (2013) Wind turbines, part2: design requirements for small wind turbines
2. Bradney D (2017) Measured and predicted performance of a small wind turbine operating in unsteady flow. <http://hdl.handle.net/1959.13/1350180>
3. Evans S (2017) Aeroelastic measurements, simulations, and fatigue predictions for small wind turbines operating in highly turbulent flow. <http://hdl.handle.net/1959.13/1349817>
4. Bechly ME, Clausen PD, Ebert PR, Pemberton A, Wood DH (1996) Field testing of a prototype 5 kW wind turbine. In: Proceedings of the 18th BWEA conference on wind energy conversion, pp 103–110
5. Evans SP, Anup KC, Bradney DR, Urmee TP, Whale J, Clausen PD (2017) The suitability of the IEC 61400-2 wind model for small wind turbines operating in the built environment. *Renew Energy Environ Sustain* 2:31
6. Wilson S, Clausen P, Wood D (2008) Gyroscopic moments on small wind turbine blades at high yaw rates. *Aust J Mech Eng* 1:1
7. IEC 61400.13 (2001) Wind Turbines, part 13: measurement of mechanical loads. Elgammi M, Sant T (2017) A new stall delay algorithm for predicting the aerodynamics loads on wind turbine blades for axial and yawed conditions. *Wind Energy* 20(9):1645–1663. <https://doi.org/10.1002/we.2115>

Dynamic Identification of a Vertical Axis Wind Turbine



Luisa Pagnini , Giuseppe Piccardo , Maria Pia Repetto 
and Giuseppe Riotto 

Abstract This paper presents the monitoring campaign carried out over a small size vertical axis wind turbine in the experimental facility of the Savona Harbor. The study is part of the on-going experimental activity investigating the wind field, power production and structural behavior in standstill parked and operating conditions of the turbine. The dynamic response is recorded by servo-accelerometers and strain gauges. Wind field is supplied by sonic anemometers installed nearby. The analysis of the acquired data under different incoming wind and turbine operational conditions provides fundamental frequencies and damping coefficients and supplies information useful to carry out structural verifications and fatigue analyses.

Keywords Small size wind turbines · Structural monitoring · Vertical axis wind turbine

1 Introduction

Small size wind turbines are becoming a very popular topic when dealing with renewable energy and smart cities [1]. Unfortunately, during the operating conditions, they may undergo to severe vibrations induced by gusty wind, turbulence as well as by sudden stops of the machine. All these phenomena have a detrimental effect on the energy production. Especially, they cause frequent damages and may give rise to fatigue collapses that are hardly predictable due to uncertainties in the expected wind velocities and in calculation models [2]. Concerning small size turbines, there exist several numerical and wind tunnel simulations with the aim to validate and develop efficient rotors and safe structures (e.g., [3, 4]); experimental investigations of the structural behavior of operating wind turbines are, however, almost entirely devoted to large size applications.

L. Pagnini (✉) · G. Piccardo · M. P. Repetto · G. Riotto
Department of Civil, Chemical and Environmental Engineering,
University of Genova, Genova, Italy
e-mail: luisa.pagnini@unige.it

Starting from these premises, an experimental campaign is on-going in the Savona harbour (Northern Italy) over a 20 kW Vertical Axis Wind Turbine (VAWT).

The first stage of the research [5] has investigated the power production of the VAWT, that was compared with the power production of a Horizontal Axis Wind Turbine (HAWT) having the same target power and installed on the dam nearby. Wind conditions turned out to be particularly interesting, characterized by two distinct regimes, corresponding to low (wind blowing from the sea) and high turbulence (wind blowing from the land). The second stage of the on-going research is investigating the structural response [6]. Structural motion is obtained from accelerometers installed at the top of the steel pole and at an intermediate position, where the contribution of the second vibration mode is significant. These measures are especially useful for the dynamic identification and for the investigation of structural response model; however, they do not supply information about mean and quasi-static part of the response. The instrumentation is therefore completed by strain gauges positioned at the bottom of the steel pole and in some constructive details interested by possible critical stress. All these measures supply static, quasi-static, resonant components of the response; in this way, they are useful to carry out structural verifications, investigating fatigue damage and response models. The present paper describes new results obtained at persistent strong wind conditions and coming from an improved set of sensors.

2 Experimental Facility

The investigated turbine is located in the touristic and commercial port of Savona, Northern Italy, which integrates wind power production, PV fields and suitable procedures in waste management that allow using renewable resources in an environmental and economical sustainable way. Since 2012, the wind power production facility included a 6 kW VAVT placed on the roof of an industrial building and two 20 kW turbines having vertical and horizontal axis, installed on the dam in front of the sea and equipped by cup anemometers. A monitoring system managed by the stakeholder records and collects power production, rotational speed of the rotor and wind velocity with a sampling rate of 10 s. Unfortunately, cup anemometers are partially sheltered by the turbine and the shaft. In the framework of the European Project “Wind and Ports” (www.ventoeporti.net), tri-axial sonic anemometers were installed in the harbour, nearby the turbines, registering continuously the wind velocity with a frequency rate of 10 Hz.

Figure 1a shows the area and the location on the harbour dam. Figure 1b shows the power production facility, the position of the wind turbines, PV field and the sonic anemometer that has been selected for the description of the wind field at the site of the investigated turbine.

The 6 kW turbine was dismantled soon after its installation, as it was causing strong vibrations on the roof below. The other two systems immediately suffered several problems often experienced by small wind turbines. The energy production was

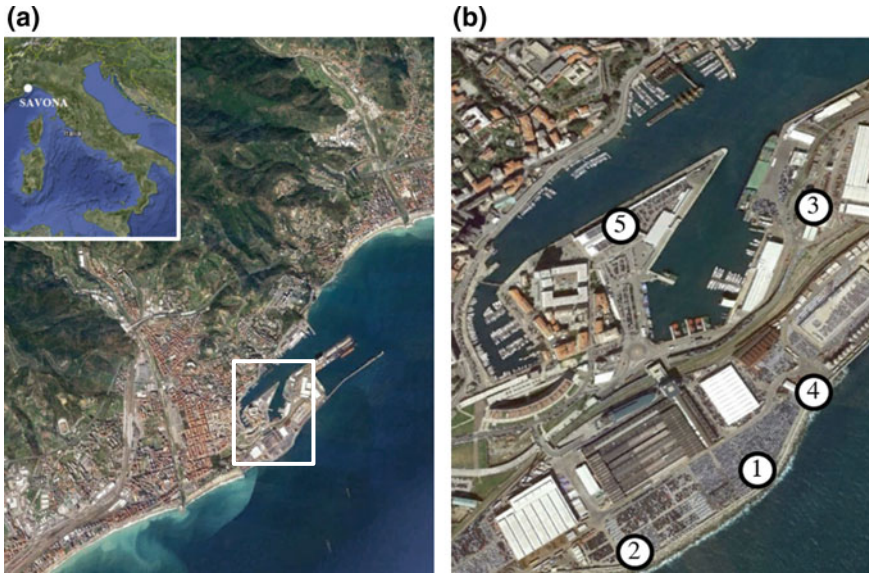


Fig. 1 Location of the wind turbine in the Savona harbour (a) and (b) the power facility with the location of the 20 kW VAWT (1), the 20 kW HAWT (2), the 6 kW VAWT (3), the sonic anemometer (4) and the 121 kW PV field (5)

significantly affected by the turbulence of the incoming wind; moreover, they were struck by a lightning in the subsequent years. After the repair, in 2014, improvements were made to the control apparatus and to the safety system. However, the supporting steel pole of the HAWT suffered fatigue phenomena that originated from the welding of the bottom and stiffener flanges. The turbine has been therefore dismantled.

The 20 kW VAWT is still operational, with some further interruptions in the first months of 2018.

Figure 2a shows the VAWT. It is characterized by a H-rotor with 8 m diameter and 5.8 m height; it is equipped with 5 aluminum, steel and fiberglass blades. The control system provides a regenerative braking; the rotor is slowed by a hydraulic and electrical brakes. It is supported by a 10.5 m high steel pole, placed upon the dam, at 4.5 m above the ground.

The structural response is monitored by two biaxial servo-accelerometers recording the acceleration in the two horizontal directions within an operating range of ± 2 g. They are positioned at the top and at an intermediate level of the supporting pole, corresponding to the anti-nodes of the first and second modes of the pole, respectively. The structural monitoring is completed with strain measurements at the base of the tower. Eight uni-axial and one tri-axial strain gauges give information on the nominal strain in the lower part of the structure. The former measure the strain in the two direction at the bottom of the steel pole; the latter measures the strain around the inspection door close to the base. These accelerometers and strain

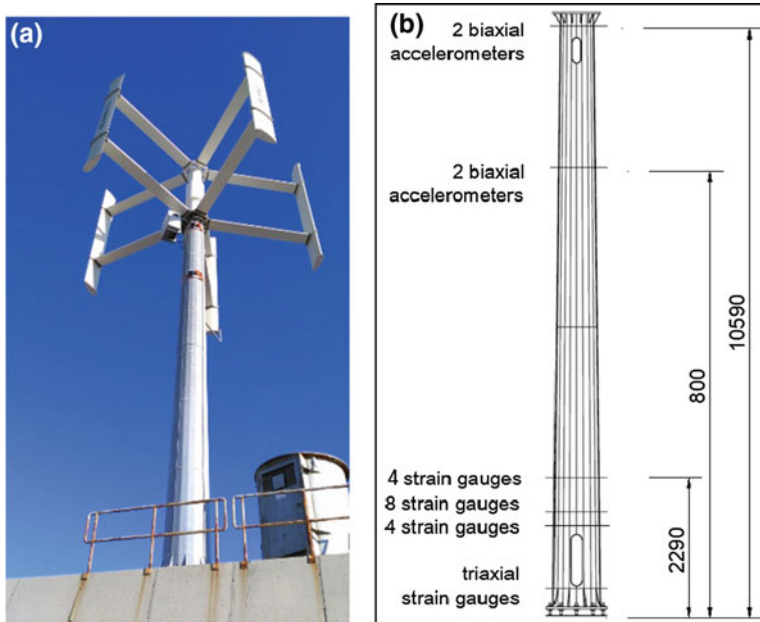


Fig. 2 The 20 kW VAWT installed on the dam (a) and position of the sensors (b)

gauges connected in a quarter bridge were installed in 2016. Unfortunately, the static and quasi static components supplied by strain gauges resulted affected by electrical interference and by the thermal state of the environment and the support. For this reason, the investigation of the wind-induced response and fatigue damage models was not fully developed.

In late 2017, the monitoring system have been enriched with new strain gauges, arranged according a new layout, and connected in a half bridge reducing the effects of thermal excursion.

The acquisition frequency of the structural response is set to 200 Hz; the signals of the accelerometers are pre-conditioned by a low-pass analogical Butterworth filter set to 60 Hz. Accelerometers and strain gauges are cable-connected to an acquisition system positioned inside a watertight booth at the foot of the turbine. A real time internet connection allows checking the acquisition from a remote station; it also shows the real time 10 min time histories and corresponding harmonic contents. Figure 2b shows the sensor position.

3 Wind Field and Power Production

The turbine is overlooking the sea, so that, from 30° to 235° with respect to the North, wind is blowing from the sea and is characterized by low turbulence. In the other sectors, wind is blowing from land and is characterized by high turbulence, suffering the effect of complex orography behind the city of Savona. Figure 3 shows the rose of the longitudinal turbulence intensity, revealing the prevalence of turbulent wind blowing from North-West sectors. The anemometer time series have been transferred to the turbine considering the roughness at the site for each sector of the incoming wind, according to the procedures introduced by the Engineering Sciences Data Unit [7]. Figure 4 shows the histogram of the non-directional wind velocity in year 2016 and the power curve of the turbine for sea and land sectors, respectively, together with the curve supplied by the manufacturer. Referring to the wind speed range of interest for the problem dealt with [8], the regression of the Weibull distribution model of the wind velocity at the site supplies the dimensionless and scale parameters $k = 1.80$, $c = 4.72$, respectively. The mean wind velocity is 4.2 m/s.

It is apparent that power production is almost in line with expectations when wind is blowing from sea sectors. On the contrary, when wind is blowing from land sectors, it is affected by the detrimental effect of high turbulence intensity. Unfortunately,

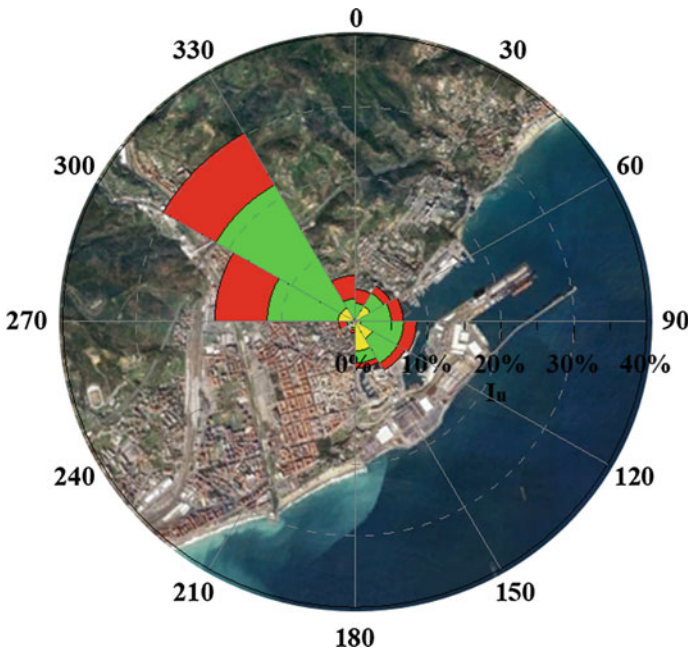


Fig. 3 Turbulence intensity for the different wind directions

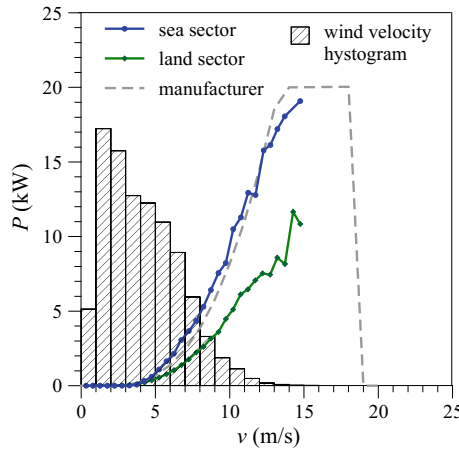


Fig. 4 Wind velocity and power curves in 2016 showing sea and land sectors

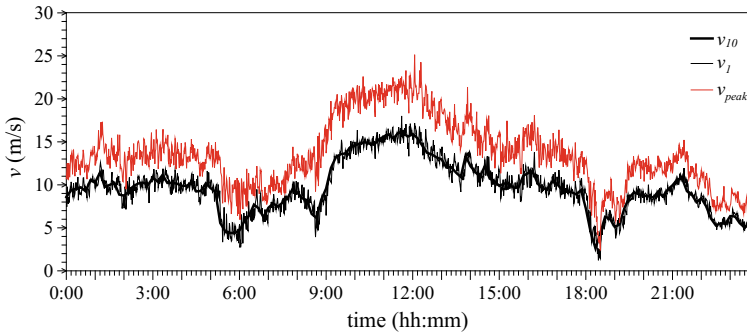


Fig. 5 Wind velocity during April 30th, 2018

this is the prevalent condition for the turbine under investigation, and it is a very common situation in the Mediterranean area.

4 Structural Response

Structural behavior is illustrated with reference to a selection of representative records during April 30th, 2018. During the whole day, strong wind has been blowing from the southern direction, which means wind coming from the sea. Figure 5 shows the wind record, reporting the mean values averaged over 10 min and 1 min, respectively, and the 1 min peak values. The average values of wind velocity and turbulence intensity during the whole day are 10 m/s and 18%, respectively.

The diagram shows an increasing trend of the windiness at about 08:00 a.m. and peak values of about 25 m/s around 12:00 a.m. At the beginning of this time window, the turbine is rotating at the rated value of 48 rpm until 9:16 a.m. At this time, the anemometer records mean wind velocity of about 12 m/s, peak values of about 20 m/s. Therefore, the turbine is stopped by the safety system. In the following time, the wind velocity grows progressively up.

Figure 6a reports the structural acceleration at top from 8:00 to 10:00 by a channel recording in the alongwind direction; grey dotted line reports the standard deviation over a 10 min time interval. The diagram shows two different behavior, respectively during the operating and the parked condition of the turbine. Notwithstanding the response follows the trend of wind speed, it is apparent that structural acceleration is much higher when the turbine is rotating. In particular, it undergoes to sudden acceleration peaks when the turbine is braked and stopped due to strong wind, pointing out that this situation represents a criticality from a structural point of view. Figure 6b shows a strain gauge record by a channel recording the response in the alongwind direction. The diagram also reports the 10 min mean values (solid grey line) and the standard deviation (dotted grey line). The strain record allows appreciating the static and quasi static component of the structural response, highlighting the role of the turbine rotation on both the fluctuating and the mean component.

Figure 7 shows the structural strain versus the wind speed reporting the mean values (Fig. 7a) and the standard deviation (Fig. 7b) of the stress averaged on 10 min time intervals, during April 30th, 2018. The diagrams report with different symbols the quantities related to the rotating turbine (void circles) and to the parked turbine after it is stopped by the safety system at 09:16 a.m. and before it starts again. This diagram clearly shows the two different structural behaviors in the two conditions, highlighting the stress burden due to the turbine rotation and to the sudden stop. This behaviour points out critical conditions for the structure, especially concerning fatigue phenomena.

The investigation of the Power Spectrum Density (PSD) of the structural response is carried out over time histories characterized by almost stationary values of the wind velocity and of rotational speed of the rotor. Figure 8 shows the PSD of the structural response during a wind calm (1 h record); the turbine is not operating due to low wind speed under the cut-in threshold. Black line and grey line reports the structural acceleration and the strain, respectively. With the support of a finite element model and referring to the parked condition, we can identify the following principal vibration modes. Mode No.1 reproduces the principal bending mode of the cantilever beam (along two principal inertia axes of the structure, for its almost perfect symmetry) at the frequency $n_1 = 1.47$ Hz. Mode No. 2 concerns flatwise bending modes of the horizontal arms supporting the blades, which involve two or three blades vibrating both in-phase and out-of-phase at the frequency $n_2 = 2.56$ Hz. Mode No. 3 reproduces the torsional mode of the shaft, $n_3 = 7.46$ Hz. The next mode, reproducing a second mode of a cantilever beam, occurs beyond 15 Hz.

Working in the framework of the Frequency-Domain Decomposition [9] and using accelerometer recordings, damping ratios have been estimated by line-fitting the singular value of the 2×2 power spectral density matrix of the measured response. In

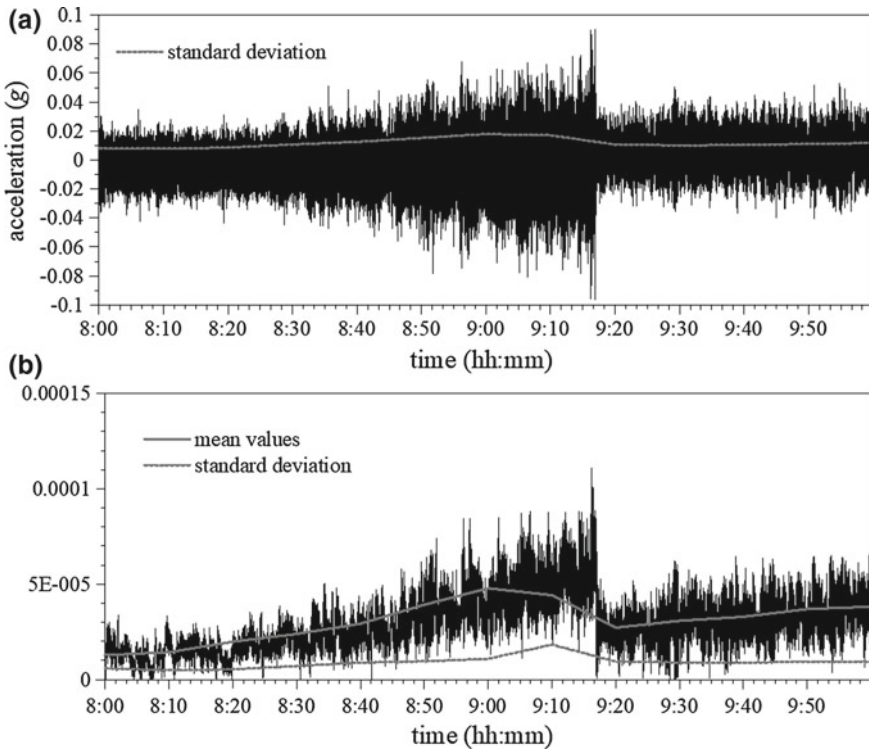


Fig. 6 Alongwind response from 8:00 a.m. to 10:00 a.m. in April 30th, 2018; acceleration at top (a) and strain close to the bottom (b)

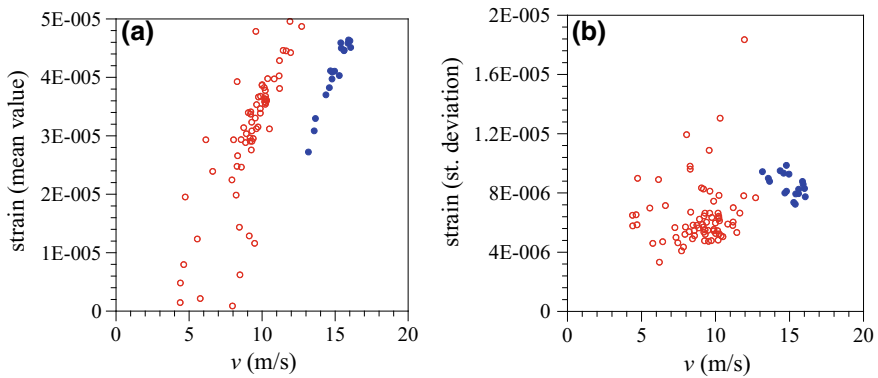


Fig. 7 Strain versus the mean velocity; mean value (a) and standard deviation (b). Void circles refer to the rotating turbine; solid circles report the structural response of the parked turbine after 09:16 p.m

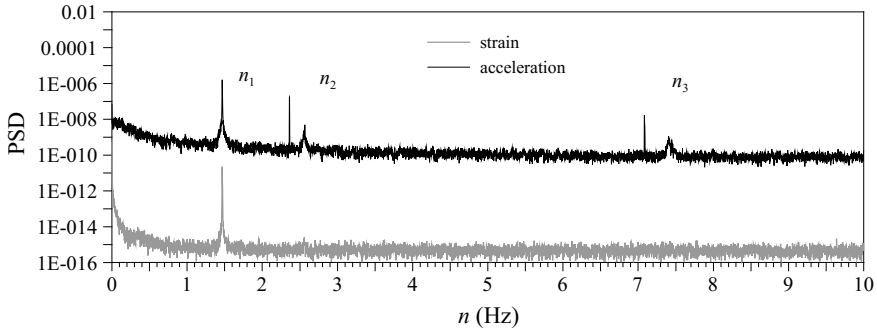


Fig. 8 PSD during a wind calm, from 10:00 p.m. to 11:00 p.m. in April 24th, 2018

the neighborhood of each resonance frequency, the response can be approximated by the square modulus of the frequency response function of single degree-of-freedom systems (e.g., [10]). The search for the optimal solution also provides an estimate of the frequency and peak value that best approximate the experimental response. For the selected record, the damping ratio of the first mode is estimated as $\xi_1 \cong 0.06\%$ revealing a quite small structural dissipation.

With the same meaning of the notation, and still referring to the investigated day on 30 April, 2018, Fig. 9 shows the PSD of the structural response from 03:00 to 04:00 a.m. Wind speed is about 10 m/s, turbine is rotating at 48 rpm., before it is stopped by the safety system. The figure highlights notable differences with respect to the previous case. Harmonic rotor loads occur at multiple of the rotor speed according to the number of the blades. These frequencies are labeled as 1P (one-per-revolution), 5P (five-per-revolution), 10P (ten-per-revolution). Moreover, the rotor undergoes centrifugal forces resulting in a steady force plus a negative contribution to the stiffness matrix (i.e., spin softening) in a rotating reference frame due to centripetal accelerations, leading to pseudo-natural frequencies in a stationary reference frame. Consequently, in stationary coordinates, frequencies may vary with rotor speed, some increasing monotonically, some decreasing monotonically. In particular, for forward-whirling (FW) modes in the rotating coordinate system, the rotor spin speed is added to the natural frequency. For backward-whirling (BW) modes, the rotor spin speed is subtracted from the natural frequency. Therefore, if we consider the VAWT horizontal supports like a rotating beam attached to a rigid shaft, Fig. 9 shows the existence of FW and BW modes, which involves edgewise vibrations of the blade support arms. As a consequence, the rotor fundamental mode having frequency n_2 is split up into two well separated modes, characterized by frequencies n_{2-a} and n_{2-b} , with $n_{2-a} < n_2 < n_{2-b}$.

Another effect of the turbine rotation concerns the harmonic content related to the first structural bending mode. Compared to the turbine in stand still parked condition, the fundamental frequency n_1 appears split up into two closely spaced frequencies. This can be due to some relative movement originated by a possible imbalance

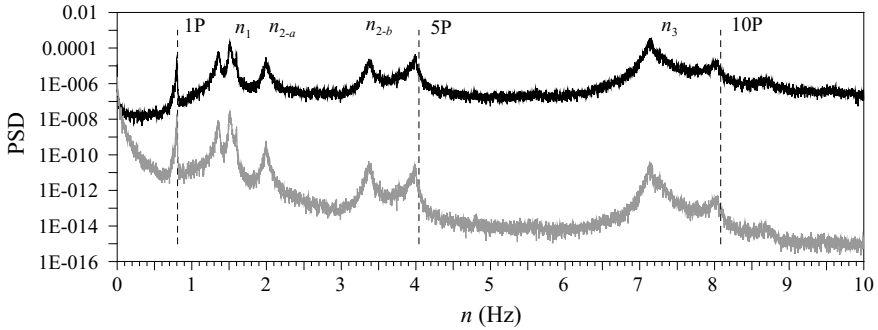


Fig. 9 PSD from 03:00 to 04:00 a.m. in April 30th, 2018; mean wind velocity is 10 m/s, the rotational velocity of the rotor is 48 rpm

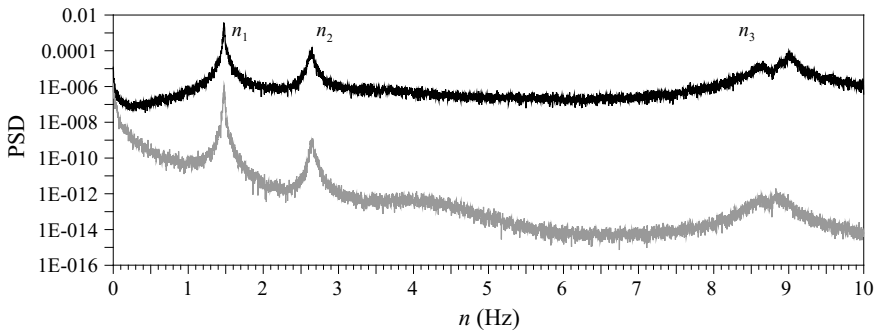


Fig. 10 PSD from 11:00 to 12:00 a.m. in April 30th, 2018; mean wind velocity is 15.8 m/s, the turbine is in parked conditions

between the supporting pole and the rotor, acting like a sort of tuned mass on the pole itself.

The estimate of the damping ratio of the first mode is $\xi_1 \cong 0.8\%$, including the aerodynamic contribution related to wind speed and turbine rotation. However, dissipation is still quite low, pointing out possible criticalities for fatigue. In order to limit vibrations, the use of piezoelectric transducers seems promising (e.g., [11]).

Figure 10 shows the PSD from 11:00 to 12:00 a.m. during the same day, under a persistent wind of about 15.8 m/s, when the turbine is not operating due to strong wind above the cut-out threshold. In this case, dynamic behavior is similar to the behavior shown by Fig. 8. Damping estimate is $\xi_1 \cong 0.52\%$, mainly originating from the aerodynamic contribution of wind velocity blowing on the standstill parked structure.

5 Conclusions and Perspectives

This paper describes the on-going experimental campaign carried out over a small size vertical axis wind turbine in the facility of the Savona Harbour investigating the wind field, power production and structural response.

The study enriches the research with investigations obtained under persistent strong wind. Moreover, the improved set of sensors installed in late 2017 supply new measures of the structural strain that allow appreciating the static and quasi static components of the structural response. In this way, the joint use of the accelerometers and strain gauges give complete information on the structural behaviour concerning the static, quasi-static and resonant response, useful to carry out structural verifications at the design wind speed and fatigue analyses. Authors intend to compare experimental measures with the estimates provided by a response model of slender vertical towers subjected to turbulent wind [12] for estimating of equivalent aerodynamic coefficients of the whole system.

References

1. Bracco S, Delfino F, Ferro G, Pagnini LC, Rossi M, Robba M (2018) Energy planning of sustainable districts: towards the exploitation of small size intermittent renewables in urban areas. *Appl Energy* 228:2288–2297
2. Repetto MP, Pagnini LC (2012) The role of parameter uncertainties in the damage prediction of the alongwind-induced fatigue. *J Wind Eng Ind Aerodyn* 104–106:227–238
3. Rolland SA, Thatcher M, Newton W, Williams AJ, Croft TN, Gethin DT, Cross M (2013) Benchmark experiments for simulations of a vertical axis wind turbine. *Appl Energy* 111:1183–1194
4. Battisti L, Brighenti A, Benini E, Castelli MR (2016) Analysis of different blade architectures on small VAWT performance. *J Phys Conf Series. Design and systems engineering* 753:062009
5. Pagnini LC, Burlando M, Repetto MP (2015) Experimental power curve of small-size wind turbines in turbulent urban environment. *Appl Energy* 154:112–121
6. Pagnini LC, Piccardo G, Repetto MP (2018) Full scale behavior of a small size vertical axis wind turbine. *Renew Energy* 127:41–55
7. Engineering sciences data unit (1993) Computer program for wind speeds and turbulence properties: flat or hill sites in terrain with roughness changes ESDU Item 92032, London
8. Pagnini LC, Solari G (2016) Joint modelling of the parent population and extreme value distributions of the mean wind velocity. *J Struct Eng ASCE* 142(2):04015138
9. Brincker R, Zhang L, Andersen P (2001) Modal identification of output-only systems using frequency domain decomposition. *Smart Mater Struct* 10
10. Carassale L, Percivale F (2007) Frequency-domain output-only identification of linear structures subject to stationary excitation. In: *Proceedings of the 5th International Conference on Computational Stochastic Mechanics*, Rhodes, Greece. Millpress, Rotterdam, pp 147–156
11. Pagnini LC, Piccardo G (2016) The three-hinged arch as an example of piezomechanic passive controlled structure. *Continuum Mech Thermodyn* 28(5):1247–1262
12. Pagnini LC (2017) A numerical approach for the evaluation of wind-induced effects on inclined, slender structural elements. *Eur J Environ Civ Eng* 21(7–8):854–873

Experimental Assessment of an Actuator-Line Simulation Tool for VAWTs



Pier Francesco Melani, Paolo Schito and Giacomo Persico

Abstract The paper presents the detailed experimental assessment of an intermediate-fidelity computational model for the resolution of the flow around Vertical Axis Wind Turbine (VAWT) rotors. This technique, which treats the blade aerodynamics using an actuator-line (ACL) representation, allows largely limiting the computational effort normally associated to 3D calculations, thus providing the ideal framework for simulating wind turbines immersed within the atmospheric boundary layer or operating in the urban environment. The highly unsteady and fully three-dimensional character of VAWT aerodynamics complicates the model implementation and makes it prone to reliability issues; for this reason, experimental validation is decisive for evaluating the reliability of the simulation tool, and for investigating the impact of the various corrective sub-models implemented. In this paper, such procedure is carried out by comparing the ACL prediction with the data coming from an extensive wind tunnel characterization of a real-scale model of a H-shaped VAWT for micro-generation, for which both performance and detailed wake measurements are available. The comparison is made for different tip-speed ratio conditions and combinations of sub-models in the ACL tool. Results show that the turbine performance and the main features of the rotor aerodynamics are well reproduced by the model, resulting in a very good prediction of the wake profile in the equatorial section of the turbine. The quantitative agreement between experiments and calculations locally drops close to the blade tip, where the flow field is fully dominated by 3D effects, even though the model is still able to reproduce qualitatively the most relevant wake features.

Keywords VAWT · CFD-ACL · Wake

P. F. Melani · G. Persico (✉)
Dipartimento di Energia, Politecnico di Milano, I-20156 Milano, Italy
e-mail: giacomo.persico@polimi.it

P. Schito
Dipartimento di Meccanica, Politecnico di Milano, I-20156 Milano, Italy
e-mail: paolo.schito@polimi.it

© Springer Nature Switzerland AG 2019
L. Battisti (ed.), *Wind Energy Exploitation in Urban Environment*,
Research Topics in Wind Energy 8, https://doi.org/10.1007/978-3-030-13531-7_11

Nomenclature

Acronyms

ACL	Actuator Line Method
AOA	Angle of attack
BEM	Blade Element Method
CFD	Computational Fluid Dynamics
EVM	Effective Velocity Method
FV	Finite Volume
LE	Leading Edge
SST	Shear Stress Transport
URANS	Unsteady Reynolds-Averaged Navier–Stokes
VAWT	Vertical Axis Wind Turbine

Symbols

α	angle of attack [deg]
α_{SS}	static stall angle of attack [deg]
ν	freestream flow kinematic viscosity [m ² /s]
Ω	turbine rotational speed [rad/s]
ω	turbulent frequency [1/s]
ρ	freestream flow density [kg/m ³]
θ	turbine blade angular position [deg]
U_0	freestream flow velocity [m/s]
U	local flow velocity [m/s]
v_r	blade relative flow velocity [m/s]
A	turbine front section area = $2HD$ [m ²]
A_m	Berg model constant [-]
c	turbine blade chord [m]
C_D	drag coefficient [-]
C_L	lift coefficient [-]
C_P	turbine average power coefficient = $P_{avg}/(0.5\rho AU_0^3)$ [-]
C_T	blade torque coefficient = $T(\theta)/(0.5\rho ADU_0^2)$ [-]
C_X	turbine average thrust coefficient = $F_{thrust}/(0.5\rho AU_0^2)$ [-]
D	turbine diameter [m]
H	turbine blade half height [m]
I	turbulence intensity [-]
k	turbulent kinetic energy [m ² /s ²]
N_b	turbine number of blades [-]
Re	blade Reynolds number [-] = $v_r c/\nu$
T	turbine revolution period [s]
TSR	Tip Speed Ratio = $\Omega D/2U_0$ [-]

X	transversal coordinate
Y	streamwise coordinate
Z	spanwise coordinate

1 Introduction

In the urban environment, where highly complex flows result from the interaction between the buildings and the atmospheric boundary layer, vertical axis wind turbines (VAWTs) can be competitive with the more conventional horizontal axis technology, thanks not only to their insensitivity to yaw, but also to their reduced acoustic pollution, caused by the lower optimal tip-speed ratio (TSR). Among the several concepts proposed for VAWTs, the lift-driven Darrieus turbine is probably the most promising, as it might provide performance comparable to the ones of horizontal rotors at small-scale.

To exploit properly the wind resource in such a complicated environment, the installation of the rotors demands a dedicated optimization, which in turn requires advanced models, able to capture the interaction between the atmospheric boundary layer, the buildings, and the turbine. The ideal simulation tool for such complex configuration, or at least the unique that leads to a reasonable computational cost, is the so-called actuator-line CFD model, proposed in [30] for VAWTs and further developed by one of the present authors [29].

The Actuator Line Method (ACL) combines a BEM-based modeling of the turbine with the Finite Volume (FV) discretization of the flow domain; in particular, each blade is replaced by a dynamically equivalent actuator line, introducing aerodynamic forces into the computational grid basing on its current position and the local flow conditions. Such strategy allows reducing the efforts associated to a fully 3D CFD modeling of the flow around the rotor, which is now technically feasible [16] even though still very demanding. As the ACL model is based on the blade-element theory, it does not require the resolution of the boundary layer encompassing the blade surfaces, with a corresponding strong decrease in the required computational cost. However, the solutions of ACL simulations are particularly sensitive to input aerodynamic data, which, as it will be discussed in detail in Sect. 3.2, demands extreme care in its derivation both in the stall-free and in the post-stall regions.

Due to the significant modeling effort required by the method, its reliability must be assessed via proper experimental validation. For the purpose, the results obtained with the simulation tool introduced in [29] and further extended in the present work were compared to data coming from an extensive wind tunnel testing of a real-scale model of a H-shaped VAWT for micro-generation [12], in terms of turbine performance and wake representation. The comparison was performed for different operating conditions and combinations of sub-models, in order to highlight their qualitative and quantitative relevance.

Table 1 Characteristics of the H-shaped Darrieus turbine used in wind tunnel tests

Blade height ($2H$) (m)	1.457
Rotor diameter D (m)	1.030
Blade profile	NACA0021 (unstaggered)
Number of blades N_b	3
Solidity ($N_b c/D$)	0.25

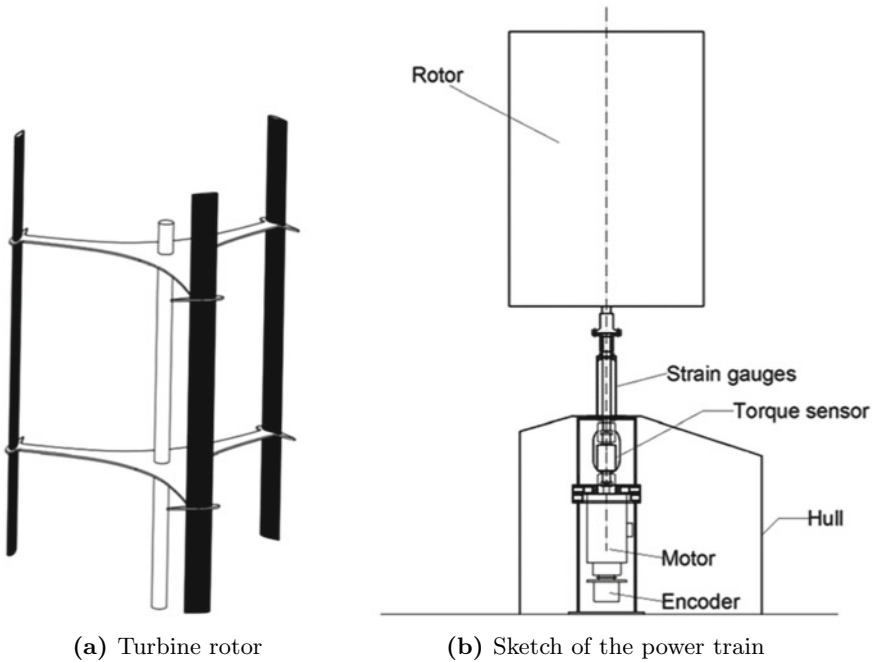


Fig. 1 Test H-shaped Darrieus turbine

2 Wind Tunnel Tests

The validation process was supported by a wide experimental campaign on a real-scale H-shaped Darrieus turbine for micro-generation (see Fig. 1a, whose specifics are reported in Table 1).

The tests were carried out in the large-scale wind tunnel of the Politecnico di Milano (Italy), in particular in the high speed (up to 50 m/s), low turbulence ($I < 1\%$) section of the facility; in order to mimic the open-field operation of the turbine, the full cross-section (3.84×4 m) of the test chamber was exploited, removing the mobile test room and placing the machine in the centre of the jet. According to [12], this allowed to minimize the blockage effect associated to the presence of the wind tunnel itself.

Depending on the considered quantity, different measurement techniques were adopted; performance data were obtained by combining the experimental profiles of turbine rotational speed and shaft torque, coming respectively from an absolute encoder and a precision torque meter (see Fig. 1b). The associated level of uncertainty varies with the TSR. Measurements of velocity in the wake were performed instead via two hot wire traverses, positioned $0.75D$ and $1.5D$ downstream of the shaft, with an uncertainty of about 2%. Full documentation of the experimental campaign can be found in [2], while information about adopted post-processing techniques is available in [27].

3 CFD Model

3.1 ACL Code

The simulations presented in this work are based on the research code *Darrieus-Solver*, which integrates the ACL method in the incompressible transient solver *pisoFoam*, available in the open-source framework OpenFOAM and based on the PISO solution scheme [17].

The code operation, described in detail in [5, 11, 28, 29], can be summarized as follows. At the generic time step, the position and the extension of each blade of the turbine is evaluated basing on input geometric and kinematic data. Then, discretization of the latter in 2D blade elements is performed on the basis of its intersection with the computational grid. For each blade element, relative velocity magnitude and angle of attack are evaluated from the local velocity field via the Effective Velocity Method (EVM) [29]; from these two quantities, local aerodynamic forces are computed, basing on profile geometry and polar data, possibly corrected by additional sub-models. They are then inserted into the computational domain as volume source terms via an ad hoc smearing function (Regularization Kernel), in order to improve the code robustness. The system of equations constructed in this way is finally resolved using the PISO algorithm and then transition to the following time step occurs (Fig. 2 and Table 2).

For the resolution of the flow field developing around the turbine, a URANS approach was adopted, coupled with the $k-\omega$ SST [24] turbulence model. Employed discretization schemes are reported in Table 3; it can be noted in particular how, due to the high regularity of the grid allowed by the ACL approach in the turbine region, no non-orthogonality correction was required for the laplacian term, thus improving the stability of the simulation.

An open-field configuration was chosen for the employed numerical domain, so that the flow conditions of the open-jet wind tunnel tests taken as benchmark for the current analysis (see Sect. 2) could be properly reproduced with a relatively high accuracy; in the open-jet configuration in fact, as reported in [12], the blockage effect associated to the presence of the wind tunnel is estimated to be sufficiently small

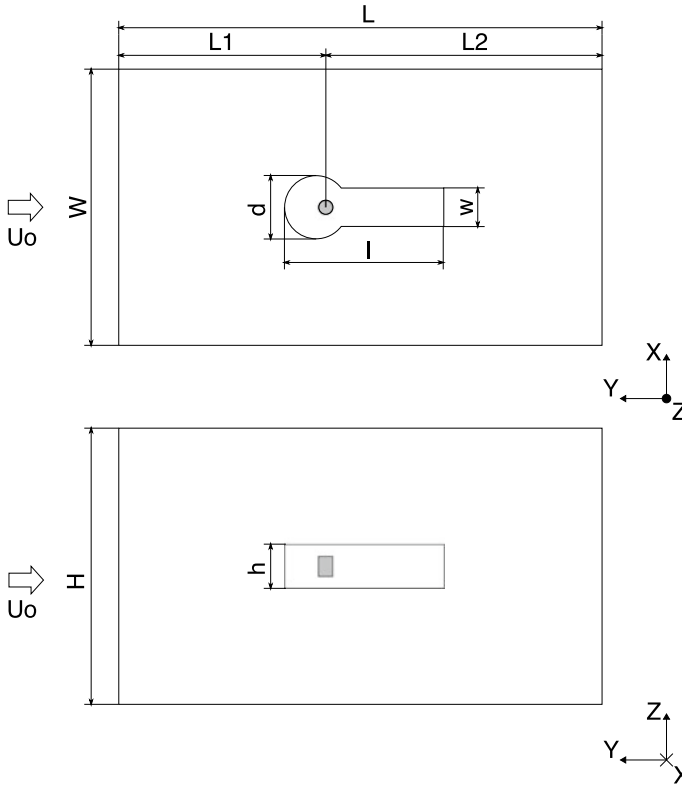


Fig. 2 Top and side view of the employed computational domain, identified by the continuous lines. The position of the turbine is represented instead by the gray shaded region

Table 2 Dimensions of the domain adopted for the simulation campaign

(a) External domain dimensions	
L [m]	35
L ₁ [m]	15
L ₂ [m]	20
W [m]	20
H [m]	20
(b) Internal domain dimensions	
l [m]	11.5
w [m]	2.8
h [m]	3.2
d [m]	4.6

to be neglected without compromising the quality of the results. The computational domain was divided into an internal region, where the interaction between the wind and the turbine blades could be resolved via ad hoc refinement, and an external one,

Table 3 Numerical schemes used for the temporal and spatial discretisation of the domain

Term	Scheme	Properties
Time derivative	Euler	1st order bounded
Spatial gradient	Linear	2nd order unbounded
Spatial divergence (\mathbf{U})	LinearUpwind grad(\mathbf{U})	2nd order bounded
Spatial divergence (k, ω)	LimitedLinear 1	2nd order bounded
Spatial laplacian	Linear uncorrected	2nd order, no correction for non-orthogonality

Table 4 Statistics of the mesh adopted for the simulation campaign

N_{cells}	Cell dimension (m) (ext. region)	Cell dimension (m) (int. region)
13'472'396	0.33	0.020

necessary to correctly propagate the effects of such interaction to the far field and impose the proper boundary conditions. Dimensions of both regions were derived from a dedicated sensitivity analysis, aimed at ensuring the optimal compromise between accuracy and computational effort [23]. Same strategy was employed for the construction of the hexahedral, structured mesh used to define the computational grid, whose characteristics are reported in Table 4, adopting as convergence index the power coefficient C_p .

Consistently with the domain definition and the incompressible nature of the flow, the following set of boundary conditions was specified. At the inlet, the freestream velocity U_0 was imposed according to the TSR under consideration, while a Neumann condition (*zeroGradient*) was adopted for pressure; values for k and ω were derived instead basing on a turbulence intensity I of 0.2% and on a mixing length of 0.5% the height of the wind tunnel nozzle employed in the experimental campaign [15], respectively (see Sect. 2). At the outlet, all variables were set to *zeroGradient* except pressure, whose value was fixed equal to the atmospheric one. For the remaining patches, i.e. lateral, upper and lower surfaces, a symmetry condition (*symmetryPlane*) was employed, assuming they are sufficiently far from the turbine for the flow to be considered undisturbed.

3.2 Construction of Polar Data

As in every BEM-based method, the ACL overall accuracy is extremely sensitive to input aerodynamic data, whose collection and validation thus represents a fundamental step for the implementation of such approach. In the frame of VAWTs, this task becomes extremely challenging due to the specific working principle of the rotor. As a matter of fact, during a revolution each single blade experiences large oscillations of angle of attack, with increasing amplitude going towards the lower TSRs; at start-up such range can extend up to $[-180^\circ, 180^\circ]$. As a consequence, polar data

must cover not only the attached flow region, as in most aerodynamic problems, but also the post- and deep-stall ones, where it is notoriously difficult to obtain accurate results, both experimentally and numerically. The situation is made even more complex by the simultaneous fluctuation of the blade relative velocity magnitude v_r , and so of the local Reynolds number, with a corresponding great variety of the resulting characteristic curves; such issue is particularly severe for small VAWTs as the one under study, where the variation of curve parameters (static stall angle, linear region slope, etc. ...) is enhanced by the oscillation of the flow configuration in the laminar-to-turbulent transition region.

Owing to these difficulties, combined to the relatively recent interest in these machines for small-scale applications, data available in literature are restricted to a few papers, among which the one of Sheldahl and Klimas [31] stands out; in this study, polar data for the seven symmetrical airfoils commonly mounted on VAWTs (NACA0009-0021) were derived from an extensive experimental campaign, considering $\alpha \in [-180^\circ, 180^\circ]$ and $Re \in [10^4, 10^7]$. According to various authors [10] however, data for thicker profiles (NACA0018-0025) and for low Re are not reliable, being extrapolated via an ad hoc synthesizer code from experimental data for thinner profiles (NACA0009-0015) and for higher Reynolds number values. Discrepancy with more recent studies is particularly evident in the attached flow region, where the influence of airfoil maximum thickness is the highest.

For this reason, it was chosen to build the aerodynamic database from scratch, by combining various numerical and semi-empirical methods. Lift and drag coefficients in the attached flow region, i.e. up to the static stall point, were derived via the open-source application XFli5, based on the popular code XFoil [13, 14]. For the N_{crit} threshold parameter required by the e^9 -type free turbulent transition model embedded in the code, a value of 9 was chosen, according to the surface roughness and turbulence intensity levels commonly found in wind tunnel tests. An empirical correlation was applied in the deep-stall region and finally a semi-analytical technique was adopted for modeling the intermediate post-stall region. This section provides details on all these techniques.

The polars in the attached flow region were constructed in two alternative ways. In the first—and most obvious—set of data, the calculation was performed with the original geometry of the NACA0021 profile. In fact, such approach implicitly assumes that the aerodynamic forces can be determined considering Reynolds numbers and angles of attack evaluated from the local relative velocity vector established at a reference location on the blade, usually identified with the blade-support arm attachment point.

Such hypothesis is nonetheless an approximation, since, from a physical point of view, the finite extension of the blade chord implies a variation of the translation velocity along its chord and as a consequence, a non-homogeneous distribution of both relative velocity and angle of attack. In particular, while the variation of the former remains fairly limited, the latter experiences a strong change from the leading to the trailing edge of the airfoil, resulting in a relevant variation of aerodynamic forces with respect to the non-rotating case [25]. This so-called flow-curvature effect becomes more and more important with increasing chord-to-radius ratio c/R ,

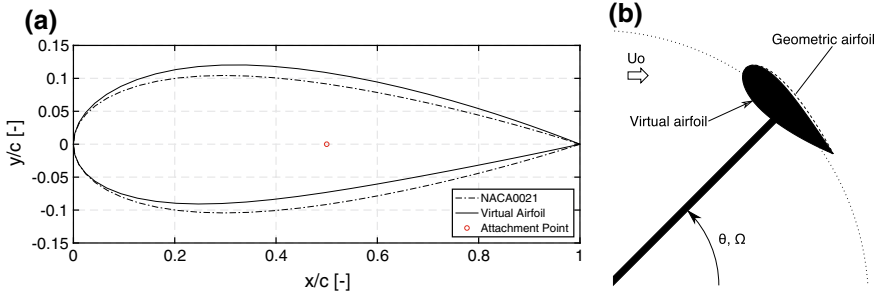


Fig. 3 Comparison between original NACA0021 profile mounted on the turbine and the virtual one derived from Migliore conformal mapping technique

acquiring an extremely relevant impact (given a certain number of blades N_b) for small VAWTs, which feature a relatively high rotor solidity to maximize the blade Reynolds number. Its correct modeling is therefore pivotal for the overall accuracy of the simulations.

To account for the flow-curvature effect, an alternative set of polars was constructed in the attached region, considering a transformed NACA0021 airfoil derived from the original one via a proper conformal mapping, as shown in Fig. 3a. As postulated from a theoretical point of view in [25], and verified both numerically and experimentally in [7, 9], the behaviour of the original airfoil in curved flow can be mimicked by a virtual profile in straight flow, characterized by a certain virtual camber and incidence, with its mean line curving towards the center of rotation of the turbine (see Fig. 3b).

The transformation was carried out for the maximum tip-speed ratio available in the experimental data ($TSR = 3.53$), and then extended to the other operating conditions. Such strategy allowed to strongly reduce the overall computational effort, introducing a relatively small error, as highlighted by Bianchini et al. [7]; due to the absence of flow deflection associated to wind-blade interaction (blockage effect) in fact, Migliore’s theory tends to overestimate the sensitivity of virtual parameters with respect to TSR. For the same reason, the dependence of the virtual airfoil configuration on the blade angular position θ was neglected, averaging instead the values of virtual camber and incidence over one blade revolution.

Extension of the polar curves in the deep stall region ($\alpha > 40^\circ$) was performed by means of the semi-empirical correlation proposed by Battisti [1]. Starting from flat plate theory and the work of Lindeburg [19], he proposed and experimentally validated a new set of equations, which could embed the effects of airfoil maximum thickness t/c and Reynolds number on the blade deep-stall behaviour:

$$C_N = C_{D_{90}} \frac{\sin(\alpha^*) + 0.019 \sin(2\alpha^*)}{0.382 + 0.618 |\sin(\alpha^*)| + 3.82 \frac{t}{c} \cos^8(\alpha^*)} \quad (1)$$

$$C_T = 0.29 C_{D_{90}} \frac{t}{c} |\sin(\alpha^*)| (1 - 1.9 \cos(\alpha^*)) - C_{D_f} \cos(\alpha^*) \quad (2)$$

$$C_L = C_N \cos(\alpha) + C_T \sin(\alpha) \quad (3)$$

$$C_D = C_N \sin(\alpha) - C_T \cos(\alpha) \quad (4)$$

where $\alpha^* = \alpha - \alpha_0 \cos(\alpha)$ is a modified angle of attack accounting for possible airfoil camber ($\alpha_0: C_L(\alpha_0) = 0$), while C_{D_f} is a friction coefficient which depends on the blade Reynolds number Re :

$$C_{D_f} = \frac{0.43}{\log^{2.56}(Re) - 1742/Re} \quad (5)$$

The maximum drag coefficient $C_{D_{max}}$, i.e. $C_{D_{90}}$, required by Eqs. (1) and (2) was computed via the empirical law from Timmer [32]:

$$C_{D_{max}} = 1.994 - 5.4375 \frac{y}{c} \quad (6)$$

where y/c is the leading edge upwind thickness, evaluated from airfoil profile coordinates (y/c at $x/c = 0.0125$).

In order to obtain a smooth transition between the two regions, the ubiquitous Viterna–Corrigan extrapolation method [33] was employed in the post-stall zone ($\alpha_{SS} < \alpha < 40^\circ$). As demonstrated by Bianchini et al. [20], this approach increases not only the robustness of the simulation, but also the accuracy of the results both with and without the presence of a dynamic stall model; in dynamic conditions as the ones actually experienced by VAWT blades, the continuous variation of angle of attack does not give flow separation enough time to complete, preventing the corresponding discontinuity in the aerodynamic curves to occur.

Eventually, polar data was completed in the reversed flow region ($\alpha > 135^\circ$) with the data from Sheldahl and Klimas [31]. The behaviour of the airfoil in such condition is in fact not of interest for the current analysis, since it occurs only during the start-up phase.

The two classes of polars, obtained with the basic and the flow-curvature-corrected models, are reported in Fig. 4. Both of them were validated in a comparative way via the available experimental data.

3.3 Sub-models

In order to investigate the quantitative relevance of specific physical effects within the ACL context, two further sub-models were implemented into the *DarrieusSolver* code and were evaluated in this study.

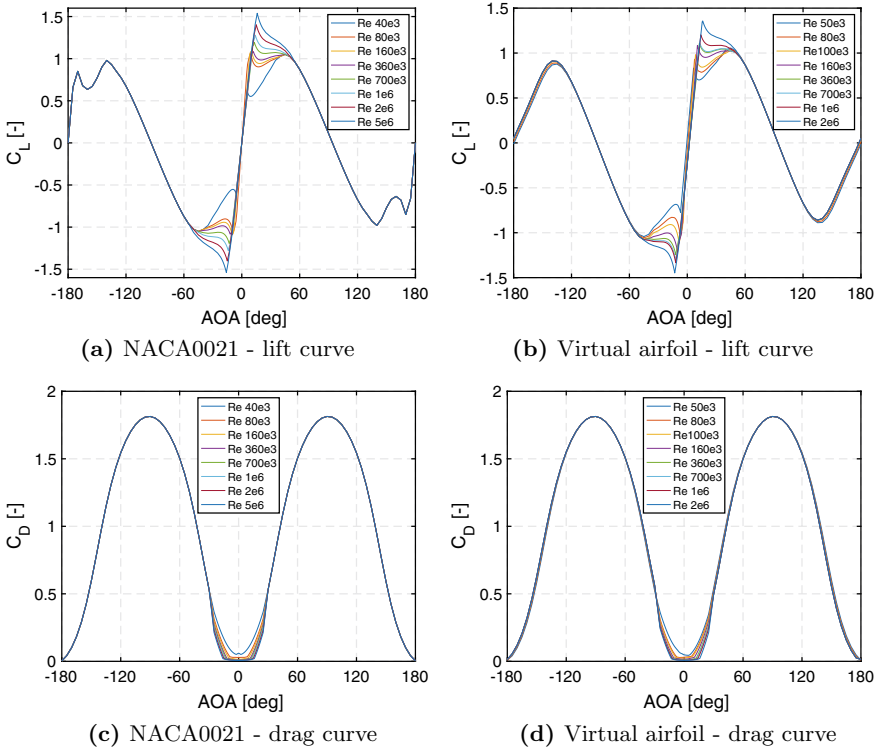


Fig. 4 Comparison between the polar curves of the original NACA0021 profile mounted on the turbine and the virtual one derived from Migliore conformal mapping technique

Tip loss correction Due to the finite blade extension in the spanwise direction, the flow developing around VAWT blades is fully three-dimensional, with vortex-like structures shedding from the blade trailing edge along its full length and gathering at its extremities to form the so-called tip vortices.

From an aerodynamic point of view, the effects of these phenomena are various and hard to decouple. Spanwise flow deviation, whose tip vortices are the most evident manifestation, reduces the blades efficiency, penalizing lift and enhancing drag (induced drag). For the same reason, blade loading decreases approaching the tip region, with a significant drop in performance at blade ends [1]; velocity measurements in the tip region of the wake, reported in [3, 12], show that the wind-turbine interaction and the corresponding wake shape are severely distorted by the presence of tip vortices, so that the entire flow field is markedly altered with respect to the midspan region.

The final consequence of these phenomena is a considerable loss in the turbine efficiency; therefore, their proper evaluation and integration in the solution procedure is necessary for a correct performance prediction. In such perspective the ACL, thanks to its fully three-dimensional formulation, should be inherently capable to resolve

all the features described so far without additional modelling effort; however, the tip vortex shedding event and the corresponding spanwise variation of blade loading might be underestimated. Thus, in order to better investigate the code prediction capabilities, the Glauert's tip correction model (largely used for horizontal axis rotors) was implemented into the solver, after having adapted it to work with VAWTs:

$$F = \frac{2}{\pi} \cos^{-1} \left[\exp \left(-\frac{N_b(H-h)}{2h \sin(\phi)} \right) \right] \quad (7)$$

where h is the local distance of the considered section from blade midspan, and ϕ the local incidence angle. Such correction is directly applied to the computed volume force, before plugging it into the computational grid. Calculations were performed with and without tip correction model for comparison.

Dynamic stall model In case of large and rapid oscillations of the angle of attack as those experienced by VAWT blades, the dynamic lift and drag coefficients present a marked hysteretic behaviour with respect to their static counterparts, associated to the shedding of a coherent vortex-like structure from the airfoil leading edge [18].

This phenomenon, commonly known as dynamic stall, has proved to be determinant [6] in the performances of small machines at low TSRs, not only from the performance perspective, since the overall power extraction is altered by the lift and drag hysteresis cycle, but also from a structural one, due to the higher oscillation in exchanged aerodynamic forces and the damping introduced by the LE vortex shedding event, which in some cases may lead to flutter instability [18]; an additional source of disturbance may also derive from the interaction of vortices shed from one blade with neighboring ones. For this reason, the development and implementation of an accurate model is fundamental for the correct design of these machines.

In the current work, it was chosen to implement the dynamic stall model proposed by Massé [21] and improved by Berg [4], since, according to various authors [6, 22], it represents the optimal trade-off between accuracy and computational effort. A complete description is reported in [26]. For the empirical constant A_m required by the model it was decided to adopt the value of 20, which in a recent study [6] was found to be particularly predictive for small VAWTs.

4 Results

In this section, the most relevant results of the validation campaign are presented. All simulations were run with the same rotational speed of the machine ($\Omega = 400$ rpm), shifting from one operating condition to the other by changing the freestream wind velocity ($U_0 = 6-15$ m/s).

For each one of them, a temporal resolution of 500 time steps per revolution was considered to be sufficient to resolve all relevant flow features and ensure simulation stability, while the number of revolutions required to achieve periodic convergence

varied between 10 and 25 among the different TSR; the percent deviation between the mean torque coefficients over two subsequent revolutions was adopted as convergence index, considering a threshold of 1%.

The analysis first considers the overall power exchange and the aerodynamics of the blades, and then focuses on the turbine wake.

4.1 Rotor Aerodynamics and Performance

The turbine performance data coming from ACL simulations, expressed in terms of average power and thrust coefficients characteristic curves, were validated against their experimental counterparts. In particular, the C_p curve was brought to the comparison after the application of a proper correction for the drag losses associated to the presence of the support arms connecting the blades to the central shaft, following the method proposed in [8] and used to successfully correct 2D CFD simulations performed considering the midspan section only. As a matter of fact, the struts are not included in the ACL model of the turbine.

As reported in Fig. 5a, the adopted simulation tool reproduces with high fidelity the experimental C_p -TSR curve, being within the error bar of the experiments in all the measurement configurations except for a small discrepancy at $TSR = 1.8$. The highest degree of correspondence, however, is achieved with the application of the flow curvature correction, confirming its importance in the modelling of small VAWTs.

On the contrary, a relatively large deviation between simulations and experimental data is observed for the C_x curve, particularly evident at the lower TSRs (see Fig. 5b); such discrepancy is probably related to the absence in the ACL model of the turbine shaft and support arms, which represent a relevant source of drag for the machine [1].

In order to gain a deeper understanding of the shape assumed by the performance curves and so of the global turbine behaviour, various aerodynamic quantities of interest are reported in Figs. 6, 7 and 8, for three benchmark operating conditions.

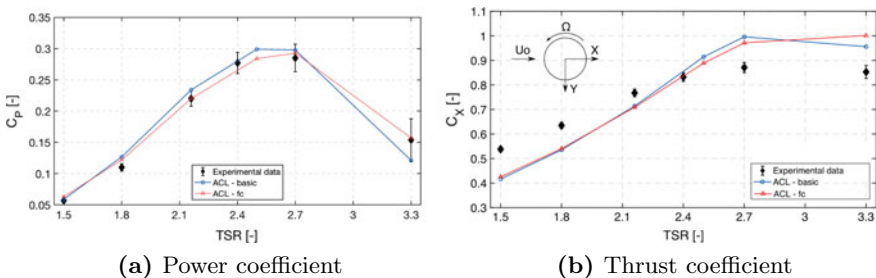


Fig. 5 Average turbine power and thrust coefficients for different tip-speed ratios; basic: full polar of NACA0021 airfoil; fc: Migliore flow curvature correction

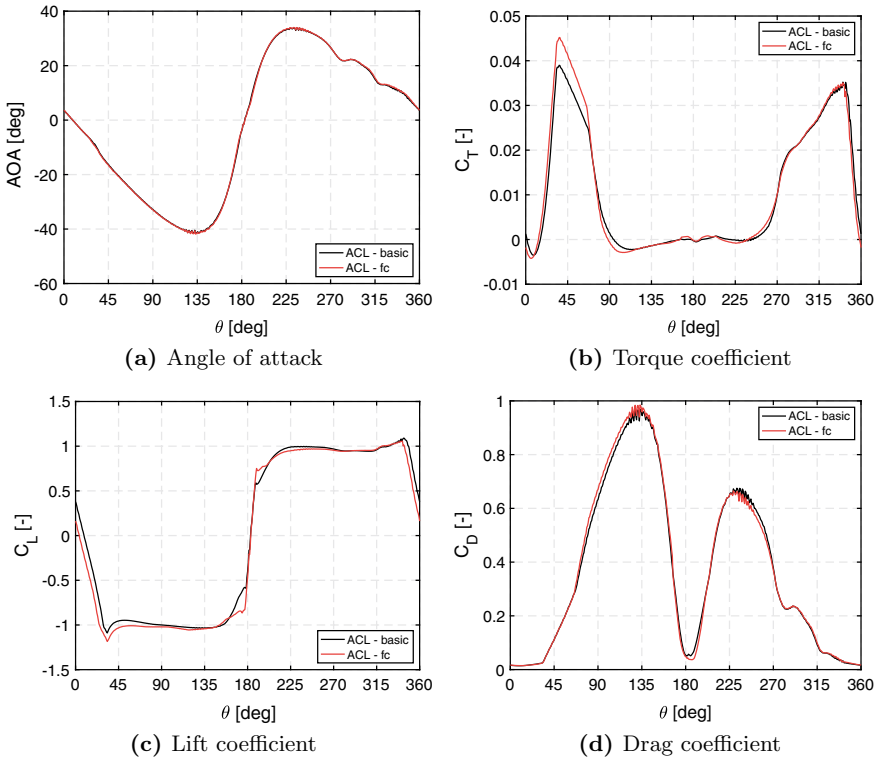


Fig. 6 Profiles over a single blade revolution of various aerodynamic quantities of interest, for $TSR = 1.5$; basic: full polar of NACA0021 airfoil; fc: Migliore flow curvature correction; tl = Glauert tip loss correction

Such conditions are considered to be representative of the turbine behaviour over its whole operative range, i.e. for a high ($TSR = 3.3$), optimal ($TSR = 2.5$) and low ($TSR = 1.5$) loading conditions. At the lowest tip-speed ratio, the power extraction is severely penalized by the stall occurring for most part of the revolution due to the large oscillation in the AOA ($\pm 40^\circ$), whose peak values correspond to steep drops in the blade efficiency C_L/C_D (see Fig. 6). Thanks to the low blockage effect, the behaviour of the machine is nearly symmetric between the upwind (I + II quadrant) and downwind regions (III + IV), apart from the hysteresis in the force exchange associated to flow unsteadiness and highlighted in Fig. 6c, d. For the lowest TSR, the adoption of flow-curvature corrected polars has a very marginal impact on the rotor aerodynamics, coherently with what observed in the C_P curve at integral level.

At higher tip-speed ratios, turbine operation is progressively stabilized, with reduced oscillation of all flow quantities (see Figs. 7 and 8). In fact, due to the global mitigation of stall effects and the consequent improvement of the blades aerodynamic efficiency, a high lift condition is established on a growing portion of the turbine revolution; such trend is particularly evident in the upwind region, where the peak torque production zone tends to assume a nearly symmetric configuration,

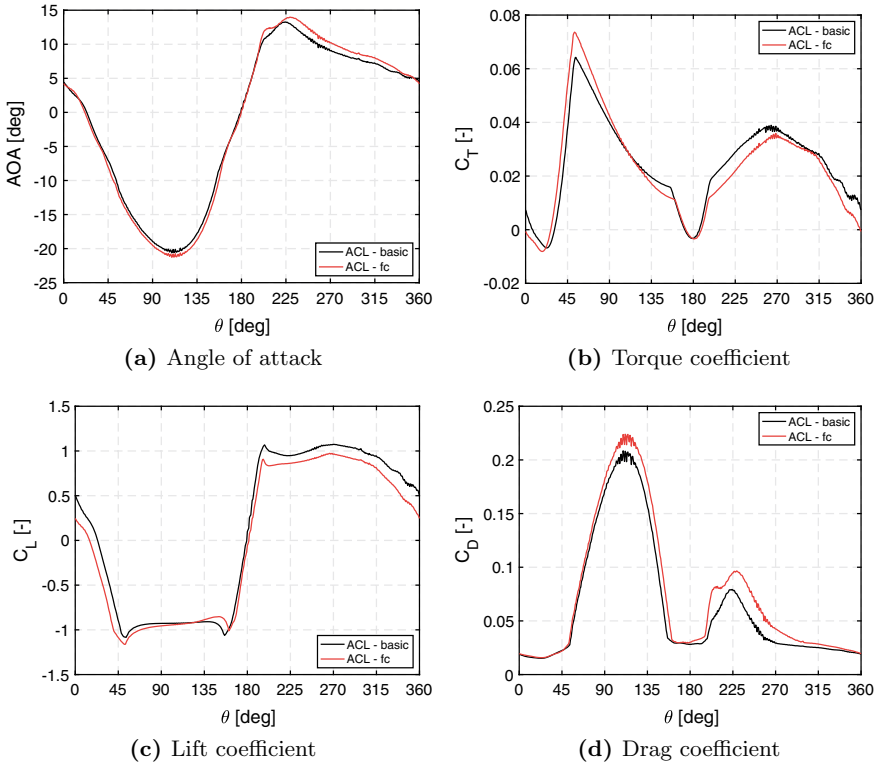


Fig. 7 Profiles over a single blade revolution of various aerodynamic quantities of interest, for TSR = 2.5; basic: full polar of NACA0021 airfoil; fc: Migliore flow curvature correction; tl = Glauert tip loss correction

centered in $\theta = 90^\circ$ and covering the whole range between $\theta = 45^\circ$ and $\theta = 135^\circ$ (see Fig. 8b). If on one side this phenomenon enhances the power extraction in the upwind region, on the other side it amplifies the blockage induced by the turbine on the incoming flow (see Fig. 5b), penalizing the machine global performance; as a matter of fact, flow deceleration in the upwind region determines a decrease in the relative velocity magnitude and angle of attack seen by the blades in the downwind one, causing a strong asymmetry of the global torque profile over a revolution, as reported in Fig. 8b. The latter effect is partially mitigated by the deflection of the incoming flow in the cross-wise direction, which results in a positive offset of the AOA profile, particularly evident for $\theta = 0^\circ$ (see Fig. 8a).

The final result of the combination of these two opposite trends is the C_p -TSR curve shown in Fig. 5a; the power coefficient reaches its peak at TSR = 2.5, where the proper balancing of all these aspects is reached, for then decreasing due to the excessive weight of flow blockage over the global turbine behaviour.

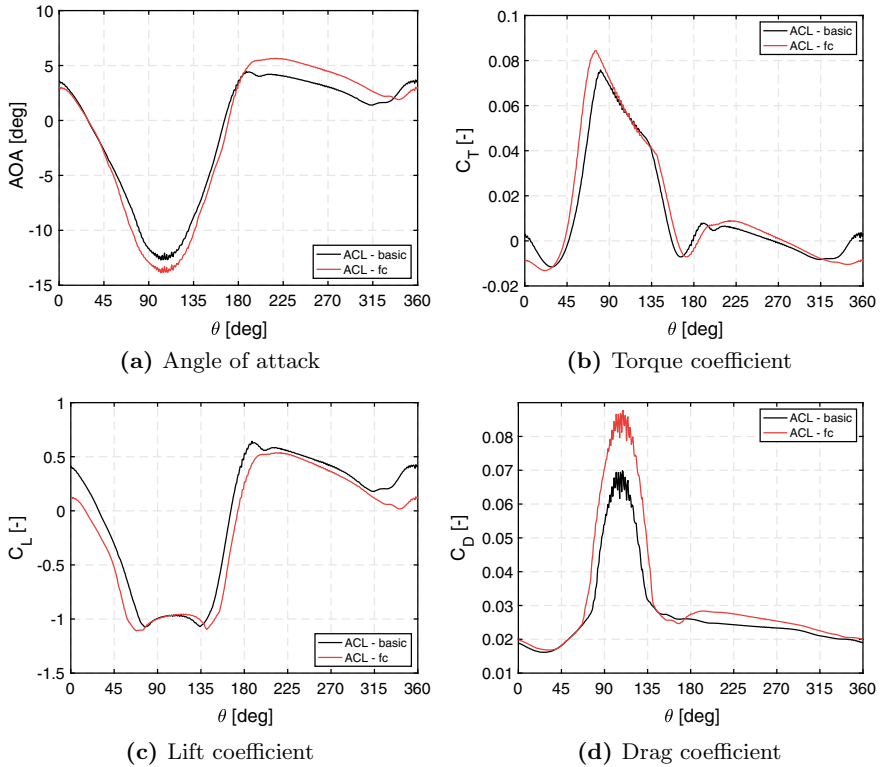


Fig. 8 Profiles over a single blade revolution of various aerodynamic quantities of interest, for $TSR = 3.3$; basic: full polar of NACA0021 airfoil; fc: Migliore flow curvature correction; tl = Glauert tip loss correction

For the two higher TSR values considered in this analysis the use of flow-curvature corrected polars grows in relevance, as the progressive increase of aerodynamic loading enhances the curvature of the streamlines encountered by the rotating blades. As it can be seen from Figs. 7c and 8c, the main effect of the correction is the amplification of the asymmetry in the performance between the front and rear parts of the turbine; as a matter of fact, blade loading is enhanced in the upwind region, while weakened in the downwind one. The consequences of this phenomenon on the turbine efficiency are somewhat contrasting and depends on the considered operating conditions; in the optimal loading case, i.e. around $TSR = 2.5$, the downwind performance penalty dominates over their upwind enhancement, leading to a global power coefficient reduction (see Fig. 5a). The opposite trend is encountered in the high loading branch of the C_p curve, with a corresponding increase in efficiency with respect to the base model. In this context, the enhanced blade loading in the upwind region strengthens the blockage exerted by the turbine on the crossing flow, promoting an increment in the global thrust coefficient (see Fig. 5b) and in the oscillation of all flow quantities, in particular of the angle of attack (see Fig. 8a).

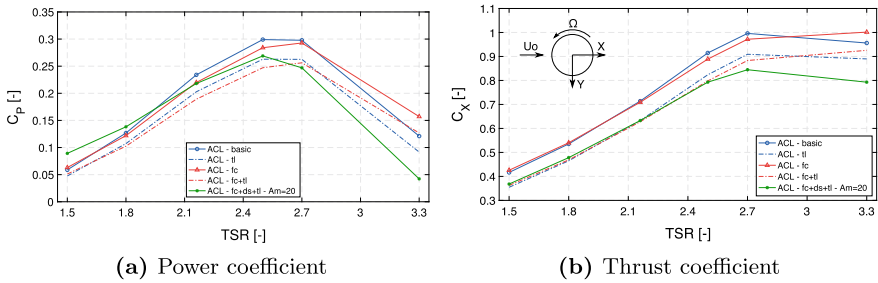


Fig. 9 Average turbine power and thrust coefficients considering different models; basic: full polar of NACA0021 airfoil; fc: Migliore flow curvature correction; tl: Glauert tip correction; ds: dynamic stall correction

Effects of applied sub-models on turbine performances prediction Despite the fully satisfactory reliability demonstrated by the ACL model once equipped with the proper polar data, further calculations were performed to investigate the qualitative and quantitative effects of the sub-models implemented. Figure 9a, b synthetically report the results of all the models implemented in terms of non-dimensional power and thrust exchanged by the machine; for clarity, these figures do not show the experimental data, that nonetheless are very well represented by the calculation with the flow-curvature correction only.

The Glauert correction for tip effects results in a drop of the power coefficient, increasing with the tip speed ratio; a detailed analysis reveals that such overall drop results from a significant reduction of torque in the upwind phase of the revolution, when the maximum lift is established. A similar drop appears also on the thrust coefficient, even though it is nearly independent on the tip speed ratio. This sub-model tends clearly to overestimate the weight of tip losses over whole range of operation of the turbine, introducing a significant discrepancy between the ACL and the experimental curves. So, for the present rotor, the inherent 3D character of the ACL formulation allows capturing the performance degradation due to the tip effect, once the proper polars are used.

The addition of the Berg dynamic stall model further modifies the predicted blade power and thrust profiles. The dynamic stall model was only applied in combination with both the flow-curvature correction and the tip loss model. At low tip speed ratio the hysteretic behaviour of lift coefficient plugged by the dynamic stall model into the polars results in a strong asymmetry in the torque exchange between the upwind and the downwind regions, raising the torque exchange with respect to the static case. Such phenomenon results in an overestimation of the C_p when combined with the absence of losses related to LE vortexes shedding and transport along the flow domain; conversely, the thrust coefficient results insensitive with respect to the dynamic stall model at low TSR. For high TSRs, the dynamic stall correction is still active as the AOA excursion during the revolution still exceeds the static stall limit even at the highest TSR considered. The model tends to distort the predicted torque profile, as the large hysteresis cycle in the upwind region induces a severe

performance drop in the downwind one. The global effect is a significant underestimation of the average power and thrust coefficients with respect to the experimental ones.

4.2 Wake Analysis

The time-mean profiles of the wake released by the machine, coming from ACL simulations, were validated against available experimental data (see Sect. 2).

Such operation allows understanding not only the suitability of the ACL solver to simulate the complex turbine-environment interaction found in urban applications, but also its capability to reproduce the implications of such effects on the wake shed by the rotor for the wide variety of flow configurations experienced by the machine during its operation. In such perspective, the analysis focuses on the three benchmark operating conditions considered above, and representative of high (TSR = 3.3), optimal (TSR = 2.5) and low (TSR = 1.5) loading conditions. The wake was monitored in two flat surfaces downstream of the rotor, one in the near wake and one in the far wake of the turbine as reported in Fig. 10, where velocity measurements are fully available.

The comparison was carried out choosing as reference parameter the time-mean non-dimensional velocity U/U_0 , defined as the ratio between the arithmetic average of the local flow velocity U and the (incoming) freestream one U_0 . The reference time interval for the averaging procedure is the turbine revolution period T . The selected sub-models for tip effects and dynamic stall are not considered in the following wake analysis as their application was found to induce a reduction of reliability with respect to the available experiments.

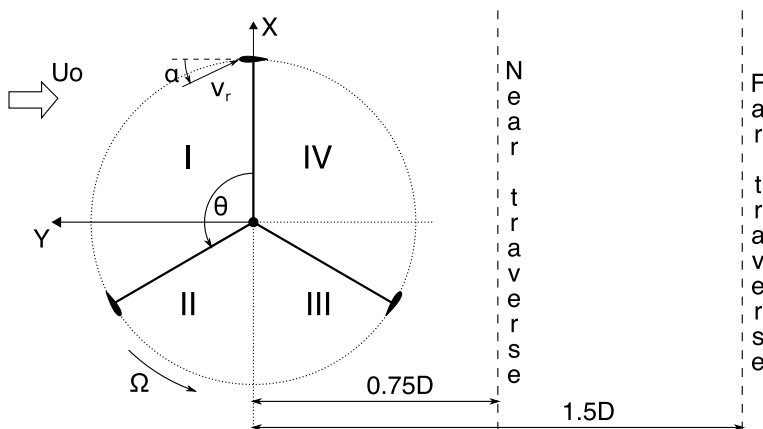


Fig. 10 Signs and conventions used for the analysis

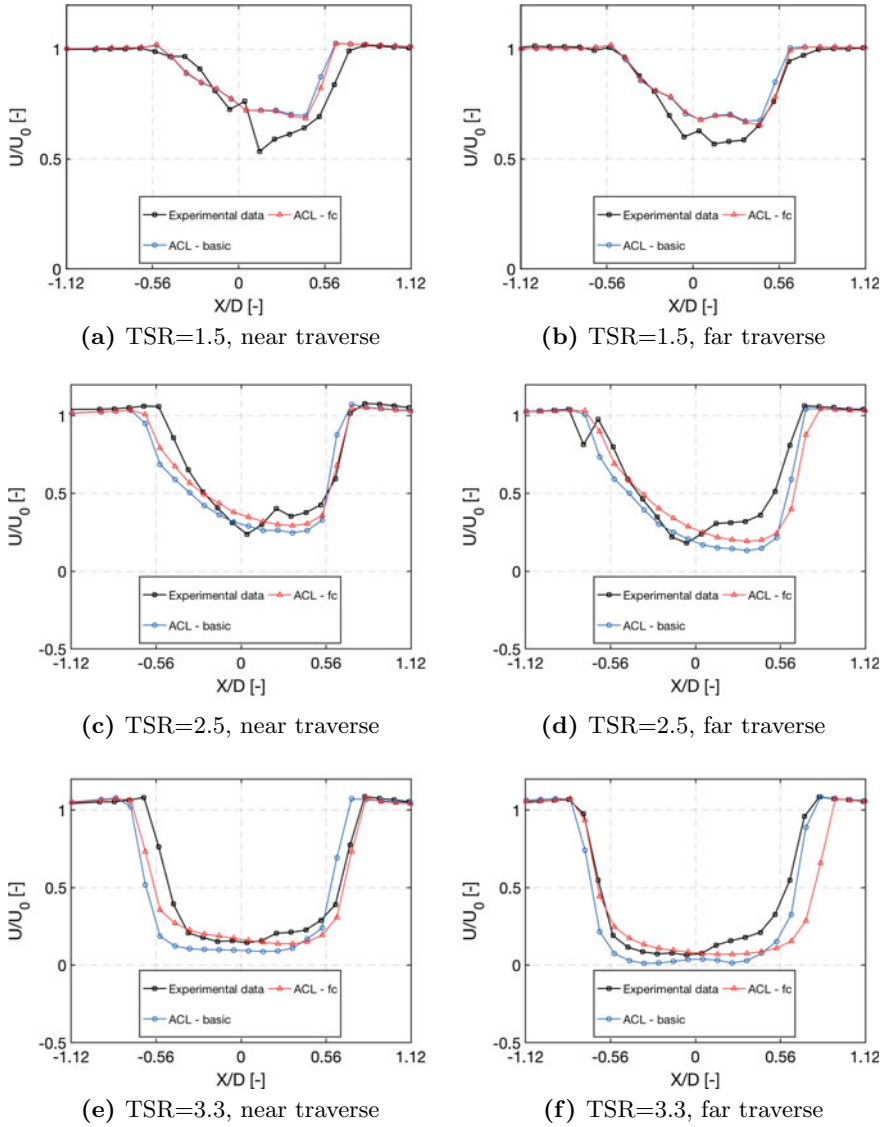


Fig. 11 Turbine wake velocity defect profile on the equatorial plane ($Z/H = 0$) for different loading conditions and combinations of the following sub-models; basic: full polar of NACA0021 airfoil; fc: Migliore’s flow curvature correction

Equatorial region In the midspan region, where the flow field is dominated by the vorticity shed by the single blades due to large aerodynamic loading [3], the code is able to reproduce with a relatively good accuracy the wake profile; in particular, the accuracy of the prediction grows for higher TSRs, as reported in Fig. 11.

At low tip-speed ratios, the wake extension is limited to the turbine front section, due to the relatively low blockage effect offered by the machine. The combination of large angle of attack and low relative speed in the II quadrant results in fact in the onset of dynamic stall (see Sect. 3.3), with corresponding significant drop in blade aerodynamic efficiency C_L/C_D ; for this reason, the maximum velocity defect is shifted towards the I quadrant, where the flow is more stable, ending up in a substantial asymmetry of the wake, progressively reducing downstream [12]. As it can be seen from Fig. 11a, b, all these features are well captured by the ACL simulations, even though the degree of asymmetry of the wake is underestimated with respect to the experimental case; this is probably a result of the inherent inability of the ACL model in reproducing the LE vortex shedding event typical of deep stall.

As the tip-speed ratio increases, the loading and hence the blockage exerted by the turbine on the crossing flow becomes more and more relevant, with the wake extending well beyond the machine front section and further enlarging as it develops downstream; such phenomenon is also highlighted by the over-speed ($U/U_0 > 1$) of the streamlines surrounding the wake itself, reported in Fig. 11f. The reduction in oscillation amplitude of both blade angle of attack and relative speed with respect to the lower TSRs minimizes the influence of dynamic stall, allowing the onset of an high lift condition in both I and II quadrants [12]; the maximum velocity defect zone is thus shifted towards the turbine axis and enhanced in both intensity and extension, leading to a nearly symmetrical wake configuration, with a wide region of stagnant flow. Despite some local differences, the ACL model is able to capture the evolution of the wake maximum velocity defect and the wake width with the increase of tip speed ratio.

In terms of modeling, the wake profiles confirm the progressive higher impact of using flow-curvature corrected polars for increasing TSR; in particular at TSR 3.3, the correction improves the prediction of the wake velocity deficit, as it does for the estimate of rotor aerodynamic forces and turbine performance.

Spanwise wake evolution By virtue of the large data-base of experiments in the wake of the turbine, a comparison is possible along the whole blade height. Figure 12 reports the non-dimensional velocity distributions in the far traverse for simulations and experiments, extending from the midspan section to sections beyond the tip; simulations refer to the model with flow-curvature corrected polars, which exhibited the highest accuracy with the experiments along the whole performance curve of the machine.

As already commented, the midspan section shows a good agreement between experiments and simulations; the flow remains mainly two-dimensional up to about $Z/H = 0.5$. In the subsequent tip region, where the flow becomes fully three-dimensional and is dominated by the trailing vorticity released by the blade extremities [3], the reliability of the code tends to reduce; more in detail, the deviation between CFD simulations and experimental data increases going towards higher TSRs, where the onset of a high load condition on most part of the turbine revolution amplifies the effects of the tip vortex-like structures.

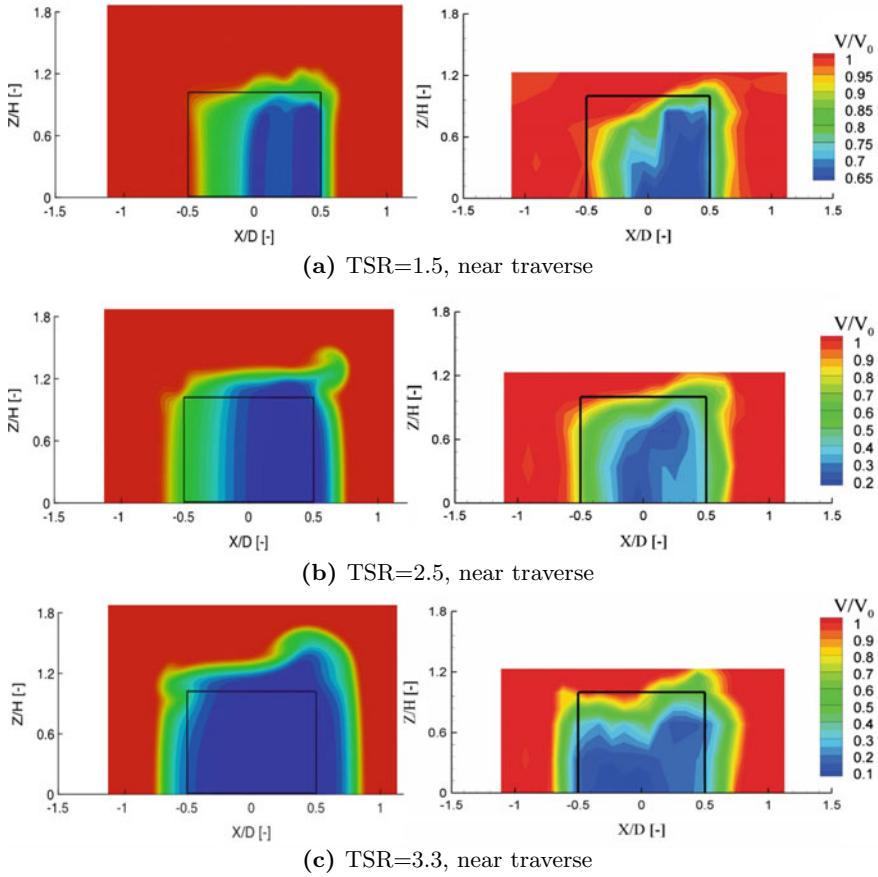


Fig. 12 Turbine wake velocity distributions; left: prediction with the flow-curvature corrected model; right: experiment

As visible from the frames of Fig. 12, the ACL method is able to capture qualitatively the shape assumed by the wake, which is deformed by the presence of persistent tip vortices generated in the upwind region (I and II quadrants), where the blade loading is much higher than in the downwind one (III and IV quadrants). However, the deformation of the wake and especially the enlargement in spanwise direction is not properly captured by the CFD simulations.

At the highest tip-speed ratio (Fig. 12c), wake deformation is almost anti-symmetric with respect to the turbine axis; a strong vortex is shed from the blade tip in the I quadrant, inducing a strong deceleration of the downstream flow. The same phenomenon occurs in the II quadrant, although with lower magnitude and in the opposite direction, leading to a lower deceleration of the corresponding streamtube. Going towards lower loading/lower TSRs (Fig. 12a, b), the strength of the tip

flow structures, together with the corresponding wake deformation, is damped out by the decreasing blade loading; such effect is particularly pronounced on the II quadrant tip vortex due to the periodic onset of stall, leading to a substantial shift of the wake velocity defect towards the I quadrant. With the reduction of loading also the quantitative agreement with the experimental wake profile raises significantly.

In conclusion, although capable to capture the qualitative features of the flow in the tip region, at least at high loading the ACL technique here used does not provide an accurate quantitative estimation of the tip vortex strength. The use of the Glauert's tip correction, not shown for sake of brevity, has only a very minor effect on the wake profile at the tip and does not improve the reliability of the ACL solution. The present results indicate that an interest exists in the development and validation of more advanced correction models for the tip effects. Even though they seem to be of minor relevance for the turbine performance prediction, they might improve the prediction of the three-dimensional profile of the wake, with beneficial effects on the integration between the turbine and the urban environment.

5 Conclusions

This paper has shown that the Actuator Line Method has the potential to become a reliable tool for the design and study of VAWTs, when supported by advanced modeling techniques and numerical schemes, together with an accurate aerodynamic database.

The turbine performance is reproduced with high accuracy by the code over a wide range of operating conditions, once the airfoil polars are extended to include post-stall and deep-stall regions and are corrected in the attached region to account for the flow-curvature effect. However, an additional correction was required in the post-processing phase to account for struts-related drag losses; this correction can be easily eliminated by integrating the support structures in the ACL model of the turbine. Their implementation, together with the one of the central shaft, may also compensate the relatively large deviation between simulations and experimental data observed for the C_x curve.

The present results also indicate that, at least for this turbine, the ACL model does not need a dedicated correction to predict the tip losses. Such correction has proved to be redundant, since the ACL own formulation is able to account, at least in terms of average power extraction, for the three-dimensional features of the flow developing around the turbine blades. In such perspective, also the Berg dynamic stall model has demonstrated to be detrimental for the code accuracy, both in terms of predicted performances and wake shape; dynamic stall models are, therefore, a clear area of future development for the ACL model.

The agreement between predicted and experimental wake shape has also been found to be globally good at midspan, in terms of both wake width and maximum velocity defect. The reliability of the simulations decreases approaching the blade tip, where the flow field is fully dominated by 3D effects, especially for high loading;

in that region nonetheless the model is still able to reproduce qualitatively the most relevant flow features. Further developments on blade end effects are welcomed for capturing with more accuracy the evolution of the tip vortex.

References

1. Battisti L (2012) *Gli impianti motori eolici*. Lorenzo Battisti Editore
2. Battisti L, Persico G, Dossena V, Paradiso B, Castelli MR, Brighenti A, Benini E (2018) Experimental benchmark data for h-shaped and troposkien vawt architectures. *Renew Energy* 125:425–444
3. Battisti L, Zanne L, Dell'Anna S, Dossena V, Persico G, Paradiso B (2011) Aerodynamic measurements on a vertical axis wind turbine in a large scale wind tunnel. *J Energy Resour Technol* 133(3):031201–1–9
4. Berg D (1983) An improved double-multiple streamtube model for the darrieus-type vertical axis wind turbine. In: *Sixth Biennial wind energy conference and workshop*, pp 231–233
5. Bernini L, Caccialanza M (2014) Development of the effective velocity model for wind turbines aerodynamics numerical simulation through an actuator line approach. Master's thesis, Politecnico di Milano
6. Bianchini A, Balduzzi F, Ferrara G, Ferrari L (2016) Critical analysis of dynamic stall models in low-order simulation models for vertical-axis wind turbines. In: *71st conference of the Italian thermal machines engineering association*. Turin, Italy
7. Bianchini A, Balduzzi F, Ferrara G, Ferrari L (2016) Virtual incidence effect on rotating airfoils in darrieus wind turbines. *Energy Convers Manag* 111:329–338
8. Bianchini A, Balduzzi F, Ferrara G, Ferrari L, Persico G, Dossena V, Battisti L (2017) Detailed analysis of the wake structure of a straight-blade h-darrieus wind turbine by means of wind tunnel experiments and cfd simulations. *J Eng Gas Turbines Power* 140(3):032604–032604–9
9. Bianchini A, Balduzzi F, Rainbird J, Peiro J, Graham J, Ferrara G, Ferrari L (2016) An experimental and numerical assessment of airfoil polars for use in darrieus wind turbines - part i: flow curvature effects. *J Eng Gas Turbines Power* 138(3):032602–1–10
10. Bianchini A, Balduzzi F, Rainbird J, Peiro J, Graham J, Ferrara G, Ferrari L (2016) An experimental and numerical assessment of airfoil polars for use in darrieus wind turbines - part ii: post-stall data extrapolation methods. *J Eng Gas Turbines Power* 138(3):032603–1–10
11. Caglioni M (2015) Actuator line method based on the effective velocity model for CFD simulations of vertical-axis wind turbines. Master's thesis, Politecnico di Milano
12. Dossena V, Persico G, Paradiso B, Battisti L, Dell'Anna S, Brighenti A, Benini E (2015) An experimental study of the aerodynamics and performance of a vertical axis wind turbine in a confined and unconfined environment. *J Energy Resour Technol* 137(5):051207–1–12
13. Drela M (1987) Viscous-inviscid analysis of transonic and low reynolds number airfoils. *AIAA J* 25(10):1347–1355
14. Drela M (1989) Xfoil: an analysis and design system for low reynolds number airfoils. In: *Conference on low reynolds number airfoil aerodynamics*. University of Notre Dame
15. Ferlini M (2017) CFD model of a vertical-axis wind turbine in open-jet wind-tunnel. Master's thesis, Politecnico di Milano
16. Franchina N, Persico G, Savini M (2019) 2D–3D computations of a vertical axis wind turbine flow field: modeling issues and physical interpretations. *Renew Energy*
17. Issa R (1986) Solution of the implicitly discretised fluid flow equations by operator-splitting. *J Comput Phys* 62(1):40–65
18. Leishman J (2002) Challenges in modeling the unsteady aerodynamics of wind turbines. In: *21st ASME wind energy symposium and the 40th AIAA aerospace sciences meeting*. Reno, NV, 14–17 Jan 2002

19. Lindeburg C (2003) Investigation into rotor blade aerodynamics. Analysis of the stationary measurements on the uae phase-vi rotor in the nasa-ames wind tunnel 3. Technical report ECN-C-03-025, Energy research center of The Netherlands
20. Marten D, Bianchini A, Pechlivanoglou G, Balduzzi F, Nayeri C, Ferrara G, Paschereit C, Ferrari L (2017) Effects of airfoil's polar data in the stall region on the estimation of darrieus wind turbine performance. *J Eng Gas Turbines Power* 139(2):022606–1–9
21. Massé B (1981) Description de deux programmes d'ordinateur pour le calcul des performances et des charges aérodynamiques pour les éoliennes à axe vertical. Technical report IREQ-2379, Institut de Recherche de l'Hydro-Québec
22. Masson C, Leclerc C, Paraschivoiu I (1998) Appropriate dynamic-stall models for performance predictions of vawts with nlf blades. *Int J Rotating Mach* 4(2):129–139
23. Melani PF (2018) Experimental assessment of an actuator line simulation tool for vertical axis wind turbines. Master's thesis, Politecnico di Milano
24. Menter F (1994) Two-equation eddy-viscosity turbulence models for engineering applications. *AIAA J* 32(8):1598–1605
25. Migliore P, Wolfe W (1980) The effects of flow curvature on the aerodynamics of darrieus wind turbines. Technical report ORO-5135-77/7, U.S. Department of Energy
26. Paraschivoiu I (2002) Wind turbine design: with emphasis on darrieus concept. Polytechnic International Press, Québec
27. Persico G, Dossena V, Paradiso B, Battisti L, Brighenti A, Benini E (2017) Time-resolved experimental characterization of the wakes shed by h-shaped and troposkien vertical axis wind turbines. *J Energy Resour Technol* 139:031203–1–11
28. Schito P (2012) Large eddy simulation of wind turbines: interaction with turbulent flow. PhD thesis, Politecnico di Milano
29. Schito P, Zasso A (2014) Actuator forces in cfd: rans and les modeling in openfoam. In: The science of making torque from wind 2014 (TORQUE 2014)
30. Shamsoddin S, Agel FP (2014) Large eddy simulation of vertical axis wind turbine wakes. *Energies* 7(2):890–912
31. Sheldahl R, Klimas P (1981) Aerodynamics characteristics of seven symmetrical airfoil sections through 180-degree angle of attack for use in aerodynamic analysis of vertical axis wind turbines. Technical report SAND80 2114, Sandia National Laboratories, Albuquerque, New Mexico
32. Timmer W (2010) Aerodynamic characteristics of wind turbine blade airfoils at high angles-of-attack. In: TORQUE 2010 - the science of making torque from wind. Crete, Greece, p 71, 28–30 June 2010
33. Viterna L, Corrigan R (1981) Fixed pitch rotor performance of large horizontal axis wind turbines. Technical report CP-2230, NASA, USA

Wind Regimes in Urban Environments: Experimental Comparison with the IEC 61400.2-2013 Open Terrain Wind Model



Muhammad Iftekharul Rakib, Shaun Nay, Samuel Evans and Philip Clausen

Abstract Small wind turbines are usually sited in more complex environments than the open terrain sites, such as urban built environment. However, the international small wind turbine design standard IEC61400.2 is based on the measurements of flat and open terrain. Failures of SWTs operational in urban area predicts the inadequacy of turbine design for the turbulent wind resource at the sites. This study investigates the wind speed in the vertical direction at a complex terrain site, where a small 5 kW Aerogenesis horizontal-axis wind turbine is in operation and subject to an ongoing research. Wind measurements were acquired at 20 Hz using 3 three-axis ultrasonic anemometers equispaced around the tower of the wind turbine. The results show significantly high wind speeds ($8\text{--}12\text{ ms}^{-1}$) in the vertical direction. High fluctuation of vertical wind speed was observed with standard deviation $>2\text{ ms}^{-1}$. In addition, the turbulence in vertical direction was found to be 20% higher than the IEC 61400.2 level. The result of this study is important for the small wind turbine developers as they seek best practice for determining turbine operating loads.

Keywords Urban environments · Small wind turbines · IEC wind model

1 Introduction

Commercial scale wind turbines are typically sited in regions of open terrain wind resource in order to minimize the levelized cost of energy (LCOE) [1]. Recently, there has been an increasing tendency of installing small-scale wind turbines in non-open terrain, such as in urban areas [2]. Small wind turbines (SWTs) are defined by the International Electrotechnical Commission standard IEC 61400.2-2013 Wind Turbines Part 2: Design requirements for small wind turbines as having a swept area less than 200 m^2 , and they have usually been installed in off-grid areas in open terrain exposed to the wind [3]. In both the US and UK, where significant markets

M. I. Rakib (✉) · S. Nay · S. Evans · P. Clausen
School of Engineering, The University of Newcastle, Callaghan, NSW 2308, Australia
e-mail: MuhammadIftekharul.Rakib@uon.edu.au

© Springer Nature Switzerland AG 2019
L. Battisti (ed.), *Wind Energy Exploitation in Urban Environment*,
Research Topics in Wind Energy 8, https://doi.org/10.1007/978-3-030-13531-7_12

201

for SWTs have been established, the proportion of systems that are grid-connected is increasing whereas the proportion of systems off-grid is decreasing [4, 5].

Unlike open terrain that is mostly flat and free of obstacles such as tree and buildings, urban wind environments are not leading to wind flow that can be rapidly fluctuating and turbulent [6]. This results from various factors including high surface roughness, the interaction between incoming flows and complex local building structures, and atmospheric instabilities caused by local heat sources [7]. IEC61400.2 standard (hereinafter referred to as *the IEC standard*) details design wind conditions for four turbine classes (based on open-terrain inlet wind conditions), and a ‘special’ class whereby the user can define a wind condition for a specific site. *The IEC standard* states that random turbulent fluctuations are assumed to have a zero-mean Gaussian distribution [3]. However, Sunderland et al. [8] concluded that a Weibull distribution better accounted for the effects of turbulence in urban sites. The standard also defines inlet wind turbulence through the normal turbulence model (NTM). In this case, turbulence intensity is defined as the ratio of standard deviation to mean wind velocity within a 10 min sample period. A mean turbulence level is defined for turbine design, however, studies have shown that this may not be fully adequate for complex terrain sites, or built environment locations [2, 9, 10]. *The IEC standard* specified Kaimal and Von Karman turbulence models were developed for flat and open terrain inlet conditions [11]. While these may be appropriate for commercial wind farm installations, the same is not necessarily true for small wind turbine installations. Therefore, it is needed to investigate and assess the appropriateness the NTM and the respective von Karman and Kaimal turbulence models for non-open terrain.

Urban built environment sites may experience turbulence intensity many times greater than an open field site [2]. Many rooftop installations have suffered damage due to poor siting and failing to undertake a sufficient wind resource feasibility study prior to installation [4, 12–14]. A wind resource assessment is essential for all wind projects identifying the exact and real situation that the wind turbine will experience [11]. Wind monitoring campaigns, therefore, render an important role for assessing the turbulence of any given site. Notably, the turbine blade’s fatigue life and power output are significantly affected by the level of turbulence [11]. There have also been some notable failures of small wind turbines in the built environment [15, 16]. There are many indications that these failures are related to inadequate turbine design considering the wind resource at the turbine site [4]. Importantly, most of these complex terrain sites are usually characterised by highly turbulent wind flow. *The IEC standard* is based on wind turbines in open terrain and does not include specific design parameters for highly turbulent sites. These turbines are often installed in the built environment, nevertheless, there is no indication in *the IEC standard* about the suitability and accuracy of the aforementioned models for such an environment [6, 11].

Tabrizi et al. [1, 4, 10] studied turbulence power spectra for SWTs installed on the rooftop of a warehouse in the built environment. The studies found the wind at the site was highly three-dimensional. It also included the effect of different sampling rates on the power spectral density of the longitudinal, lateral and vertical component of turbulent wind fluctuation in neutral and slightly unstable atmospheric conditions for different heights. The studies suggested that an assessment with sonic anemome-

ter with a sampling rate of 10 Hz (or above) could predict an accurate turbulence intensity in vertical direction when a large fluctuation of vertical wind speed was present. *The IEC standard* suggests the standard deviation of the wind speed in the vertical direction is half of the standard deviation of longitudinal wind speed [3]. However, to the best of the authors' knowledge, it is not experimentally verified by any previous or recent studies. Therefore, the wind resource assessment campaigns at a site located in a built environment particularly focused on the wind characteristics in vertical direction is necessary. This paper discussed an experimental assessment of wind resource in urban environment and its characteristics in vertical direction using three ultrasonic anemometers at a data-sampling rate of 20 Hz. It also includes a comparison with *the IEC standard's* open terrain wind model.

2 Methodology

2.1 Aerogenesis 5 KW Wind Turbine

The wind Turbine Group at the University of Newcastle has an experimental small horizontal-axis 2-bladed 5 kW Aerogenesis wind turbine located on the University's Callaghan campus. This wind turbine (Fig. 1) is being used for research purpose and does not supply power to the grid. The turbine blades are constructed from glass fibre reinforced polymer and are 2.5 m long. The turbine has a rated power generation capacity of 5 kW at a wind speed of 10.5 ms^{-1} and has a design rotor speed of 320 rpm at a tip speed ratio of 8. The turbine has a self-excited induction generator with a variable speed control system in order to maintain the design tip speed ratio. The wind turbine is mounted on top of an 18 m high monopole tower which is hinged halfway up to allow easy access to the turbine for maintenance and instrumentation purposes. The turbine was designed as an IEC class III turbine with an average wind speed of 7.5 ms^{-1} . The location of the wind turbine can be described as a complex terrain as it is surrounded by a car park, trees and vegetation, an electrical substation, open field, train station and rail lines, and commercial and residential buildings [11]. A satellite map of the site has been shown in Fig. 2.

2.2 Wind Resource Assessment

An ultrasonic anemometer is an instrument that measures the wind speed and direction by detecting variations in the speed of ultrasound (sound waves whose frequency is above the range of human hearing) transmitted between fixed points [17]. It captures the difference in time taken for an ultrasonic pulse to travel in each direction between pairs of transducers caused by motion of the wind. In this project, three 3D ultrasonic WindMaster anemometers, manufactured by Gill Instrument, UK, are



Fig. 1 Overview of the 5 kW Aerogenesis turbine

being used to measure the wind speed in three mutually perpendicular directions at the turbine site. As they have no rotational inertia, sonic anemometers are more responsive to rapid speed and direction fluctuations than cup or propeller anemometers [18], and are therefore more accurate.

The three anemometers are mounted at a height of 15 m on the wind turbine tower and are equispaced at 120° around the tower. The anemometers are installed this way in order to remove the tower shadow effect in the wind data collection process. The wind data from the anemometers are acquired at a rate of 20 Hz using an ATEN-UC4854 USB-hub data logging system and controlled by a computer in the site control room approximately 30 m from the turbine. The system runs continuously and obtains the wind data using WindView software. The acquired data includes time, vertical wind speed, two horizontal wind speeds, and temperature. All the data collected by the anemometers are processed and analysed by code written in Matlab. All the data have been processed removing the tower shadow effect by Matlab script. To date, some four and a half months of data has been acquired and analysed.

The wind speeds for this research were instantaneously recorded at 20 Hz. The instantaneous horizontal wind speed and wind flow direction were calculated using



Fig. 2 Location of Aerogenesis turbine (red circle) at the University of Newcastle, Callaghan. A 200 m radius surrounding the turbine is indicated in black circle (Google Maps, 2018)

$$U_{inst} = \sqrt{U_x^2 + U_y^2} \quad (1)$$

$$\theta = \tan^{-1} \frac{U_y}{U_x} \quad (2)$$

$$U_{vertical} = U_z \quad (3)$$

where U_x , U_y and U_z are the components of the instantaneous horizontal wind speed (ms^{-1}) in x, y and z directions, respectively. All the data obtained from the WindView were processed in Matlab. After obtaining the corrected wind velocity U_{inst} and adjusting the time, the data was then suitable for a variety of necessary calculations. U_{inst} and $U_{vertical}$ are used to compute the 10 min average wind speed U_{10min} , and 10 min average wind speed in vertical direction.

The anemometers were mounted around the tower as mentioned the angular position in Fig. 1. The north spar of all the anemometers were kept close to 0° degree with North. After mounting the anemometers on the tower, a survey was conducted

in order to determine the true position of the north/reference spars. Theodolite station and reflectors were used for the surveying and the methodology of traversing was followed. The angular displacement of north-spars with respect to true north was considered for estimating the wind flow direction during the post-process of wind data. Ultrasonic data that retrieved from the University of Newcastle wind turbine tower are extremely valuable for investigating the wind speed in vertical direction at Callaghan site or urban environment.

2.3 Normal Turbulence Model

To characterize the turbulent velocity and estimate dynamic loads, the probability density function of wind fluctuations is expressed as a Gaussian distribution. *The standard* uses a normal turbulence model to describe turbulence and turbulence intensity [3]. The characteristic value of the standard deviation of the longitudinal wind velocity is given by

$$\sigma_1 = I_{15}(15 + aV_{hub})/(a + 1) \quad (4)$$

where, I_{15} is the characteristic longitudinal turbulence intensity for $V_{hub} = 15 \text{ ms}^{-1}$, a is a dimensionless slope parameter, and V_{hub} is the magnitude of the three dimensional wind speed at the hub averaged over 10 min. The characteristic longitudinal turbulence intensity is expressed as the 90th percentile of longitudinal turbulence intensity measurements binned with respect to wind speed, assuming a Gaussian distribution.

From *the standard*, I_{15} and a are 0.18 and 2 respectively. Nevertheless, these values are site dependant but they are prescribed for all kind of small wind turbine classes. This simplification allows designers to use typical values instead of undertaking expensive monitoring campaigns at specific sites. Equation (4) thereby reduces to:

$$\sigma_1 = 0.9 + 0.12V_{hub} \quad (5)$$

Equation (5) can be rearranged in terms of longitudinal turbulence intensity (I_u) as follows:

$$I_u = \frac{\sigma_1}{V_{hub}} = \frac{0.9}{V_{hub}} + 0.12 \quad (6)$$

Stork et al. [19] suggested Eq. (6), which is based on the assumptions of flat and open terrain and hub-height wind speed ranging from 10 to 25 ms^{-1} .

The NTM is the basis of turbulence spectral parameters for Kaimal model that prescribes the relationship between the standard deviation of longitudinal and vertical wind speed. The turbulence spectral parameters for Kaimal model are mentioned in Table 1. Here k is the index referring to the velocity component direction (i.e.

Table 1 Turbulence spectral parameters for Kaimal model

	Velocity component index (k)		
	1	2	3
Standard deviation, σ_k	σ_1	$0.8 \sigma_1$	$0.5 \sigma_1$

1 = longitudinal, 2 = lateral, and 3 = vertical). The standard deviation of wind speed in the vertical direction is described as $0.5\sigma_1$. Here, σ_1 is the standard deviation of longitudinal wind speed [3]. This relationship would be compared with the experimentally collected wind data at the Callaghan site.

3 Results and Discussions

3.1 IEC Wind Model and Comparison with the Callaghan Site Data

Approximately four and a half months of detailed wind data has been recorded at the wind turbine site. Wind speed in 3-axis and longitudinal wind direction were recorded at a rate of 20 Hz for the duration of measurement campaign. Figure 3 shows a scatter plot of 10 min standard deviation with respect to 10 min average wind speed. The longitudinal standard deviation in wind speed specified by the standard is also plotted. The UoN measured data 90th percentile fit shows that the 10 min standard deviations for the 10 min average wind speeds $>2.8 \text{ ms}^{-1}$ are higher than that prescribed by the standard. This follows a similar—albeit more extreme trend than reported by Tabrizi et al. [1]. The 10 min standard deviations for the 10 min average wind speeds $<2.8 \text{ ms}^{-1}$ are lower than that described by the standard. It also shows a number of extreme events with large standard deviation ($\sigma_1 > 2.5 \text{ ms}^{-1}$) occurred at high wind speeds that may have been related to high turbulence.

3.2 Vertical Component of Wind Velocity

High fluctuation of wind speed in vertical direction reported by Tabrizi et al. [12], have also been measured at the Callaghan site. Nevertheless, most of the time of the four and half months measurement campaign, the longitudinal wind speed was less than 5.0 ms^{-1} and vertical wind speed less than 1.0 ms^{-1} in both the positive and negative directions, as shown in the histograms in Fig. 4. Around 25% of time the wind speed in longitudinal direction was higher than the turbine cut-in speed 3.5 ms^{-1} and the average longitudinal wind speed was 2.5 ms^{-1} (Fig. 4a). During the measurement campaign, less than 1% of wind speed in vertical direction was

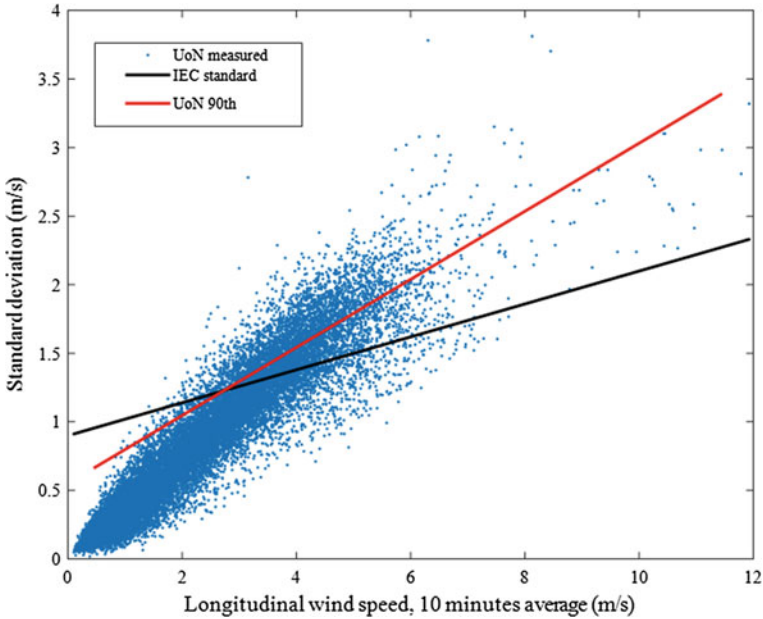


Fig. 3 Statistics for measured site turbulence and that specified by the *IEC standard*

found to be greater than 3.5 ms^{-1} in positive or negative direction (Fig. 4b). In many cases, the value of vertical wind speed was found to be reached 12 ms^{-1} in both positive and negative direction. However, the acquired wind data contains (less than 1%) significantly high vertical wind speed ($8\text{--}12 \text{ ms}^{-1}$) and should be considered as it caused high fluctuation of wind speed or gust in the vertical direction, which the *standard* has not fully accounted.

The standard deviation of vertical wind speed was plotted against the 10 min average vertical wind speed as shown in Fig. 5. It shows a number of extreme events with large standard deviation ($\sigma_3 > 2 \text{ ms}^{-1}$) that may have led to high fluctuation of the wind speed in the vertical direction. The Fig. 5 also implies that this wind turbine site, located in urban built environment, is highly turbulent.

In the *IEC standard*, the power spectral densities describing the wind velocity components (x, y, and z axis) are mentioned as the turbulence spectral parameters for Kaimal spectral model. The standard deviation of wind speed in the vertical direction is defined as $0.5\sigma_1$ in the *IEC standard* (Table 1). However, the Fig. 6 shows the standard deviation in the vertical direction of the measured wind speed at the Callaghan site to be $0.6\sigma_1$ (slope of the line presented in Fig. 6) showing the *IEC standard* underestimated the wind turbulence in the vertical direction.

Wind turbines are fatigue critical machines and are similar in this aspect to other rotary machines [11]. Investigating high wind speed in vertical direction could have important implications for a safe wind turbine design. A high vertical component of wind speed ($8\text{--}12 \text{ ms}^{-1}$) was observed in both positive and negative directions

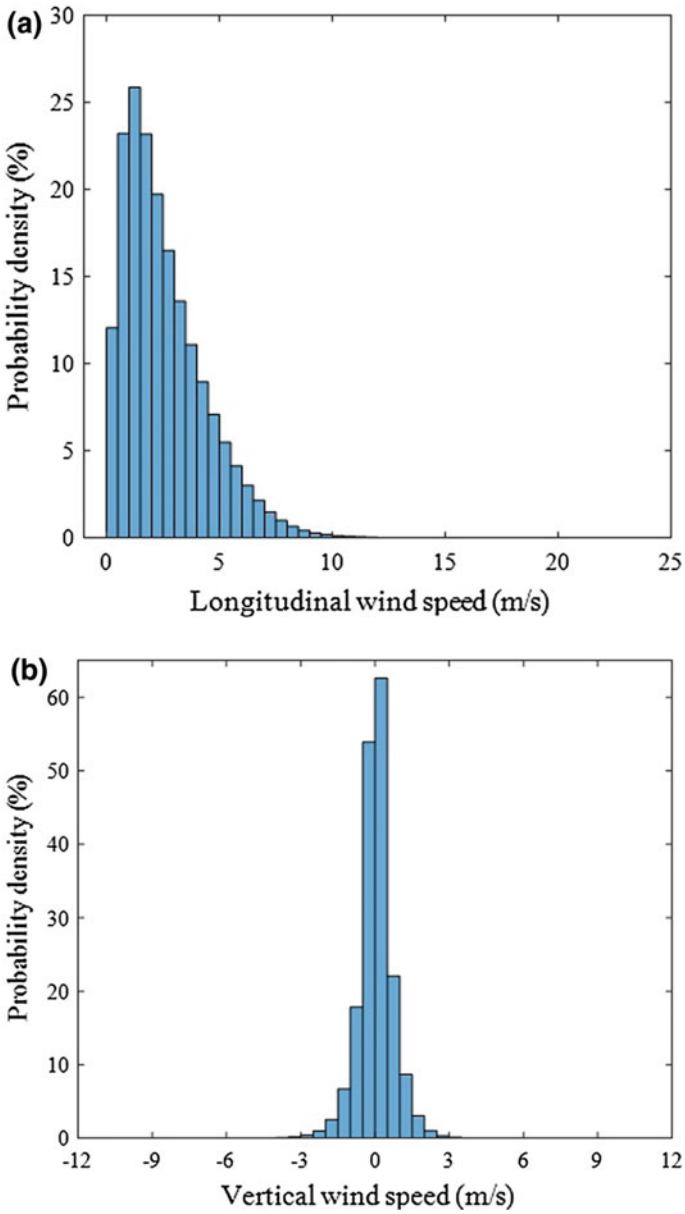


Fig. 4 Histogram of wind speed in a longitudinal and b vertical direction

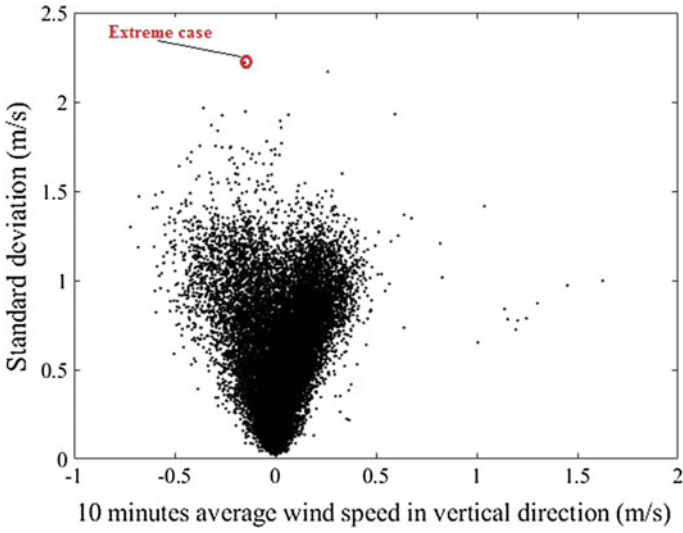


Fig. 5 Turbulence of wind speed in vertical direction

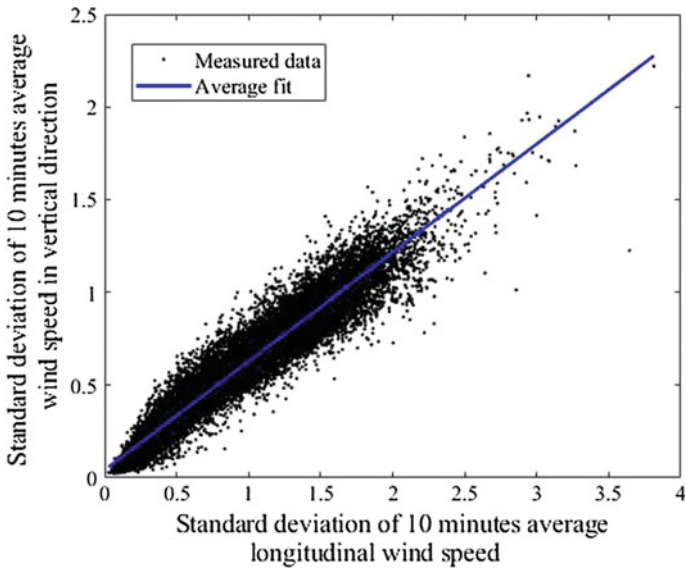


Fig. 6 Relation between the standard deviation of 10 min average vertical wind speed and longitudinal wind speed

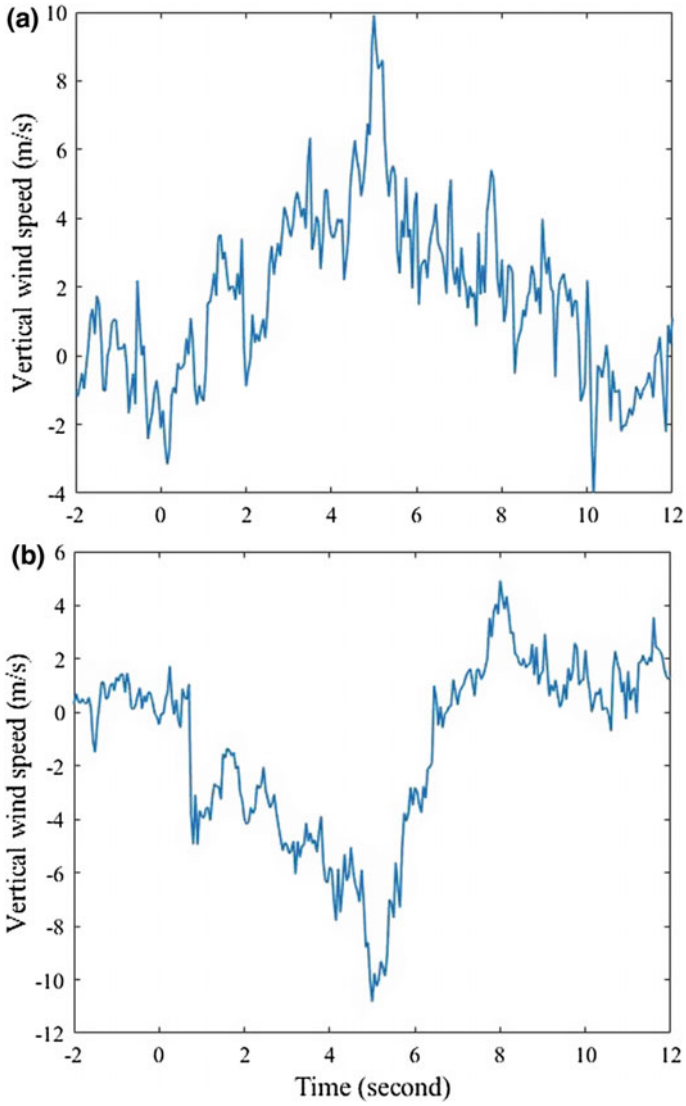


Fig. 7 Example of high wind speed in vertical axis along a positive and b negative direction

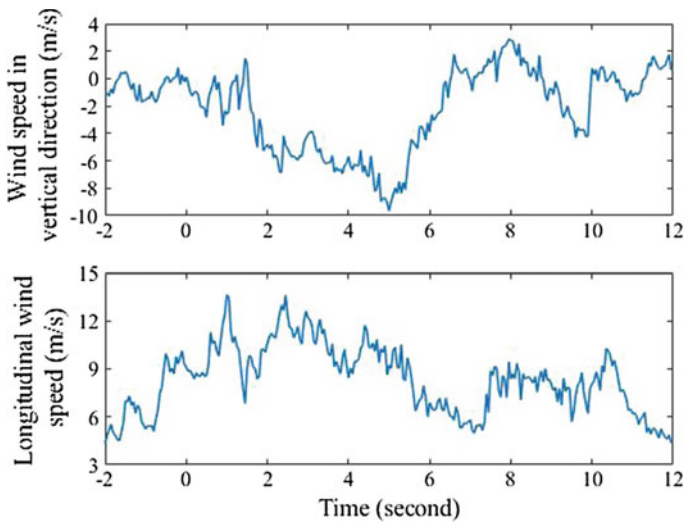


Fig. 8 An example of high wind speed in vertical direction coincident with high longitudinal wind speed

at the Callaghan site. Figure 7 shows examples of instantaneous high wind speed in the vertical direction, both positive and negative cases, with the magnitude of the vertical wind speed around 10 ms^{-1} and lasting for 2–4 s. In addition, high longitudinal wind speed was also observed during these high vertical wind speed events. An example has been shown in Fig. 8, at the time of a negative vertical wind speed of 9 ms^{-1} coinciding with a longitudinal wind speed is 13 ms^{-1} . The resultant velocity is 15.8 ms^{-1} and acts at an angle of 55° to with the longitudinal wind velocity component. The effects of large vertical instantaneous wind velocities on both the aerodynamic and structural performance of a wind turbine is unknown and needs to be explored in detail. Nevertheless, the normal wind profile model used in *the IEC standard* does not put adequate importance on the wind speed in vertical direction, and needs to be included as an increasing number of small wind turbines are expected to be installed in the built environment.

4 Conclusions

In this study, detailed wind velocity measurements have been undertaken at a complex terrain urban site used for a small wind turbine. To the best of the authors' knowledge, the wind speed in the vertical direction at an urban site has not previously been investigated experimentally in detail. The wind assessment was conducted using three ultrasonic anemometers installed 15 m above the ground and 3 m below the hub height of a 5 kW horizontal-axis wind turbine. The wind data was collected at a sampling rate of 20 Hz. The turbulence of wind resource at Callaghan site was

measured and compared with the IEC 61400.2 normal turbulence model. The results of this investigation show that:

1. Significantly high value wind speed ($8\text{--}12\text{ ms}^{-1}$) in vertical direction is present at the Callaghan site;
2. Highly turbulent wind speeds were found in vertical direction having a standard deviation of greater than 2 ms^{-1} .
3. Turbulence in vertical direction was found to be higher than the level assumed in the IEC standard. The standard deviation of wind speed in the vertical direction is given as $0.5\sigma_1$ in the IEC standard, whereas, it was measured to be $0.6\sigma_1$, that is 20% higher than the assumed level.

Further research effort are required to investigate the height effect on the wind speed in vertical direction. In addition, the effect of turbulent vertical wind speed on wind turbine structure will be investigated. For this, aeroelastic simulations using the turbulent vertical wind speed data will be conducted in order to calculate its effect on structural loading and fatigue life.

References

1. Tabrizi AB, Whale J, Lyons T, Urmee T, Peinke J (2017) Modelling the structural loading of a small wind turbine at a highly turbulent site via modifications to the Kaimal turbulence spectra. *Renew Energy* 105:288–300
2. Evans SP, Bradney DR, Clausen PD (2018) Assessing the IEC simplified fatigue load equations for small wind turbine blades: how simple is too simple? *Renew Energy* 127:24–31
3. IEC 61400.2-2013 Wind turbines—design requirements for small wind turbines (2013)
4. Tabrizi AB, Whale J, Lyons T, Urmee T (2015) Rooftop wind monitoring campaigns for small wind turbine applications: effect of sampling rate and averaging period. *Renew Energy* 77:320–330
5. Whale J, McHenry MP, Malla A (2013) Scheduling and conducting power performance testing of a small wind turbine. *Renew Energy* 55:55–61
6. Evans SP, Anup KC, Bradney DR, Urmee TP, Whale J, Clausen PD (2017) The suitability of the IEC 61400-2 wind model for small wind turbines operating in the built environment. *Renew Energy Environ Sustain* 2:31
7. Britter R, Hanna S (2003) Flow and dispersion in urban areas. *Annu Rev Fluid Mech* 35(1):469–496
8. Sunderland K et al (2013) Small wind turbines in turbulent (urban) environments: a consideration of normal and Weibull distributions for power prediction. *J Wind Eng Ind Aerodyn* 121:70–81
9. Wilson S, Clausen P (2007) Aspects of the dynamic response of a small wind turbine blade in highly turbulent flow: part 1 measured blade response. *Wind Eng* 31(1):1–16
10. Tabrizi AB, Whale J, Lyons T, Urmee T (2015) Extent to which international wind turbine design standard, IEC61400-2 is valid for a rooftop wind installation. *J Wind Eng Ind Aerodyn* 139:50–61
11. Evans S (2017) Aeroelastic measurements, simulations, and fatigue predictions for small wind turbines operating in highly turbulent flow, in School of Engineering. The University of Newcastle, Australia
12. <http://www.bergeng.com/technical/warwick-trials-of-building-mounted-wind-turbines>

13. <http://www.cyclopicenergy.com/news/20100812-TurbineFailureHobart/Hobart-Marine-Board-Turbines.shtml>
14. Tabrizi AB, Whale J, Lyons T, Urmee T (2014) Performance and safety of rooftop wind turbines: use of CFD to gain insight into inflow conditions. *Renew Energy* 67:242–251
15. American wind energy association (2011) U.S. Small wind turbine market report, year ending
16. Foster R, Ghassemi M, Cota A (2009) *Solar energy: renewable energy and the environment*. CRC Press, Boca Raton
17. Brower M (2012) *Wind resource assessment: a practical guide to developing a wind project*. Wiley, New York
18. Antonio O (2017) *Extreme wind speed estimation for calgary*. University of Calgary, Calgary, Alberta
19. Stork CHJ, Butterfield CP, Holley W, Madsen PH, Jensen PH (1998) Wind conditions for wind turbine design proposals for revision of the IEC 1400-1 standard. *J Wind Eng Ind Aerodyn* 443:74–76

Structural Optimisation of 3D Printed Small Diffuser Augmented Wind Turbine Blade Using Bi-directional Evolutionary Layout Optimisation Method



Mariana S. P. da Costa, Joss Kesby and Philip D. Clausen

Abstract This paper briefly describes the optimisation method and presents the results of the theoretical structural optimisation of a small wind turbine blade. The bi-directional evolutionary layout optimisation method was applied to the design of a 3D printed blade suitable for a diffuser augmented wind turbine. The turbine blades were manufactured (printed) with PET-G polymer, which required the mechanical properties of the material to be determined prior to the finite element modelling of the blade. Blade material properties used in this study were determined by means of simulation, with the aid of experimental results. This paper also presents the experimental results of the PET-G material analysis. After applying the bi-directional evolutionary layout optimisation method to the blade, a 15% reduction in blade mass was achieved without compromising its structural integrity.

Keywords Small turbine blades · 3D print · Structural optimisation · BELO method

1 Introduction

In the current global scenario, renewable energy sources are becoming more important as they will help to drive down global carbon dioxide emissions in a cost-effective manner. Investment in all forms of renewable energy technology is growing and wind energy is following this trend. Most of the research and development undertaken on wind turbines to date has focused on large wind turbines. Small wind turbines have seen limited investment including a subset of small wind turbines, Diffuser Augmented Wind Turbines (DAWTs). A DAWT is a turbine usually housed concentrically in a cylindrical shrouding with inlet and exit diffusers fitted to the shrouding. The diffuser typically has an aerofoil shaped cross section and it is used to increase

M. S. P. da Costa (✉) · J. Kesby · P. D. Clausen
Faculty of Engineering and Built Environment, School of Engineering, The University of Newcastle, University Drive, Callaghan, NSW 2308, Australia
e-mail: c3106982@uon.edu.au

© Springer Nature Switzerland AG 2019
L. Battisti (ed.), *Wind Energy Exploitation in Urban Environment*,
Research Topics in Wind Energy 8, https://doi.org/10.1007/978-3-030-13531-7_13



Fig. 1 Diffuse energy DAWT

the turbine's power output by increasing the wind speed through the rotor plane of the turbine; Fig. 1 shows a DAWT.

Research studies into DAWTs began in the 1950s, however, it was not until the late 1990s that research interest significantly increased [1]. DAWTs have several advantages over open-bladed wind turbines, including reduced sensitivity to turbulence, better resistance to fatigue, lower operating noise and same power generation at lower torque [2].

As small wind turbines are often used for off-grid power generation and placed close to where the power is needed (such as on roof tops or next to buildings in the urban environment), the location of the turbine may not offer good wind resource. Some of the advantages that DAWTs have over open-bladed turbines make them better candidates for these applications.

The University of Newcastle wind energy group has combined the research of DAWT with rapid manufacturing process (3D printing) and has successfully developed a prototype. This DAWT prototype is entirely 3D printed and capable of 35 W power output at its rated wind speed of 10 m/s. The use of rapid manufacturing processes has allowed the DAWT blades to be specifically tailored for the turbine operating conditions. The six-bladed turbine was manufactured (printed) with PET-G material. Each blade is close to 146 mm long and weighs approximately 320 grams. The shape of the turbine blades and the exit diffuser were simultaneously optimised to maximise the turbine's annual energy production in a "typical" wind environment [3]. The optimisation design process of the turbine and diffuser considered the power output, cut-in wind speed and starting time of the turbine [3].

The cross-sectional shape of a small wind turbine blade is mostly dictated by aerodynamic considerations, with the blade structural design dictated by both uli-

mate and fatigue strength considerations, as well as manufacturing costs. Designing blade structure using the simplified load model from IEC standard [4] leads to an overly conservative design resulting in heavy and possibly costly blades. Optimising the blade structure can significantly reduce its mass and consequently is likely to reduce manufacturing costs leading to an overall reduction in turbine cost. Furthermore, reduction in blade mass will reduce blade inertia, which is likely to reduce the gyroscopic moment on the blade and the starting time of the wind turbine.

To minimise the material used in the blade without affecting blade strength and its operating longevity, the bi-directional evolutionary layout optimisation (BELO) method developed to redesign material layout of the outer shell of a blade's composite structure based on a strain energy criterion [5], will be used. The BELO method was originally developed to take into consideration blade stiffness as well as fatigue life. However, as the DAWT prototype has only been recently developed, no fatigue data is available for the material used to manufacture the blades and therefore this study will only take into consideration the blade's stiffness.

The BELO method is based on the bi-directional evolutionary structural optimisation method (BESO) [6], mostly used for topology optimisation of stationary structures [7]. Usually combined with finite element analysis (FEA), the basic idea behind the BESO method is to remove unnecessary structural material and add material to weaker parts of the structure [7]. The BELO method is used for the optimisation of wind turbine blades, as it does not alter the blade's geometry. In the BELO method, elements are not added or removed from the design domain, they are replaced by other elements of different stiffness, as opposed to the BESO method that alters the geometry of the structure within the design domain by adding or removing elements.

As the optimisation method requires an accurate finite element model of the blade, an investigation of the PET-G material mechanical properties was undertaken. To the best of the authors' knowledge, PET-G material mechanical properties (for 3D printed structures) have not been extensively reported in the open literature. Szykiedans [8] performed experimental tests with solid samples of PET-G, whereas in this study the PET-G samples were printed to match the blade's geometry (solid outer shell with honeycomb internal structure). Despite the different geometry of the samples, Young's Modulus of Elasticity values determined by [8] were calculated using the same method and yielded similar results to the ones found in this study.

To determine the relevant mechanical properties of PET-G, Young's Modulus of elasticity, E , and the material's ultimate strength, two experiments were undertaken: a three-point bending test, using PET-G beam samples and a deflection test, and subjecting the 3D printed blade to a point load and recording its tip deflection. Results from both tests were used to aid the modelling process with further details presented in Sect. 3 of this paper.

Due to the layer-by-layer procedure of the 3D printing process, PET-G behaves with anisotropic characteristics and its mechanical properties will depend on the direction used to print the object. In the particular case of a wind turbine blade, the printing direction must be vertical and along the length of the blade. If the blade is printed horizontally, the supports needed during the process cause the blade surface to be very rough, altering the blade's aerodynamic characteristics. For the purposes of

calibrating the blade model and verifying its stiffness after the optimisation method has been applied, only the deflection on the direction perpendicular to length of the blade is relevant. Furthermore, to simplify the experimental and modelling tasks the PET-G material is treated as isotropic in this study.

This paper has 5 sections. In Sect. 2, the optimisation method, its parameters and details on the blade model used in this study will be explained. Section 3 presents the experiments on PET-G material properties and their results. Section 4 presents the optimisation results and Sect. 5 contains a discussion on the implication of the results to the blade structure.

2 Method

2.1 Modelling Overview

The BELO method [5] was specifically developed to minimise the amount of material used within the structure of wind turbine blades without affecting blade strength and fatigue life. The iterative BELO method needs to interface with finite element analysis software. In this study, a MATLAB script interfaced with Strand7 finite element software via Strand7's application-programming interface (API).

The API was used to implement the optimisation routine and also to aid the modelling process. The BELO method requires an accurate model of the blade's very complex geometry, but accuracy cannot be guaranteed when blade modelling is done using a simplified representation of the blade's structure. Use of the API has allowed for high precision when placing the nodes and elements that define the basic shape of the blade structure in the FE model.

The BELO method uses a strain energy criterion for rearranging the material distribution on the outer shell of the blade [5]. The strain energy, U [J], stored in a solid due to deformation under load is given by:

$$U = \frac{1}{2}k * \delta^2 \quad (1)$$

where k is the material stiffness and δ is the displacement. The complete formulation of strain energy can be found at [9].

The outer shell of the blade model is constructed using low-order plate elements. The 3D printed DAWT blade used in this study has a honeycomb shape internal structure that it is not included in the optimisation process. The internal structure of the blade was reproduced in a FE model using low-order brick elements, however important for the accuracy of the model, the internal structure remains unchanged throughout the optimisation process.

The 35 W DAWT blade was manufactured (3D printed) with a single material (PET-G). As such, the optimisation only alters the thickness of the outer skin of the

blade. In this study, the material thickness varies in a range of 1.1–2 mm in steps of 0.1 mm. The E value of the PET-G material was computationally determined, with the aid of experimental measurements; results of the experiments can be found in the next section of this paper.

At this point, it is important to note that the blade model does not include the attachment block used to connect the physical blade to the turbine's hub. However, the blade model is restrained appropriately to represent the connection between blade and attachment block. The blade FE model was aerodynamically and centrifugally loaded with the maximum operational loads for the 35 W DAWT, which occur at 1470 rpm and 10 m/s wind speed. The aerodynamic load was determined by Blade Element Moment (BEM) theory, using BEM code written specifically for DAWT blades [3]. No gravitational effects were considered, as they are typically ignored for small wind turbines [10].

2.2 BELO Optimisation

Strain energy is the parameter used in the BELO method to determine the material property allocation in the blade's external skin. Before the optimisation can be implemented, key optimisation parameters must be decided. Firstly, the strain energy range needs to be determined. This can be achieved by observing the minimum and maximum strain energy values found in the blade model elements under design loading when the blade is constructed with a single material property. The strain energy intervals, g , are calculated according to:

$$g = \frac{U_{max} - U_{min}}{p - 2} \quad (2)$$

where U_{max} and U_{min} [J] are the maximum and minimum strain energy values found in the blade model and p is the number of available material properties [5].

It is important to observe that the number of strain energy intervals must be the same as the number of material properties available to the optimisation process. For this study, ten different properties (different thickness) are used in the optimisation process. The number of properties as well the steps between them are user defined.

The algorithm will allocate the material property to the plate elements in the blade model according to the predicted strain energy under load. The thicker property will be assigned to the plate elements with the highest strain energy values [5]. In every iteration of the optimisation process, the value of the strain energy of each plate element is recorded and the algorithm changes, if necessary, the material property.

The optimisation routine finished when the strain energy-based termination criterion is met. BELO termination criterion is defined by:

$$c = \frac{|U_{blade(j-1)} - U_{blade(j)}|}{U_{blade(j)}} \times 100 < e \quad (3)$$

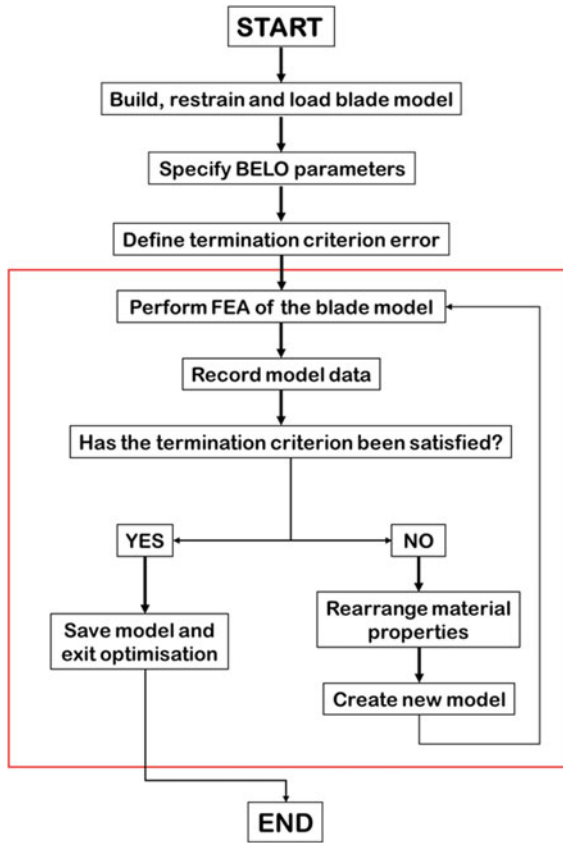


Fig. 2 BELO method flow chart [5]

where c is the percentage change between successive iterations, 1 and j , in the mean strain energy, U_{blade} , [J] of the whole blade model. The tolerance value, e , is user defined [5].

Figure 2 shows a flow chart of BELO method summarising the iterative process.

3 PET-G Material Properties

3.1 Three-Point Bending Test

As previously mentioned, the optimisation method requires an accurate FE model of the blade. The model must be geometrically accurate and use accurate values of the

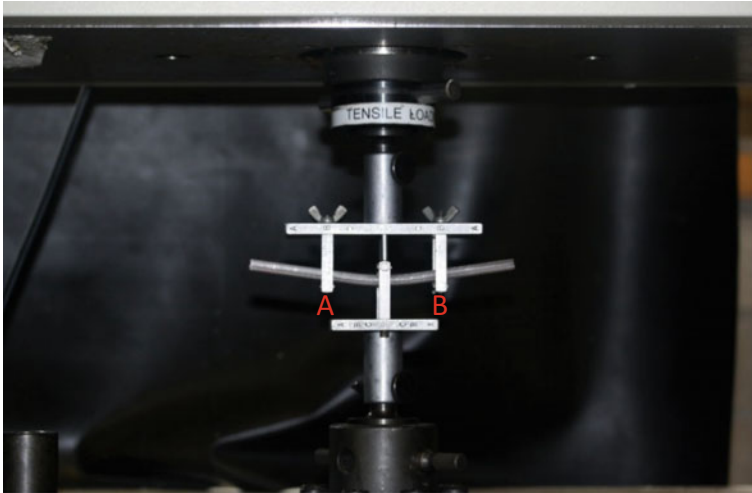


Fig. 3 Three-point bending test of PET-G sample

material properties. To correctly represent the PET-G material used to manufacture the DAWT, two tests were undertaken to determine its mechanical properties.

The first test was a three-point bending test. Sample beams were 3D printed to the same structure of the DAWT blades (vertical, with 2.5 mm wall thickness and 20% material infill for the internal honeycomb structure). Both the blades and the sample beams used in this study were printed with fused depositing modelling (FDM) process, with printing speed of 40 mm/s and printing temperature of 250 ° C. The dimensions of the test samples followed the standard [11] specifications: 150 mm long, 20 mm width and 6 mm thickness. Printing the beams in the vertical direction caused the bonding between layers to be parallel to the direction of loading during testing. Figure 3 shows the testing of one of the 24 beam samples.

Data collected during the three-point bending tests were processed and the resulting Young's Modulus of Elasticity (E) are presented in Table 1. The average E value was determined to be 915 MPa with a standard deviation of 55 MPa. The E values were calculated according to:

$$E = \frac{L^3 * m}{4 * b * d^3} \quad (3)$$

where L is the distance between A and B (Fig. 3), m is the slope of the force versus displacement graph (data acquired during the experiment) shown in Fig. 4, b and d are the width and thickness of the sample.

Table 1 Three-point bending test results

Sample	E (MPa)	Sample	E (MPa)
1	980.44	13	879.81
2	910.08	14	860.11
3	900.03	15	991.79
4	920.25	16	865.48
5	854.9	17	922.07
6	1004.5	18	870.41
7	931.32	19	1003.81
8	948.05	20	1005.57
9	870.71	21	846.78
10	860.11	22	911.03
11	983.73	23	850.7
12	935.95	24	874.28

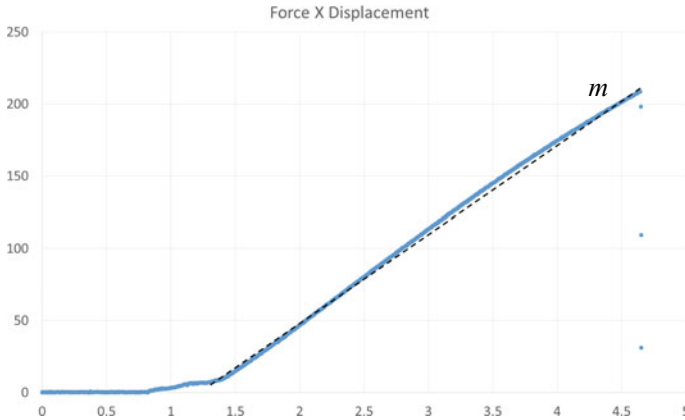


Fig. 4 Example of experimental data from three-point bending test

3.2 Blade Tip Deflection Test

The second experiment used a Shimadzu testing machine to apply a point load to the 35 W DAWT blade, and to measure the vertical and horizontal deflection near the blade tip (where the load was applied). As the blade is printed in the vertical direction, during this test the load was applied in a direction parallel to the bonding of the printed layers.

Three different loads were used during this experiment, namely 1 N, 2 N and 5 N. As the blade has an approximate 45° angle of twist at its root end the test rig had to be designed to attach the blade at a 45° angle and compensate for its initial angle of twist, minimising the horizontal deflection during the tip-loading experiment.

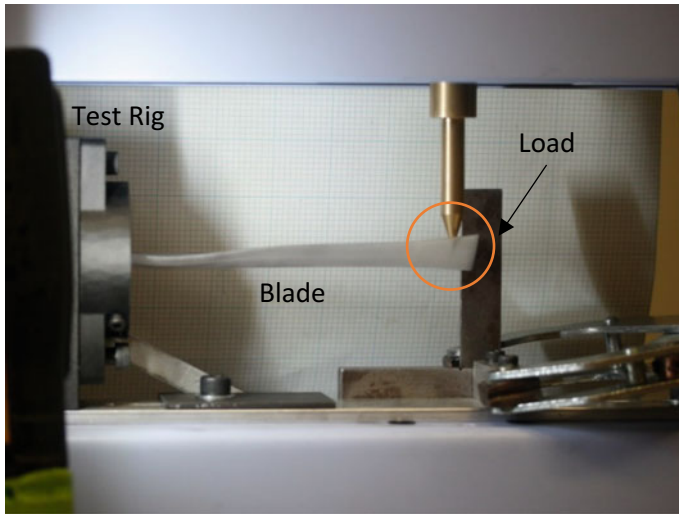


Fig. 5 Deflection experiment

Table 2 Deflection experiment results

Load (N)	Deflection (mm)	
	Vertical	Horizontal
1	3.69	0.4
2	7.04	0.25
5	17.33	0.55



Fig. 6 DAWT blade model with point load

Figure 5 shows the deflection experiment set up and Table 2 has the experiment results.

In order to calibrate the blade FE model, three loading cases simulating the deflection experiment conditions were set up as shown in Fig. 6.

The E value of 915 MPa determined during the three-point bending test was used as the starting point of the calibration process. The DAWT blade model constructed with the E value of 915 MPa predicted a much lower tip deflection than measured experimentally. Specifically, an 11.9 mm tip deflection resulted from the 5 N load, 4.7 mm when loaded with 2 N and 2.38 mm when load with 1 N. The material

Table 3 Experimental and computational results

Load (N)	Vertical deflection (mm)		Error (%)
	Experimental	Computational	
1	3.69	3.46	6.23
2	7.04	6.93	1.56
5	17.33	17.32	0.057

properties were adjusted (E value was lowered) using a heuristic process, until the resulting tip deflection on the blade model matched the experimental results. The final E value for the PET-G material was determined to be 650 MPa, on the blade model. Possible reasons for the discrepancy between the measured and used values of E are discussed in the last section of this paper. Table 3 has the experimental and computational results used to validate the DAWT blade model used in the optimisation.

4 Optimisation Results

At this point, it is important to mention that the BELO method results are independent of the initial conditions. The optimisation routine was tested starting from all possible initial conditions (initial blade models constructed with all ten material properties available). A minor variation on the number of iterations necessary for convergence of the process was observed. However, all routine arrived at the same optimum model.

The results from the BELO method, as the ones from the BESO method from which is derived, are highly dependent on the optimisation parameters chosen [7]. The problems addressed by these methods are usually not convex and there exist various local optimum [7]. As explained by [7], the local optimum can be avoided. However, theoretically a global optimum cannot be guaranteed [7], as the choice of optimisation parameters directly interferes with the solutions.

The 35 W DAWT blade model was optimised and after 15 iterations the termination criterion ($e < 1\%$) was met. Figure 7 shows the optimised final blade model and Fig. 8a, b show both surfaces (pressure and suction) of the blade model at two different stages of the optimisation process.

The different colours represent the 10 different material thickness used in the optimisation process, Table 4 relates the colours used in Figs. 7 and 8 to the material property thickness. In this study, PET-G is modelled as an isotropic material; therefore, all material properties in the blade model have the same E value of 650 MPa (determined during the calibration stage) and vary only in thickness.

The original blade model was created and calibrated to accurately represent the 35 W DAWT blade. The optimised blade model had a mass reduction of 15.6% from the original blade model as the results in Table 5 show.

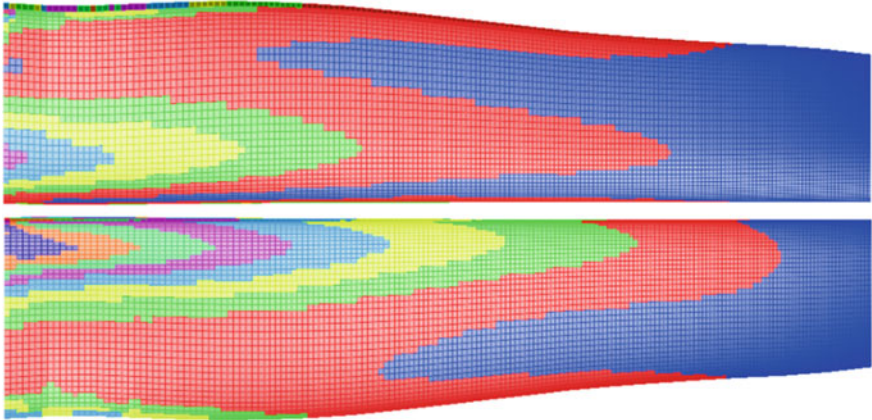


Fig. 7 Optimised final blade model

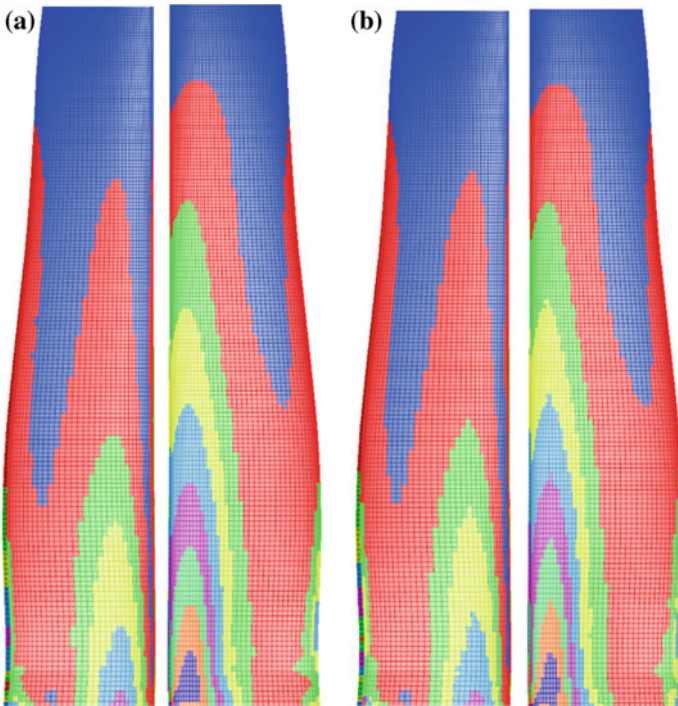


Fig. 8 a 2nd iteration, b 10th iteration

Table 4 Material properties thickness and colour scheme











Material Property Number	Thickness [mm]	Colour
1	1.1	
2	1.2	
3	1.3	
4	1.4	
5	1.5	
6	1.6	
7	1.7	
8	1.8	
9	1.9	
10	2	

Table 5 Blade model mass

Blade model	Mass (kg)
Original	0.032
Optimised	0.027

Table 6 Blade model vertical deflection

Load (N)	Blade model vertical deflection (mm)	
	Original	Optimised
1	3.46	2.76
2	6.93	5.53
5	17.32	13.83

The optimised blade model was tested for its structural stiffness. Here with a simulation done for the same three load cases (point force applied close to the blade tip) as previously used. The optimised DAWT blade model proved to be stiffer than the original one; results are presented in Table 6.

5 Summary and Conclusions

This paper presented the bi-directional evolutionary layout optimisation method applied to a 35 W 3D printed diffuser augmented wind turbine blade and the method used to determine the mechanical properties of PET-G plastic material used to construct the blade.

The results presented in Table 5 show the optimised blade model to have approximately 15% less mass than the original model. Reduction in blade mass will reduce the manufacturing cost of the blade and the overall cost of the turbine. Furthermore, blade mass reduction reduces the blade inertia and that can help lower the starting time of the wind turbine and gyroscopic loads. Table 6 shows the computational results for the original and optimised blade models, with the optimised blade stiffer and lighter than the original one.

It is important to highlight that even though the optimisation process has been successfully applied to the 35 W DAWT blade, the optimised blade model is only theoretical. To the best of the author's knowledge, with the current technology it is only possible to 3D print a blade that has a constant outer shell thickness. However, 3D printing technology is rapidly advancing and it may become a possibility in the near future to manufacture the optimised blade.

The PET-G 3D printed material was observed to have very large discrepancy in the value of E between tested beam samples and shaped blade. In this study example, the beam samples tested with three-point bending test yielded much higher E values than the ones found when calibrating the blade model according to the deflection experiments. Possible explanation for such difference can be found upon visual inspections of the cross section of both the 3D printed beam samples and DAWT blade. Two main inconsistencies were found. One is due to the blade's complex geometry and small size, there are section of its internal honeycomb structure that are ill formed, as opposed to the correctly formed internal structure of the constant rectangular cross section of the beam samples. Another difference was observed in the bonding between internal structure and outer shell of the 3D printed objects. Again, due to the blade's complex geometry bonding of the internal structure to the outer shell was inconsistent throughout the blade, as opposed to the consistent bonding of the internal structure of the beam samples. The only way to ensure that the material properties of the optimised blade model are accurately represented would be to manufacture the optimised blade and experimentally test its material mechanical properties.

References

1. van Dorst F (2011) An Improved rotor design for a diffuser augmented wind turbine. Master's Thesis, Aerospace Engineering, Delft University of Technology, Netherlands
2. Phillips DG (2003) An investigation on diffuser augmented wind turbine design. PhD Thesis, Auckland, University of Auckland, New Zealand
3. Kesby JE, Bradney DR, Clausen PD (2017) Determining the performance of a diffuser augmented wind turbine using a combined CFD/BEM method. *Renew Energy Environ Sustain* 2:22
4. IEC, IEC Standard 61400-2 (2013) Wind turbines—part 2: small wind turbines Edn 3.0 2013-12, IEC
5. Costa MSP, Evans SP, Bradney DR, Clausen PD (2017) A method to optimise the materials layout of small wind turbine blades. *Renew Energy Environ Sustain* 2:19

6. Querin OM, Steven GP, Xie YM (1998) Evolutionary structural optimisation (ESO) using a bidirectional algorithm. *Eng Comput* 15(8):1031–1048
7. Xia L, Xia Q, Huang X, Xie YM (2016) Bi-directional evolutionary structural optimization on advanced structures and materials: a comprehensive review. *Arch Comput Methods Eng* 1–42
8. Szykiedans K, Credo W, Osinski D (2017) Selected mechanical properties of PETG 3-D prints. In: XXI international Polish-Slovak conference machine modeling and simulations 2016, *Procedia Eng* 177:455–461
9. Berthelot JM (2012) *Composite materials: mechanical behavior and structural analysis*. Springer Science & Business Media
10. Wood D (2011) *Small wind turbines: analysis, design and application*. In: *Green energy and technology*. Springer, London
11. ASTM D790-15e2 (2015) Standard test methods for flexural properties of unreinforced and reinforced plastics and electrical insulating materials. ASTM International, West Conshohocken, PA. www.astm.org

Experimental Investigation of the Aerodynamic Interaction Between Ducts and Actuator Discs



J. Tang and G. J. W. van Bussel

Abstract The present study aims at providing experimental performance analysis of ducted wind turbines (DWTs) through momentum theory. To simplify the DWT model, a screen emulating the rotor is adopted by applying the actuator disc theory. Two duct models and five different screens are employed for different configurations to investigate the aerodynamic performance of the DWT in this experimental study. Duct 1 ($C_{T,duct} = 0.91$) is characterized by an aerofoil-shaped cross-section and duct 2 ($C_{T,duct} = 1.17$) has a cambered shape. Specifically, the five screens vary in porosity from low ($C_{T,screen} = 0.46$) to high thrust coefficient ($C_{T,screen} = 1.12$). Results show that the total thrust coefficient ($C_{T,DWT}$) varies with screen thrusts and ducts geometry. The aerofoil-shaped duct 1, caused by the non-linear behaviour of the aerodynamic force on an aerofoil-shaped body at increasing angle of attack, is more sensitive to the screen loading compared to duct 2. Thrust on duct 1 is highly dependent on screen thrusts owing to the existence of inward oriented lift, while thrust on cambered plate duct 2 stays constant. The high thrust and solid blockage this duct creates, accelerates the flow through the lesser loaded centre where the screen is located. The data also show that the growth of duct thrust has a positive effect on the overall performance of DWT. Both high screen loading and inappropriate aerofoil shape duct may lead to flow separation which causes the momentum loss for DWT. Moreover, the optimal value of $C_{T,screen} = 0.89$ for a bare wind turbine doesn't seem apply to the tested DWTs. The optimal value of $C_{T,DWT}$ depends both on duct geometry and the screen loading. The velocity measurements further indicate that flow separation occurs at the duct 1 external (pressure) surface, and shows the presence of stalled flow around centre line inside the duct. Finally, a comparison of the pressure distribution of duct with different screen loadings reveals that adding a screen inside duct 1 leads to loss in lift and hence to mass reduction.

Keywords Ducted wind turbine (DWT) · Thrust · Axial momentum theory · Duct · Screen · Wind tunnel experiment

J. Tang (✉) · G. J. W. van Bussel
Wind Energy Research Group, Delft University of Technology, Kluyverweg 1,
2629 HS Delft, The Netherlands
e-mail: j.tang-6@tudelft.nl

1 Introduction

The ducted wind turbine (DWT), also named as shrouded wind turbine or diffuser augmented wind turbine (DAWT), has been an intriguing topic in wind energy technologies for decades. The purpose of the duct is to increase the extracted power. This is realised by adding the duct around the rotor. A duct shape generally applied is with an aerofoil cross-section, which generates radial lift force on the flow thus providing additional expansion of the wake flow. As a consequence, the mass flow increases. This increased mass flow makes it possible to extract more power. Another duct shape is a truncated cone. This type of duct creates a sub-atmospheric region at its exit plane, which is lower than the under pressure a downwind side of the rotor plane of a bare wind turbine rotor. When the pressure at the exit plane of the duct can be reduced further without affecting the mass flow, the amount of power that can be extracted may become even larger. There are indications that such additional power augmentation can be realised, which would imply that energy extraction values are possible beyond those of a conventional wind turbine with a swept area equal to the duct exit area.

Aerodynamic loads play an essential role in the fluid behaviour of DWT's. Various theoretical, experimental and computational studies to analyse the aerodynamic loads on duct and rotor blades have been carried out. The increase of mass flow through the rotor in a DWT was shown to decrease with increased thrust coefficient by Hansen [1], suggesting that the amount of augmentation is limited. Based on an inviscid one-dimensional momentum theory, experimental data from Igra [2] and Lawn [3] manifested that the speed-up is not only influenced by the thrust coefficient but also by the duct geometry. The duct geometry can be characterised by three coefficients, namely duct inlet efficiency, pressure recovery coefficient and the back pressure coefficient (C_{pe}). When a duct has an aerofoil cross section more air is drawn into the duct according to Igra [2]. He also pointed out that the amount of air that can be "drawn" is limited by the separation of the boundary layer along the duct wall and the thrust posed by the turbine. Using the DAWT concept, Phillips [4] developed the Vortec 7 which was unsuccessful, mainly because a much lower augmentation was realised in practice compared to expectations from wind tunnel experiments; and the large loads on the duct in storm conditions and in yawed flows. Van Bussel [5] proved that power augmentation of a DAWT is directly related to mass flow augmentation which is achieved by increasing the exit area ratio. He also pointed out that decreasing the back pressure coefficient will further enhance augmentation. Shives and Crawford [6] showed that higher velocities achieved within a duct also cause higher rotor rotational speeds for a given optimum tip speed ratio. The study by Jamieson [7] confirmed these findings. However, in Jamieson's theory, the thrust on the duct and the rotor are taken independently, the axial force interaction between the flow and the duct is not taken into consideration, so the momentum balance over the entire control volume is not taken into account.

Abe et al. [8] showed that the performance of a flanged diffuser strongly depends on the rotor loading coefficient as well as the opening angle because the opening angle

greatly affects the nature of the separation appearing inside the flanged diffuser. They suggest that the loading coefficient for the best performance of a flanged diffuser is considerably smaller than that for a bare wind turbine with the same diameter. Matsushima [9] revealed that the wind speed in the diffuser is greatly influenced by the length and expansion angle of the diffuser, and maximum wind speed increase of 1.7 times the bare wind turbine velocity can be achieved with an appropriate diffuser. To investigate the influence of duct geometry, Shives [10] used CFD to investigate the effect of a diffuser with an aerofoil (NACA 0015) cross section. It was found that the diffuser inlet efficiency has only a small impact on the power output. Moreover, it was found that flow separation in the diffuser leads to a significant lowering of the pressure recovery coefficient which, in turn, reduces the overall power coefficient (C_P). Moreover, Shives and Crawford indicated that C_{pe} is the most influential parameter in C_P .

These previous studies have focused on the degree of power augmentation and its mechanisms. None of these researchers have discussed the mutual interaction between the duct and rotor thoroughly. Recently Bontempo et al. [11] investigated the effects of the duct thrust on the power extraction from a DAWT through a semi-analytical method. They reported that the power output increases by increasing the duct thrust. However, this theoretical model was only compared with numerical simulations and does not account for possible flow separation effects.

Though numerical simulations can achieve a high level of accuracy, it still requires empirical parameters to validate and quantify the mutual aerodynamic interaction between the duct and the rotor. This paper aims to fill this gap by analysing experimental data. A systematical study of the flow mechanisms with different duct types and different screen (rotor) loads is provided, and a performance comparison of different test setups is presented.

2 The DWT Momentum Theory

As mentioned above, the duct increases the mass flow at the location of the turbine allowing an augmentation of the extracted power. De Vries [12] presented a simplified explanation for the mass flow augmentation phenomenon, pointing out that if the sectional lift of the duct is directed towards the axis of rotation, then the associated circulation induces an increased mass flow through the area enclosed by the duct.

The classical axial momentum theory assumes the flow through the turbine is stationary, axisymmetric, inviscid and incompressible. In this approach, the rotor is frequently modelled by an actuator disc. Such a simplification makes it a useful tool for preliminary research. It does, however, not capture potentially interesting aspects of the flow physics near the blade the detailed interaction of the blade with the duct and the swirl in the wake of a DWT. In addition, the actuator disc model cannot predict accurately the flow separation along the walls of the duct. This effect is not addressed in this study as the investigation concentrates on the interaction between duct and rotor rather than the aerodynamic performance of rotor.

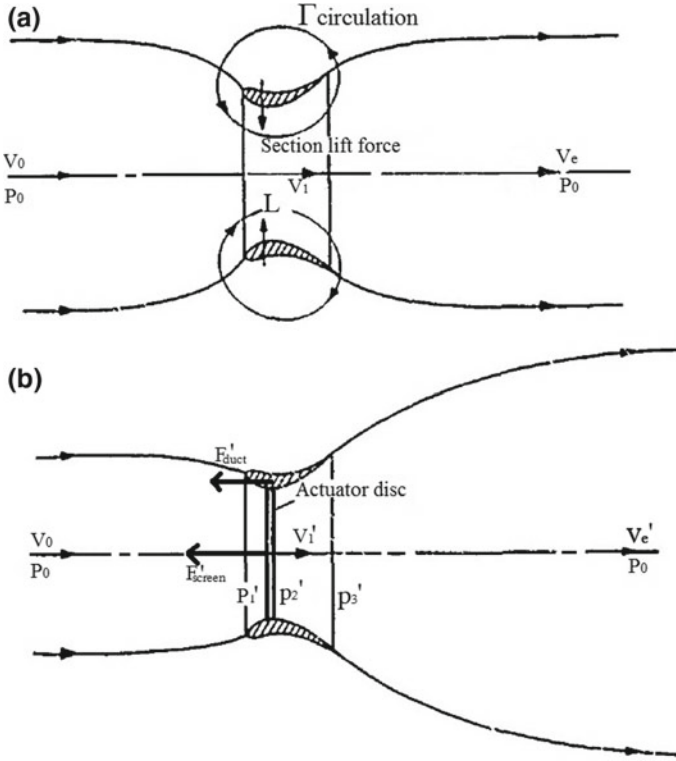


Fig. 1 Aerofoil-shaped duct in inviscid flow, without (a) and with actuator disc (b) [12]

It is worth to point out that most of the previous DWT theories assumed that a DWT has a pressure jump across the rotor similar to a bare wind turbine. This study anticipates on the fact that the pressure jump for a DWT may differ from a bare wind turbine. In the following equations, the superscript ' is used for the configuration of duct combined with the disc, while an equation without this superscript refers to an empty duct or a single disc. Moreover, the subscript *screen* and *exit* are adopted for quantities evaluated at the screen (rotor) plane and the duct exit plane respectively (Fig. 1).

$$C_{T,s} = \frac{F_{screen}}{\frac{1}{2}\rho v_0^2 A_{screen}} \tag{1}$$

$$C_{T,duct} = \frac{F_{duct}}{\frac{1}{2}\rho v_0^2 A_{screen}} \tag{2}$$

In unloaded conditions (an empty duct), the aerofoil-shaped duct generates a radially inward lift force which increases the mass flow through the duct. When incorporating an energy “processed” actuator disc, the axial momentum balance

changes. As a result, the direction of the lift on the duct also changes, and the axial component of the lift on the duct then contributes to the axial momentum equation. The momentum change should then be equal to the resultant axial force on the combined disc and duct.

$$F'_{DWT} = F'_{screen} + F'_{duct} = \dot{m}(v_0 - v'_e) \tag{3}$$

where $\dot{m} = \rho v'_1 A_s$ is the flow rate “absorbed” by the ducted turbine. The thrust on the whole DWT, F'_{DWT} , is related to both the pressure jump across the actuator disc and to the duct, which is expressed in a non-dimensional duct thrust coefficient:

$$C'_{T,DWT} = C'_{T,screen} + C'_{T,duct} \tag{4}$$

To better evaluate the mutual aerodynamic interaction between duct and disc, a thrust ratio is defined as,

$$f = \frac{F'_{duct}}{F'_{screen}} = \frac{C'_{T,duct}}{C'_{T,screen}} \tag{5}$$

So that Eq. (4) can be simplified as

$$C'_{T,DWT} = (1 + f)C'_{T,screen} \tag{6}$$

Equation (6) expresses that $C'_{T,DWT}$ depends on the mutual interaction between duct and rotor. If either the variation of the duct changes or the rotor changes, this will affect the other, and hence the operating conditions of the around DWTs.

An assumption that, by definition, has to be made in one-dimensional axial momentum theory is that the load distribution is constant in radial direction. With the help of Eq. (1), assuming that the (gross) power is the product of the load on the screen multiplied by the velocity through the screen, the power coefficient based on the rotor area can be expressed as:

$$C_p = \frac{(p'_1 - p'_3)V'_1}{\frac{1}{2}\rho V_o^3} = (1 + f)C'_{T,screen} \frac{V'_1}{V_0} \tag{7}$$

where v'_1 is velocity at the rotor plane inside the duct. If $f > 0$, the thrust on duct has the same direction of the rotor thrust, which helps to achieve high power coefficient for DWTs. For the negative value of f evidently the opposite happens. Bontempo [11] also proved that if $f > 0$ the DWT processes more mass flow than a bare wind turbine with the same $C_{T,screen}$.

Though axial momentum theory gives a good insight into the features of the DWTs flow field, it’s hard to quantify the details of the mutual interaction of an actuator

disc and the duct. For these reasons, the next section investigates the flow features of a DWT for different duct geometry and values of the rotor thrust coefficient.

3 Experimental Setup

The primary objective of the wind tunnel tests is to obtain a first set of data of the aerodynamic mutual interaction of screen loading and duct loading. Moreover, the test data can be compared with computational methods. This experimental study is fundamental, hence the conventional and classical actuator disc theory is employed, and the rotor is replaced by a uniform porous screen across which a pressure drop is imposed.

The experimental study reported in this paper consists of two parts. In the first part, the performance of different combinations of screen models and duct models are determined. In the second part, velocity and pressure measurement are carried out for some specific configurations.

In the experiments, the performance of the DWT is evaluated in terms of the relationship between thrust on the duct and the screen; the velocity profile for both inside and outside of the duct, and the pressure distribution along duct's chord length.

3.1 Wind Tunnel Description

The experiment are conducted in the Open Jet facility of the faculty of Aerospace Engineering of the Delft University of Technology. This is a closed loop open jet wind tunnel with an octagonal nozzle having a 3 m equivalent diameter and a settling chamber with a contraction ratio of 3:1, delivering a uniform stream with approximately 0.5% turbulence intensity up to 1 m from the nozzle and lower than 2% at 6 m from the nozzle exit. At the latter distance, the uniform flow region reduces to approximately lower 2×2 m². The wind tunnel is capable of producing wind speeds up to 34 m/s. Since ducted wind turbines are generally applied in an urban environment in which the wind speed is not high, the wind tunnel is operated at moderate wind speeds. Since the wind tunnel speed control is more accurate when it's set higher than 4 m/s, a test wind speed range is chosen from 5 to 10 m/s.

3.2 Aerofoil Model and Screen Model

Screen simulation has been used extensively to minimise technical complexity and costs. Since the current study focuses more on the validating theory, the experimental prototype has been designed with a simple configuration. It is composed of a duct and a perforated plate. Two duct shapes are applied in this study: duct 1 has an

Table 1 The specifications of the two tested ducts

	Length (m)	Exit diameter (m)	Rotor diameter (m)	Area ratio (β)
Duct 1	1	2	1.5	1.728
Duct 2	0.26	0.912	0.6	1.798

Table 2 Parameters pertaining to the tested screens and ducts

Duct type	Duct 1		Duct 2		
$C_{T,duct}$	0.91		1.17		
Diameter of screen	1.5 m		0.6 m		
Screen number	Screen 1	Screen 2	Screen 3	Screen 4	Screen 5
$C_{T,screen}$	0.65	0.89	0.46	0.87	1.12
$C'_{T,screen}$	1.02	1.01	0.42	0.84	1.07

aerofoil-shaped cross-section, and duct 2 has a highly cambered plate cross-section. The relevant design data of the two duct models are given in Table 1 and Fig. 3 (the area ratio β refers to the ratio of duct exit area to the nozzle area).

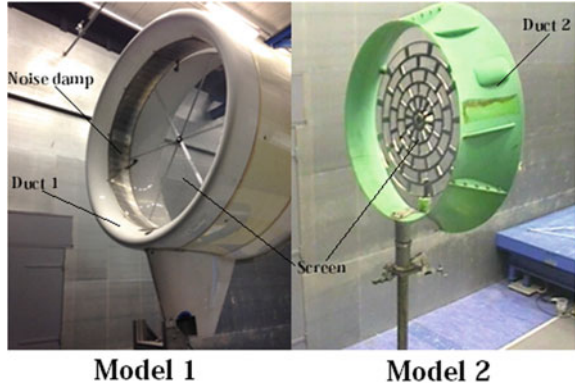
The actuator disc is realised by a uniform perforated metal screen to create the pressure drop across a working turbine. Several screens with different porosities are employed. The porosity (p) is a measure of the permeability of the area of the screen, and it is defined as the ratio between the open area and the total area of the screen. For example, for duct model 1, the three screens tested have porosities equal to $p = 0.4$, $p = 0.46$ and $p = 0.7$. wind tunnel tests on the isolated screens, resulted in thrust coefficients $C_{T,screen}$ equal to 0.92, 0.89 and 0.65, respectively. It has to be stressed that the coefficients in Table 2 are obtained for non-interfering conditions, namely a bare screen or an empty duct.

The ducts and the screens are set parallel to the flow at 0° yaw angle. The ducts are installed on a support equipped with a load cell (Model: LSB302 from FUTEK), while the screen is placed on a separate structure connected with a six-component balance system, as shown in Fig. 2. The accuracy of the balance system is $\pm 0.23\%$ of the measured load.

3.3 Measurement Techniques

Velocity measurements are obtained with two different techniques: with a pitot probe and with hotwire anemometry. Both sensors are traversed along the radial directions for both the empty duct and duct with the screen to obtain a crosssectional wind speed profile. For each measurement, the data are averaged over a sequence of 10 s to rule out the effect of turbulence. Radial measurements are performed at $x/L = 30$ mm (i.e. 0.03 m in front of the screen plane), where L is the duct length in the

Fig. 2 Ducted actuator disc models



range $0 < r/R < 1$ and $1.12 < r/R < 1.94$ (where R refers to screen radius and equals to 750 mm).

The pressure distribution around the duct is captured by 52 pressure taps connected via rubber tubes to the ports of the scanning valve. The location of the spatial pressure points is normalised by the distance along the chord line from the leading edge to each tap and from the chord line along the axis orthogonal to the chord. The pressure values are normalised with respect to the dynamic pressure values at the wind tunnel nozzle exit plane.

4 Results and Discussion

This section provides an overview of the data obtained from the wind tunnel tests conducted with the ducted actuator disc model. As stated in the description of the experimental setup, free-stream velocities from 5 to 10 m/s are investigated in the experiments.

4.1 Thrust Measurement

Since the flow around a duct can be very complex, this research only concentrates on the axial forces at present. Figure 3 presents the thrust variation between the bare screens ($C_{T,screen}$) and loaded screen ($C'_{T,screen}$) owing to the duct effect. Screen 1 and screen 2 are loaded with duct 1, screen 3–5 are combined with duct 2.

It can be seen that, regarding the thrust variation, duct 1 presents positive effect on the combined screens, while duct 2 has no distinct effect on its loaded screens (the minor decrease is within the error range). Screen 1 obtains the most pronounced increment due to the duct 1 effect, increased by 57% (from $C_{T,screen} = 0.65$ to

Fig. 3 Thrust coefficient of the DWT's with different choice of screen porosity

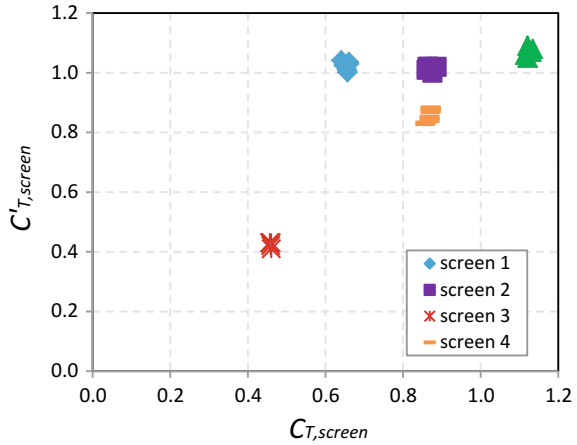
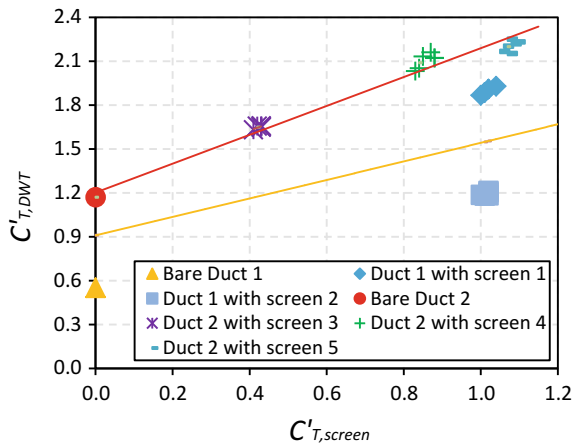


Fig. 4 Thrust coefficient of the DWT's with different choice of screen porosity



($C'_{T,screen} = 1.02$), whereas the thrust of screen 3 decreases by 8.7% for duct 2. Possible reasons are further investigated below.

Figure 4 presents the relation between the different values of ducted screen loading ($C'_{T,screen}$) and the total thrust coefficient of the DWT ($C'_{T,DWT}$). Here it must be stressed that the screen loading is obtained directly from the balance system with the duct in place and hence varies from the isolated screen loading.

The left plot depicts duct 1 and the right relates to duct 2, it can be seen that the aerofoil-shape duct 1 shows a different behaviour from the highly cambered duct 2. The $C'_{T,DWT}$ for duct 1 is non-linear, which may be caused by the non-linear behaviour of the aerodynamic force on an aerofoil-shaped body at increasing angle of attack. The increase in $C'_{T,DWT}$ for duct 2 seems to come completely from the increase in $C'_{T,screen}$: there is a linear relation between the increase in $C'_{T,screen}$ and $C'_{T,DWT}$.

The bare duct 1 ($C_{T,duct} = 0.55$, $C_{T,screen} = 0.0$) has a lower thrust than bare duct 2 ($C_{T,duct} = 1.17$, $C_{T,screen} = 0.0$). Probably due to the fact that the camber of duct 1 is much lower than duct 2, and/or to the fact that the relative frontal area of duct 2 is larger than the frontal area of the aerofoil-shaped duct 1. In summary, the effect of the duct shape on total thrust coefficient $C_{T,DWT}$ is as evident as the effect of the screen thrust coefficient $C_{T,screen}$.

Among all the force tests, duct 2 with screen 5 ($C'_{T,screen} = 1.07$) achieved the highest $C'_{T,DWT}$ (2.2), while duct 1 with screen 2 ($C'_{T,screen} = 1.01$) obtained the lowest $C'_{T,DWT}$ (1.2), excluding the empty duct cases. An example is shown in Fig. 4, taking the proximal screen 2 ($C_{T,screen} = 0.89$) and screen 4 ($C_{T,screen} = 0.87$) for duct 1 and duct 2, respectively. Though the thrust on ducted screen 2 ($C'_{T,screen} = 1.01$) increases slightly, the value of $C_{T,DWT}$ for duct 1 (1.2) is much lower than duct 2 (2.09). For screen thrust close to 8/9 duct 2 has a much higher thrust than duct 1. It indicates the growth in the duct thrust has a positive influence on the overall performance of DWT. Another conclusion that can be drawn is that the optimal value of $C_{T,screen} = 0.89$ for a bare wind turbine doesn't seem to apply to the DWTs tested here: The optimal value of $C'_{T,DWT}$ depends on both the shape of duct and the screen loading. The $C'_{T,screen}$ for the highest $C'_{T,duct}$ of duct 1 is close to 0.5. the maximum $C'_{T,screen}$ of duct 2 is not determined, but it can be seen that the increment of total thrust of duct decreases with the increase of $C'_{T,screen}$.

In addition, the bare duct 1, with a lower thrust than the bare duct 2, is more sensitive to the variation of screen thrust. Focusing on the test thrust range of $C'_{T,screen}$ from 0.4 to 1.2, duct 1 presents a higher gradient of total thrust variation. Since the thrust is related to the losses of kinetic energy of the flow, this indicates an early occurrence of flow separation around the duct inside and outside, particularly with a heavily loaded screen (high $C'_{T,screen}$).

The right plot in Fig. 5 reports the variation between thrust coefficient of the loaded duct $C'_{T,duct}$ and the thrust coefficient of the ducted screen $C'_{T,screen}$. It can be seen that the thrust on duct 1 first increases then decreases when incorporating low screen thrusts to high screen thrusts. The thrust on duct 2 is virtually constant with varying screen loading. This indicates that the aerofoil-shaped duct 1 is quite sensitive to the screen loading in contrast to the highly cambered plate duct 2.

The left plot in Fig. 5 shows that the thrust ratio keeps decreasing with the increasing screen thrust. Duct 2 with screen 3 (low thrusts) generates the highest thrust ratio ($f = 2.97$), i.e. for this configuration, the thrust on the duct 2 contributes the most to the total thrust $C'_{T,DWT}$. It can be inferred that the duct geometry, with low screen thrusts, plays a dominant role in the total DWT performance. But the screen takes over the dominant effect when the screen thrust keeps increasing towards a threshold, which varies for the two different duct geometries.

According to the axial momentum theory, the thrust on the screen located inside a duct has a linear relationship with the thrust on duct [5]. It has to be stressed that the axial momentum theory is valid for the optimal shape (and thrust) of both screen/rotor and duct only. Figure 5 shows the thrust on a ducted screen, is a nonlinear function

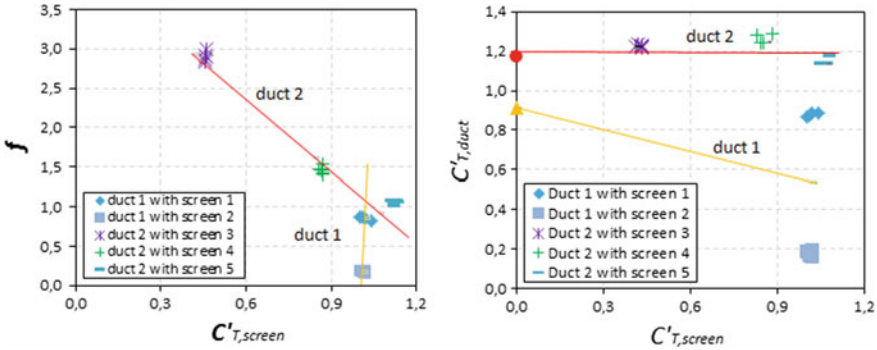


Fig. 5 Thrust interaction between the loaded duct and ducted screens

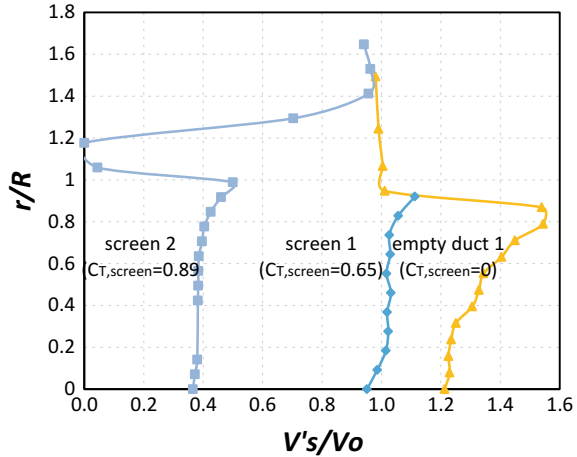
with the incorporated duct for the reason that the non-adapted duct 1 coupled to a screen with increasing thrust.

In summary, the two ducts most probably use different working principles. Duct 1 with an aerofoil-shaped cross-section, generates an inward lift pointing to the duct centre to realise more mass flow. Duct 2 uses the principle of generating a high amount of axial force and axial blockage to accelerate the flow through the lesser loaded centre where the actuator disc is located. Theoretically, the aerofoil-shaped duct 1 should perform better for the extra inward lift. But since the above analysis shows that the performance is far from optimal, a detailed flow investigation on the duct 1 is carried out to find out the reason.

4.2 The Velocity Fields of the Empty Duct and the Duct with Screen

To further explain the mutual interaction between the duct and screen, instead of continuing from the force illustration, the flow field around the DWT give another view. Hence taking the bare screen as the benchmark in the below analysis, i.e. using the thrust coefficient of a bare screen ($C_{T,screen}$) instead of the load screen ($C'_{T,screen}$). The radial velocity distribution of the configuration of duct 1 with screen 1 ($C_{T,screen} = 0.65$) and screen 2 ($C_{T,screen} = 0.92$) are shown in Fig. 6, as these are the configurations resulting in the low $C_{T,DWT}$. The displayed results are taken at the lower half of the domain considering the symmetry of the flow. As stated in the description of the experimental setup, the free-stream velocities from 5 to 10 m/s were investigated during the experiments. Only minor differences were found between these different wind speed cases. Therefore, for the sake of conciseness, the wind speed at 7 m/s is reported only for velocity profiles at screen plane for different screen loadings, as shown in Fig. 6.

Fig. 6 Velocity distribution at screen plane with different screen loadings



The reduction of the screen velocity v_S'/v_0 with the increase of $C_{T,screen}$ inside the duct is observed as can be expected. The tested model still shows a slight acceleration of the approaching flow when coupled with low screen thrust ($C_{T,screen} = 0.65$), but decelerates to 0.4 with high screen thrust ($C_{T,screen} = 0.89$). Hence increasing the screen thrusts increases the total thrust on the DWT, but hugely decreases the velocity at screen plane. Thus the mass flow passing through the screen reduces which cuts down the power output.

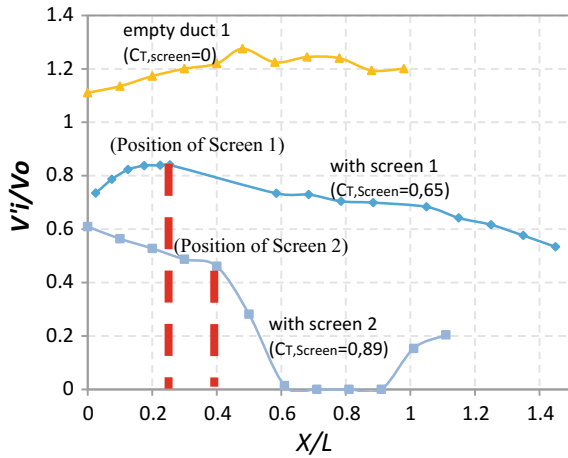
Focusing on the configuration of duct 1 and screen 1, the total thrust coefficient can be obtained from Fig. 4 ($C'_{T,DWT} = 1.9$), then, according to momentum theory in Van Bussel [5] the (gross) power coefficient can be calculated by multiplying the velocity ratio divided by the area ratio β . The velocity ratio, is close to 1.0, see Fig. 6. Hence the gross power coefficient reads: $C_p \cong \frac{1.9}{\beta} = 1.1$ (referred to the screen area). Moving to the combination of duct 1 and screen 2, it can be noticed that the high thrusts on screen 2 comes with reduced thrust on duct (from Figs. 4 and 5). Below the possible cause of this observation will be given.

The right solid line represents the radial velocity profile for the empty duct ($C_{T,screen} = 0$), it is evident that ambient velocity is present outside the duct ($r/R \geq 1$). Differently, the left solid line shows that in the presence of the high screen loading (screen 2), the velocity ratio drops to zero at $1 < r/R < 1.2$. This indicates that flow separation is present at the pressure side of the aerofoil duct, and the smoke visualization validated this assumption [13]. To summarize, the radial velocity profile at the screen plane supports the results obtained from the thrust measurements.

It should be stressed that all the experimental data presented in this study have been corrected for wind tunnel blockage. The correction due to dynamic pressure is 0.96, which means that the incoming velocities have to be corrected with a factor equal to the square root of 0.96.

Figure 7 shows the wind velocity distribution v_i/v_0 along the central axis of an empty duct and the loaded duct, for duct 1. Here, $x/L = 0$ is the duct entrance and

Fig. 7 Normalized velocity distribution along the duct centerline (axial direction)



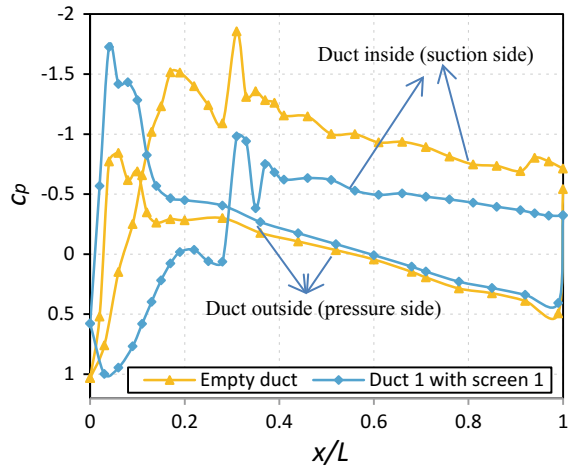
$x/L = 1$ is the duct exit. For the empty duct, a slight augmentation in wind speed is seen, with a maximum $v_i/v_0 = 1.28$ in the neighbourhood just after the nozzle plane is observed. With the presence of screen 1 ($C_{T,screen} = 0.65$), the maximum velocity ratio v_i/v_0 reduced to 0.84 and this is seen in front of the screen plane. Both configurations show a velocity increment at the entrance of the duct.

However, for screen 2 ($C_{T,screen} = 0.89$), owing to the high screen loading, the velocity inside duct keeps decreasing, particularly after the screen it reduces to zero, i.e. there is stalled flow area present around centre line inside duct 1, which clearly reduces the mass flow. It is therefore important to choose an appropriate screen loading to balance the thrust and the velocity at the screen plane to obtain optimal performance for a given duct shape. Important to know is that the position of two screens is not exactly the same due to structural limitations in the experimental setup. It is however though that this does not affect the overall evaluation of the effect of screen loading on the velocity field too much.

4.3 Pressure Distributions Along the Duct

Duct 1 is equipped with static pressure orifices and all static pressure results presented in this section are obtained from this duct. They are referenced to the atmospheric pressure as measured in the open section of the wind tunnel. The pressure coefficient c_p defined as the difference between the pressure measured on the duct surface and the reference static pressure of the wind tunnel, measured inside the wind tunnel nozzle, divided by the reference dynamic pressure measured by the Pitot static tube. To clarify the influence of screen loading on the duct performance, two configurations tests are conducted: the empty duct ($C_{T,screen} = 0$) and the loaded duct with screen 1 ($C_{T,screen} = 0.65$).

Fig. 8 Effect of different screen loadings on duct pressure distribution



The configuration of duct 1 and screen 1 is chosen in the pressure measurement campaign because of an appropriate thrust coefficient as previous results showed. Screen 2 causes too high thrusts and thus will not reveal a proper mutual interaction between the duct and the screen. Figure 8 depicts the measured c_p along the duct chord for 7 m/s. The leading edge corresponds to $x/L = 0$ and the trailing edge to $x/L = 1$.

For the empty duct, the pressure differences between the suction side and pressure side (yellow lines) show that there is total lift pointing in the inward direction. When, integrating the pressure coefficients distribution this yields a value $C_l = 0.95$. At the entrance of the duct, before the nozzle, a small area of negative lift (outboard directed) is observed. However, this negative lift is more than compensated by the positive lift beyond $x/L = 0.10$. A stagnation point is presented exactly at the leading edge, and since the curvature of the leading edge section (the first 10%) is stronger on the pressure side this results in a negative lift over the first 10% of the duct. In conclusion, the pressure distribution of a single duct implies that the duct 1 performs well concerning to lift, despite the small negative lift area just after the leading edge.

It is interesting to see the pressure distribution changes drastically when the duct 1 is loaded with screen 1 (blue lines). The total lift coefficient in this case reduces to 0.06. The stagnation point is not on the expected location but shifts backwards to $x/L = 0.03$ on the inner duct area. The screen decreases the flow velocity in front of the duct and deflects the approaching flow, resulting in a significant decrease in local static pressure, as well as a significant modification shift of the pressure pattern. In this case a negative lift over the first 30% of the aerofoil-shaped duct is generated, where the remaining part of the duct produces a positive lift. This leads to a total lift of about zero.

The intersection point of the pressure moves to $x/L = 0.28$, at the location of the screen, in contrast to the empty duct which shows the intersection at $x/L = 0.12$. A higher pressure occurs at the pressure side compared to the empty duct and the

pressure difference of loaded duct increases over the area between the leading edge and the screen plane.

It is important to know that in both cases a pressure jump is observed at the position $x/L = 0.28$. This is the result of the presence of an acoustic damper inside the duct as shown in Fig. 2. This acoustic noise damper is installed to reduce the blade tip noise from the original configuration with a real rotor instead of a screen. It has a length of 0.2 m along with the duct chord but its alignment with the inner side of the duct is not perfect hence the observed pressure jump.

5 Conclusions

This study focuses on the aerodynamic interaction between ducts and screens and the effect of different screen loading on the ducted wind turbine (DWT) performance. In particular, attention is given to differences between empty duct and duct with screen loadings, which are difficult to predict accurately. Two duct models and five different screens are employed to investigate the flow along DWT's in this experimental study. Duct 1 ($C_{T,duct} = 0.55$) has an aerofoil-shaped cross-section and duct 2 ($C_{T,duct} = 1.17$) is characterized by a cambered plate. The bare screen loadings varied from 0.46 to 1.12, but is affected by different duct geometry.

The first observation made is that the $C'_{T,DWT}$ varies with screen thrust and with duct geometry. The thrust on the cambered plate duct 2 stays constant with varying screen thrusts, which is attributed to the solid blockage the duct 2 creates. The consequence of this is an acceleration of the flow through the lesser loaded centre where the screen located. The thrust on the aerofoil-shaped duct 1 is highly dependent on screen thrust owing to the non-linear behaviour of the aerodynamic force on an aerofoil-shaped body.

The configuration of duct 2 with screen 5 ($C_{T,screen} = 1.12$) achieved the highest $C'_{T,DWT}$ (2.2) among all tested configurations, while duct 1 with screen 2 ($C_{T,screen} = 0.89$) obtained the lowest $C'_{T,DWT}$ (1.2). The effect of the duct on the total thrust coefficient $C'_{T,DWT}$ is shown and the growth in the duct thrust has a positive influence on the overall performance of DWT. Duct 1, with an aerofoil-shaped cross-section, is sensitive to the screen loading in contrast to the duct without an aerofoil-shaped cross-section. With low screen thrusts, the duct geometry plays a dominant role in the total DWT performance, but when increasing the screen thrust to a threshold, the screen takes over the dominant effect. This threshold value differs for different duct geometry.

Both high screen loading and inappropriate aerofoil shaped duct leads to flow separation which causes the momentum loss for DWT. Moreover, the optimal value of $C_{T,screen} = 0.89$ for a bare wind turbine doesn't apply to the tested DWTs. The optimal value of $C'_{T,DWT}$ depends both on duct geometry and the screen loading.

Increasing $C_{T,screen}$ increases the thrust on DWT though, but hugely decreases the velocity at the screen plane, hence reducing the mass flow passing through the screen

and the power output. For the heavily loaded screen ($C_{T,screen} = 0.89$), the velocity measurements demonstrate that flow separation occurs near the duct 1 external (pressure) surface, which supports the observations from the thrust measurements. Moreover, the axial velocity profiles show that the high thrust screen leads to a stalled mass around the centre line inside duct 1.

The total lift of $C_L = 0.95$ pointing in the right (inward) direction is derived from the pressure distribution along the empty duct 1. However, it reduces to 0.1 when the duct is equipped with screen 1. This screen decreases the of the duct and hence deflects the approaching flow outside the duct. A negative lift over the first 30% of the duct 1 (from the leading edge to the screen plane) is observed, and a positive lift over the remaining part is produced, leading to the total lift of about zero. This also shows that the duct shape is far from ideal in combination with screen 1.

In the end, it should be noted that from a quantitative point of view, the conclusions presented here are restricted to the tested ducts and screens. The aerofoil-shaped duct is proven not to work optimally with the screens in this study, but the effects observed can be qualitatively valid for other combinations of ducts and screens. Moreover, the analysis of the data demonstrates some new features of the aerodynamic performance not investigated before, it provides indications and directions for future research.

References

1. Hansen MOL, Sørensen NN, Flay RGJ (2000) Effect of placing a diffuser around a wind turbine. *Wind Energy* 3:207–213
2. Igra O (1981) Research and development for shrouded wind turbines. *Energy Convers Manag* 21:13–48
3. Lawn CJ (2003) Optimization of the power output from ducted turbines. *Proc Inst Mech Eng Part A J Power Energy* 217:107–117
4. Phillips DG, Flay RGJ, Nash TA (1999) Aerodynamic analysis and monitoring of the Vortec 7 diffuser-augmented wind turbine. *IPENZ Trans* 26:13–19
5. Van Bussel GJW (2007) The science of making more torque from wind: diffuser experiments and theory revisited. *J Phys Conf Ser* 75:012010
6. Shives M, Crawford C. Ducted turbine blade optimization using numerical simulation
7. Jamieson P (2008) Generalized limits for energy extraction in a linear constant velocity flow field. *Wind Energy* 11:445–457
8. Abe KI, Ohya Y (2004) An investigation of flow fields around flanged diffusers using CFD. *J Wind Eng Ind Aerodyn* 92:315–330
9. Matsushima T, Takagi S, Muroyama S (2006) Characteristics of a highly efficient propeller type small wind turbine with a diffuser. *Renew Energy* 31:1343–1354
10. Shives M, Crawford C (2010) Computational analysis of ducted turbine performance. In: 3rd international conference on ocean energy, Bilbao, vol 6, pp 1–6
11. Bontempo R, Manna M (2016) Effects of the duct thrust on the performance of ducted wind turbines. *Energy* 99:274–287
12. De Vries O (1979) Fluid dynamic aspects of wind energy conversion
13. Tang J, Avallone F, van Bussel GJW (2016) Experimental study of flow field of an aerofoil shaped diffuser with a porous screen simulating the rotor. *Int J Comput Method Exp Meas* 4:502–512

Analyzing the Unsteady Dynamic Behaviour of a Small Wind Turbine for Urban Applications



Francesco Castellani, Francesco Berno, Matteo Becchetti, Davide Astolfi and Emanuele Piccioni

Abstract The use of wind energy in urban areas is challenging especially for the unsteadiness of the resource on very short time scales. This makes the full conversion of the resource almost impossible because the wind turbine is not able to optimally follow the wind fluctuations exactly balancing the production and the load. Therefore the analysis and the development of conversion systems specifically suited for urban areas need to be faced with a different approach with respect to large wind power plants. In this work, a new experimental and numerical approach is proposed and tested for the development and the characterization of a small horizontal axis wind turbine. The method is aimed at studying how the turbine and the control system are able to react to a controlled turbulent wind generated experimentally in the “R. Balli” Wind tunnel at the University of Perugia. This new experimental approach is able to give useful information on how the system design can be adjusted to the specific urban conditions improving the aerodynamic and control system dynamic performance.

F. Castellani (✉) · F. Berno · M. Becchetti · D. Astolfi · E. Piccioni
Department of Engineering, University of Perugia, Via Duranti, 06125 Perugia, Italy
e-mail: francesco.castellani@unipg.it

F. Berno
e-mail: francesco.berno@studenti.unipg.it

M. Becchetti
e-mail: matteo.becchetti@unipg.it

D. Astolfi
e-mail: davide.astolfi@unipg.it

E. Piccioni
e-mail: piccioni1979@gmail.com

1 Introduction

Small wind turbines [16] are subjected to very complex loads due to several reasons (highly variable speed shaft rotation [4], sudden wind direction changes [11], turbulence [8, 10] and gusts [1] especially in urban environment [14], etc.), so that an in-depth analysis is needed to understand their dynamic behavior in order to guarantee acceptable wind kinetic energy conversion efficiency [6, 13]. The full conversion of the resource is almost impossible because the wind turbine is not able to optimally follow the wind fluctuations exactly balancing the production and the load: this is supported, for example, in [2], where the capability of a turbine to effectively adapt its rotational speed in order to satisfy a prescribed control strategy is investigated in light of two parameters: the required rotor acceleration and the available rotor acceleration. A new bound for a reliable estimation of the amount of energy a wind turbine will generate in a specific site is proposed, basing on the characteristic time scales of the wind turbine and of the wind resource on site. A similar line of reasoning has been proposed in [15], where the dynamic power reduction of wind turbines is investigated numerically and experimentally, assuming that a steady-state optimal torque control strategy is used.

As regards the study of the dynamic behavior of wind turbines, wind tunnel tests on one hand have the drawback that the low-turbulence wind time series that are commonly generated are not much representative of real ambient conditions to which wind turbines are subjected (especially in urban contexts). On the other hand, yet, wind tunnel tests have the great advantage of repeatability and the possibility to control the wind conditions.

Furthermore, having at disposal reliable computational frameworks for characterizing the dynamic behavior of wind turbines is becoming more and more important. Actually, having a digital twin of a wind turbine is gradually becoming a need for wind turbine practitioners. Robust numerical models can be reliably validated against wind tunnel tests and, vice-versa, robustly validated numerical models can extrapolate meaningful indications about wind turbine behavior under regimes that difficulty can be produced in laboratory.

On these grounds, in the present work, a small horizontal axis three-bladed wind turbine [12], having 1 kW of maximum power, has been analyzed through numerical and experimental investigations in the “R. Balli”¹ Wind Tunnel of the University of Perugia. Previous studies on this test wind turbine have been conducted for example in [4], with stationary and ramp wind: these tests have resulted useful to investigate some mechanical properties, such as vibration spectra and the natural frequencies of the machine. This kind of studies could be very useful for understanding noise and vibration problems, peculiar of small wind turbine technology [7, 9], and mitigating them.

In this work we suggest a new “unsteady” approach in order to characterize the performance of the turbine and of the control system and to obtain reliable hints for improving the dynamic behavior. It consists in investigating the transient response

¹www.windtunnel.unipg.it.

of the machine, in particular in terms of delay and amplitude magnification between a controlled unsteady input (represented by wind speed) and the output (represented by rotor speed and power).

As in [4, 5], the approach is twofold: the experimental study of the test wind turbine in the wind tunnel under controlled unsteady wind is interfaced with an aeroelastic numerical modeling of the wind turbine [3]. The one-to-one feedback between model and experiment is valuable in order to cross-check the reliability of the model and the robustness of the experimental measurements. Results from the present work clearly demonstrates pros and cons in switching from steady to sinusoidal wind test and how this kind of results can be used to characterize the machine's dynamic behaviour.

The rest of the paper is organized as follow: in Sect. 2 the numerical and experimental approaches are introduced, in Sect. 3 the results are compared and discussed while in Sect. 4 some conclusions are drawn.

2 Methods

2.1 Experimental Tests

The experimental measurements were performed in the R. Balli wind tunnel at the University of Perugia. In this facility the air can be accelerated up to a maximum speed of 47 m/s using a fan driven by a 375 kW electric motor in a closed loop circuit. The open test chamber has an inlet section of 5m² of area and a recovery section of 7m². The wind speed is measured by two Pitot tubes and a cup anemometer placed at the inlet section; in the testing room also the ambient conditions (static air pressure, temperature and relative humidity) are continuously monitored. The inverter controlling the fan drive allows to generate wind time histories that are variable in time; this feature is crucial for the purposes of this work.

The small wind turbine model is an horizontal axis, fixed pitch machine with a 2 m diameter rotor featuring three blades made of glass-fiber reinforced polymer.

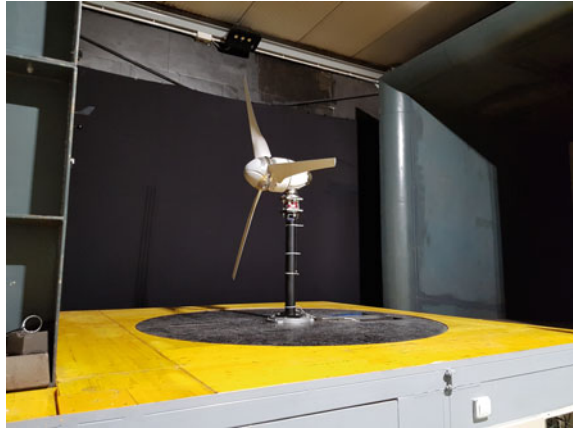
The rotor operates in a wide range of rotational speeds (from 200 up to 700 rpm) so that this configuration is considered to be representative of a small wind system used to harvest unsteady urban winds.

The turbine was placed for the unsteady test approximately in the center of the open test chamber of the tunnel (see Fig. 1). The collected measurements are:

- Wind speed (through an anemometer and a pitot);
- Rotor speed (through an optical tacho and a wind interface);
- Power output.

The turbine control is fully electric and is operated using a variable resistive load continuously adjusted through a PWM (Pulse Width Modulation) duty cycle, with a frequency of 500 Hz.

Fig. 1 The small horizontal axis wind turbine in the wind tunnel open test section



The load modulation is operated to follow the optimal rpm-power curve obtained from steady wind tests.

Unsteady behavior of the system has been investigated using a wind time history with an overall duration of 500 s arranged as follows:

1. 100 s of steady wind (approximately 8.5 m/s);
2. 300 s of sinusoidal wind with an amplitude of approximately 1.3 m/s and a variable period (three periods were tested: 10, 20 and 30 s);
3. 100 s of steady wind (same steady conditions as at the beginning of the test).

So an overall of three different unsteady conditions were analysed (named test1, test2 and test3). Finally a test of the unloaded turbine was done in a similar way (called test4) but the average wind speed was kept lower (4 m/s) in order to avoid problem of overspeed for the rotor.

2.2 Numerical Modeling

As introduced in Sect. 1, having a good model of a wind turbine is fundamental for the objectives of this work: therefore, an aeroelastic model [3] using the code *FAST v8²* is set up and tuned.

As discussed in [4], this code was not developed for micro-wind turbines and therefore must be tuned carefully when adopting it for simulating the dynamic behavior of a small device. For this reason, the Matlab-Simulink interface (available for this code) is used, in order to implement a better control of the device. The core of the code is the power control, which has the aim of representing the behavior of the real turbine. In Simulink, a sub-system controls it: in input it receives the shaft

²*Fatigue, Aerodynamics, Structures and Turbulence* achieved by NREL.

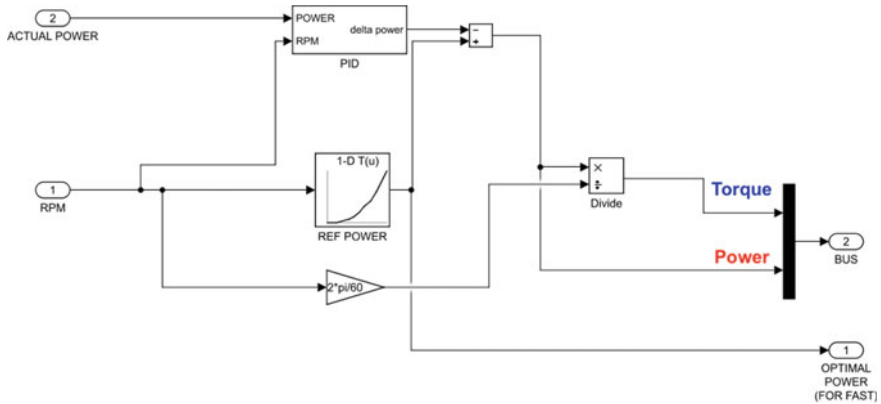


Fig. 2 Simulink model of the full-electric closed loop control

speed (in rpm) and the power and it estimates in output the requested power that the turbine should produce. A look-up table is adopted, that associates to every value of rpm a value of optimal power: these couples of values (rpm vs optimal power) are the same of the real turbine used in the wind tunnel; they were calculated on the grounds of steady-state tests with different wind speeds, changing the electrical load, until the turbine didn't produce the maximum power, according to the MPPT theory (Maximum Power Point Tracking). The power computed in this way represents the set-point value and it is used in the PID sub-system in which a value of power (called ΔP) is produced in output. This is proportional to the error, to the integral and to the derivative of the error, through the constants K_P , K_I , K_D . However they are different from the ones used by the real turbine: in fact a lot of components that influence the behavior of the turbine and its control (the electrical generator, the rectifier, inductive and capacitive loads, etc) are not represented in the Simulink code. After the ΔP is estimated (it can be positive or negative), this is added to the power requested to the machine; FAST needs also the value of the torque, which is obtained by dividing the output power by the angular speed (see Fig. 2).

Several simulations have been performed, using as inputs the same wind time series measured in the wind tunnel through the pitot, in order to compare the simulation output against the measurements. Notice that both the real turbine and the numerical model don't use the wind speed to control their power; in the simulation this is very important because the wind speed can be considered an independent input and so numerical and experimental results are obtained, that can be considered sort of different outputs from the same input and therefore they can be compared.

Table 1 Statistics of power output from numerical and experimental analysis

	Output power (W)					
	Test1		Test2		Test3	
	Average	Std	Average	Std	Average	Std
Experimental	526.7	176	528	157	526	146
numerical	533	96	537	134	537	131

Table 2 Statistics of rotor speed from numerical and experimental analysis

	Rotor speed (rpm)							
	Test1		Test2		Test3		Test4	
	Average	Std	Average	Std	Average	Std	Average	Std
Experimental	469.8	59.8	471.6	54.6	471.4	51	386	74
numerical	479	36.32	477	50.3	477.3	49	461	62

3 Results

In Tables 1 and 2, the statistical features (average value and standard deviation) of the measured and simulated time series of power and rotor revolutions per minute (rpm) are reported and compared. The main result is that there is a quite good agreement between them. Generally the experimental measurements are characterized by a higher degree of unsteadiness as demonstrated by higher values of standard deviations.

These results demonstrate how unstable can be the operation of a small wind turbine and how the unsteady electric parameters can stress the electrical interface connecting the system to the local grid.

Measuring the unsteadiness of the power output using the statistical parameter can anyway be useful in order to choose the final configuration for the connection to the local grid (if the the power fluctuations are too strong using battery storage can be a very good solution).

The most important result of the dynamic analysis should be also the characterization of the transfer function between the wind and the rotor speed in the time domain.

This task is challenging because a perfect synchronization between the wind input and the machine response need to be achieved.

Unfortunately the analysis of phase-shift between the wind speed (measured by the pitot tube, used due to its faster responde given by its lower inertia, at the inlet of the test section) and the rotor speed revealed problems with the closed-loop configuration of the wind tunnel.

From results of Table 3 a positive shift can be observed between wind and rotor speed especially for test1 (with the smallest period of 10s): this means that the rotor

Table 3 Numerical and experimental results for the phase shift (expressed in percentage of the period) between wind speed and rotor speed

	Phase shift (%)			
	test1	test2	test3	test4
Experimental	23	5	-1	-4
numerical	-7	-7	-4	-20

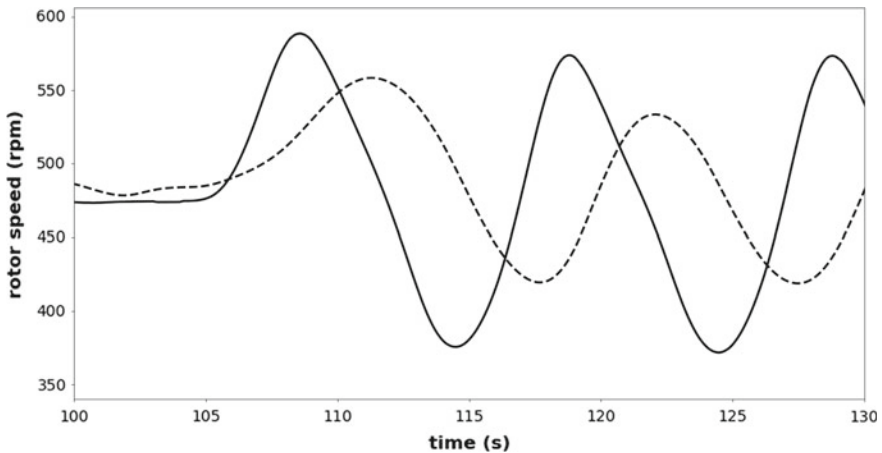


Fig. 3 Trend of the rotor speed measured (solid line) and simulated (dashed line) for test1 (sinusoidal wind with a period of 10s)

speed rise before the wind speed and this result is meaningless for the open field condition and is only due to the dynamic of the closed-loop circuit of the tunnel.

The phase shift between wind speed and rotor speed is always negative for the numerical model because the simulation is tuned to reproduce open field conditions and it doesn't account for the effects of the closed-loop configuration of the tunnel. In Fig. 3 the different behaviour between the experimental and numerical results can be clearly appreciated. These results suggest to not rely on time history but consider the unsteady statistics in the comparison between numerical and experimental result.

Another disagreement between the experimental and numerical results was discovered analysing also the shift between the rotor speed and the power output: in the numerical model the rotor speed and the power are synchronized (we are simulating an ideal perfect control) while in the experimental measurements there is a positive shift of a few percent of the period (decreasing from 4% for test1 to 2% for test3). This is mainly due to some effects of the electrical circuit (that was not simulated numerically) and the aerodynamic damping that is not correctly reproduced by the model as demonstrated by results in Table 2 (the experimental rotor speed for test4 without load is considerably lower than the numerical one).

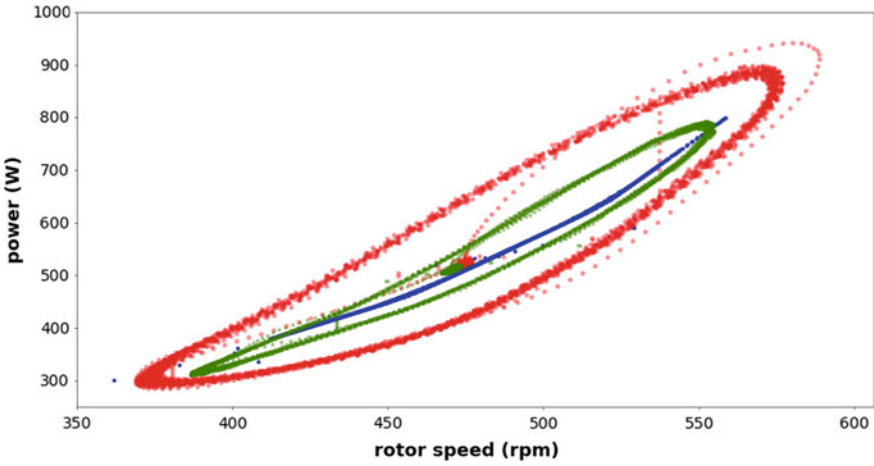


Fig. 4 Power versus rotor speed for experimental measurements of test1 (red) and test3 (green) compared to the numerical results (blue)

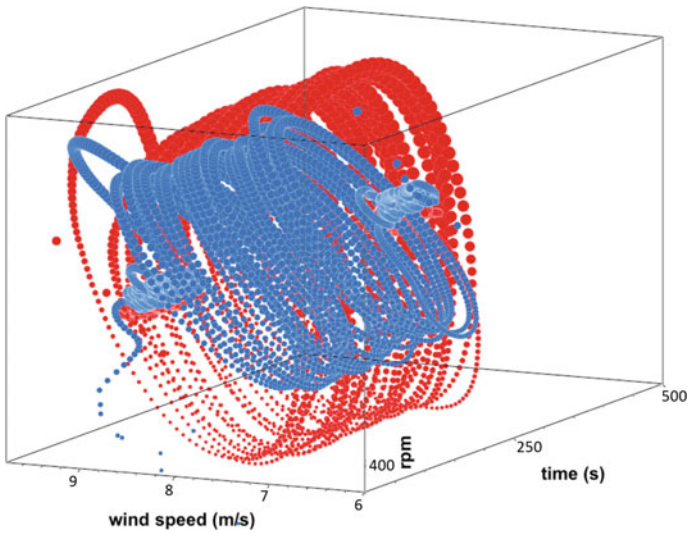


Fig. 5 Comparison of the experimental (red) and numerical (blue) trend of the rotor speed versus wind speed and time (test1)

In Fig. 4 it is possible to observe how the blue numerical trend reproduce exactly the reference optimal table obtained by the steady test (used as reference for the control) while the experimental measurements are affected by the above mentioned effects.

Figure 4 demonstrates that the numerical model is able to reproduce only very slow turbulent wind (similar to that of test3 with an overall period of 30s) in a

reliable way and that a further development of the model is necessary to reproduce the real machine dynamics.

Anyway from Fig. 3 and from the 3D plot of Fig. 5 it can be observed that the actual configuration of the model is able to correctly predict the initial overshoot in the transition between the steady wind condition and the sinusoidal regime. This somehow demonstrates that the very fast transitions are mainly governed by the aerodynamic and mechanical parameters that are already correctly included in the current version of the numerical model.

4 Conclusions

In this work, an experimental and numerical analysis has been conducted on a small horizontal axis wind turbine. The experimental analysis has been carried out at the wind tunnel “R. Balli” of the University of Perugia and it basically consists in sinusoidal wind tests aimed at analysing the dynamic behaviour of the turbine. This approach is expected to be much more useful when developing a system that is going to operate in a turbulent unsteady urban wind environment.

The numerical analysis was performed using the aeroelastic code FAST by NREL and Matlab-Simulink in order to reproduce the actual power control.

Results discussed in Sect. 3 unveiled the pros and cons of such unsteady approach and also the weakness of the model as well of the wind tunnel closed-circuit configuration.

The experimental measurements are reliable in terms of global statistics and can be considered in order to characterize the dynamic behaviour of the system and define important improvements.

Also the numerical model seems to give reliable results in term of global unsteady statistics and can be useful in the developing phase to choose the optimal mechanical and aerodynamic configuration while a further improvement is necessary to correctly reproduce the dynamic response of the control.

Unfortunately the closed-loop configuration of the tunnel doesn't allow to estimate the phase shift between the wind and the machine response in term of rotor speed or power. This can be due to the following effects that somehow can induce a delay in the wind speed measurements:

- the open test chamber can act as a sort of reservoir and store part of the air flow when the rotor thrust is suddenly rising;
- the effect of the pressure gradients can induce on the large volume of air in the tunnel loop some small changes in volume/density.

In the future it is planned to investigate such effect more in deep using some additional pressure measurements inside the wind circuit and also developing other different methods to produce unsteady wind time histories (i.e. using oscillating grids).

A further improvement of the present work could be a more detailed representation of the whole chain of the transformation of wind into power output. In particular,

the electric chain could be simulated in a more realistic way, including also the synchronous generator, the rectifier and the resistive load, as they are used during the experimental tests. In this way it will be possible to use the same control parameters of the real turbine (PID parameters, PWM control law, etc) and study how they influence the response of the machine, for example in terms of delay between the wind and the rotor rotational speed.

References

1. Alpman E (2015) Aerodynamic performance of small-scale horizontal axis wind turbines under two different extreme wind conditions. *J Therm Eng* 1(3):420–432
2. Battisti L, Benini E, Brighenti A, Dell’Anna S, Castelli MR (2018) Small wind turbine effectiveness in the urban environment. *Renew Energy* 129:102–113
3. Bradney D, Evans S, Da Costa MSP, Clausen P (2016) Comparison of computational modelling and field testing of a small wind turbine operating in unsteady flows. *J Phys Conf Ser* 753:082029 (IOP Publishing)
4. Castellani F, Astolfi D, Becchetti M, Berno F, Cianetti F, Cetrini A (2018) Experimental and numerical vibrational analysis of a horizontal-axis micro-wind turbine. *Energies* 11(2):456
5. Castellani F, Becchetti M, Astolfi D, Cianetti F (2017) Dynamic experimental and numerical analysis of loads for a horizontal axis micro wind turbine. In: *Research and innovation on wind energy on exploitation in urban environment colloquium*. Springer, pp 79–90
6. Grieser B, Sunak Y, Madlener R (2015) Economics of small wind turbines in urban settings: an empirical investigation for germany. *Renew Energy* 78:334–350
7. Lee S, Lee S (2014) Numerical and experimental study of aerodynamic noise by a small wind turbine. *Renew Energy* 65:108–112
8. Lubitz WD (2014) Impact of ambient turbulence on performance of a small wind turbine. *Renew Energy* 61:69–73
9. Mollasalehi E, Sun Q, Wood D (2013) Contribution of small wind turbine structural vibration to noise emission. *Energies* 6(8):3669–3691
10. Pagnini LC, Burlando M, Repetto MP (2015) Experimental power curve of small-size wind turbines in turbulent urban environment. *Appl Energy* 154:112–121
11. Sang LQ, Murata J, Morimoto M, Kamada Y, Maeda T et al (2017) Experimental investigation of load fluctuation on horizontal axis wind turbine for extreme wind direction change. *J Fluid Sci Technol* 12(1):JFST0005–JFST0005
12. Scappatici L, Bartolini N, Castellani F, Astolfi D, Garinei A, Pennicchi M (2016) Optimizing the design of horizontal-axis small wind turbines: from the laboratory to market. *J Wind Eng Ind Aerodyn* 154:58–68
13. Sunderland K, Woolmington T, Blackledge J, Conlon M (2013) Small wind turbines in turbulent (urban) environments: a consideration of normal and weibull distributions for power prediction. *J Wind Eng Ind Aerodyn* 121:70–81
14. Tabrizi AB, Whale J, Lyons T, Urmee T (2014) Performance and safety of rooftop wind turbines: use of CFD to gain insight into inflow conditions. *Renew Energy* 67:242–251
15. Tang C, Soong WL, Freere P, Pathmanathan M, Ertugrul N (2013) Dynamic wind turbine output power reduction under varying wind speed conditions due to inertia. *Wind Energy* 16(4):561–573
16. Tummala A, Velamati RK, Sinha DK, Indrajya V, Krishna VH (2016) A review on small scale wind turbines. *Renew Sustain Energy Rev* 56:1351–1371

Effectiveness of Wind Turbines in Urban Environment



L. Battisti, S. Dell'Anna, M. Raciti Castelli and A. Brighenti

Abstract The urban environment is generally characterised by highly unsteady wind conditions that represent a challenge for both gust and direction tracking capabilities of small wind turbines, which usually rely on passive alignment systems. The resulting penalties in terms of energy harvest and structural issues are well documented from many reports. The here proposed work addresses the impact of the response time of urban wind energy conversion systems on the global amount of energy production at an urban site. For this purpose, the results of a campaign of measurements conducted at the urban test site of the University of Trento (IT) is presented with particular regard to the kinetic energy content of the gusts, which is estimated by resorting to a high temporal resolution of the measured wind velocities.

Nomenclature

Symbols

ARA	available rotor acceleration [m/s^2]
A_s	rotor swept area [m^2]
c	chord length [m]
C_P	power coefficient [-]
E	specific energy [Wh/m^2]
$f(x)$	probability distribution function of variable x [-]
$F(x)$	cumulative distribution function of variable x [-]
Q	torque [Nm]
R	radius [m]

L. Battisti (✉) · S. Dell'Anna · M. Raciti Castelli · A. Brighenti
Department of Civil Environmental and Mechanical Engineering, University of Trento,
Trento, Italy
e-mail: lorenzo.battisti@unitn.it

M. Raciti Castelli
e-mail: marco.raciticastelli@unitn.it

I	rotor inertia respect to the axis of rotation [kgm ²]
P	power [W]
RRA	required rotor acceleration [m/s ²]
TI	turbulence intensity [-]
U	rotor peripheral speed [m/s]
V	wind speed [m/s]
\dot{V}	wind acceleration [m/s ²]
WTI	wind tracking index [-]

Greek Letters

Δt	time variation [s]
ΔV	wind speed variation [m/s]
λ	tip speed ratio [-]
ω	rotational rotor speed [rad/s]
$\dot{\omega}$	rotational rotor acceleration [rad/s ²]
ρ	air density [kg/m ³]
τ_0	natural time constant [s]
τ	time scale [s]

Subscripts

aero	aerodynamic
gen	electric generator
MAX	maximum
opt	optimum
TOT	total
∞	free stream

Abbreviations

CDF	cumulative distribution function
HAWT	horizontal axis wind turbine
PDF	probability distribution function
RS	roughness sublayer
SBL	atmospheric sublayer
URS	urban roughness sublayer
VAWT	vertical axis wind turbine

1 Introduction

Even though the growth of the wind energy industry mostly concerned large-scale power plants located both in upland rural areas and offshore, usually characterized by high wind potential, the opportunity of exploiting wind energy also in the urban setting has recently arisen some public interest [1], in the perspective to help reducing the energy demand, providing a source of clean and distributed power while lowering capital investments in transmission lines at the same time [2]. However, early experiences have immediately made clear that this field of application needed new knowledge areas, in resource analysis, fluid-dynamics and structural design. As a matter of fact, the wind distribution over and around buildings appears quite complex, usually characterised by lower average wind speeds and higher turbulence levels and wide wind direction variance with respect to conventional open field sites [3].

Vertical axis wind turbines (VAWTs) can in principle offer some advantages with respect to their horizontal axis counterparts (HAWTs), namely because of their potential capability of harvesting wind energy independently from the incoming wind direction (presenting superior performances in skewed flows at the same time [4]), this feature overcoming misalignment problems which traditionally affect HAWTs [5]. However, practical application has shown that their response time to varying wind intensity appears quite long due to their high inertial characteristics [6]. This problem seems to affect also small wind turbines of relatively large diameters (above about 5 m). Such considerations raise the question of whether small wind turbines can effectively operate within the built areas, taking advantage from a strong gusty environment characterised by frequent and unexpected wind direction changes.

A wide measurement campaign on small turbine operation at the urban experimental test site of the University of Trento [7] allowed the collection of wind data for a period of about 7 years, from 2007 to 2013. Located in the Adige valley, which is oriented along the North–South direction (Fig. 1), the test site is characterized by a flat terrain within the industrial estate of Trento city. Buildings (maximum height 20 m) are disseminated around the test site, apart from the East sector, which is covered by apple trees and a few small houses. Due to the presence of many obstacles in the vicinity of the turbines and the measuring masts, this site can be classified as urban, or sub-urban, and its wind feature can be considered as representative of typical urban sites. More details can be found in [8].

Among the wide quantity of data harvested from 2007 to 2013, this work presents the elaboration of high acquisition rate wind data taken during a three months measurement campaign, aimed to classify the characteristics of the urban resource with particular regard to gusts distribution and duration, as well as wind speed direction changes.

Additionally, a further statistical analysis is here performed on raw data, to deduce also wind speed accelerations and wind direction change rates. The former can be compared to the acceleration rate of the wind turbine rotor, and the latter to the yawing rate of the rotor. A simple model has been used to compute the potential energy loss for an ideal wind turbine, i.e. able to fully track wind characteristics.

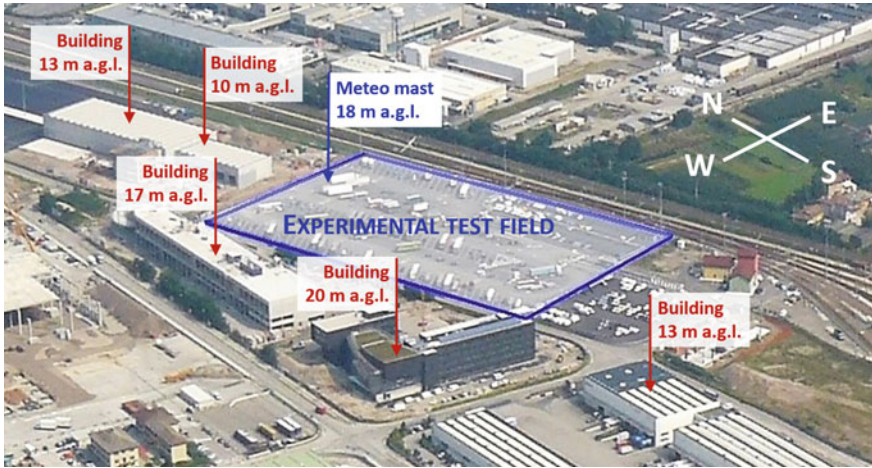


Fig. 1 Test site view (in the blue rectangular) and the neighbour obstacles

2 Methodology and Data Processing

The high variability of wind in time, in terms of both module and direction, requires high frequency measurements. To perform a proper assessment of the wind resource in a typical urban site, the data used for this study were collected during a three months period (summer 2013). The adopted sensor was an ultrasonic anemometer characterised by a wind speed accuracy lower than 1% rms and a resolution of 0.01 m/s on the intensity measurements, and lower than $\pm 1^\circ$ rms and a resolution of $< \pm 1^\circ$ on the direction measurements. The sensor was installed on a meteo mast at 18 m a.g.l. serving as reference tower for one of the tested wind turbines. The resulting database consists of 44167 files of one minute duration at a sampling rate of 20 Hz. In order to consider only the environmental turbulence, measured data were elaborated according to IEC 61400-12 [9], thus excluding all occurrences affected by obstacles in the proximity of the mast. The data were stored in a relational database that allows to extract selectively number of events of wished characteristics.

A gust is generally considered as a sudden, short lasting increase/decrease in speed intensity of the wind. This event is typically accompanied by an inherent change of wind direction. The phenomenon can be characterised by an initial instantaneous wind speed magnitude V_∞ and direction θ_∞ . During gust events lasting for a duration time Δt , a wind speed magnitude variation or acceleration/deceleration $\dot{V}_\infty = dV_\infty(t)/dt$, and a directional variation $\dot{\theta}_\infty = d\theta_\infty(t)/dt$ can be inferred. In the present analysis, a gust is an event which ends when the rising wind speed start decreasing, while the direction change lasts until a change in the direction (from clockwise to anticlockwise direction or viceversa) can be recorded.

A sample of wind gusts variation in intensity (left) and direction (right) during a time history of 50 min are presented in Fig. 2. A clear relationship between the

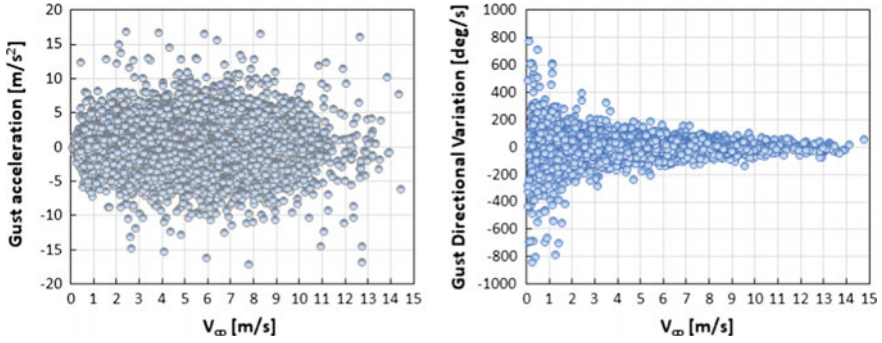


Fig. 2 Wind speed variation in intensity (left) and direction (right) during a time history of 50 min recorded at the test site

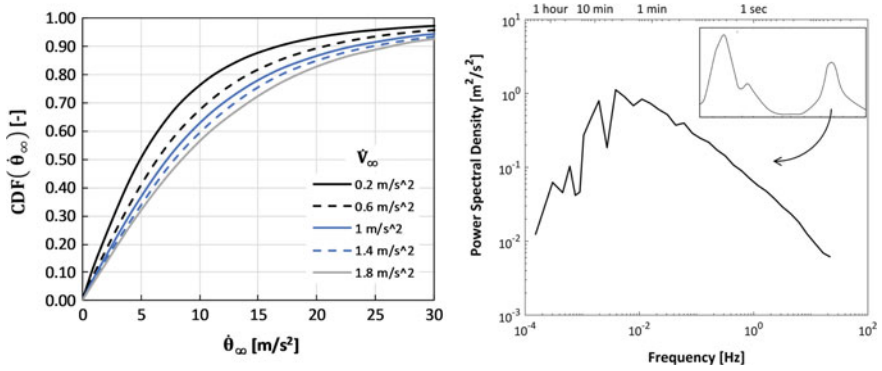


Fig. 3 Wind speed magnitude versus wind directional rate (left) and power spectral density, recorded at the test site and limited to the high frequency events (right)

wind speed acceleration and directional rate is shown in Fig. 3 left. Lower wind accelerations show an higher probability to have low directional rates. The high intensity fluctuations are well documented in the power spectral density diagram [10] reconstruction of Fig. 3 right, limited to the high frequency events (from 10⁻³ to 10¹ Hz). Data were obtained during a period of 40 min (the sampling rate was 50 Hz at a 10-min mean wind speed of 7 m/s and turbulence intensity of 0.27). The area below the spectral curve represents the significant amount of energy stored within the higher frequency components of the gusts (being the peak at about 0.01 Hz, or 100 s).

3 Results and Discussion

The results of the elaborations of the wind measurements data are discussed in Sects. 3.1 and 3.2. Section 3.1 characterises the main features of the wind speed gusts, while Sect. 3.2 addresses the wind direction changes. Section 3.3 illustrates the results of a model developed to evaluate the energy lost of an ideal turbine subjected to site wind speed acceleration and deceleration with limited gust tracking capability. Section 3.4 uses a similar model to evaluate the energy lost by an inadequate yawing characteristic of an ideal turbine under varying wind directions. These models are of general validity, regardless to turbine type, and maintain validity under the hypothesis that the wind lateral coherence is higher than the rotor diameter due to the punctual measurement performed.

3.1 Wind Statistics on Wind Speed Magnitude

Although all three wind components were measured, the acceleration was computed only on the basis of the variation of the wind speed module in the horizontal plane. The time window adopted to observe the accelerations was set to 0.2 s (5 Hz), thus allowing the investigation of all phenomena bound to a time scale of the second with a suitable time resolution capable of satisfying common sampling rate criteria. A matrix of occurrences was obtained by dividing the measured wind speeds into bins of 0.5 m/s and the resulting accelerations into bins of 0.2 m/s². The distribution of the recorded gust durations is represented in the left chart of Fig. 4 and it shows that the 56% of the gusts last less than 1 s, while 82% less than 2 s. The right chart of Fig. 4 illustrates the frequency distribution curves of the accelerations \dot{V}_∞ for different initial wind speeds V_∞ . The resulting curves are almost symmetrical with respect to zero, where they achieve the maximum value. On the whole, it is possible to say that the wind accelerations and decelerations rates show a similar frequency. Such result is consistent with previous findings [11].

90% of the gusts presents an acceleration rate less than 2.5 m/s² (Fig. 5, left). Moreover, lower wind speed magnitudes are characterised by lower accelerations (Fig. 5, right): 90% of the gusts at 4 m/s show wind accelerations up to 3.0 m/s², whereas 90% of the gusts at 8 m/s accelerate up to 4.5 m/s². All trends are of exponential type.

3.1.1 Modeling of Gusts

An analytical model is here developed to generalise the relationship between wind speed magnitudes V_∞ and accelerations \dot{V}_∞ described by the cumulative frequency distributions shown in Fig. 5 (right):

$$\dot{V}_\infty = -\frac{\ln(1 - F(\dot{V}_\infty))}{aV_\infty^3 + bV_\infty^2 + cV_\infty + d} \quad (1)$$

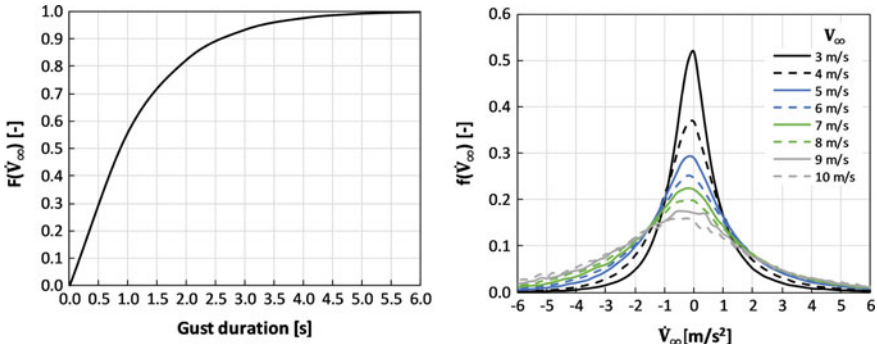


Fig. 4 Variation of wind speed magnitude: the cumulative distribution of the duration (left) and the frequency distribution (right) as a function of the initial wind speed

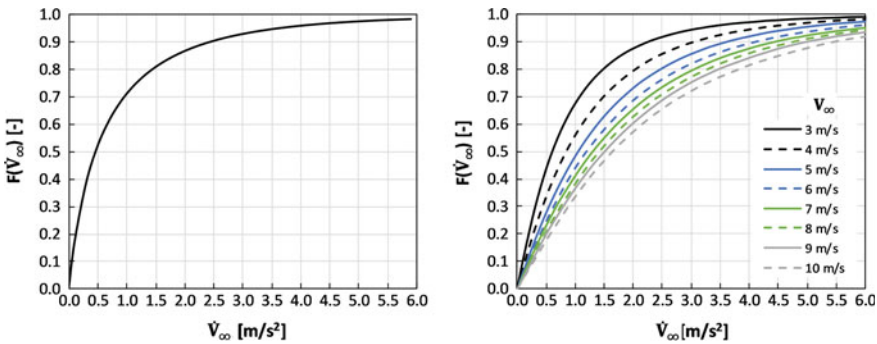


Fig. 5 Cumulative frequency distribution of the wind speed variation: the full range of wind speeds (left) and a selection of some wind speed magnitudes (right)

where $a = -0.001862$, $b = 0.04790$, $c = -0.4365$, and $d = 1.864$. The theoretical curve overlap the experimental data in the wind speed range from 5 to 11 m/s with a correlation R^2 of 0.98.

3.2 Wind Statistics on Wind Speed Direction

Figure 6 shows the frequency distribution of wind direction displacements $\Delta\theta$ for different initial wind speeds V_{∞} . The positive values are referring to clockwise displacements, while the negative ones to counterclockwise displacements. The resulting curves indicate only a moderate range of displacements (up to $\pm 60^\circ$), and the dependency on wind speed magnitude is limited to very small changes in wind directions (between zero and $\pm 8^\circ$), thus allowing the general statement that the amplitude

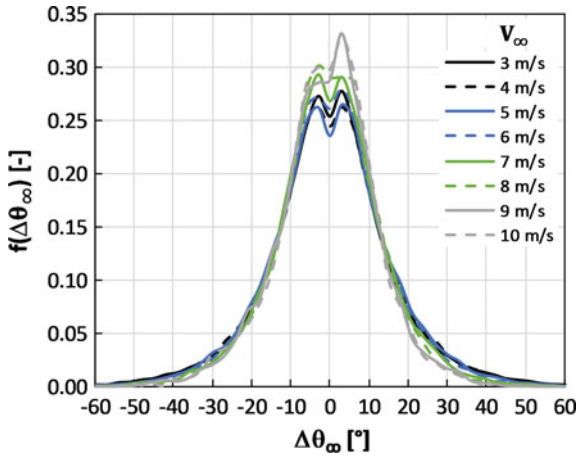


Fig. 6 Wind direction displacements: frequency distribution as a function of the initial wind speed

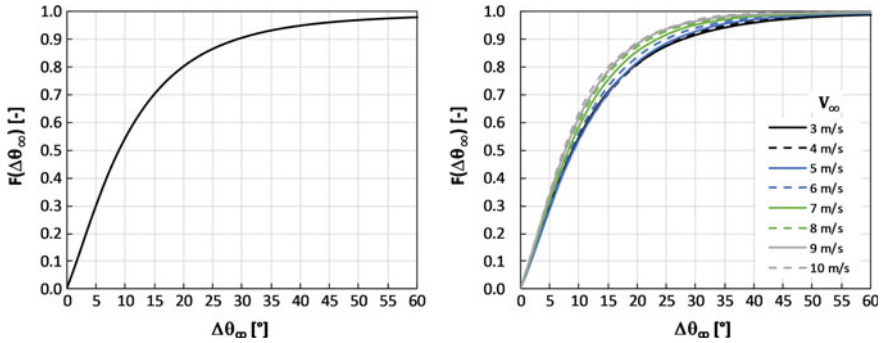


Fig. 7 Cumulative frequency distribution of the wind direction displacements $\Delta\theta$: the full range of wind speeds (left) and a selection of some wind speed intensities (right)

of wind direction change is about independent on wind intensity, at least in the range of data investigated with statistical significance. By considering the absolute value of displacements, the cumulative frequency distributions reported in Fig. 7 (left graph) show that 90% of the gusts vary between few degrees and 30°, and decrease up to 22° at 10 m/s (Fig. 7, right graph).

By analysing the wind direction displacements in time, it once more appears that the gust event is a very quick phenomenon: 90% of the directional gusts present a duration time lower than 2.5 s (Fig. 8, left). Considering both possible rotation directions (clockwise and counterclockwise), the distribution of the wind directional variation shown in the right part of Fig. 8 follows a symmetrical distribution (as for the wind magnitude, right chart of Fig. 4) and seems not so dependent on wind speed magnitude.

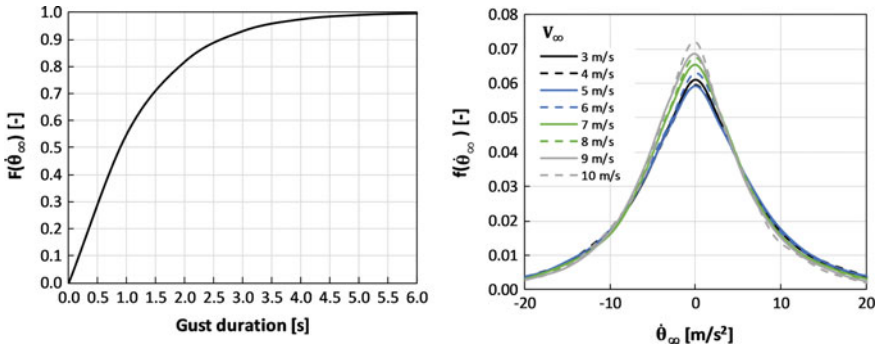


Fig. 8 Variation of wind speed direction: the cumulative distribution of the duration (left), and the frequency distribution (right) as a function of initial wind speed

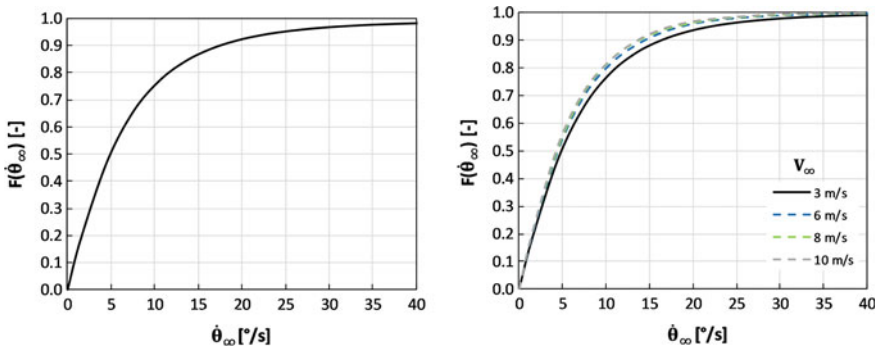


Fig. 9 Cumulative frequency distribution of the wind speed directional variation: the full range of wind speeds (left) and a selection of some wind speed intensity (right)

In addition, 90% of the gusts present a wind directional variation less than 16.5°/s (Fig. 9, left), and it clearly appears that the lower wind speed values are characterised by an higher directional amplitude: 90% of gusts at 3 m/s present a wind speed directional variation up to 16.5°/s, whereas 90% of gusts at 8 and 10 m/s present the same maximum directional variation of 13.5°/s. Recalling also the right chart of Fig. 5, it is apparent that lower wind speed magnitudes are characterised by lower accelerations and higher directional variations.

3.2.1 Modeling of Direction Change

A proper mathematical relationship can be found to model the cumulative frequency distributions shown in Fig. 9 (right chart) between wind speed magnitudes V_∞ and directional variation rates θ_∞ :

$$\dot{\theta}_\infty = -(eV_\infty + f) \ln(1 - F(\dot{\theta}_\infty)) \tag{2}$$

where $e = -0.10$ and $f = 7.0$. The theoretical curve overlap the experimental data with a correlation R^2 of 0.99.

3.3 Energy Exploitation Under Wind Speed Gusts

The capability of a generic wind turbine to harvest the kinetic energy content in a gusty environment depends on the capability of the system to adapt the rotational speed of the rotor to the changed conditions of wind speed intensity (sometime referred as “capturability”). This ensures to maintain the design maximum coefficient of performance over a wide range of wind speeds, typically from cut-in velocity to rated velocity. In principle a wind turbine adapting instantaneously its rotational speed to incoming wind is regarded here as an ideal turbine, harvesting the maximum available energy in the site. Any deviation from this behaviour determines a loss of energy. This loss can be represented by the aid of the simple scheme of Fig. 10 (left): the gust presents an initial wind speed magnitude V_∞ , a duration time Δt , and a final wind speed magnitude $V_\infty + \Delta V_\infty$.

The kinetic energy content of the gust is also represented (right scheme of Fig. 10) as a sum of two terms:

- $E_{0,i}$, that is the specific power $1/2\rho V_{\infty,i}^3$ available in the period Δt_i (the rectangular area),
- and $E_{\dot{V}_{\infty,i}}$, namely the specific power $1/2\rho(\dot{V}_{\infty,i}\Delta t_i)^3$ available in the period Δt_i because of the wind speed increase (well approximated by a triangular area for a short duration gust).

Fig. 10 Schematic representation of the i th gust characterised by an acceleration $\dot{V}_{\infty,i}$, duration time Δt_i , initial $V_{\infty,i}$ and final wind speed $V_{\infty,i} + \Delta V_{\infty,i}$ (left), and its qualitative specific energy content (right, shaded area)

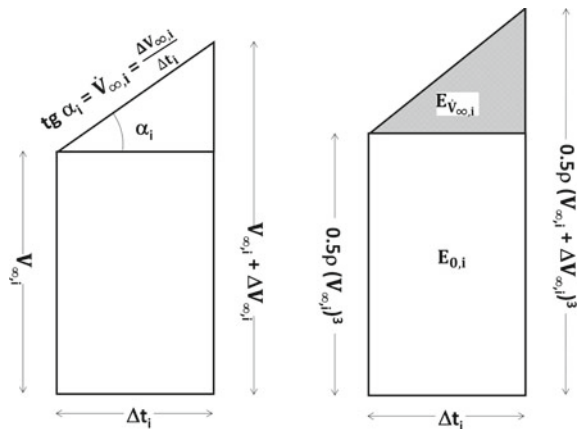
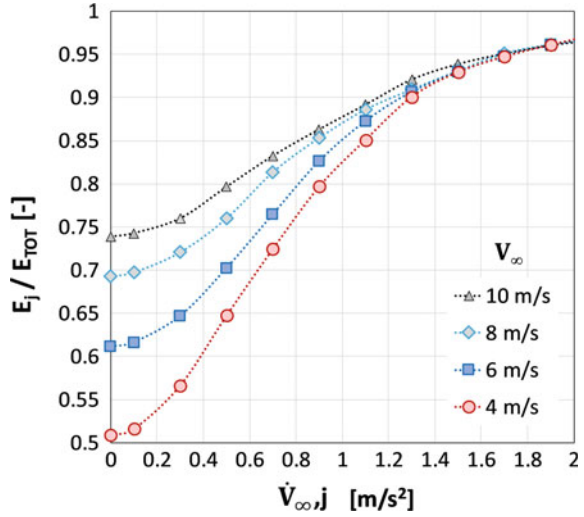


Fig. 11 Cumulative representation of the energy exploitation rate E_j/E_{TOT} as a function of wind acceleration bin $\dot{V}_{\infty,j}$ for four selected speeds V_{∞}



For any given initial wind speed $V_{\infty,i}$ the acceleration values were divided into a series of m j -bins of 0.2 m/s^2 ($\dot{V}_{\infty,j} = 0.2j$ where $j = 1, \dots, m$).

Moving to the energy exploitation, the cumulative energy content E_j is normalised to the global energy content E_{TOT} and the gust events versus wind accelerations $\dot{V}_{\infty,j}$ are plotted for different velocities $V_{\infty,i}$ in the right graph of Fig. 11. Four initial wind speeds $V_{\infty,i}$ are here considered, as representative of wind turbine operation in an urban site: 4 m/s and 6 m/s (close to the cut-in wind speed), 8 and 9 m/s. For each $V_{\infty,i}$, the selected wind speed set is limited to the range $V_{\infty,i} - 0.25\text{ m/s} \leq V_{\infty,i} \leq V_{\infty,i} + 0.25\text{ m/s}$ and a number n of gusts are recognised.

The global energy content E_{TOT} of the wind accounts for any wind speed transition in the time Δt and can be quantified according to the equation:

$$E_{TOT} = \frac{1}{2} \rho \sum_{i=1}^n \frac{V_{\infty,i}^3 + (V_{\infty,i} + \dot{V}_{\infty,i} \Delta t_i)^3}{2} \Delta t_i \tag{3}$$

The energy content E_j of the gust is estimated according to the equations:

$$E_j = E_{\dot{V}_{\infty,j}} + E_0 \tag{4}$$

$$E_{\dot{V}_{\infty,j}} = \frac{1}{2} \rho \sum_{i=1}^n \frac{(\dot{V}_{\infty,i} \Delta t_i)^3}{2} \Delta t_i \quad \text{where} \quad \dot{V}_{\infty,i} \leq \dot{V}_{\infty,j} \tag{5}$$

$$E_0 = \sum_{i=1}^n E_{0,i} = \frac{1}{2} \rho \sum_{i=1}^n V_{\infty,i}^3 \Delta t_i \tag{6}$$

Two situations can be recognised:

- E_j/E_{TOT} is equal to 1, when the turbine is taking full advantage from all the gusts (under the hypothesis of ideal wind turbine, i.e. all $\dot{V}_{\infty,j}$ can be tracked and $\dot{V}_{\infty,j} = \dot{V}_{\infty,i}$);
- $E_j/E_{TOT} \leq 1$, only a partial gust energy exploitation is possible.

Figure 11 shows that if no gust can be tracked at all but the turbine is able to fully exploit the steady deterministic part of the wind resource, the maximum energy fraction harvestable on the site ranges from $E_0/E_{TOT} = 0.51$ at 4 m/s to 0.74 at 10 m/s.

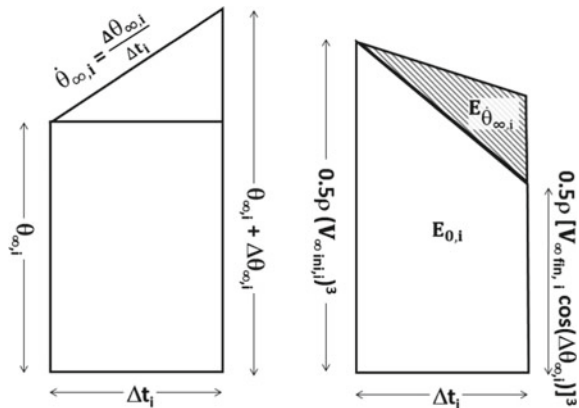
The results show that, for instance, in order to increase the energy exploitation at 6 m/s from $E/E_{TOT} = 0.61$ to 0.73 (a gain of about 20%), the wind turbine has to track all the accelerations from 0 up to 0.7 m/s^2 . Similarly, an energy gain of about 20% at 8 m/s requires the capability to process all the gusts from 0 up to 0.8 m/s^2 , and at 10 m/s from 0 up to 1.1 m/s^2 . Higher energy gains can be achieved by an higher range of “capturability” of gusts for any wind speed.

3.4 Energy Exploitation Under Wind Direction Variation

Analogously to the previous paragraph, energy exploitation under wind direction changes can be analysed by the model of an ideal turbine capable to yaw instantaneously to provide the maximum wind component perpendicular to the rotor plane, i.e. keeping zero misalignment $\Delta\theta$ between wind and rotor plane ($\cos\theta = 1$). Figure 12 left shows a schematic representation of a wind directional gust, characterised by an initial wind speed direction θ_{∞} , a duration time Δt , and a final wind speed direction $\theta_{\infty} + \Delta\theta_{\infty}$. In the right sketch the single directional gust presents a reduction of the wind speed magnitude, from $V_{\infty ini,i}$ to $V_{\infty fin,i}$.

All directional gusts represented in the frequency distribution of Fig. 6 are statistically evaluated, starting from the absolute value of their displacement θ_{∞} . For each

Fig. 12 Schematic representation of the i th directional gust, its acceleration $\dot{\theta}_{\infty,i}$, duration time Δt_i , initial $\theta_{\infty,i}$ and final direction $\theta_{\infty,i} + \Delta\theta_{\infty,i}$ (left), and its qualitative specific energy content (right, shaded area)



V_∞ , the selected displacement set is limited to the range $V_\infty - 0.25 \text{ m/s} \leq V_\infty \leq V_\infty + 0.25 \text{ m/s}$ and a number n of directional gusts are recognised.

For every wind speed $V_{\infty ini,i}$, the range of displacement rates $\dot{\theta}_{\infty,j}$ are divided into m bins of $3^\circ/\text{s}$, and the kinetic energy content E_j of the directional gusts contained in each j -bin can be seen once more as a sum two terms (similarly to the right scheme of Fig. 10) for the simplest case of a single i th event:

$$E_j = E_{\dot{\theta}_{\infty,j}} + E_0 \tag{7}$$

$$E_{\dot{\theta}_{\infty,j}} = \frac{1}{2} \rho \sum_{i=1}^n \frac{V_{\infty fn,i}^3 - [V_{\infty fn,i} \cos(\Delta\theta_{\infty,i})]^3}{2} \Delta t_i \quad \text{where } \dot{\theta}_{\infty,i} \leq \dot{\theta}_{\infty,j} \tag{8}$$

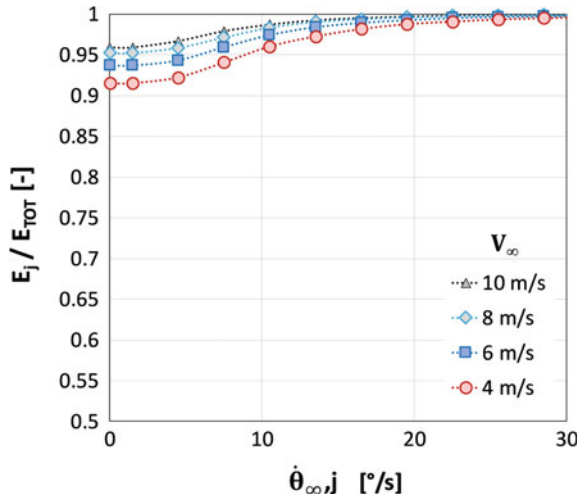
$$E_0 = \sum_{i=1}^n E_{0,i} = \frac{1}{2} \rho \sum_{i=1}^n \frac{V_{\infty ini,i}^3 + [V_{\infty fn,i} \cos(\Delta\theta_{\infty,i})]^3}{2} \Delta t_i \tag{9}$$

The global energy content E_{TOT} of the wind includes every directional transition and can be quantified according to the equation:

$$E_{TOT} = \frac{1}{2} \rho \sum_{i=1}^n \frac{V_{\infty ini,i}^3 + V_{\infty fn,i}^3}{2} \Delta t_i \tag{10}$$

The cumulative normalised energy content E_j/E_{TOT} versus wind accelerations $\dot{V}_{\infty,j}$ is shown in the right graph of Fig. 13 for the selected velocities $V_{\infty,i}$ of 4, 6, 8 and 10 m/s. If no directional gust can be tracked at all, the energy harvesting on the

Fig. 13 Cumulative representation of the energy exploitation rate E_j/E_{TOT} as a function of wind direction variance bin $\dot{\theta}_{\infty,j}$ for four selected speeds V_∞



site corresponds to $E_0/E_{TOT}=0.91$ at 4 m/s up to 0.96 at 10 m/s. Comparing these results with the ones shown in Fig. 11, it is clear that the ability of the turbine to adapt the rotational speed to the wind speed is far more important than a prompt yawing.

4 Conclusions

The wide data measurement campaign at the test site of the University of Trento allowed to characterise the distribution of wind accelerations and wind direction changes for a typical urban or sub-urban site at 18 m a.g.l. The presented elaborations can serve as a reference database to set proper boundary conditions for wind turbine design and performance evaluation.

90% of gust duration lasts less than 2.5 s. Wind positive and negative accelerations probability are well distributed and symmetrical around zero, and accelerations tend to be higher at higher wind speeds. An accurate correlation was found between frequency of a given gust magnitude and the wind initial intensity from which the gust progresses.

90% of wind direction change has a displacement lower than 30 °/s. Also direction changes appear symmetrical regardless to wind speed intensity, and the probability of a given displacement is only weakly dependent on wind speed. This dependence is even less evident for the angular acceleration.

The impact of wind intensity variation and direction change on energy harvest is evaluated by resorting to the model of an ideal turbine: it quantifies the penalty in terms of energy harvest for different degrees of ability of the rotor to track gusts and wind direction changes. It is apparent that the penalty is higher when gust tracking is of concern, compared to yaw tracking. By considering that real turbines suffer from non ideal behaviour in terms of rotor angular acceleration/deceleration and yawing acceleration/deceleration, real operating losses are expected to be higher compared to the present ideal turbine model. Direct analyses on real performances penalty of the wind turbines installed at the test field, which are currently in progress, seem to confirm such considerations. As general consequences, as far as the same diameter is of concern, the VAWT architecture, being characterised by a higher inertia compared to its horizontal axis counterpart, is more penalised in tracking the maximum power by rotor acceleration and deceleration. The loss of energy relative to yaw tracking is lower, and despite the claimed ability of VAWTs to track any wind direction, this characteristic seems to be overwhelmed by the limited acceleration and deceleration capability of this architecture, leading intrinsically to poorer infield performances.

References

1. Stankovic S, Campbell N, Harries A (2015) *Urban wind energy*. Routledge
2. Mertens S (2006) *Wind energy in the built environment*, Multi-science Publishing, United Kingdom
3. Encraft, Warwick wind trials final report. Available from <http://www.microwindturbine.be>. Accessed 9 Mar 2018
4. Mertens S, van Kuik G, Van Bussel G (2013) Performance of an H-Darrieus in the skewed flow on a roof. *Trans ASME* 125:434. <https://doi.org/10.1115/1.1629309>.
5. Kooiman SJ, Tullis SW (2010) Response of a vertical axis wind turbine to time varying wind conditions found within the urban environment. *Wind Eng* 34(4):389–401
6. Battisti L, Raciti Castelli M, Brighenti A, Dell'Anna S (2017) The down side of inertia for VAST. *Kleinwindkrafttagung 2017*, Munich (DE), 4–5 Oct 2017
7. Ionescu D, Battisti L, Dell'Anna S, Benini E (2013) The influence of turbulence on the power curve at small power urban wind turbines. In: *INCER 2013 conference*, 20–22 June 2013, Bucharest (RO)
8. Trivellato F, Battisti L, Miori G (2012) The ideal power curve of small wind turbines from field data. *J Wind Eng Ind Aerodyn* 107–108(2012):263–273. <https://doi.org/10.1016/j.jweia.2012.04.026>
9. IEC 61400-12: Wind-turbine generator systems. Part 12: wind-turbine power performance testing
10. Van der Hoven I (1957) Power spectrum of horizontal wind speed in the frequency range from 0.0007 to 900 cycles per hour. *J Meteorol* 14:160–164
11. Bashirzadeh Tabrizi A, Whale J, Lyons T, Urmee T, Peinke J (2017) Modelling the structural loading of a small wind turbine at a highly turbulent site via modifications to the Kaimal turbulence spectra. *Renew Energy* 105:288–300
12. Wind turbines test field of the University of Trento (IT). <http://www.eolicotrento.ing.unitn.it>